

**ACCELERATED TESTING OF TIDAL
TURBINE MAIN BEARING IN A FULL
SCALE NACELLE TEST RIG**



KARIKARI-BOATENG KWAKU AMPEA

A thesis submitted in partial fulfilment of the requirements for the award of an
Engineering Doctorate

University of Exeter

2016

IDCORE

This thesis is submitted in partial fulfilment of the requirements for the award of an Engineering Doctorate, jointly awarded by the University of Edinburgh, the University of Exeter and the University of Strathclyde. The work presented has been conducted under the industrial supervision of the Offshore Renewable Energy (ORE) Catapult as a project within the Industrial Doctoral Centre for Offshore Renewable Energy.



Declaration

I hereby declare that except where specific reference is made to the work of others, the contents of this dissertation are original and have not been submitted in whole or in part for consideration for any other degree or qualification in this, or any other University. This dissertation is the result of my own work and includes nothing which is the outcome of work done in collaboration, except where specifically indicated in the text.

KARIKARI-BOATENG KWAKU AMPEA

2016

Acknowledgements

I would like to express my sincere gratitude to Dr Chong Ng and Professor. Lars Johanning for their profound support encouragement, and leadership throughout my research project. I would also like to acknowledge Professor Markus Mueller and Professor Nigel Barltrop for their guidance and support. I am gratefully to my colleagues at ORE Catapult who were very supportive, encouraging and have contributed to the wonderful environment which allowed be to successfully conduct my research. My special thank you goes to Mr Robert Fox of ORE catapult for the many discussion and presentations we had over drivetrain testing activities.

I gratefully acknowledge my fellow IDCORE cohort members, Alberto, Gabriel, Raffaello and Rebecca who have been a great bunch, and with whom I shared a friendly network which encouraged each other throughout the course.

Finally I would like to thank my whole friends and family, for the support, encouragement and prayers which have helped me on my way thus far.

This research was funded by the Energy Technologies Institute (ETI) and the RCUK Energy Programme for the Industrial Doctoral Centre for Offshore Renewable Energy (Grant number EP/J500847/1) and is gratefully acknowledged

Abstract

Tidal Energy is one of the growing renewable energy technologies that is aimed at tackling global energy challenges. The Horizontal Axis Tidal Turbine (HATT) is an in-stream Tidal Energy Converter (TEC) which extracts kinetic energy from tidal flows. These tidal turbines face many reliability challenges due to their complexity, harsh operating environment and low accessibility. One of the component contributing significantly to the reliability of a TEC is the bearing supporting the rotating shaft within the nacelle. The reliability assessment of this component is essential during the design process and before their eventual deployments. This work describes shaft bearing reliability assessment procedures.

In recent years, the Offshore Renewable Energy (ORE) Catapult's National Renewable Energy Centre has developed a dedicated multi axis test facility for full scale testing of tidal turbine nacelles and components (i.e. Nautilus). This work presents a methodology for testing tidal turbine shaft bearings in a representative manner in the full scale nacelle test rig, Nautilus.

Two aspects are considered, namely the damage assessment and the damage replication in an accelerated manner. The damage assessment process considers the global loading on the shaft bearing and a Rigid Dynamics (RD) model has been applied to identify the local bearing loads. Local loads are converted to stress enabling the identification of stress-life relationship and bearing damage.

The damage replication process is aimed to evaluate the 20 year damage and the Acceleration by Phase-shift (AbP) method has been developed to accelerate the cumulative damage. The AbP method enables the assessment of performance characteristics of shaft bearings in a laboratory environment, reducing failure rates, validate performance in a cost effective manner by reduced testing times. Within this work, novel processes for shaft bearing reliability assessments and demonstration are suggested and it concludes with the presentation of a recommended test plan for carrying out accelerated tests on a full scale bearing.

Contents

Chapter 1	Background.....	1
1.1	Aims and Objectives.....	3
1.1.1	Aim	3
1.1.2	Objectives	3
1.2	Methodology.....	4
1.3	Thesis structure/ layout.....	9
Chapter 2	Literature Review	11
2.1	Tidal Energy	11
2.1.1	Vertical Axis Tidal turbines.....	12
2.1.2	Horizontal Axis Tidal Turbine.....	12
2.1.3	Tidal Turbine Drivetrain Components.....	13
2.2	Tidal Environmental	14
2.2.1	Tidal dynamics.....	14
2.2.2	Velocity profile.....	19
2.2.3	Directionality of the flow.....	20
2.2.4	Turbulence	20
2.2.5	Wave climate	23
2.2.6	Vertical static Pressure Variation.....	25
2.2.7	Cavitation.....	26
2.2.8	Dynamic Modelling of Tidal Turbine.....	29
2.3	Reliability	30
2.3.1	Structural Reliability.....	31
2.3.2	Fatigue assessment.....	34
2.3.3	Reliability Prediction	40
2.3.4	Failure rate prediction.....	43
2.3.5	System Modelling.....	47
2.3.6	Test methodologies.....	52
2.3.7	Drive train component reliability.....	55

2.4	Rolling Bearings	56
2.4.1	Types of rolling element bearings.....	56
2.4.2	Bearing Geometries	59
2.4.3	Bearing Failure modes	60
2.4.4	Static Load distribution radial roller bearings	71
2.4.5	Contact Mechanics.....	73
2.4.1	Dynamic Bearing simulations.....	86
2.4.2	Rolling Contact Fatigue (RCF analysis).....	88
Chapter 3	Main Shaft Load Case Evaluation	99
3.1	Introduction.....	99
3.2	Generic Tidal turbine.....	100
3.3	Flow Speed Variation	102
3.4	Flow field modelling.....	105
3.4.1	Super positioning of Wave orbital velocities.....	108
3.5	Influence of Turbulence Drivetrain Loads.....	109
3.5.1	Effect of turbulent eddy components on main shaft loads.....	121
3.6	Influence of Wave action Main Shaft Loads	126
3.7	Influence of velocity Shear profile.	128
3.8	Summary of Main Shaft Load characteristics.....	131
3.8.1	F _x -axial thrust force.....	132
3.8.2	F _y -lateral force.....	132
3.8.3	F _z vertical force	133
3.8.4	M _x -torque	133
3.8.5	M _y - bending moment about lateral plane	133
3.8.6	M _z - Bending moment about vertical plane.....	133
3.9	Potential effect of Cavitation	134
3.10	Conclusions.....	137
Chapter 4	Bearing Component Load Assessment.....	139
4.1	Introduction.....	139
4.2	Main Shaft bearing system	139
4.2.1	Bearing geometry.....	141
4.3	Numerical modelling	142
4.3.1	Rigid dynamics modelling.....	142
4.3.2	Rigid Dynamics Bearing model.....	142
4.3.3	Rigid dynamics Results.	148
4.4	Particulate modelling.....	161
4.4.1	Contact modelling.....	162

4.4.2	Contact modelling results	167
4.5	Bearing Damage Assessment.....	180
4.5.1	Stress aggregation in elemental bearing inner race volumes	182
4.5.2	Linear Damage Accumulation	191
4.6	Stress life method	197
4.7	Conclusion	197
Chapter 5	Accelerated Test Planning	199
5.1	Introduction.....	199
5.2	Full Scale Marine Drivetrain Test Rig.....	200
5.3	Popular Accelerated Test Plan for Tidal Turbine Drivetrains	202
5.4	Damage acceleration.....	206
5.4.1	Damage acceleration by increase in load magnitude	207
5.4.2	Damage acceleration by changing load signal.....	208
5.4.3	Influence of axial load.	217
5.5	Limitations of acceleration methods.....	217
5.6	Conclusion	219
Chapter 6	Accelerated testing –a case study	221
6.1	Introduction.....	221
6.2	Damage evaluation	221
6.2.1	Design load cases.....	222
6.2.2	Bearing component Loads	225
6.2.3	Bearing component stresses.....	231
6.2.4	Inner race damage profile.	233
6.2.5	Velocity bin size sensitivity analysis	235
6.3	An accelerated test plan for tidal turbine main bearings.....	238
6.3.1	Maximum test load & design load	239
6.3.2	Fatigue test plan development	241
6.3.3	Generalised test plan for main bearings.....	252
Chapter 7	Conclusions.....	257
7.1	Introduction.....	257
7.2	Main shaft load case evaluation.....	258
7.3	Bearing component load analysis	259
7.4	Accelerated test methodologies for turbine main bearings.....	260
7.5	Future work.....	261
Chapter 8	References.....	1
Appendix A	Publications.....	A-2
Appendix B	Tidal Turbine Modelling.....	B-4

B.1	Turbine Blade properties	B-4
B.2	Sample Aerodyne input file	B-8
B.3	Sample FAST input file	B-9
Appendix C Rigid Dynamics Input Files		C-15
C.1	Python Code Input File	C-15

List of Figures

Figure 1.1– Drivetrain Test rig	3
Figure 1.2– Methodology Flowchart	7
Figure 1.3– Shorter alternative Methodology Flowchart.....	8
Figure 2.1–Vertical axis Tidal turbine	12
Figure 2.2–Horizontal axis Tidal turbine.....	13
Figure 2.3– Components of wind (or tidal) turbine drivetrain [5].....	14
Figure 2.4–: Schematic of celestial bodies and their influence on tidal dynamics ..	15
Figure 2.5–: The effect of predicting tides with different constituents.....	17
Figure 2.6–: Variation of mean flow speed at Fall of Warness[11].....	18
Figure 2.7– Variation of velocity with height above sea bed (seabed fixed turbine)	19
Figure 2.8– velocity profile at fall of Warness tidal energy site; source[14].....	19
Figure 2.9– Average Power density at Fall of Warness Tidal site; [14].....	20
Figure 2.10– Variation of TKE with frequency[25].....	23
Figure 2.11– Wave scatter diagram[12].....	24
Figure 2.12– Simulated Wave climate frequency distribution[12].....	25
Figure 2.13- Conditions for cavitation inception.....	26
Figure 2.14– Influence of added mass force on thrust force.....	28
Figure 2.15– Shaft coordinate referencing	30
Figure 2.16– Failure rate and associated downtime for wind turbine components[43]	31
Figure 2.17– Interference diagram of strength and load.....	33
Figure 2.18– Fatigue behaviour of steel and aluminium [75].....	35
Figure 2.19: Variation of crack size with stress intensity factor.....	37
Figure 2-20: Material S-N curve.....	40
Figure 2.21– Bathtub curve representing failure rate evolution in a product lifetime	43
Figure 2.22–Typical stress range for components.....	54

Figure 2.23– (a) Underlying distributions at different stress levels (b) Mapping high stress data to use stress data different acceleration models	55
Figure 2.24–Typical parts of a components bathtub curve where reliability tests may apply	55
Figure 2.25– Common types of ball bearings.....	57
Figure 2.26– Common types of roller bearings	59
Figure 2.27– Typical components of a rolling element bearing	60
Figure 2.28–Bearing Damage classification as per ISO 15243[96]	61
Figure 2.29–Schematic representation of pitting and spalling[97].....	62
Figure 2.30– False Brinelling on bearing raceway [98]	64
Figure 2.31– Micropitting of a 230/600 series spherical roller main.....	66
Figure 2.32– scuffing on the high speed stage of wind turbine [107]	67
Figure 2.33– Effect of internal clearance on load distribution.	73
Figure 2.34– Moments on main shaft(output of elastic simulation).....	74
Figure 2.35– Moments on main shaft(output of elastic simulation).....	75
Figure 2.36– Physical description of the source of Heathcoat slip in a spherical roller bearing.....	78
Figure 2.37–:Traction distribution in Carter’s theory[136].....	79
Figure 2.38–:Comparison between the tangential stress distributions for 3D contacts[136].....	81
Figure 2.39–:Traction creepage curve for theoretical frictional contacts	81
Figure 2.40–:Pressure distribution and film-thickness variation in an EHD contact83	
Figure 2.41–: Lubrication regimes.....	84
Figure 2.42–: traction properties.....	85
Figure 2.43– Various levels at which rolling contact fatigue has been studied[157] .	
.....	89
Figure 2.44–: Common Bearing failure causes	91
Figure 2.45–: Duplex SN Curve of JIS SUJ2 bearing steel[170]	92
Figure 2.46–: Rolling Contact fatigue SN curve for M50-Nil bearing steel[173] ...	93
Figure 2.47–: SN Curve for JIS:SUJ2 steel in axial loading [177].....	94
Figure 2.48– Designs for bearing endurance testers[94]	96
Figure 3.1–: Power curve of generic 1 MW turbine	101
Figure 3.2–: Doppler Current Profiler measurement of tidal Velocity	102
Figure 3.3–: Comparison of measured tidal flow speeds with TTide predicted flow speeds.....	103
Figure 3.4–: Comparison of measured tidal flow speeds with TTide predicted flow speeds.....	103
Figure 3.5–: predicted tidal velocities over a year	104
Figure 3.6–: Probability distribution of flow velocities.....	105

Figure 3.7– Axial variation of flow speeds.....	107
Figure 3.8– Lateral variation of flow speeds	107
Figure 3.9– Axial flow speeds with a superimposed 1.5m, 7.5 period wave on a 2.5m/s flow speed.	109
Figure 3.10– Time series of axial flow speeds at hub height for a range of turbulence intensities.	110
Figure 3.11– Time series of lateral flow speeds at hub height for a range of turbulence intensities.	111
Figure 3.12– Time series of vertical flow speeds at hub height for a range of turbulence intensities.	111
Figure 3.13– Time series of axial thrust force at different turbulence intensity levels.	112
Figure 3.14– Time series of Lateral Shear force at different turbulence intensity levels.....	113
Figure 3.15– Time series of Vertical Shear force at different turbulence intensity levels.....	113
Figure 3.16– Time series of Torque at different turbulence intensity levels.	114
Figure 3.17– Time series of MY bending moment at different turbulence intensity levels.....	115
Figure 3.18– Time series of MZ bending moment at different turbulence intensity levels.....	115
Figure 3.19– Time series of Torque at different turbulence intensity levels.	116
Figure 3.20– Time series of shaft speed at different turbulence intensity levels..	117
Figure 3.21– Effect of turbulence intensity on RMS shaft loads at expected velocity range	118
Figure 3.22– Effect of turbulence intensity on standard deviation shaft loads at expected velocity range	119
Figure 3.23– Effect of turbulence intensity on percentage increase RMS shaft loads at expected velocity range	120
Figure 3.24– Effect of turbulence intensity on increase in standard deviation of shaft loads at expected velocity range	121
Figure 3.25– Influence of turbulence components on RMS of main shaft Loads.	123
Figure 3.26– Influence of turbulence components on standard deviation of main shaft Loads.....	124
Figure 3.27– Influence of turbulence components on mean of main shaft Loads.	125
Figure 3.28– RMS of axial force for variation of waves	127
Figure 3.29– range of axial forces for the variation of waves	128
Figure 3.30– Lateral variation of flow speeds	129
Figure 3.31– Effect of shear profile power exponent on mean drivetrain loads....	130
Figure 3.32– Effect of shear profile power exponent on mean drivetrain loads....	131

Figure 3.33– Variation of pressure along the chord of an S1012 aerofoil at a 6° angle of attack.....	135
Figure 3.34: Loss of coefficient of lift with cavitation number for different angles of attack.....	136
Figure 3.35– Variation of cavitation number along blade annuli	136
Figure 3.36– Power generated by a single blade under cavitation.....	137
Figure 4.1- CAD Rendering of main bearing system	140
Figure 4.2- Static representation of moment load on bearing system.....	141
Figure 4.3- Rendering of the components of the 230/630- w33 series bearing....	141
Figure 4.4- A) schematic of bearing model B) Rendering Rigid body simulation of bearing	142
Figure 4.5- Schematic of rolling element representation.....	144
Figure 4.6-Bearing model	145
Figure 4.7–Bushings Joint Stiffness and Damping	146
Figure 4.8–Variation of rolling element load when subjected to 200kN of radial load	148
Figure 4.9–Variation of rolling element load when subjected to 200kN of radial load	149
Figure 4.10–Variation of rolling element load when subjected to 100kN of radial load and 5kN axial force.....	149
Figure 4.11– Variation of rolling element load when subjected to 100kN of radial load and 10kN axial force.....	150
Figure 4.12– Variation of rolling element load when subjected to 100kN of radial load and 15kN axial force.....	150
Figure 4.13– Variation of rolling element load when subjected to 100kN of radial load and 20kN axial force.....	151
Figure 4.14– Variation of rolling element load when subjected to 100kN of radial load and 25kN axial force.....	151
Figure 4.15– Variation of rolling element load when subjected to 100kN of radial load and 50kN axial force.....	152
Figure 4.16–Specified bearing loads is static conditions.....	153
Figure 4.17–Dynamic force on static rolling element bearing at a static load.....	153
Figure 4.18–Dynamic force on rollers when bearing is subjected to a 200 kN static load and a constant rotational speed	154
Figure 4.19–Loads on a bearing rotating at constant speed with constant rotation of radial load	155
Figure 4.20–Variation of roller loads when subjected to 200kN rotating radial load on a stationary bearing.....	156
Figure 4.21– Loads on a bearing rotating at constant speed(reverse direction to Figure 4.19) with constant rotation of radial load.....	157

Figure 4.22–Variation of rolling element load when subjected to 200kN of radial load and 5kN axial force.....	157
Figure 4.23– Loads on a bearing rotating at constant speed(twice the speed of Figure 4.19) with constant rotation of radial load.....	158
Figure 4.24–Variation of rolling element load when subjected to 200kN rotating radial load and twice the rotating frequency.....	159
Figure 4.25–Random dynamic bearing load.....	160
Figure 4.26–roller loads under random dynamic loads	161
Figure 4.27– Stress-strain relationship of materials	162
Figure 4.28– Symmetries of Finite Element Model of Contact.....	164
Figure 4.29– Symmetries of Finite Element Model of Contact.....	165
Figure 4.30– Summary of applied Boundary Conditions (B.C.)	166
Figure 4.31– Comparison of roller loads in whole contact model and half contact model	166
Figure 4.32–Contact implementation	167
Figure 4.33–Increase of contact length with roller load	168
Figure 4.34–Variation of roller contact stiffness with applied force	169
Figure 4.35–Hertzian vs FE contact deformation.....	170
Figure 4.36–Contact Annuli	171
Figure 4.37–Contact pressure at 160 kN roller load.....	172
Figure 4.38– Location of the Maximum Stress	173
Figure 4.39–Normal stress on an annulus of the inner race surface when under a 160 kN load	174
Figure 4.40–Comparison of FEM and Hertzian predictions of subsurface stresses at the middle of a roller.....	175
Figure 4.41– Comparison of FEM and Hertzian predictions of subsurface plane stresses at the middle of a roller.....	175
Figure 4.42– Comparison of FEM and Hertzian predictions of subsurface stresses at edge A of a roller	176
Figure 4.43–Comparison of FEM and Hertzian predictions of subsurface stresses at edge B of a roller	176
Figure 4.44–von-Mises stress variation along the length of the roller. This shows there is a very high stress concentration at both ends of the roller (i.e edge loading).	178
Figure 4.45– Comparison of force stress relationship (FE-mid: stress at middle of rolling element, FE- edge: edge loading, Hertzian: stress as calculated by (EQN 2.37).....	179
Figure 4.46–stress changes with load and distance from contact point	179
Figure 4.47–stress changes with load and distance from contact point	180
Figure 4.48: division of components into sections	181

Figure 4.49–Coordinate system definition for roller raceway contact.....	183
Figure 4.50–Variation of stress across contact showing the maximum stress is located subsurface and the high stress region is much smaller compared to the overall geometry	183
Figure 4.51–Variation of stress in circumferential direction for different depths when rolling element is subjected to 270 kN for force.....	184
Figure 4.52–Variation of stress in the circumferential direction for different depths when rolling element is subjected to a variation of forces.....	185
Figure 4.53–Variation of stress in circumferential direction for different depths when rolling element is subjected to 270 kN for force.....	186
Figure 4.54–Variation of stress in circumferential direction for different depths when rolling element is subjected to 270 kN for force.....	187
Figure 4.55–Modelling of circumferential stress variation with polinomial and exponential equations	187
Figure 4.56–Variation of stress in circumferential direction for different depths	188
Figure 4.57–stress variation in all the circumferential strips of the bearing (all strips in the circumferential direction).	189
Figure 4.58– Stress variation in roller bearing.....	189
Figure 4.59–Enlarged view of Stress Variation in roller bearing	190
Figure 4.60– stress history of single strip of inner race.....	191
Figure 4.61– load history on single strip of inner race	191
Figure 4.62– Rainflow cycle count matrix	192
Figure 4.63– Probability of failure of M50-Nil steel [188]	193
Figure 4.64– Probability of failure of M50-Nil steel [188]	193
Figure 4.65– Probabilistic S-N curve for JIS SUJ2 bearing steel.....	194
Figure 4.66– Rain flow damage matrix	195
Figure 4.67– Calculated bearing strip damage per day.....	196
Figure 4.68– Sample time to failure of bearing inner race	196
Figure 5.1– Test Setup at Nautilus Test Rig.....	201
Figure 5.2– Common method of accelerating testing of tidal turbines.....	203
Figure 5.3– Sinusoidal half cycle of a semidiurnal tide with a peak of 2.5 m/s and 3.5 m/s	204
Figure 5.4– Sinusoidal half cycle of a semidiurnal tide with a peak of 2.5 m/s and 3.5 m/s	205
Figure 5.5–Maximum loaded strip as a result of the resultant radial load direction.	210
Figure 5.6–Definition of strips A-D in Figure 5.7	212
Figure 5.7–Calculated inner race damage for a rang or ωr	212
Figure 5.8–Inner race stress history for a rang or ωr	214
Figure 5.9–Influence of parameter θr in bearing inner race damage	215

Figure 5.10–: Influence of parameter θg in bearing inner race damage	216
Figure 5.11– Influence of parameter ωg in bearing inner race damage	216
Figure 6.1–Velocity probability density function at the chosen tidal site	222
Figure 6.2–Hub Height flow speeds at rated conditions(average 2.5m/s)	223
Figure 6.3– Low Speed Shaft Forces at rated speed(2.5 m/s)	223
Figure 6.4–Low Speed Shaft Moments at rated speed(2.5 m/s)	224
Figure 6.5– Distribution of drivetrain loads and their frequency of occurrence....	225
Figure 6.6–Low Speed Shaft loads at rated speed(2.5 m/s).....	226
Figure 6.7–Low Speed shaft moments at rated speed(2.5 m/s)	226
Figure 6.8–Bearing downwind Row Roller load	227
Figure 6.9–Upwind Row Roller load.....	227
Figure 6.10–Bearing Load distribution at 60s at average speed of 0.5 m/s.....	228
Figure 6.11–Bearing Load distribution at 60s at average speed of 1 m/s.....	229
Figure 6.12–Bearing Load distribution at 60s at average speed of 1.5 m/s.....	229
Figure 6.13–Bearing Load distribution at 60s at average speed of 2 m/s.....	230
Figure 6.14–Bearing Load distribution at 60s at average speed of 2.5 m/s.....	230
Figure 6.15–Stress History of a single strip at 2.5 m/s tidal speed.....	232
Figure 6.16–Expanded view of stress history of inner race sections.....	232
Figure 6.17–Rainflow counting of stress history.....	233
Figure 6.18–Accumulated damage in 10 minutes for different operating speeds)	234
Figure 6.19–Predicted lifetime damage at individual average flow speed bins....	235
Figure 6.20–Predicted Damage for smaller tidal velocity bins.....	237
Figure 6.21–Summary of test procedure.....	239
Figure 6.22–Expanded view of stress history of inner race sections.....	240
Figure 6.23–Functional test profile showing loads as a percentage of device specification loads	242
Figure 6.24–Static radial force test profile 50% test radial load.....	243
Figure 6.25–Static radial and axial force test profile.....	244
Figure 6.26–Operational (temperature and vibration) characterisation test profile	245
Figure 6.27–Example of a dynamic test profile with varying speed, varying radial force magnitude and direction at a constant axial load.....	246
Figure 6.28–:Incurred damage for proposed testing loads.....	248
Figure 6.29–Estimated time to reach 20 year damage by using AbP method	249
Figure 6.30–Estimated Time to failure in testing under various testing condition	250
Figure 6.31–Accelerated fatigue test profile.....	251
Figure 6.32–Extreme loads test profile.....	252

Figure 7.1: Schematic for wear evolution evaluation tool..... 261

List of Tables

Table 2.1 – Ranking of tidal constituents	16
Table 2.2 -Turbulence Characteristics at tidal energy sites, adapted from[15]	21
Table 2.3: Statistics of wave action at tidal sites[12].....	24
Table 3.1 - Properties of generic 1 MW turbine	101
Table 5.1: Parameters ofNautilus Marine Test Rig	200
Table 5.2: NTL Operating Window.....	201
Table 6.1: Tabulated values of flow speed probabilities	236
Table 6.2: Maximum design loads.....	239
Table 6.3: Maximum Test loads	241
Table 6.4: summary of test plan for an accelerated testing campaign	254

Chapter 1 Background

Future energy supply faces two main challenges. With rising global energy demand there is a potential shortfall between supply and demand. In addition, there is strong evidence to suggest the carbon emissions from fossil fuels used in energy production may contribute to rapid climate change. With the majority of current production coming from fossil fuels, renewable energy is a promising solution to the global energy problem. This has led to ambitious targets such as the UK government's target of producing 20% of its electricity from Renewable sources by 2020 and a reduction of carbon dioxide emissions by 60% as compared to 1990 levels. In 2013, renewable energy constituted 14.9 of the UK's electricity production[1]. Global and regional targets for carbon emissions and use of renewable energy means successful commercialisation of renewable energy devices is more pressing than ever.

To satisfy the increasing global energy demand while reducing the impact of energy use on the earth's climate, renewable forms of energy are being frantically pursued throughout the world. So far, major focus on delivering the renewable energy has focused on solar, wind and, biofuels. More recently, the untapped energy in the earth's oceans has caught the public eye drawing more and more attention to technologies such as wave and tidal energy.

One of the renewable energy sources at the forefront of the renewable energy surge is tidal energy. Tidal energy is a very promising source of renewable energy because of its high degree of predictability. Primarily, two approaches for extracting energy from the tides can be distinguished. The first utilises conventional water turbines to extract energy from the potential energy created by the elevating of water during the tidal cycle. In recent times, efforts are being made to harness the renewable and sustainable energy from free flowing tidal currents in the world's

oceans. This type of tidal energy extraction (often called Tidal stream energy) has taken roots in the 21st century compared to tidal range which tends to require very high capital and possess severe ecological risks.

Currently, there are no fully operational commercial devices but there are many pre-commercial prototypes undergoing testing. A recent investigation about the risks facing wave and tidal technologies revealed one of the primary technical risks arises from our understanding of the reliability of devices throughout their lifetime [2].

Several researchers have investigated the reliability of tidal turbine rotor blades [1][2][3]. Very little effort has been made in comparison to quantifying the reliability of tidal turbine drivetrain components. Iliev and Val [4] conducted failure rate assessments for tidal turbine drivetrains by considering failure rate of individual components. In Delorm et al [5], the reality of different tidal turbine configurations was analysed which depended on system components.

Concern has been raised about the lack of reliability data for tidal energy converters by [6] [7][5]. In reported cases, surrogate data from the wind industry has been suggested as a possible source of similar data because of the similarity between the two technologies. These studies adopted environmental adjustment factors as advocated by [8]. Given that these adjustment factors are crude and were developed for electrical components, they may introduce errors into the analysis. The uncertainties surrounding the use of surrogate data and adjustment factors were addressed by including confidence bands [9]. The lack of commercial devices has contributed to the drought in reliability data for tidal devices.

In many industries where high levels of reliability is required but very little data exists, testing has been suggested for demonstrating the reliability of components, assemblies and sub-assemblies.

To reduce risks associated with tidal energy, the National Renewable Energy Centre UK has developed a marine turbine test rig (i.e. Nautilus). In addition to the dynamometer feature that allows controlled torque and speed to be applied to the test turbine, the test rig with its bespoke Force Application System (FAS) is able to replicate non-torque loads on the tidal turbine drivetrains in all 6 Degrees of Freedom (DoF). The test rig aims to demonstrate the reliability, functionality and

performance of tidal turbines through testing. However, there are currently no globally agreed procedures for testing tidal turbine drivetrains to prove their functionality, performance and reliability. Given that tidal devices in general are designed to have a service life of 20 years, an accelerated testing methodology is more desired for compressing test time.



Figure 1.1– Drivetrain Test rig

1.1 Aims and Objectives

1.1.1 Aim

This project aims to develop an effective methodology for proving the reliability and performance of tidal turbine drivetrains with focus on accurately representing damage on main bearings. The research will present a method to accelerate the degradation of the main bearing thereby reducing testing time.

1.1.2 Objectives

- Set out a methodology for assessing main shaft loads
- Identify primary loading on drivetrain main shaft
- Develop load cases for bearing based on main shaft loads
- Develop method for assessing bearing component loads
- Develop a methodology for assessing the lifetime fatigue damage on main bearings.
- Develop methodology for accelerating fatigue damage during testing

- Demonstrate the relevance for reliability demonstration
- Demonstrate the application of the proposed methodology in a realistic test plan

1.2 Methodology

The common reliability demonstration approach for tidal turbine drivetrains has shown some weaknesses unrepresentative damage and long test times. Consequently a new methodology for analysing and replicating the damage on bearing components is presented in this work. The inner race of the bearings is identified as the most susceptible to fatigue damage hence is the focus of this work. The methodology to address the aims and objective as highlighted in section 1.1 above is presented below. A flowchart which shows the proposed methodology can be found in Figure 1.2. The methodology is broken down into two sub components: Damage assessment and Damage replication.

Damage assessment process begins by analysing the conditions at a potential tidal site. Generally, Acoustic Doppler Current Profilers (ADCP) are utilised to obtain the potential flow fields at tidal sites for average energy yield calculation. This can also be utilised to analyse potential damage caused by tidal turbine. As ADCPs often collect statistics, the methodology highlighted here presents a process through which realistic flow field that are encountered by tidal turbines can be simulated.

Initially, Tidal Harmonic Analysis is performed to extract the long term velocity variation at the chosen tidal site. The method of bins as described by IEC 61400 is used to group the tidal velocities into bins. For each bin, a realistic flow field incorporating turbulence and wave action is generated. With the realistic flow field in hand, the impact it has on the tidal turbine performance and loading is analysed.

A generic 1 MW tidal turbine was developed for the analysis in this research. The turbine has pitching and yawing capabilities and is controlled with a variable speed controller. The dynamic behaviour of the turbine is analysed using the elastic Blade Element Momentum Code, FAST. Elastic-dynamic analysis using FAST delivers the global loading on the turbine thus the loading on the main shaft is a typical output.

To understand the localised loading due to the global loads, the main bearing of the tidal turbine is analysed using a rigid dynamics package. Rigid body simulations enable the computation of forces, moments and displacement of rigid bodies with less computational cost compared to Finite Element modelling (FEM). Unlike flexible body modelling (Via FEM) which discretises bodies into small element, each with its own set of degrees of freedom, rigid dynamics represent each body with a single 6DOF coordinate system. This enables analysis with lower computational cost.

The drawback of Rigid Dynamics(RD) compared to FE is that FE analysis yield stresses in the bodies. The geometric symmetry enables the roller bearing to be simulated by using a fraction of the whole model and saving on computational cost. A look up table is generated to relate the stresses to the forces. This delivers time varying stresses on bearing components which can be analysed further.

In a typical rolling element bearing with a rotating inner race, the inner race is subjected to the highest number of loading cycles. Consequently, the inner race generally has the highest risk of failure. As such this work focuses on the damage caused on the inner race.

The Stress-Life method via rainflow counting and miner's linear damage accumulation rule is a well-accepted technique for analysing High Cycle fatigue (HCF). Stress analysis is performed using the stress history of the inner race using the stress -life method. The inner race is discretised into elemental volumes in the circumferential direction. For each volume(called a strip) the stress history is extracted and the damage induced by the stress history analysed. This concludes the first of the two stages of the proposed methodology "damage evaluation"

Reliability tests sought to demonstrate, improve or quantify reliability goals. The second stage of the proposed methodology focuses in demonstrating the twenty year reliability of a main bearing by replicating the twenty year damage which must be sustained by the bearing. Conventional approaches which have been used to demonstrate reliability of tidal turbines have proved inaccurate and more accurate approaches are generally too slow

Accelerated testing is required to reduce the time required to apply the twenty year lifetime damage on a bearing in a practical and reasonable time frame. The conventional approach used to accelerate testing of bearings involves increasing the bearing load or speed. Although this is able to achieve a substantial level of acceleration, the reductions which can be achieved fall far short of the desired and practical level.

A new acceleration method, Acceleration by Phase-shift (AbP) is proposed to further accelerate testing. The technique which enables flexible control of how much damage is applied to sections of the inner race can reduce tests time significantly.

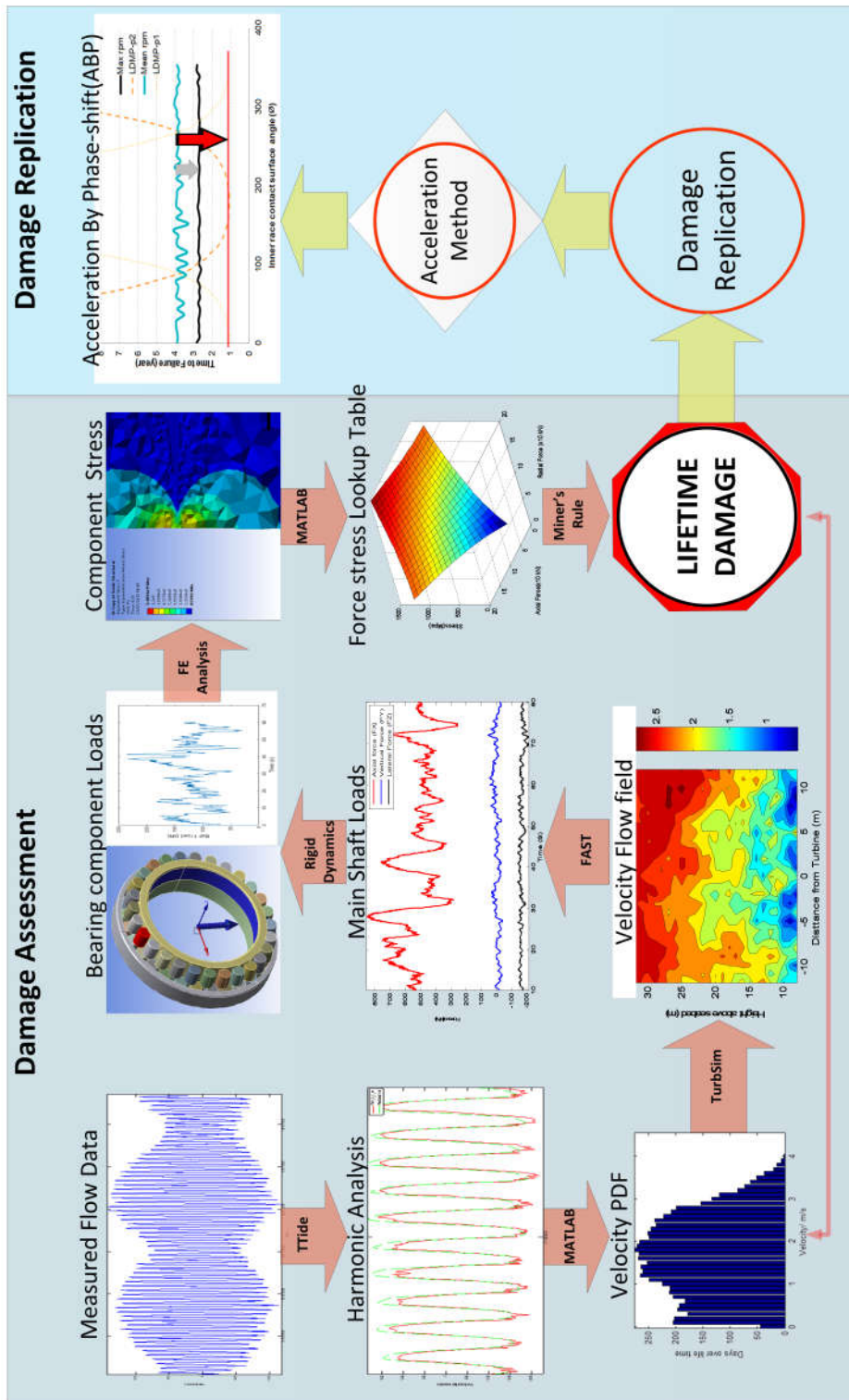


Figure 1.2– Methodology Flowchart

In most cases, device developers may not supply detailed turbine and site data for the holistic evaluation of the bearing damage. Instead, pre-calculated shaft load cases are supplied. In such cases, the flow chart depicted in Figure 1.3 shows the methodology for evaluating the bearing load cases. This contains extracted parts of the holistic methodology flow chart shown in Figure 1.2.

In this case, the shaft load cases are converted to local bearing components load, and then the finite element model translates the local loads into stress. The stress history is analysed to obtain which is used in conjunction with material SN data. Finally the evaluated damage can be replicated just as described above.

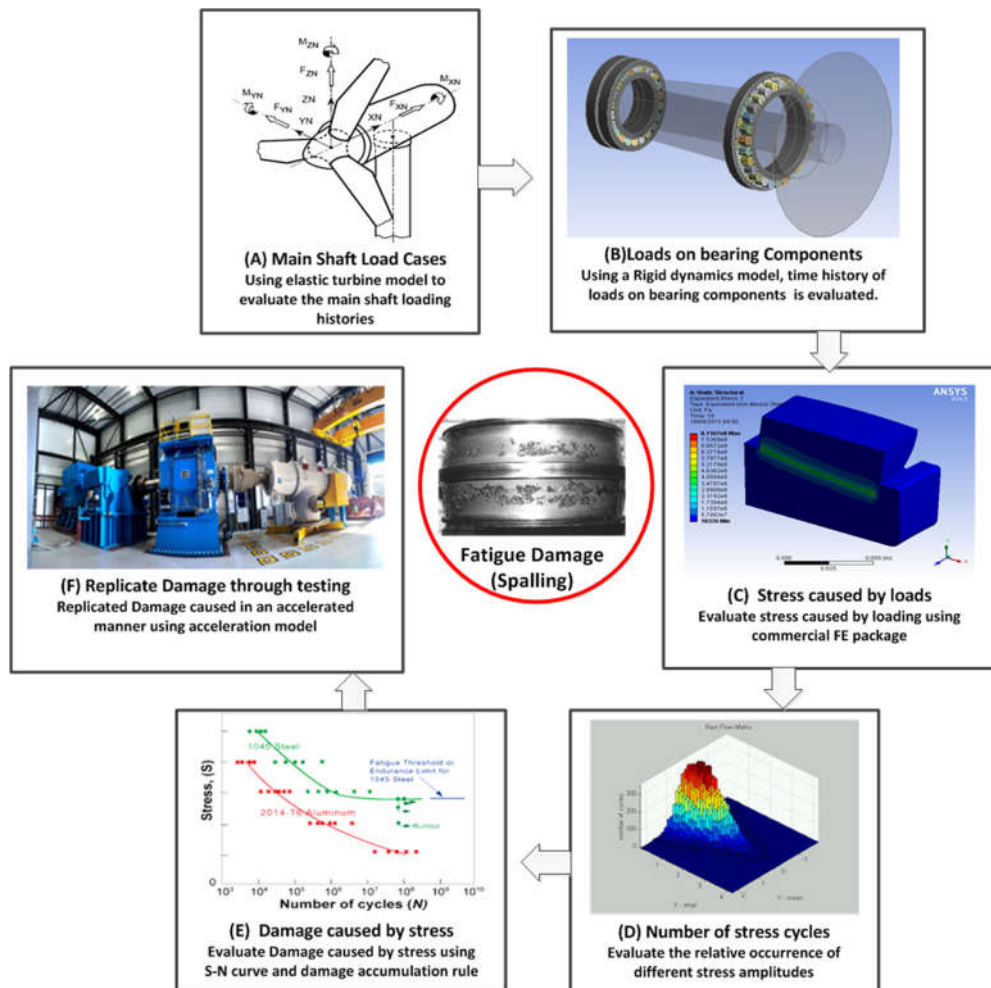


Figure 1.3– Shorter alternative Methodology Flowchart

1.3 Thesis structure/ layout

The work presented from here on is designed to demonstrate the methodology presented in Figure 1.2. 1.1 is dedicated to contextualising the work from the perspective of the literature. It focuses on the general background of the work carried out in the following chapters. First introducing tidal energy and tidal devices and the environments within which these are located before moving on to treat relevant reliability issues in Chapter 2.3. The following section chapter 2.4 discuss the types of rolling element bearings, their geometries life estimations and testing methodologies.

The main bearing which is the focus of this work supports the main shaft which is loaded due to the turbine's environment, components and control strategies. Chapter 3 focuses on analysing the loading on the main shaft and how they are derived. It further looks into the effect of some input parameters and their impact on the main shaft load and therefore the main bearings loads and life.

The main bearings itself consist several parts which are loaded in different ways. Section 4.2 introduces a potential bearing arrangement for a tidal turbine. Chapter 4.3 introduces a rigid dynamics model which is used to analyse the loading in individual bearing components. Chapter 4.4 discusses a Finite Element (FE) model which is used to obtain stresses on bearing components for a given load. Chapter 4.5 combines work in the previous sections to emulate the potential life of the inner race of the main bearing.

In Chapter 5, the different options for replicating the lifetime damage calculated in the previous chapter are presented. The chapter focuses on the application of a new approach (AbP) which accelerated the damage on bearing components by manipulating the phase difference between the maximum loaded roller and specific sections of the inner race.

A case study incorporating the work done in 1.1 to Chapter 5 is presented in Chapter 6. A potential test plan for such a bearing as discussed in this work is also presented. A critical discussion of the overall methodology is presented in Chapter 7, Chapter 7 also includes concluding remarks and future work.

Chapter 2 Literature Review

2.1 Tidal Energy

Nicholls-Lee and Turnock [1] define tides as the periodical rise and fall of the surface of the oceans and seas generated by the gravitational attraction and subsequent relative motion of the earth, moon and sun. Two distinctive types of tides exist depending on the moon's position in relation to the sun and earth; when the sun and moon are aligned the tide is a spring tide whereas when the moon is at right angles with the sun tide is a neap tide. Spring tides produce bigger tidal ranges (overall difference in height of water between high tide and low tide) which can be double the range of neap tides; thus spring tides can generate more energy than neap tides over the same amount of time.

Distinction is made between tidal technologies as either tidal range or tidal stream devices. Tidal range devices harness potential energy generated by tidal elevation, often by using a dam which captures the ocean water at high tides and releases it through turbines during low tides. Alternatively, tidal stream machines extract kinetic energy from the movement of a body of water under tidal action.

Tidal stream machines, also known as Tidal Energy Converters (TECs) can be characterised by their rotational axis orientation with regard to the water flow direction. According to the European Marine Energy Centre (EMEC), there are approximately 90 tidal developers around the world who use six main types of existing TECs namely: Horizontal Axis Turbine, Vertical Axis Turbine, Oscillating Hydrofoil, Enclosed tips, Archimedes Screw and Tidal Kites[2]. Out of these TECs the two most popular are the horizontal axis turbine and vertical axis turbine, both of which are reminiscent of submerged wind turbines. A short summary of the

major configurations is presented but more complete review of tidal energy technologies can be found in [2]–[4].

2.1.1 Vertical Axis Tidal turbines

When the rotational axis of turbine rotor lies on a vertical plane such that it is orthogonal to the incoming water stream, the turbine is referred to as a vertical axis turbine. A typical and popular example is Darrieus turbine as shown in Figure 2.1.

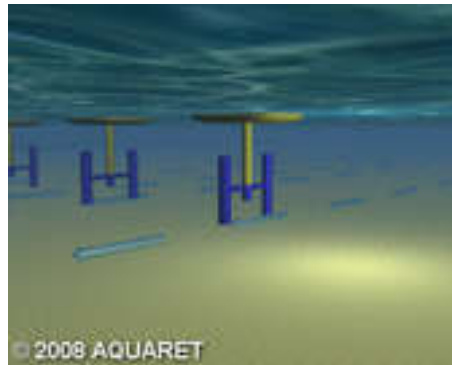


Figure 2.1–Vertical axis Tidal turbine

2.1.2 Horizontal Axis Tidal Turbine

The rotational axis of the horizontal axis turbine is horizontal to the water stream direction. Two types exist: the rotational axis of the first is parallel to the direction of water stream (Axial flow) whilst the rotational axis of the other is perpendicular to the water stream direction (Cross flow). The tidal stream causes the rotors to rotate around the horizontal axis and generate power. A typical Horizontal axis tidal turbine is shown in Figure 2.2.

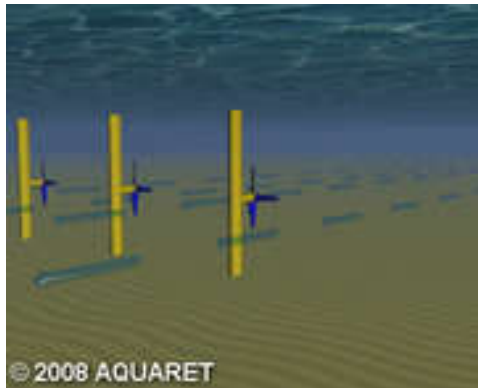


Figure 2.2–Horizontal axis Tidal turbine

Among the many devices used the most advanced regarding development is the horizontal axis turbine design. Many of these turbines are in full scale prototype developmental stage.

2.1.3 Tidal Turbine Drivetrain Components

Among the prototype turbines which are near commercialisation, the horizontal axis type which employ main bearings, a gearbox and a generator are the most common. In terms of configuration and components, these are quite similar to medium sized wind turbines. Figure 2.3 is a depiction of a wind turbine drivetrain. In fact all the components shown in Figure 2.3 are typically components of a horizontal axis tidal turbine.

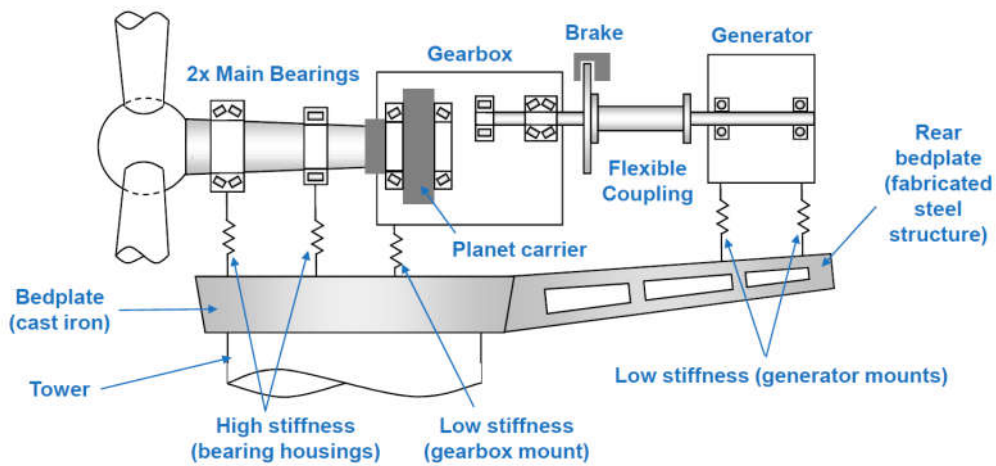


Figure 2.3– Components of wind (or tidal) turbine drivetrain [5]

Given the similarity in terms of configuration and operating principles between wind and tidal turbines, it is possible and reasonable to use experience in the wind industry to investigate the potential reliability issues that may occur in the tidal industry as has been done by [6][7].

2.2 Tidal Environmental

The environments in which tidal devices are placed have a profound influence on not only their energy capture but also their reliability. The least is the average flow velocity at the tidal site. This is generally governed by the factors discussed below.

2.2.1 Tidal dynamics

Tides are generated as the liquid oceans on the earth's surface are attracted by the gravitational field of celestial bodies. The gravitational fields cause the earth to bulge in the direction of the gravitational force thus creating tidal elevations as shown in Figure 2.4. The relatively short distance to the moon and the size of the sun make them the most influential gravitational forces exerted on the earth. The monthly revolution of the moon around the earth creates a monthly tidal pattern. From this, two primary tidal characteristics can be distinguished. When the gravitational force of the moon is in unison with the sun's gravitational force, their

synergetic effect causes a higher distortion of the ocean surface leading to a higher tidal elevation. In this case, a spring tide is observed. Conversely, the gravitational force of the sun and moon may counteract each other when they are at right angles and cause a lower tidal elevation called a neap tide. The gravitational force of other celestial bodies influence the tidal cycles. However their size and proximity limits their influence.

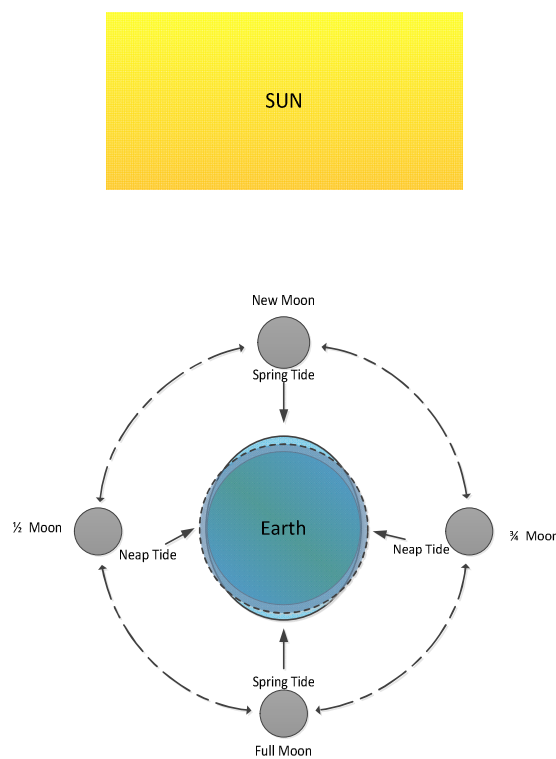


Figure 2.4–: Schematic of celestial bodies and their influence on tidal dynamics

Generally tidal elevations are dictated by celestial bodies. Nonetheless, local amphidromic systems, bathymetry and shape of the coast line may alter the dynamics of the tidal system locally. Locally rising tidal elevation is called a flood tide while the falling of the tidal elevation is called ebb tides. At the point at which flood tides change to ebb tides or vice versa, there exist a point where the tidal elevation is neither rising nor falling, creating a slack tide.

2.2.1.1 Harmonic Analysis

The variation of tidal elevations over time does not stay constant because of the movement of the earth and other celestial bodies. The influence of these movements on tides can be analysed by a harmonic analysis. The basic assumption behind tidal harmonic analysis is that the tidal variations can be represented by a finite number (n) of harmonic terms in the form.

$$(t) = v_n \cos(\sigma_n t - g_n) \quad (\text{EQN 2.1})$$

Here v_n is the amplitude g_n is the phase and σ_n is the angular speed.

The harmonic constituents are cause variations which have periods shorter than a day while other variations which take longer are long period constituents. With a high number of harmonic constituents that impact the tidal dynamics, the tidal constituents are ranked base on their degree of influence. Table 2.1 gives the common name of the tidal constituents, their periods and their ranking. Figure 2.5 shows how the tidal velocity may change in the presence of the different tidal constituents. The use of such tidal harmonics is well accepted in the tidal industry and is advocated by EQUIMAR protocols [8] [9]. Currently, software programs such as T_Tide [10] perform harmonic analysis for a given site and time series data of tidal elevations or tidal current speeds. With the derived tidal constituents and their phasing's, the tidal velocity can forecasted.

Table 2.1 – Ranking of tidal constituents

Common name	Period(h)	Rank
M2	12.42	1
S2	12	2
N2	12.66	3
K1	23.93	4
M4	6.21	5
01	25.82	6
M6	4.14	7

MK3	8.18	8
S4	6	9
MN4	6.12	10

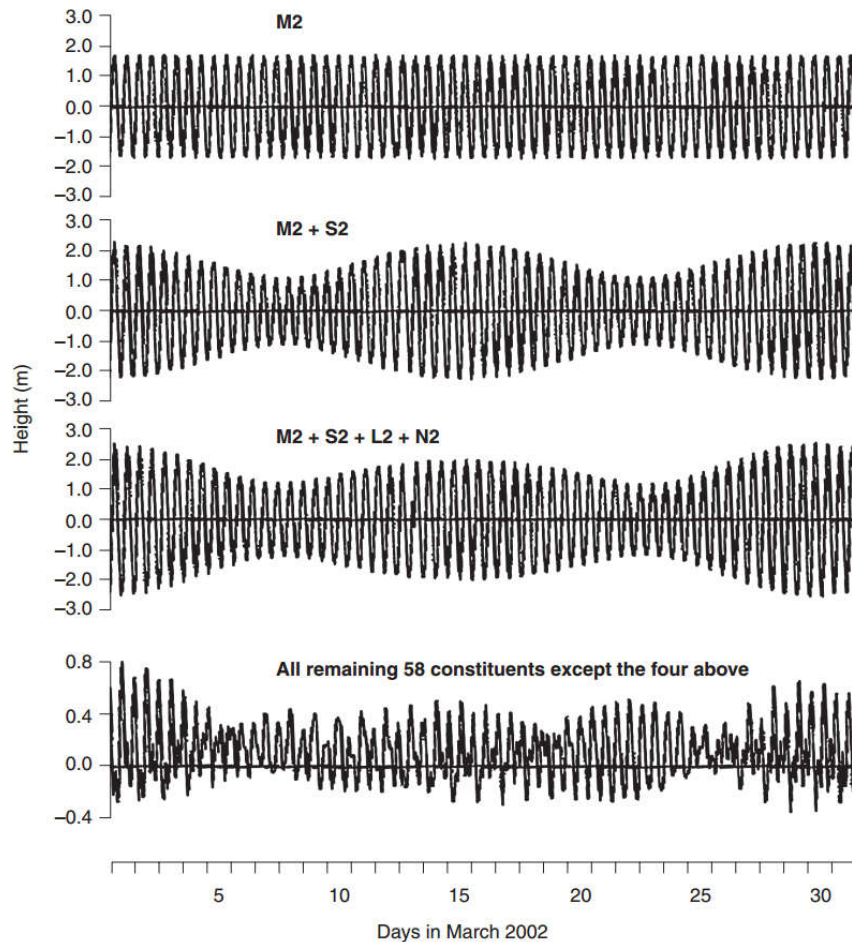


Figure 2.5—: The effect of predicting tides with different constituents

Tidal flow speeds are generally the main factor that affect the potential of tidal energy developments at a particular site. Due to the fact that the power in the flow stream scales with a cube of the flow speed, it is desirable to position a tidal farm at high energy sites. This gives rise to the use of power density as a measure of available tidal resource. Power density is given by

$$P_w = 0.5\rho U_c^3 \quad (\text{EQN 2.2})$$

In high energy locations, the velocities could be well in excess of 5 m/s. To increase the chance of survivability, turbines in extreme conditions are designed to cut out at high velocities to avoid damage. Measurement campaigns carried out in tidal sites show a high spatial variation in flow speed. This is primarily influenced by the local bathymetry. Measurement campaigns are therefore needed to characterise a site in detail.

Many of the factors which influence site selection are tied with the velocities in the flow. Turbulence is has been shown to be highly influenced by velocities. The Velocity magnitude may be of critical importance for power extraction however the vertical velocity profile is an important characteristic of flow through a tidal channel.

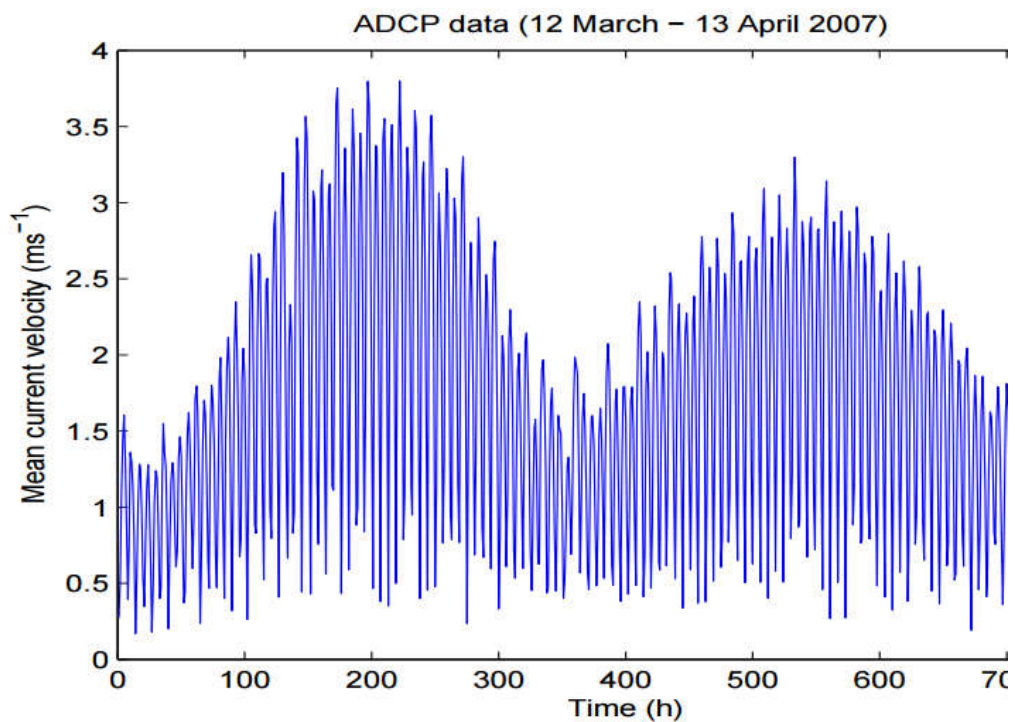


Figure 2.6—: Variation of mean flow speed at Fall of Warness[11]

2.2.2 Velocity profile.

Viscous effects between the fluid flow and the seabed cause a retardation of fluid near the seabed. This causes a velocity shear profile as shown in Figure 2.7. In many high energy tidal sites, the seabed is of the layer or soured rock as sediment will have been weathered away through time. McCanne et al[12] found the velocity profile at an EMEC tidal site was roughly given by a $1/5^{\text{th}}$ power law. However, a seventh power law has been advocated by many researchers[13].

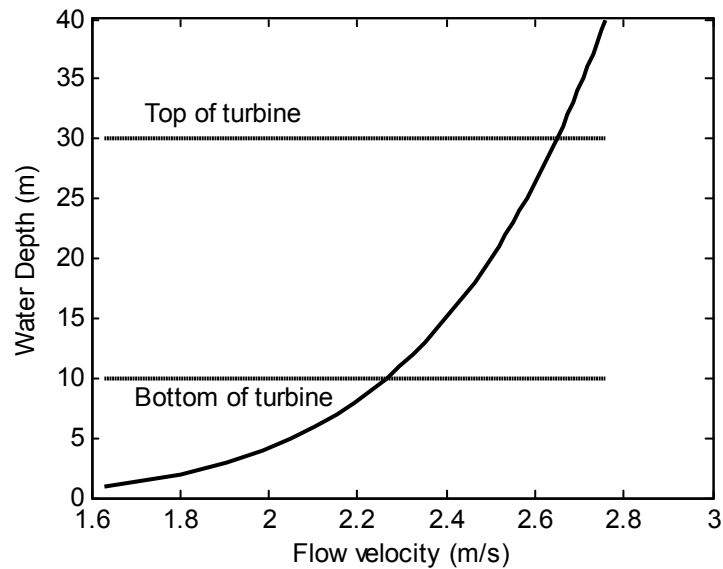


Figure 2.7– Variation of velocity with height above sea bed (seabed fixed turbine)

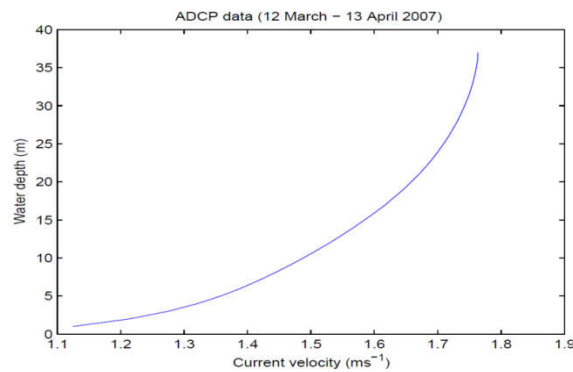


Figure 2.8– velocity profile at fall of Warness tidal energy site; source[14]

2.2.3 Directionality of the flow

Due to the location of high energy sites, the direction of flow is usually bidirectional as was measured at Fall of Warness[14]. It can be observed that the power density is strongly directional dependent. This is due to the fact that tidal energy sites are often boarded by headlands or restrictions.

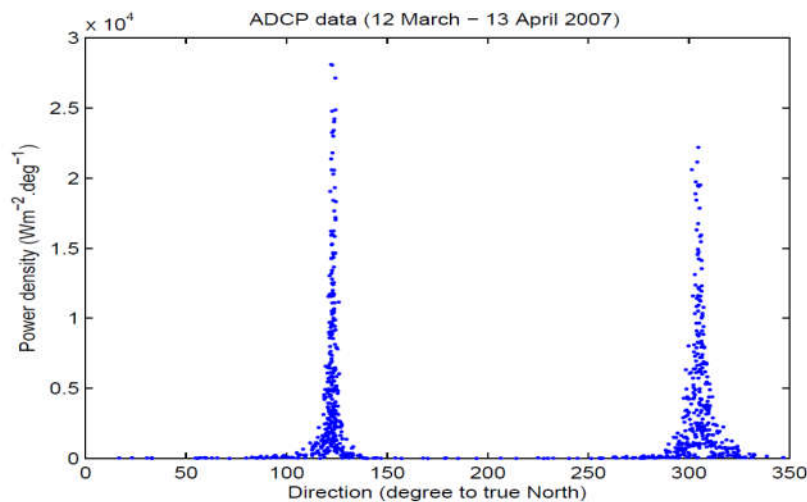


Figure 2.9– Average Power density at Fall of Warness Tidal site; [14]

2.2.4 Turbulence

Turbulence can be induced by wave action. However the turbulence caused by viscous effects between the flow and the seabed are discussed herein. The frictional effect causes fluctuations in the flow velocity. For a given flow field, with changing velocity $U(t)$ over time the flow is treated as a combination of a mean flow $\bar{U}(t)$ and fluctuations caused by turbulence $u(t)$.

Several metrics for depicting turbulence effects are presented in the literature including Turbulence Kinetic Energy (TKE), Turbulence Frequency Energy (TFE), Turbulence Strength (TS), and Turbulence Intensity (TI). By definition, the TI, which is the most common metric for measuring turbulence levels in tidal flows is given by:

$$I_t = \sqrt{\frac{\sigma_U^2}{\bar{U}^2} + \frac{\sigma_V^2}{\bar{V}^2} + \frac{\sigma_W^2}{\bar{W}^2}} \quad (\text{EQN 2.3})$$

$$I_t = \sqrt{I_U^2 + I_V^2 + I_W^2} \quad (\text{EQN 2.4})$$

That is the total turbulence intensity I_t is made up of the axial component, I_U , vertical component I_V and Horizontal component I_W . A Study of turbulence eddies at a tidal energy site revealed the ratio between the various components of the turbulence as $(I_U, I_V, I_W) = (1, 0.75, 0.56)$.

Table 2.2 -Turbulence Characteristics at tidal energy sites, adapted from[15]

Location	I_u [%]	U_∞ [m/s]	Technique	Ref
Fall Of Warness	10-11	1.5	ADCP	[14]
Sound Of Islay	12-13	2	ADV	[16]
Puget Sound	8.4-11.4	1.3±0.5	ADCP,ADV	[17]
Strangford Narrows	4-9	1.5-3.5		[18]
East River ,New York	20-30	1.5-2.3	ADCP	[19]

A study by Gooch[17], characterised flow properties which are relevant for TEC. It has been shown that the fluctuation caused by turbulence increases the fatigue cycle on the rolling element bearing. The turbulence intensity varies with flow velocity. The value can be as high as 50% near the slack period and reduces to about 10% at velocities above 1.5ms^{-1} [20].

The typical turbulence intensity for a tidal site with peak flow rates above 2.5 m/s was found to be in the range of 12-70 %[19]. Analysis carried out from a bottom mounted ADCP data at tidal sites in the Americas found the turbulence intensities are generally distributed within 5 and 15% .

The turbulence intensity is chosen as a metric, for depicting the turbulence in the flow stream. In 1961, Grant et al [21] measured flows in an energetic tidal channel and confirmed that the relation given by Kolmogorov [22] for the inertial sub-range of the turbulence energy spectrum applies. The energy in the inertia sub-range is proportional to the wavenumber k by $k^{-5/3}$.

Walter et al's [23] measurement of flood and ebb tides also showed good agreement with the classical power law spectra as presented by Kolmogorov[22] as well as Kaimal spectrum [24]. Variance in the measured curves were shifted towards the higher frequencies. Velocity spectra are more energetic at low frequencies but co-spectra (v' and w') were weaker. The turbulent kinetic energy defined by

$$TKE = \bar{e} = \frac{1}{2}(u^2 + v^2 + w^2) + m \quad (\text{EQN 2.5})$$

Figure 2.10 shows measured variation of horizontal and vertical components of the turbulence kinetic energy.

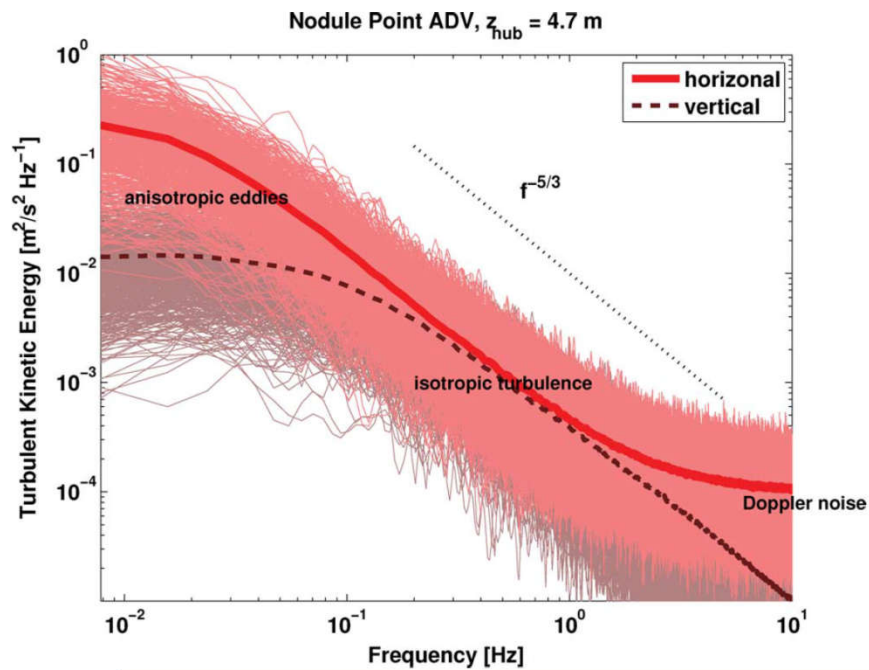


Figure 2.10– Variation of TKE with frequency[25]

2.2.5 Wave climate

The wave climate at a tidal development site is very important for its reliability. By nature, tidal developments are often located in tidal straits where flow tends to be accelerated. Due to this, there is often little fetch for waves to develop all round most sites. Waves however may propagate from the open sea or in the direction of flow which tends to be not bounded by headlands. Typically, sheltered sites are ideal for tidal turbine development at least to aid installation, and maintenance throughout the life of the turbine. Consequently, a tidal turbine may not need to be subjected to harsh wave conditions.

Due to the exponential decay of the wave orbital velocities with depth, placing a turbine in deeper waters provide some isolation from severe wave loads. The effect of wave loads on a tidal turbine may be included through the super position of water particle velocities as defined by linear wave theory. Barltrop et al [5] included the effect of linear wave particle velocities and accelerations into a mathematical blade element momentum theory model and showed this has good agreement with experimental data.

According to linear wave theory, three (regions) may be distinguished based on the interaction of the wave with seabed, namely shallow water, finite depth and deep water equations. The classification is carried out according to the depth and wavelength of the wave and the depth of the water.

The typical sea state consist several waves (different frequencies and wave heights). Commonly, a typical site is characterised by a chart which indicates the various wave heights, peak frequencies and their relative occurrence. The wave climate over a period of time is thus characterised by a Scatter diagram as shown in Figure 2.11

Hs (m)	Tz (s)						
	1.5	2.5	3.5	4.5	5.5	6.5	7.5
0.25	7.14	0.69	0.10				
0.75		26.78	27.16	0.58	0.03		
1.25			9.39	2.10	0.28	0.05	
1.75			0.79	8.09	5.83	0.06	0.02
2.25			0.02	2.05	2.97	1.05	0.19
2.75				0.31	2.31	1.20	0.26
3.25					0.22	0.25	0.07

Figure 2.11– Wave scatter diagram[12]

Recently, Lewis et al.[26] Presented simulated wave conditions at numerous potential tidal energy sites for the period between the year 2007 and 2011.

Table 2.3: Statistics of wave action at tidal sites[12]

Site	Mean wave climate		s.d. of wave climate		Maximum	
	Hs (m)	T (s)	Hs (m)	T (s)	Hs (m)	T (s)
1	1.38	2.70	1.04	1.00	9.59	8.70
2	1.13	2.40	0.78	0.80	7.08	7.40
3	1.15	2.50	0.75	0.70	6.53	6.40
4	2.06	3.20	1.41	1.00	11.91	8.10
5	2.05	3.20	1.41	1.00	1130.00	8.00
6	1.97	3.10	1.30	0.90	9.79	7.50
7	1.20	2.40	0.88	0.80	7.34	6.20
8	0.92	2.10	0.68	0.70	4.89	4.90
9	1.22	2.40	0.96	0.90	7.66	6.20
10	1.50	2.70	1.17	1.00	10.40	7.50
11	0.81	2.00	0.65	0.80	5.78	6.30
12	1.16	2.30	0.95	0.90	9.15	7.60
13	0.98	2.20	0.64	0.70	5.12	5.40
14	0.83	2.00	0.57	0.60	4.35	4.50

15	1.10	2.30	0.78	0.70	8.02	6.60
16	1.32	2.50	1.01	0.90	11.09	7.90
17	1.25	2.50	0.88	0.80	9.70	7.50
18	1.73	3.00	1.28	1.10	12.49	8.40

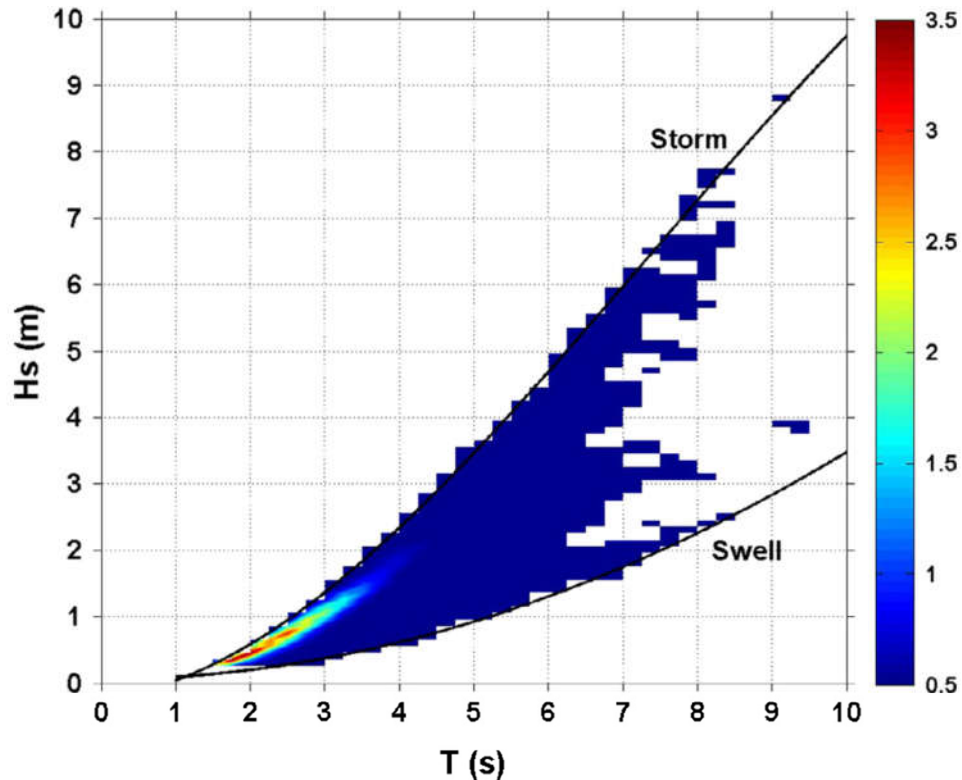


Figure 2.12– Simulated Wave climate frequency distribution[12]

2.2.6 Vertical static Pressure Variation

An issue unique to axial-flow tidal turbines is the static pressure variation experienced by a rotor blade as it rotates through the water column. This is enough to induce large forces in the rotor blade skins similar to ‘breathing’ as the blades move from the top of the swept circle to the bottom[27]. The variations in static pressure and velocity across the vertical water column also imposes cyclic dynamic loads on the rotor blades[28]. To resolve this problem, Fraenkel [27], proposed flooding the rotor blades of the Seaflo device to achieve internal and external pressure equalization.

2.2.7 Cavitation

Cavitation phenomenon has been observed and reported scientifically on marine propellers for over a hundred years. Cavitation occurs where the local static pressure falls below that of the vapour pressure of water resulting in bubbles of gas being formed near the surface of the blades. Different types of cavitation may occur (eg. tip, vortex, sheet, bubble, cloud) depending on the operating conditions and other factors such as blade geometry, and water quality. Cavitation is known to cause erosion, noise, structural vibration and reduction in performance. Experimental studies on tidal turbine blades have revealed cavitation may be experience. Figure 13 shows the flow conditions for which cavitation is likely to occur[27]

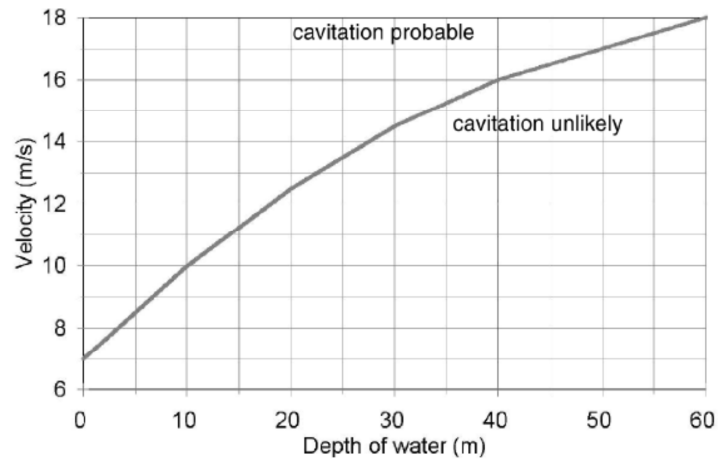


Figure 2.13- Conditions for cavitation inception

The possible influence of cavitation on tidal turbines has been studied by a few researchers but to date, most of the research [29][30][31] have focused its effect on energy yield rather possible effects on drivetrain reliability. Cavitation arises when there is a phase change in water from a liquid state to a gaseous state. The mechanism may be driven by either a temperature rise at constant or near constant pressures or by a drop in pressure at constant temperature. Cavitation is considered to be possible when the cavitation number (σ) is equal to or less than unity.

$$\sigma = \frac{(P_{\infty} - P_v)}{0.5 \rho V^2} = \frac{(P_a + \rho g - P_v)}{0.5 \rho V^2} \quad (\text{EQN 2.6})$$

$$C_p = \frac{(P_l - P_{\infty})}{0.5 \rho V^2} \quad (\text{EQN 2.7})$$

$$V = \sqrt{(U^2(1 - a)^2 + \Omega^2 r^2(1 + a'^2))} \quad (\text{EQN 2.8})$$

For practical purposes, cavitation inception and developed cavitation are considered. The complexity in cavitation problems arise given that cavitation is influenced by many factors including

- Geometry.
- Shear flow
- Roughness of local blade surface
- Vibration
- Strong fluid acceleration
- Fluid properties (temperature, surface tension, air saturation.)

The occurrence of cavitation in HATT is likely to cause.

- Blade erosion
- Noise and vibration
- Additional loading of blade
- Change in power performance.

Byrne et al [32] studied the conditions which affect horizontal axis turbines numerically using a computational fluid dynamics code and concluded that it is highly likely that cavitation will influence the performance of tidal turbine. The occurrence of cavitation during the operation of a horizontal axis turbine is greatly influenced by the tangential speed of the blade, blade orientation and flow velocity. Gounder et al [33] investigated the performance of hydrofoils and concluded that it's appropriate to use lower TSR to reduce the probability of cavitation while maximising blade solidity to improve hydrodynamic performance.

The minimum hydrostatic pressure is experienced at the blade tip when the blade is positioned vertically. Consequently, the tidal turbine is most susceptible to cavitation at the tip of blades when they are vertical. On the contrary, the flow

velocity decreases as depth increases. Thus it is lucrative to place turbines near the surface which intern increases the probability of cavitation. Tip loss may however reduce the minimum pressure coefficient at the tip of the blade where cavitation is more likely to occur.

$$V_{\infty} = (U(1 - a^2) + \Omega_r(1 + b^2))^{1/2} \quad (\text{EQN 2.9})$$

2.2.7.1 Added mass force.

Maniachi and Li,[34] investigated the effect of added mass on Tidal turbines and concluded that the added mass force is an important factor which has to include in the analysis for tidal turbines. Whelan[35], on the other hand demonstrated the axial added force is negligible.

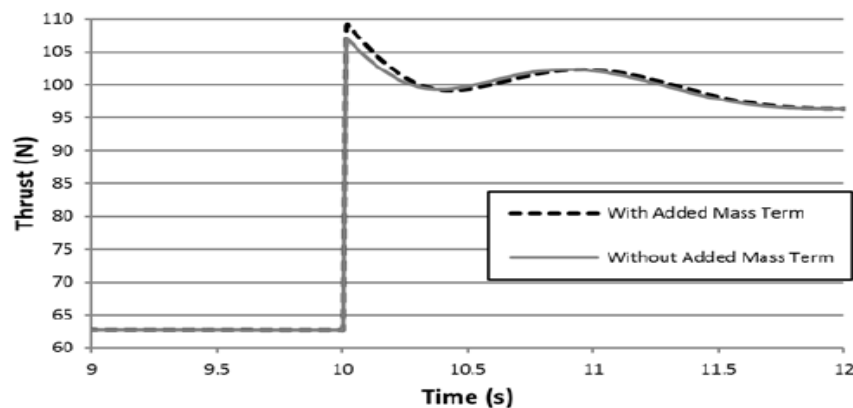


Figure 2.14– Influence of added mass force on thrust force

Faudot and Dahlhaug,[36] compared two different method for inserting an added mass force into BEM code. A noticeable influence of added mass force on blade loading was observed. However very little influence was noticed by Whelan[35]. The difference between the two may be explained by the fact that Whelan considerer a turbine with infinitely stiff blades which have no pitching capabilities while Maniachi considered pitching of turbine blades.

2.2.7.2 Marine growth

Marine growth can strongly affect the hydrodynamic response of a submerged structure. Bio-fouling is influenced by factors such as water depth, salinity, weather and nutrients in the water stream. Shi et al [37] found large differences in the maximum hydrodynamic loads on an offshore wind turbine jacket for different fouling thicknesses values. The analysis revealed that not only the jacket mass was affected but also the added mass was increased. However, the type of fouling (soft or hard) did not significantly influence the response. The presence of fouling however has been shown to have a detrimental effect on the performance of tidal turbine blades, submerged weight and turbine performance as a whole [38] .

Polagy and Thompson [39] investigated bio fouling of aluminium, stainless steel, structural steel, glass and other steel materials. In the ten month period tested, no significant fouling was found on the tested material although some had corroded.

2.2.8 Dynamic Modelling of Tidal Turbine

McCann et al [40] presented GH Tidal Bladed a design and certification tool for tidal turbines. This program was an adaptation of the wind turbine design tool GH Bladed. Although GH Tidal Bladed included adaptations which make it more suitable for tidal flow, such a wave loads, they both generally work on the same principle based on Blade Element Momentum Theory (BEMT) and Dynamic inflow conditions[41].

An alternative to Bladed, FAST (Fatigue, Aerodynamics, Structures, and Turbulence) was developed by the National Renewable Energy laboratory (NREL). Just like, GH Bladed, FAST uses a multi-body representation of the turbine to construct a global turbine model which delivers loads on major turbine components. Typically shaft loads are readily extracted in the coordinate system as shown in Figure 2.15. All loads in this work refer to this coordinate system.

Other researchers have used in-house codes to model their tidal turbines[42]. In general their results agree well with both experimentation and numerical modelling using these commercial design tools.

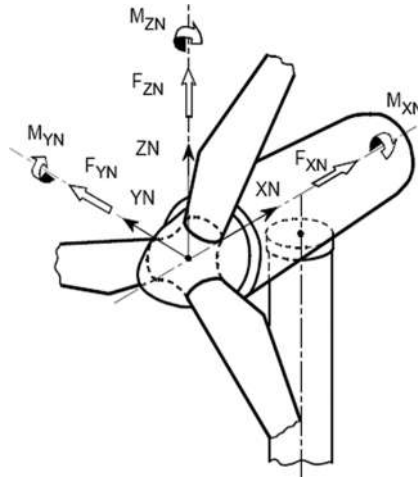


Figure 2.15– Shaft coordinate referencing

2.3 Reliability

Tidal energy offers a great solution to global energy security and sustainability. As an emerging technology, tidal energy faces a number of risks. In the development of many technologies, valleys of death exist which have to be carefully navigated to ensure success.

The potential unreliability of tidal turbines poses a major risk to tidal industry. With the much reduced accessibility of tidal turbines, the level of failures that were observed in the onshore wind industry cannot be sustained in the tidal industry. Faulstich et al [43] evaluated how the move from onshore wind to offshore wind will affect reliability and availability of turbines. Figure 2.16 shows major (high downtime per failure) and minor (low downtimes per failure) failures for a fleet of onshore turbines from [43]. They concluded that downtime associated with both major and minor failures are likely to increase due to longer waiting times, travel and working times.

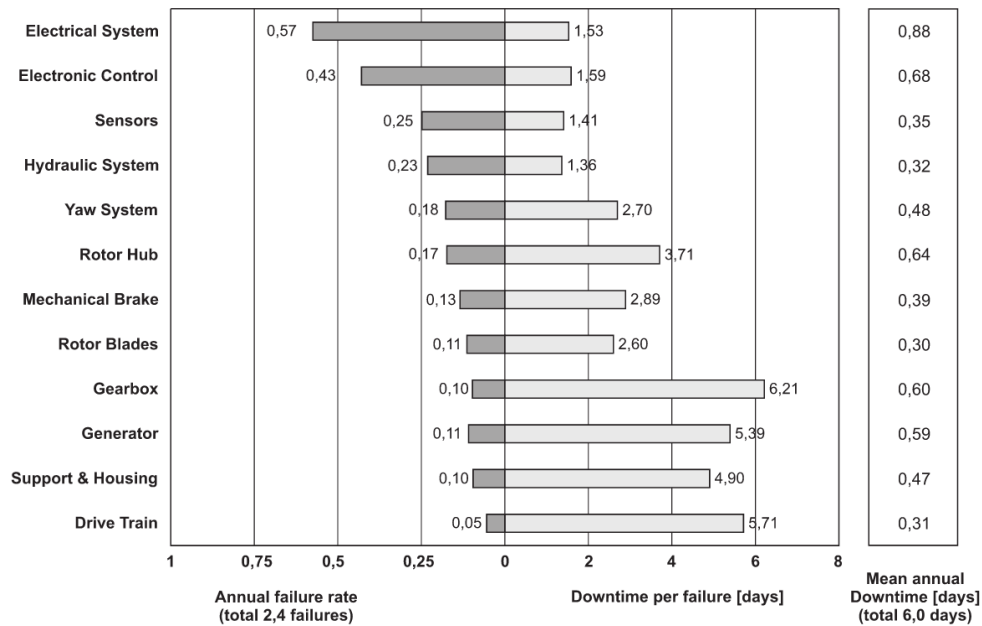


Figure 2.16– Failure rate and associated downtime for wind turbine components[43]

The downtimes associated with such failures if they were to occur in the tidal industry will result in a much higher downtime than anticipated of offshore wind turbines. In addition to the travel and waiting times and weather windows as highlighted above, tidal energy devices are often placed in higher energy areas where slack tides may be observed for a very short period of time.

The cost of failures are likely to be higher not only in terms of production lost to downtime but also higher cost of transport (such as DP vessels) and higher risk to personnel in the offshore locations.

2.3.1 Structural Reliability

Traditional methods used in design impose large safety factors to guarantee the reliability of a component. This approach inherently assumes the strength of the structure or system is deterministic thus has no uncertainty. This leads to over conservative designs. Accordingly the strength of the structure and loads in it tend to be nondeterministic but may assume a range of values in a random fashion. A probabilistic approach is therefore more suited to such analysis because it deals with uncertainties associated with both the strength of material and loading. By applying

probabilistic approaches, it is conceded that failure is possible unlike traditional methods which imply failure is impossible. The models used for predicting mechanical process plant are largely based on models developed for the electronic industry. The assumption of random failure rate in electronic systems is supported by the fact that failure is often caused by random stresses such as power surges. Mechanical components however tend to fail due to degradation mechanisms such as creep, fatigue and stress corrosion. It is worth pointing out that factors such as material inconsistency tends to be rather randomly distributed thus the assumption of a constant failure rate can remain true for mechanical components given that their primary failure modes are related to such random phenomena.

Due to the complexity and structure of mechanical systems, their reliability is not easily assessed using conventional reliability theory. This was first pointed out by Yoshikawa [44] and reiterated by Moss and Andrews[45].

Structural reliability analysis involves three main steps. Firstly the dominant failure modes of the component have to be identified. Subsequently the probabilities of failure with respect to design loads are evaluated. Finally the upper bounds of the correlation between the dominant failure modes and their probability of failure is calculated.

Sharma and Gandhi [46] presented a method for assessing the reliability of a gear set using a digraph and failure tree. They suggested the reliability of mechanical components can be assessed as follows.

- List all possible failure modes
- Identify the inputs and outputs of the component
- Develop a model for the input and output
- Define undesired failure symptoms
- Develop a failure tree for each of the undesirable symptoms
- Assess reliability of the component using the lowest level primal event

Classical reliability modelling of mechanical components determines the probability of a device encountering a load which will cause it to fail. This probability is diagrammatically illustrated using an interference diagram in Figure 2.17.

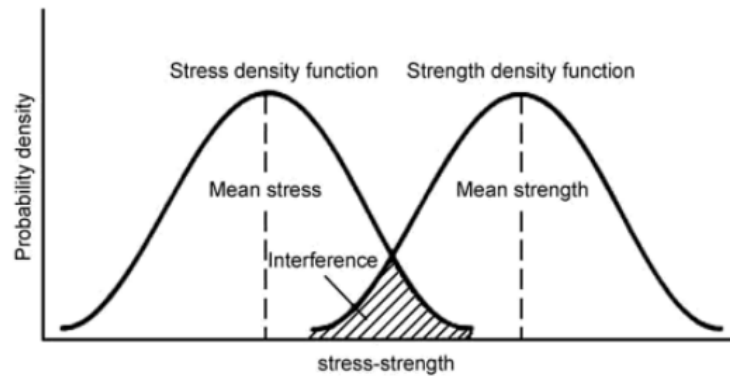


Figure 2.17– Interference diagram of strength and load

$$g(L, S) = S - L \quad (\text{EQN 2.10})$$

We define failure by F which contains the realisation of those instances where the limit state function is a non-positive number.

$$F = \{g(x) \leq 0\} \quad (\text{EQN 2.11})$$

Where \mathbf{x} is a vector of the realisations of the basic random variable (failure mode) \mathbf{X} which represents all the uncertainties those inferences the failure probability. The probability of failure may be written as

$$P_f = P(L > S) = P(S < L) \quad (\text{EQN 2.12})$$

$$P_f = \int_{g(x) \leq 0} f_x(x) dx \quad (\text{EQN 2.13})$$

Obtaining the solution to the integral is however non-trivial thus requires a numerical solution. Several methods have been proposed for carrying out this including Monte-Carlo, asymptotic Laplace expansion and numerical integration methods

2.3.2 Fatigue assessment

The concept of fatigue in metals have been studied for many years but yet not fully understood. The predictions of fatigue life of cyclically loaded components are classily based on three approaches, namely stress-life, strain life and linear elastic fracture mechanics. These methods estimate the time to failure in terms of number of cycles. The type of fatigue failure is distinguished by the number of cycles to failure n , where the failure is termed low cycle fatigue when $1 < N < 1E3$ and similarly called high cycle fatigue when the $N > 1E3$.

2.3.2.1 Stress-life method

Although the accuracy of the stress life method in comparison to other methods has been disputed, it remains the most traditional method of evaluating fatigue life because there is ample data to support it. In addition, it has been shown to predict life accurately for high cycle's applications. Stress-life method predicts the fatigue life of a component for a given stress level in terms of number of cycles to failure. The relationship between the stress and the number of cycle s to failure is obtained through testing.

While testing, specimens are subjected to specified varying loads while the number of stress cycles or stress reversals is counted till destruction. The most common type of fatigue tester is the rotating beam machines, axial stresses, torsional stresses and combined stresses.

Due to the statistical nature of fatigue, a great number of specimen is required. Typically, for a rotating bending test , the specimen is subjected to a stress below the ultimate tensile stress of the material. The number of loading cycles or revolutions to failure is recorded. Specimens are then tested at levels below the previous limit with their corresponding cycles to failure recorded. The date from fatigue tests are often plotted on a logarithmic or semi-logarithmic paper. Typically, the material cycle to failure exhibit a linear relationship with a negative slope with the applied load. At low loads, this turns horizontal. This is indicative of an endurance limit. The endurance limit is used to distinguish two phases of the S-N relation. The region of slopping stress-life relationship and the region where further

reduction in stress does not lead to a considerable increase in fatigue life. As such, the S-N relation has a horizontal relation. The part of the S-N relationship which is above the endurance limit is called the finite life region whereas the part after the endurance limit is called the infinite life region.

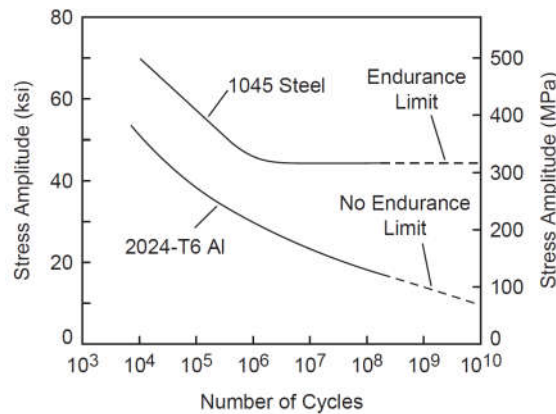


Figure 2.18– Fatigue behaviour of steel and aluminium [75]

$$\sigma_{mean} = \frac{\sigma_{max} + \sigma_{min}}{2} \quad \text{EQN 2.14)}$$

Generally fatigue test are conducted in fatigue machines which apply constant amplitude reversing stress at constant frequency often at a zero mean stress. Analytical models have been suggested for including the effect of the mean stress on a fatigue life. The most popular of these is a linear model proposed by Goodman (EQN 2.15). Gerber proposed a parabolic model. His relationship has been shown to be more representative for ductile metals. Due to the high scatter of fatigue data, test data generally follow the more conservative Goodman's relation. Solderberg also proposed a linear relationship which is more conservative than the Goodman's relation. This is suggested for applications where the component of interest is designed based on yield rather than ultimate tensile strength.

$$\sigma_a = \sigma_e \left[1 - \left(\frac{\sigma_m}{\sigma_u} \right) \right] \quad \text{(EQN 2.15)}$$

2.3.2.2 Strain life method

In contrast with the stress life method, the strain life method involves the use of local stresses and strains to aid life estimation. Consequently, this approach involves more detailed analysis and study of the localised plastic deformations. The strain life method is generally ideal for low cycle fatigue. Here, the material undergoes strain hardening/ softening loops with every applied strain cycle. In the region where the nominal strain is elastic, the Basquin's equation describes the high cycles where there is low strain. The Coffin-Manson and Basquin equations can be summed up to evaluate the fatigue life based on summation of elastic and plastic strains

$$\frac{\varepsilon}{2} = \frac{\varepsilon_e}{2} + \frac{\varepsilon_p}{2} \quad (\text{EQN 2.16})$$

2.3.2.3 Linear elastic fracture mechanics

An alternative to the stress and strain life approach is linear elastic fracture mechanics which divides the fatigue process into three phases, crack initiation, crack growth/propagation and termination/failure. In this approach, cracks are assumed to begin from discontinuities in the material arising from features such as non-metallic inclusions, surface roughness, and dents and notches.

Stage two sees the initiated crack propagate and create new crack area. Typically, the propagation of the crack increases the size of the crack enabling it to be seen on micrographs and through visual inspection. When the crack length reaches a critical length, catastrophic failure occurs. This is observed in stage three fatigues.

Considering a material being subjected to fatigue loading, with a maximum stress σ_{max} and minimum stress σ_{min} and a stress range defined by $\sigma = \sigma_{max} - \sigma_{min}$, a stress intensity factor may be defined by

$$K_I = \beta(\sigma_{max} - \sigma_{min})\sqrt{\pi a} = \beta \sigma \sqrt{\pi a} \quad (\text{EQN 2.17})$$

Where β is the sensitivity parameter for the stress intensity factor. When the rate of crack growth dN/da is plotted against the stress intensity factor it results in a graph similar to Figure 2 19.

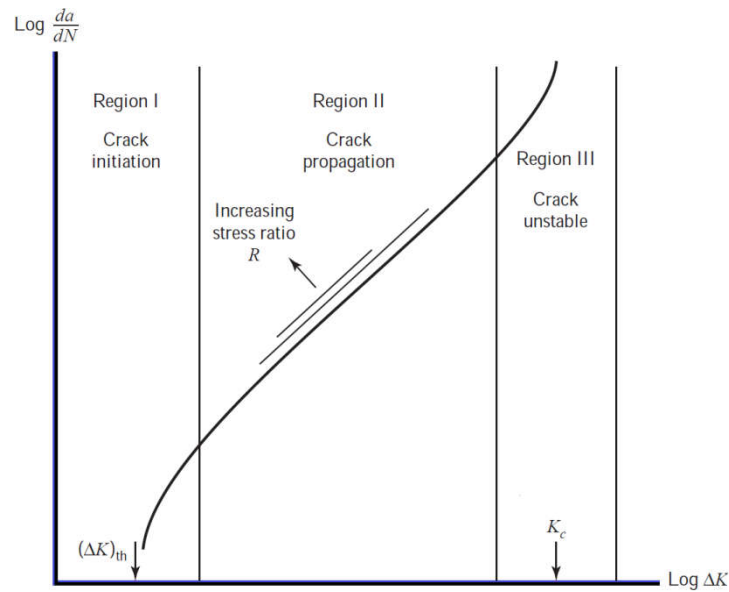


Figure 2 19: Variation of crack size with stress intensity factor

At stage two, where the crack propagates, the crack growth can be estimated as by the so called Paris law

$$\frac{da}{dN} = C (K_I^m) \quad (\text{EQN 2.18})$$

Where C and m are empirical values which are derived from testing. The number of cycles to failure can be evaluated for an initial crack length and a failure crack length.

$$\int_0^{N_f} dN = N_f = \frac{1}{c} \int_{a_i}^{a_f} \frac{da}{(\beta \sigma \sqrt{\pi a})^m} \quad (\text{EQN 2.19})$$

2.3.2.4 Stress counting method

For fatigue failure to occur, certain conditions must be met. Firstly, the stress amplitude must be high enough. Additionally, the applied stress must be fluctuating. And finally, there must be a sufficient number of cycles. Classical S-N curves show the amplitude of the stress and the number of cycles to failure. In fact, the nature of the fluctuation influences key part of the fatigue process. The nature of the fluctuation may be instrumental in the fatigue damage.

The classical method of assessing fatigue is based on the application of regular loading on a specimen. To account for the fact that a component may not necessarily be subjected to a zero mean loading, the Goodman's relation is applied. In-field loading may not just have a non-zero mean but is often not applied in regular discrete amplitudes and frequencies. The loading is often a combination of several load signals of varying amplitudes and frequencies. To make it possible to apply classical fatigue assessment techniques on randomly varying loads, fatigue stress counting algorithms have been established. The algorithms disentangle the mixture of load signals into discrete amplitude loading and loading frequency. This enables accumulation laws to be applied for the various stresses and their respective frequency.

The three commonly used fatigue assessment procedures, stress life method, strain life method and linear elastic fracture mechanics all rely on the cycle ratio $n_i/N_{i,f}$. Cycle counting algorithms are used to disentangle the complex variable amplitude load time history into discrete constant amplitudes. Primarily two groups of counting algorithms are popular, the one parameter and two parameter counting strategies.

There are many one parameter cycle counting methods. They include level crossing, peak -valley and range counting to name a few. Generally, these approaches are shown to lack the rigour in accurately representing the stress-strain hysteresis behaviour that impacts fatigue failure. Consequently, the two parameter cycle counting methods are accepted for adequately representing the variable amplitude load histories. The rainflow counting method is one of the most common and accepted in industry. Many variants of the rainflow counting methods have

been presented since it was introduced in 1968. The three point cycle counting is one of the most popular variant. This variant is adopted by ASTM standards. The three point cycle counting method uses three conservative points in the load time history. To initialise the analysis, the peaks and valleys are extracted from the load time history. Peaks are defined as a point from which the slope of the time history turns from positive to negative and valleys are described as points from which negative slopes turn positive. Considering three conservative points in the time history, s_1, s_2, s_3 , two conservative ranges S_1 and S_2 are defined such that $S_1 = |s_1 - s_2|$ and $S_2 = |s_2 - s_3|$. A cycle is therefore counted when $S_1 > S_2$ while no cycle is counted if $S_1 \leq S_2$.

Several stress counting algorithms are available for counting stress cycles for fatigue assessments. For example the range-mean cycle counting which filters the peaks and troughs and assigned to each segment of the in time history. The amplitude is thus defined from the range from a mean to a peak. Recently Anes et al [47] proposed a multi-axial counting method for counting cycles on complexly loaded components. With the help of these stress counting methods, the damage over the various stress levels can be aggregated to find the total damage using a damage accumulation law.

2.3.2.5 Cumulative Damage

Fatani and yang[48] produced a comprehensive review of the damage accumulation theories from the early 1970s to the early 90's. The life of a bearing is classically defined as the time to the initiation of the first fatigue spall. A common method of evaluating the time to initiation of cracks in structures is through the use of appropriate S-N curves for a material and Palmgren-Miner linear damage rule given by

$$D = \sum_{i=1}^k \frac{n_i}{N_i} \quad (\text{EQN 2.20})$$

In conjunction with S-N curve data such as shown in Figure 2-20 the relative damage caused by a stress history can be analysed. This assumes failure occurs when damage reaches unity.

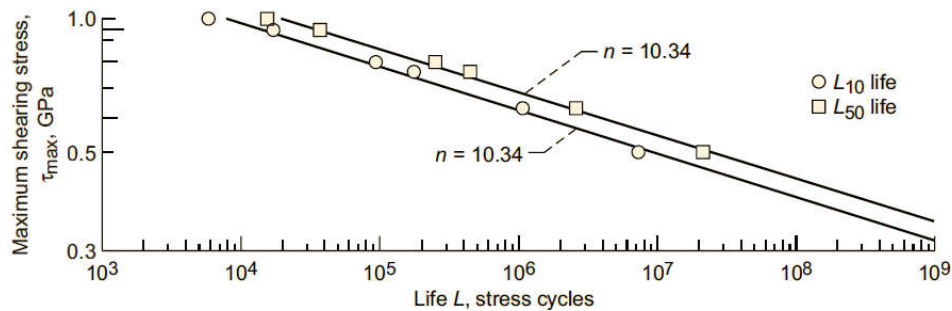


Figure 2-20: Material S-N curve

2.3.3 Reliability Prediction

Reliability is generally defined as the probability that an equipment or system will perform its assigned task without failure for a given period and under defined environmental and operating conditions. In classical reliability assessment, the failure rate is the central parameter from which various reliability goals can be estimated. The failure rates are often obtained by reliability testing, field/ system specific data, generic industry averaged data[49][50][51][52] or expert opinions and engineering judgment. Currently there are a few public databases which can be used to obtain either system specific or industry average failure rates. Industry average failure rates of wind turbine components, similar to those in tidal turbines have been published by[53][54][55][56]. Guo et al [57] pointed out that some of the field data may be tainted or incomplete.

Using the publicly available data, reliability goals such as Mean Time Before Failure (MTBF) can be calculated by assuming a constant failure rate. The assumption of a constant failure rate is completely adequate for performing preliminary design comparative studies as conducted by[51][58]. A constant failure rate is more suited for electronic and electrical systems where failure is often caused by random loads such as electric surges. Mechanical systems on the contrary tend to fail due to wear out mechanisms such as fatigue. The assumption of a constant failure rate does to accurately represent repairable systems such as tidal turbines. It is well known that the probability that a component will fail at the next time step (hazard rate) follows the so called “bath tub curve” depicted in Figure 2.21 . In

order to accurately depict failure distribution over time mean failure rate, variance or standard deviation has to be known. Currently the quality of data available is such that these quantities cannot be adequately assessed.

A reliability analysis carried out in 1981 on three wind turbines in the United States using FMEA showed that the limited data used in the analysis implied the validity of the analysis is limited [59]. The need for failure data for probabilistic reliability assessment was highlighted decades ago [60]. Despite the decades of experience in the wind industry there are still concerns raised by researchers concerning the quality and quantity of data available in the industry [61] and [56]. Due to the rapid advancement of wind turbine technology the data which is publicly available is more representative of old smaller turbines [62] and this is likely to continue as turbine design and capacity changes rapidly. The reliability of wind turbines depend on many parameters ranging from wind speeds to temperature and so on [63].

Qualitative reliability analyses are often used to identify critical components in turbines thus aid reliability improvement but these methods cannot predict probability of failure. The qualitative Failure Mode and Effect Analysis (FMEA) are suggested by design guidelines for wind turbines. Fault trees offer a qualitative and quantitative approach to assessing reliability.

For structural components a clear guideline for assessing reliability is defined by several guidelines [64][65] [66]. It involves the calculation of the reliability index. This method evaluates the reliability considering the load and strength interference. The method is very exhaustive and requires defining all the failure modes of each of the components in the subsystem and evaluating the load strength interaction for each failure mode. The Physics of Failure (PoF) approach is based on the same philosophy as structural reliability methods, that is, it endeavours to address the probability of failure based on the physics of the failure mechanism. Physics of Failure approach to reliability prediction has been extensively used in the electronics industry [67]. Gray and Watson [68] demonstrated that this approach is not limited to electronic components but also to mechanical systems by evaluating the probability of a wind turbine gearbox by bearing failure. Kostandyan and Sørensen [69] applied a structural reliability method incorporating a damage accumulation model based on miner's rule, S-N curves and the Coffin–Manson's

law. Assessing the reliability of structural components based of physics is a common place in the wind turbine industry[70]. Although this method is time consuming and difficult it has the potential to increase the accuracy of reliability prediction when extended to all the relevant failure modes and loading conditions of a system and its components.

2.3.3.1 Reliability Prediction Methods

Reliability prediction can be used to evaluate the reliability goals of a system as well as identifying weaknesses in alternative designs, establishing life cycle costs and support logistics strategy planning. For most systems the Mean Time Before Failure(MTBF), is critical reliability goal and it is given in terms of failure rate (λ)

$$MTBF = \frac{1}{\lambda} \quad (\text{EQN 2.21})$$

The failure rate is describes as the number of failures per unit time. The failure rate of a system changes through time and can be characterised by the so called “bathtub curve” which is shown in Figure 2.21. The curve depicts the three typical stages of a product’s life. The initial stage, known as the “burn in” or “infant mortality” phase is typically characterised by high but reducing failure rates. The burn in phase leads on to the “useful life” of the product which is a period where only random failures occur, hence leads to a constant failure rate. The useful life is followed by the “wear out” phase where the product progressively deteriorates due to wear. Reliability prediction is generally carried out to predict the constant failure rate over the useful life of the system. The failure rate is the central parameter from which various reliability goals can be estimated. Consequently, identifying the failure rate is vital for reliability analysis. The failure rate may be predicted by using a reliability model, testing, field data or using a Physics of Failure (PoF) approach. Usually failure analysis assumes a constant failure rate therefore reliability can be predicted by:

$$R = e^{-\lambda t} \quad (\text{EQN 2.22})$$

For complex systems consisting of many sub systems and sub components, the overall reliability may be evaluated using a system model incorporating the failure rate of each sub component. Reliability is a measure of the probability that a system will survive between two time intervals $[0, t]$.

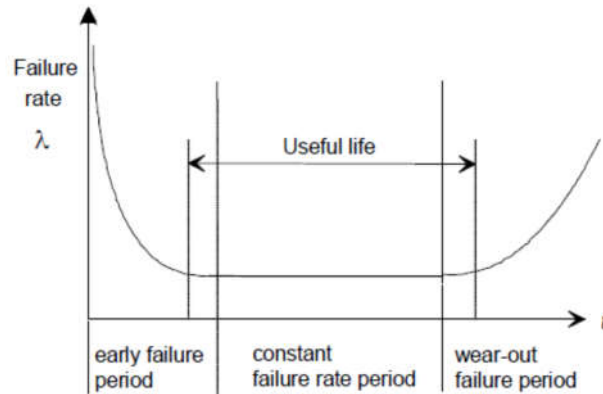


Figure 2.21– Bathtub curve representing failure rate evolution in a product lifetime

2.3.4 Failure rate prediction.

2.3.4.1 Part count

During the preliminary stages of a project where the environmental loading on components of a system is not known, a part count failure rate prediction may be used. The part count method calculates failure rate at a reference condition[71] and is expressed as

$$\lambda_{S,i} = \sum_{i=1}^n (\lambda_{ref})_i \quad (\text{EQN 2.23})$$

Where

λ_{ref} is the failure rate at the reference condition

n is the number of components in the system (s)

Delorm et al [7] used the part count approach while evaluating the reliability of different tidal turbine concepts. They obtained surrogate data from various sources and used them for the reliability analysis while applying adjustment factors based on the environment of operation only. Note that the operating condition was not taken into account, but the operating environment.

2.3.4.2 Part stress.

Alternatively to the part count method, a part stress approach can be employed[71]. This method accounts for the deviation of the system from the reference operating condition

$$\lambda_{S,i} = \sum_{i=1}^n (\lambda_{ref})_i \quad \text{EQN 2.24}$$

$$\lambda_{S,i} = \sum_{i=1}^n (\lambda_{ref} \times \pi_U \times \pi_I \times \pi_T)_i \quad \text{EQN 2.25}$$

Where

λ_{ref} is the failure rate at the reference condition

π_U , π_I , and π_T are factors which account for operating conditions

n is the number of components in the system (s)

The part stress approach is a popular method for predicting failure rate. Smolders et al [49] used this approach while investigating the reliability of various wind turbine gearbox architecture. They use a method given by Mil-Hdbk -217F [50] to evaluate the gear reliability λ_G

$$\lambda_G = \lambda_{G,B} C_{GS} C_{GP} C_{GA} C_{GL} C_{GT} C_{GV} \quad \text{(EQN 2.26)}$$

Where $\lambda_{G,B}$ is the base failure rate, C_{GS} is the speed deviation factor, C_{GP} actual gear loading factor, C_{GL} is the misalignment factor, C_{GT} takes the operating temperature

into account and C_{GV} is the America Gear Manufacturers Association (AGMA) service factor. Similarly, the failure rates for the bearings were calculated by

$$\lambda_{BE} = \lambda_{BE,B} C_y C_n C_{CW} C_t \quad (\text{EQN 2.27})$$

Where

$\lambda_{BE,B}$ Base failure rate.

C_y Applied load

C_n Lubricant specification

C_t Water contamination

C_t Operating temperature

Note that some adjustment factors in Mil-Hdbk -217F [50] including lubricant contamination, servicing condition and a life adjustment factor were neglected. Val and Chernin [72] presented reliability models for the main shaft, main bearing and main seal of a tidal turbine. The study adopted the part stress approach to calculate failure rates of the components and followed up with a developed reliability model of the main bearing which takes uncertainties associated with its operation and environment.

Thies et al [73] used a hybrid part count-part stress approach. The method employed crude adjustment factors for failure mode at the operating condition. This method is seen as a hybrid because adjustments are made to account for the deviation from reference condition; however, operating stresses were not applied to come up with the adjustment factor. For example the failure rate of a seal was adjusted to compensate for its reverse use and high frequency operation.

2.3.4.3 Base failure rate.

Several handbooks for predicting failure rate include both part count and part stress techniques [74]. The presented failure rate prediction methods require the use of a Base failure rate. This may be obtained from sources including laboratory testing or field data.

2.3.4.4 Failure rate prediction models

Models are available for predicting the base failure rates. Such models for predicting base failure rate of mechanical components can be found in [50] whereas base failure rate prediction models can be obtained from [75] for electrical/electronic equipment. Both [50] and [75] have developed these models by fitting curves to data obtained by carrying out extensive testing of equipment. Zagher et al [51] used models given by [50] to predict the reliability of various wind turbine gearbox configurations.

2.3.4.5 Field data

An alternate way of obtaining base failure rate is by using field data [65] [76]. Field data is a useful source of failure rates but they are often hindered by their incompleteness and ambiguity. Field data, therefore, requires more complex mathematical methods and algorithms to model a system [57].

2.3.4.6 Similar item data

When carrying out reliability analysis for new technologies, a problem which is often encountered is the lack of failure rate data or appropriate model for predicting the failure rate of a component. In this instance, the failure rate of a similar item may be used. An example of this is illustrated in Thies et al [77] where the failure rate of a generator was taken from [75] and used directly in the reliability analysis because they are similar items in a similar environment and operating conditions.

2.2.3.7 Life test

Carrying out a life test is a possible way of conducting a reliability assessment in itself. However, in most systems this is not practical due to the long time required and the expenses incurred while testing. Carrying out accelerated tests is common practice in many industries. It is a reliable way of obtaining base failure rates under specified in a controlled environment. This is usually not applicable to the actual operating environment of the tested system, thus the failure rate may be used as a base failure rate for a part count or a part stress failure rate prediction technique.

2.3.5 System Modelling

Generally failure rate data is available for components or sub-systems of complex systems. System reliability modelling methods provide a process of aggregating the failure rates of all system components to arrive at a system failure rate or reliability prediction.

2.3.5.1 Reliability Block Diagram (RBD)

Reliability block diagrams (RBD) are a popular method for modelling a system while carrying out a reliability assessment and have been used in [7],[47] [49] [77] [78]. RBDs are used for reliability prediction and life cycle management because they can diagrammatically represent a system's reliability performance. RBDs require defining what is considered as a successful operation of the system and is hence often contracted based on the functional block diagram of a system[78]. It comprises equipment (represented by blocks) which represent the logical behaviour of the system. The blocks are statistically independent and are preferably large. A stochastic representation of the system's probability of failure is obtained by linking these blocks and forming a success path. The final failure rate of the system is calculated by converting the failure rates from all branches (series and parallel) of the block diagram into a series and then summing them up.

RBDs are suitable for modelling systems with non-repairable sub components and can model systems which have either failed or in operation. They may be used to model repairable systems to some extent, in that they may be used to obtain probability of failure between two failures. The interconnection between components may be in Series, Parallel or cross linked.

2.3.5.2 Fault Trees

By using this Fault trees, it is possible to identify events which interact with other events through logic gates to form new events. The analysis starts with an undesirable event. To carry out the analysis, the failure modes of the components have to be identified. The interconnection between components also needs to be identified. This is easily done by a functional layout diagram. Boundary conditions

are also required to identify the situations in which the fault tree is to be drawn. Fault tree analysis may be either qualitative or quantitative. Qualitative methods use Monte-Carlo simulations or deterministic methods to define minimum cut sets or path sets. The Monte Carlo simulation assigns a failure rate to each of the components usually based upon exponential distribution. A comprehensive review of the early works of fault tree analysis is given by [79].

2.3.5.3 Reliability Allocation

Some components of a system are more critical to reliability than others. This has been confirmed by Thies et [80] highlighted that some components in marine energy converters are more critical than others. A reliability apportionment method may be implemented to influence how the reliability of a system is affected by its various components. The reliability goals may be spread across the system using one of the allocation methods presented below [81]

- Equal apportionment-The dependence of the system's reliability on its components is equally shared among all the components.
- Base apportionment- this involves applying normalised weight factor to subsystems to compensate for the difference in complexity, environment and manufacturing and other variables.
- ARINC-This method is similar to Base apportionment however weight factors are determined by the predicted failure rates of the components of the system
- AGREE- in this system reliability is allocated by a formula which is based on the systems importance, number of sub systems and mission time.
- Feasibility of objective- this is uses a weight factor to allocate reliability goal based on four ranking values of complexity, state of the art, performance and environment.
- Repairable system- the reliability allocation is carried out based on the required availability, mean time to repair (MTTR) and number of sub systems.

2.3.5.4 Failure rate modelling (Failure rate function)

Reliability analysis is often carried out to find the constant failure rate at the bottom of the bathtub curve, however it is understood that failure rate evolved over time.

Several failure rate distributions have been presented in the literature based on statistical probability distributions due to their ability to mimics the evolution of failure rates of components over time.

- Exponential model

The exponential model is used for simple systems where a constant failure rate is observed. Given that that reliability analysis is often carried out over the useful life period, this is not often applicable for modelling many components. The exponential model is given by

$$f(x) = \frac{1}{\beta} \exp(- (x - \mu)/\beta) \quad (\text{EQN 2.28})$$

- Weibull model

This is a very common statistical distribution which has been used to model various behaviours, for example wind speeds. The Weibull distribution can be used to model a non-constant failure rate and may come in the form of a single parameter, a two parameter and the three parameter failure rate model. The three parameter Weibull distribution which forms the basis for the Weibull model is given by

$$f(x) = \frac{\gamma}{\alpha} \left(\frac{x - \mu}{\alpha} \right)^{(\gamma-1)} \exp\left[- \left(\frac{x - \mu}{\alpha} \right)^\gamma \right] \quad (\text{EQN 2.29})$$

Here, γ is called the shape parameter, α is called the scale parameter and μ is the location parameter. The equation reduces to a two parameter version when $\mu = 0$, and further reduces to a single parameter when $\alpha = 1$ and $\mu = 0$.

The single parameter Weibull model takes the same form as the exponential model thus is appropriately used in the same context as when the exponential model applies. The two parameter model was used in [82] to model the “infant mortality stage” of the bathtub curve. The Weibull distribution is suitable for representing failure rate distribution in many components including electronic components, gears, ball bearings and relays [83] [84] advocated the three parameter Weibull distribution for the failure rates of mechanical components, but insisted the addition of more parameters to account for environmental factors and processing anomalies which may lead to variation in failure rate will help model failure rates more

accurately. Although the Weibull distribution is eminent, other like Wolfram [78] suggested a lognormal distribution for modelling changing failure rates.

2.3.5.5 Bayesian statistics

Fitting data of failure rates to form a model requires the estimation of parameters of the statistical distribution being used. The most common method for estimating the parameters of the Weibull probability density function (PDF) include maximum likelihood estimation, probability plot and regression analysis such as least squares [85] [86]. Andrawus et al [85] proposed a quantitative technique for maintenance optimisation using a two parameter Weibull probability density function to predict failure rate. The parameter estimation for the Weibull PDF was carried out using maximum likelihood. An alternative to the afore-mentioned techniques (classical techniques) is the Bayesian Statistics approach. Theis et al [82] demonstrated how the Bayesian technique can be used to reduce the uncertainties surrounding failure rate predictions of a marine energy converter.

2.3.5.6 Repairable systems

Most complex systems such as Tidal and wind turbines, aircrafts and communication systems are repairable; hence the treating failure rate by a homogeneous Poisson process may be erroneous. Efforts have been made by various researchers to accommodate this error. Crow [87] presented a non-homogenous Poisson process model for evaluating the reliability of repairable systems. The model applies a generalised form of the Poisson process which allows failure intensity to be dependent on age. Cateneanu and Milhalache [88] proposed a reliability model for mechanical components which exhibit age-dependant failures and may recover to their original state (good as new) or operate at a deteriorated state. They also propose that the minimum cut sets can be evaluated using fault trees and followed by a Monte Carlo simulation to obtain failure distribution.

A three parameter Weibull distribution was used by Guo et al [57] to model the reliability growth of German and Danish wind turbines. The three parameters included the common shape and scale parameters and a bespoke time factor parameter which describes the past running time. The parameters of the Weibull

distribution were estimated using the maximum likelihood technique and the regressive least squares method. Modelling a system using Markovian method has also been suggested by [89]. Moss and Andrew [45] described how reliability of age dependent mechanical systems can be addressed by using fault trees, Failure mode and effect (FMEA) , and Monte Carlo simulations.

2.3.5.7 Physics of failure

Reliability prediction can be carried out using the Physics of Failure approach. Components incur some damage as they are subjected to loads in their environment. These are irreversible changes to the microstructure of the components which evolve with time and number of load cycles. The expected life of the component can be estimated if the physics that defines the damage evolution is well understood. The Physics of failure approach has been used extensively in the electronics industry and entails the combination of damage calculation with the root cause analysis and probabilistic methods. The analysis is initiated by obtaining the accurate definition of the system under consideration. This includes material specifications, details of component design and after processes. The potential failure modes for the individual components are identified. Each component can have several modes of failure hence its essential that the significant ones are identified. A damage model is developed which is used to calculate the rate of damage accumulation due to the operating environment of the component. This model is supposed to capture the accurate description of the damage kinetics, such that the relative impact of the different load conditions on damage can be quantified, as well as critical operating conditions.

Gray and Watson [68] used this technique to predict the reliability of a 3 stage gearbox of a wind turbine. McLeish [90] suggested incorporating this technique into the Mil HDBK to improve reliability prediction. White and Bernstien [67] described how the PoF technique can be applied to determine the reliability of electronic components. They also presented the difference between the PoF approach and traditional approaches as one advocated by Mil HDBK [91].

2.3.6 Test methodologies

Testing has been used as a method of proving performance for century's years. A wide range of tests are carried out on Tidal turbine drivetrains to demonstrate their performance. Some common tests include:

1. Thermal characterisation
2. Power performance
3. Fault ride through
4. Functional tests
5. Reliability tests

2.3.6.1 Reliability test

Reliability testing is the corner stone of reliability engineering. Reliability tests are generally focussed on demonstrating, improve or estimate reliability. The reliability of components is strongly tied with their failure rate. As such the bath tub curve which is often used to describe the failure rate of mature technologies qualitatively gives the reliability profile of the product. Consequently, reliability tests target specific sections of the bath tub curves shown in Figure 2.24.

For components which have long lives, performing reliability tests can be extremely time consuming and expensive. To reduce the testing time while allowing the acquisition of reliability data in a reasonable time, accelerated test methodologies are exploited to shorten the testing time.

2.3.6.2 Accelerated test

Accelerated tests can be grouped under two taxonomies based on the type of output expected from the test. Qualitative accelerated tests deliver qualitative results which can be used to improve reliability. Qualitative Accelerated Tests are therefore suitable for making design and process improvements which lead to better reliability. Quantitative methods on the other hand aim to deliver time to failure data and distribution or track the wear out phase of the bathtub curve. Shows the

typical areas of a products life that specific accelerated test may be focussed in increase reliability.

Accelerated tests aim to accelerate failure mechanisms of interest while ensuring impractical failure modes do not develop. Consequently, possible failure modes must be investigated. Tidal turbine drivetrains are nonetheless complex systems that exhibit coupled failure mechanisms. Often, components have fewer failure modes, so it is far easier to identify the failure modes of a component than those of a system. Nevertheless, components such as a bearing in tidal turbine drivetrains comprise several sub-components; therefore the component is complex in itself.

Quantitative Accelerated Tests- Qualitative Accelerated Tests are suitable for making design improvements leading to design modifications. The most common qualitative accelerated test include Highly Accelerated Stress Screening (HASS) and Highly Accelerated Life Test(HALT). HASS is a screening process which applies loads within the design limit on a sample of products to identify inherent defect caused by manufacturing process. On the other has HALT applies Loads which may exceed the design limit on a product till failure is observed. The failed component is identified as the weakest link thus is redesigned and tested to failure again. After several interactions, the weakest links in the products initial design are redesigned to make the make the product more reliable. As such this pushes down the failures observed in the useful life of the bath-tub-curve.

Accelerated Life Tests (ALT) -Accelerated Life Tests (ALT) has been extensively used in the electronic industry with many successes. These enable developers to evaluated warranty periods and expected cost of warranties.

Accelerated tests often utilise use stress acceleration where the magnitude of the stressor which causes damage is increase or usage rate acceleration where the frequency of the stressor is increased. For products which do not operate continuously, the frequency of operations can be increased to accelerate the degradation process. For example, a washing machine being used continuously in 24 hours a day may simulates a weeks' worth of washing.

A fundamental step for designing an ALT is the selection of a failure distribution. Ideally, a Physics of Failure (PoF) approach should be used to determine failure

distribution of each component, subsystems and systems. Nevertheless, PoF approach is very data and resource intensive even at component level thus a probabilistic approach based on failure rates is impractical for more complex systems such as a tidal turbine drivetrain. The reliability of less complex components such as the low speed shaft can still be assessed by using an interference diagram approach. The failure distribution of a tidal turbine can be evaluated by building a probabilistic model based on the system's structure and component failure rates.

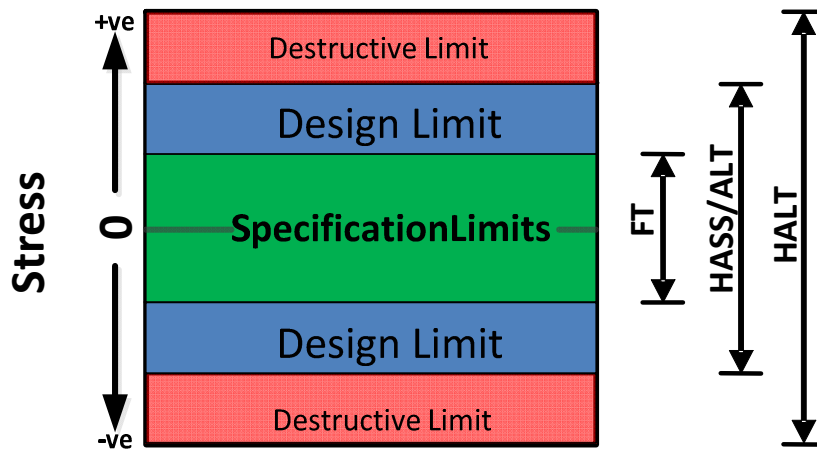


Figure 2.22–Typical stress range for components

ALTs then map the failure distribution at high stress to failure at use rate level through the use of an acceleration model. Figure 2.23 a shows how failures may be distributed as a high stress and use stress. The acceleration model which transforms the failure at high stress level may vary as shown in Figure 2.23b. By testing at a number of stress levels, the failure mechanism is captured in an acceleration model which can then transform test data at a particular stress level to other stress levels

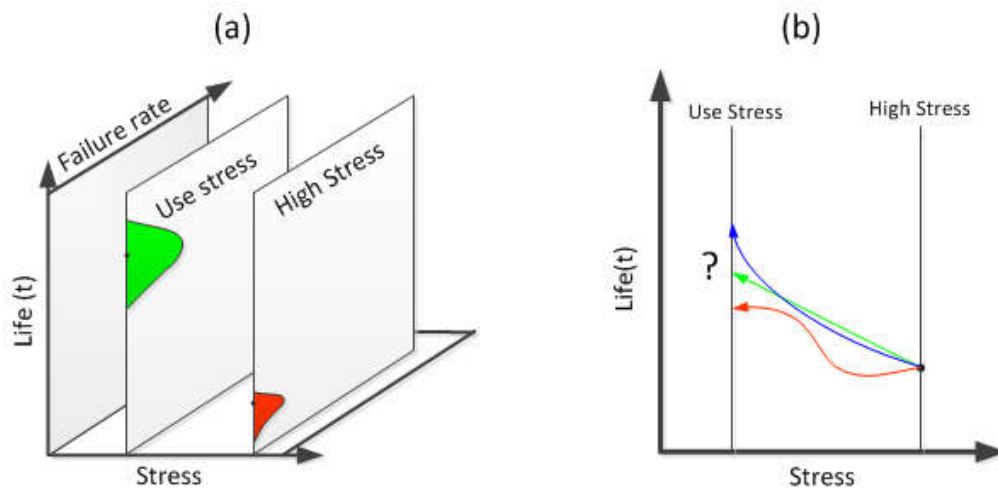


Figure 2.23– (a) Underlying distributions at different stress levels (b) Mapping high stress data to use stress data different acceleration models

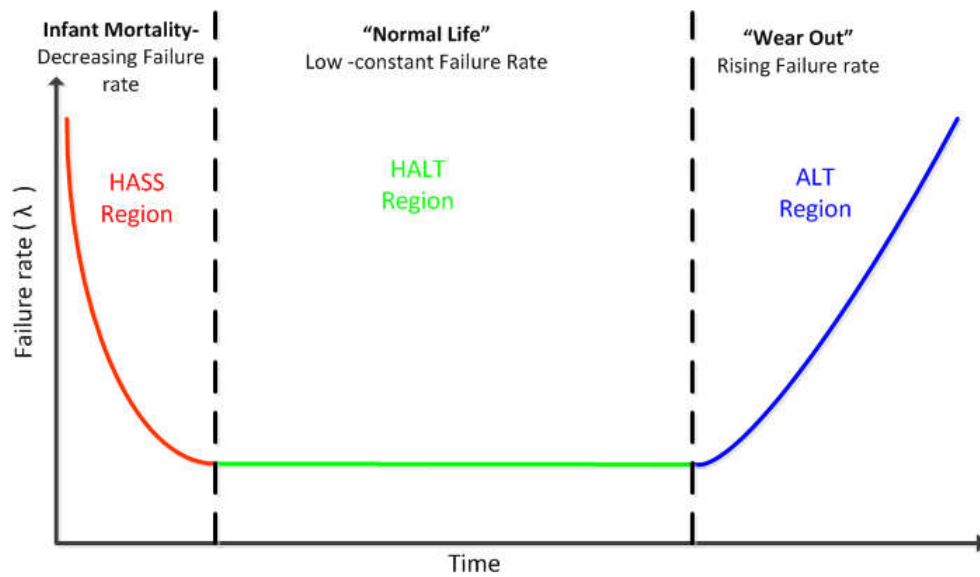


Figure 2.24–Typical parts of a component's bathtub curve where reliability tests may apply

2.3.7 Drive train component reliability

The components of typical horizontal axis tidal turbine are generally similar to components of medium sized wind turbines. Wind turbines are by and large designed for operational lives circa 20-25 years. However the experienced lifetime of some nacelle components fall far short this figure [92]. Design deficiencies caused by the lack of in-depth understanding of the operating conditions has been

suggested as the possible cause of drivetrain failures [93]. Others have suggested other reasons such as poor maintenance, and improper installation. From examining field gearbox failures, 10% of them can be attributed to manufacturing anomalies and quality issues [93]. It is critical that significant failure modes and their root causes are clearly identified and monitored to increase reliability

2.4 Rolling Bearings

Today a wide variety of rolling element bearings exist ranging from ones that are used in translational allocations to rotational applications. Due to their versatility and low operating friction, rolling element bearings are widely used in many applications compared to hydrodynamic bearings. In addition, their dependency on lubricant is not as severe as compared to hydrodynamic bearings. Rolling element bearings support a wide range of loads while permitting constrained relative motion between two bodies. In general, they utilise rolling elements in rolling contact with little or no sliding between two raceways. Bearings are generally selected to suite a particular operating speed, load characteristics, temperature, misalignment, noise motion error, dynamic stiffness, available space, installation and maintenance procedures.

2.4.1 Types of rolling element bearings

Although rolling element bearings can be categorised by various metrics (means) such as thermal features, thrust carrying capabilities and so on, they are generally categorised by geometry. Two major categories can be distinguished, namely roller bearings and ball bearings. Each of these can be sub divided into further categories. Detailed listing of bearings types and their applications can be found in manufacture's catalogues. A short summary of some common types is provided below.

2.4.1.1 Ball Bearings

Ball bearing utilise a spherical rolling element hence the name ball bearing. Most popular of these include the Deep Groove Ball Bearing, Angular Contact Bearing and Thrust Bearing

Deep Groove Ball Bearings as shown in Figure 2.25a can generally carry substantial amount of radial and thrust load due to the high degree of conformity between raceways and rolling elements (balls). In deep groove ball bearings the balls roll between inner and outer races which have high shoulders on each side.

Angular Contact Ball Bearings can be considered a variant of the deep groove ball bearing with the exception that at least one of the race rings has a lower shoulder as shown in Figure 2.25b. Due to this design, the angular contact bearing can support thrust loads in one direction and needs a thrust load to maintain the contact between races and the balls thus eliminating endplay. Typical contact angles for angular contact bearings range from 15° to 40° . They are often used in a range of mounting configurations to support complex loads.

Thrust Ball Bearing- Generally, Ball bearings with a contact angle greater than 45° . are classed as thrust bearings. Most thrust bearings have a contact angle of 90° . Thus are only suitable for supporting thrust loads.

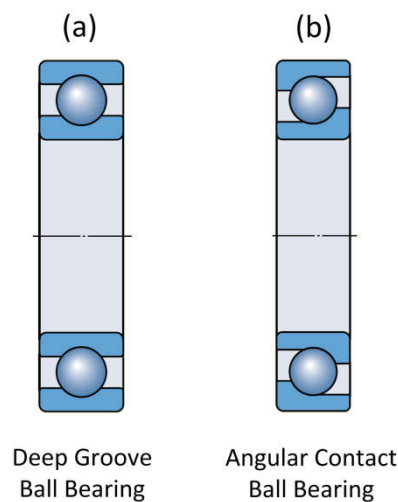


Figure 2.25– Common types of ball bearings

2.4.1.2 Roller Bearings

The rolling elements in roller bearings generally referred to as rollers and comprise a circular cross-section which is extruded in the direction transverse to rolling. Similar to ball bearings, roller bearings can be designed to primarily carry thrust load and thereby become thrust roller bearings. Thrust roller bearings have a higher capacity of trust loads compared to their radial counterparts. In most cases the ability to support a much higher thrust load is achieved by an aggressive contact angle. Roller bearings are often crowned to avoid excessive edge loading

Cylindrical Roller bearings(CRB) have a cylindrical rollers that are axially guided between integral flanges on at least one of the bearing rings as shown in Figure 2.26a. Needle roller bearings may be considered cylindrical roller bearings with a length much greater than the diameter of the cylindrical rollers. To avoid roller skew double row arrangements are often preferred to simply making the rollers longer to carry more load.

Although cylindrical roller bearing offer great radial load carrying capacity they often cannot support any axial load. Consequently, they are used in non-locating positions in many wind turbine drivetrains including as secondary main bearing and in many gearbox positions.

Tapered Roller Bearings (TRB) have tapered race ways as well as the roller which is guided in-between them by an accurately placed rib as shown in Figure 2.26b. In TRBs, the outer race is often called the Cup while the inner race is called the cone. The curvatures of the cup and cone are designed such that the extension of the raceways will converge to a common apex point which lies at the axis of rotation. The tapered raceways make TRB suitable for carrying combined radial and axial load as well as axial loads only.

TRBs are common in the wind and marine renewable industries. Nowadays, tapered roller bearings form a major part in the drivetrains of wind and tidal turbines. They tolerate axial loads to a higher degree compared to other radial roller bearings. They also support moment loads which are quite significant in main bearing applications.

Spherical roller bearings (SRB) as shown in Figure 2.26c consist an outer raceway which forms part of a sphere. The roller is often symmetric barrel shaped although asymmetric designs are also available. The raceways are designed to have a high degree of conformity with the roller. Due to the high degree of conformity SRB geometries they can carry heavy loads

The Geometry of SRB make them self-aligning which is advantageous in most cases. However, this introduces higher frictional torque which makes them unsuitable for high speed applications. SRBs have been used in many wind turbine main shaft bearing arrangements because of their high load carrying capacity, tolerance to axial load and tolerance to misalignment [94].

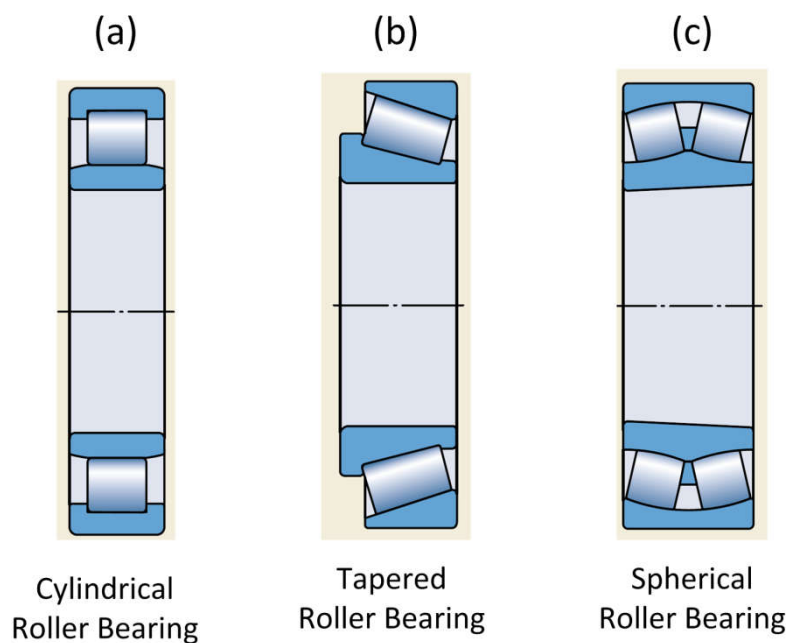


Figure 2.26– Common types of roller bearings

2.4.2 Bearing Geometries

A standard rolling element bearing comprises an inner race and a set of rolling elements arranged to separate the inner and outer races as shown in Figure 2.27. Most bearings utilise a cage to maintain the proper angular spacing between rolling element with the exception of full complement bearings where the need for a cage is

eliminated by having no gaps between rolling elements. Integrated Seals are also common in some rolling element bearings for retaining the lubricant.

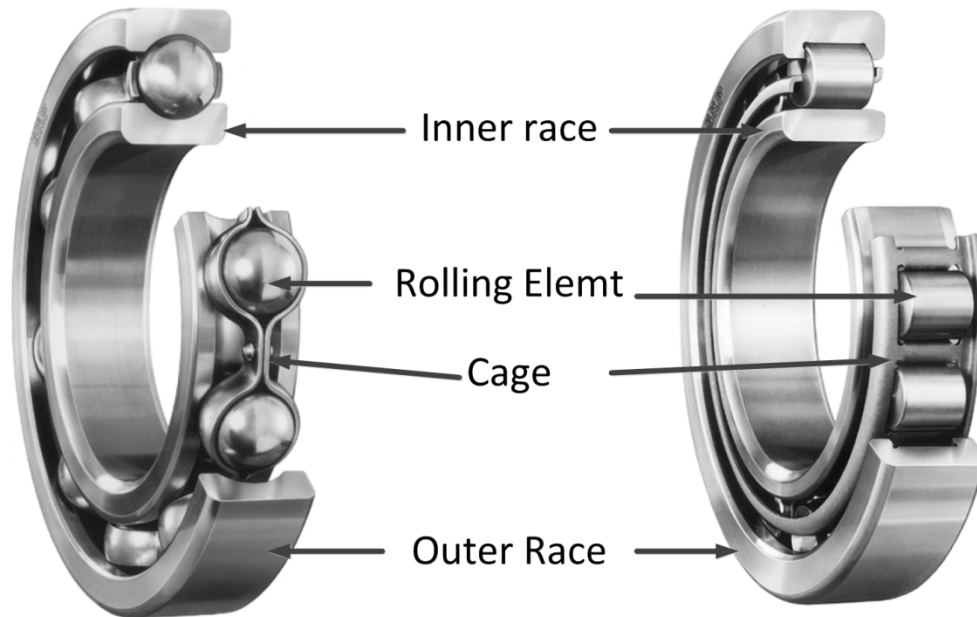


Figure 2.27– Typical components of a rolling element bearing

For a specific design of bearings, different types of cage designs and cage materials can be used. Other bearings avoid the use of cages altogether. These are usually full complement bearings. The increased number of rolling elements enables the bearing to be used in higher load applications.

2.4.3 Bearing Failure modes

A failure mode of a component defines the manner in which the component has lost its ability to function as desired. As Tavner [95] states, 'the root cause of failure initiates the failure sequence while the failure mode terminates it'. The failure mechanism links the root cause of a failure to the failure mode. Some failure mechanisms may accelerate other mechanisms or themselves. Figure 2.28 shows the classification of common bearing failures modes as given by ISO :15243[96]. Since

bearings and gears operate under rolling contact, these failure modes are also present in many gear sets and drivetrain components. The most relevant failure modes are discussed further below.

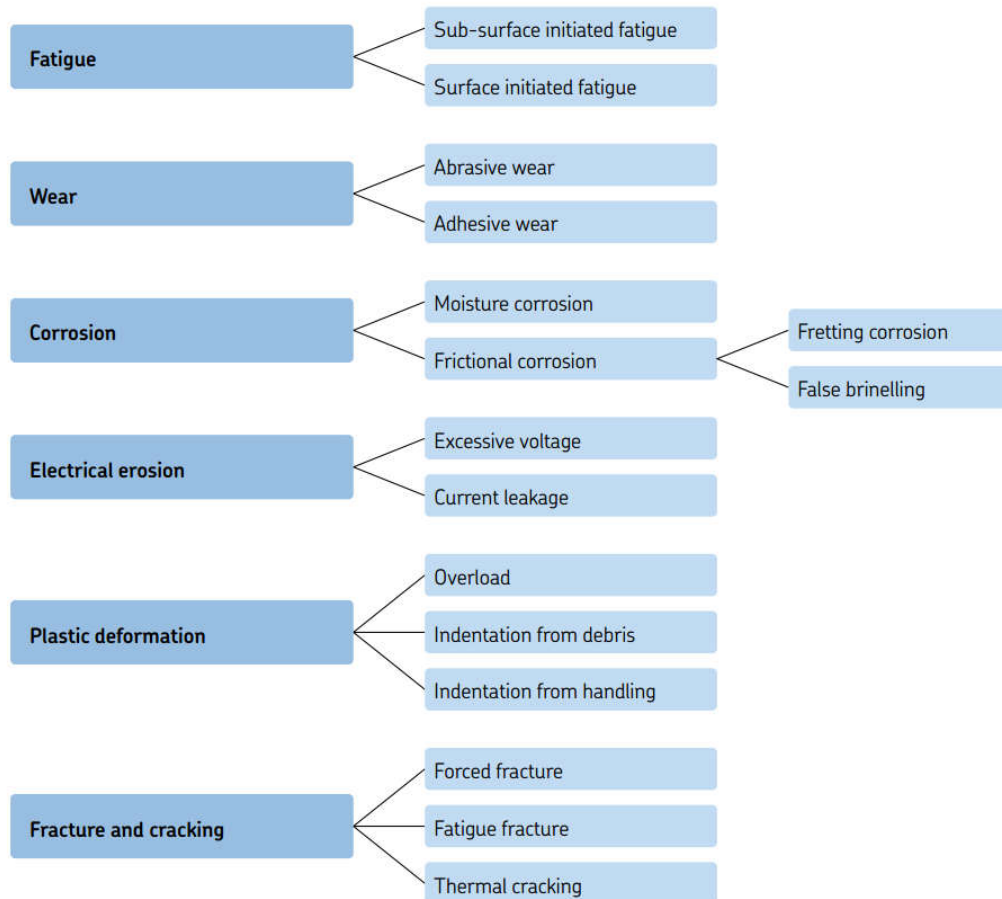


Figure 2.28–Bearing Damage classification as per ISO 15243[96]

2.4.3.1 Spalling-Sub surface Initiated Rolling contact Fatigue

Supposing a bearing is used in the correct application, mounted well and lubricated well, it will eventually fail due to Spalling. Spalling is caused by the propagation of subsurface cracks, often developed from inclusions in the material matrix. After continued crack propagation towards the surface, cracks agglomerate to result in the removal of material from contact surface. Spalling mechanism is

influence by factors such as overloading (above fatigue limit), hydrogen ingress, wrong Preload/clearance, interference fits (Hoop Stresses), misalignment and Non-metallic inclusions in bearing material. Figure 2.29 shows how the geometry of a spall compares to the other Hertzian contact failure mode 'pitting'.

2.4.3.2 Pitting(Micro/macro)- Surface Initiated Rolling contact Fatigue

Pitting is a surface fatigue failure mode similar to spalling. Micro-pitting is often caused by asperity to asperity contact in the contact surface. This causes plastic deformation at the asperity tips. Micro pitting may cease sometimes after initiation due to averaging of surface asperities. On the other hand, Macro pitting is caused by crack growth at or near the contacting surfaces. Factors such as frictional sliding draw the maximum stress in the contacting bodies from the sub-surface to the surface or near surface region. Macro-pitting can also arise due to hydraulic fracturing caused by lubricant pressures in small cracks in the surface. Pitting is influenced by poor lubrication (low λ values), High Surface friction/traction, Overloading, operating speed(leading to poor lubrication), Edge loading

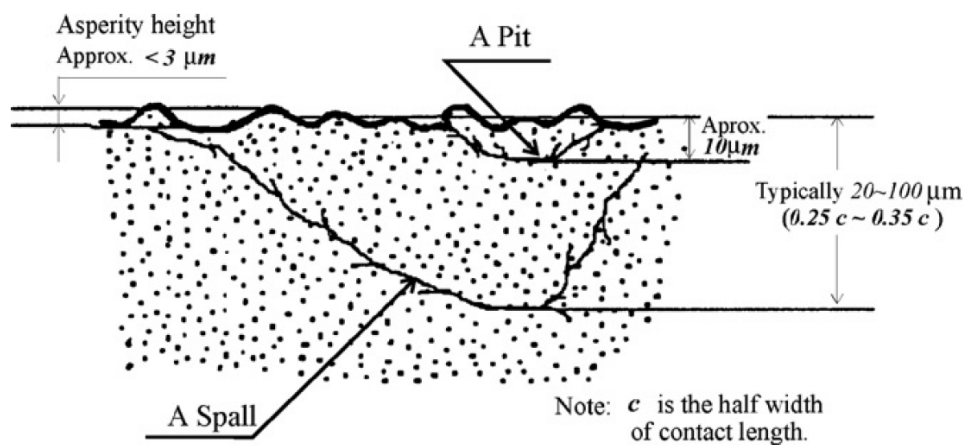


Figure 2.29–Schematic representation of pitting and spalling[97]

2.4.3.3 Scuffing-Adhesive wear

Also called smearing, Scuffing usually follows skidding. Skidding usually occurs under light load conditions. Sliding of the contact surface under frictional loading leads to a high flash temperature which causes the asperities on the surface to weld together and rip apart from their relative motions.

2.4.3.4 False Brinelling and Fretting Corrosion - Frictional corrosion

Caused by external structural borne vibrations on stationary contacts. Under these conditions, lubrication may be squeezed out of the contact. Since the motion caused by vibration is too small, the lubricant is not replenished between the contacting surfaces, leading to metal-to-metal contact of surface asperities. False brinelling is the first to occur under these conditions. After the onset of false brinelling, the wear debris may hinder lubricant from reaching the contact surface. Severe adhesive wear called fretting may set in where the natural oxide layer is removed and the contacting surfaces are welded together. The wear rate is drastically increased at this stage to fretting corrosion. Relative motion will cause the weld to break leaving a hematite ($\alpha\text{-Fe}_2\text{O}_3$) residue. Figure 2.30 shows Brinelling on the raceway of a bearing.

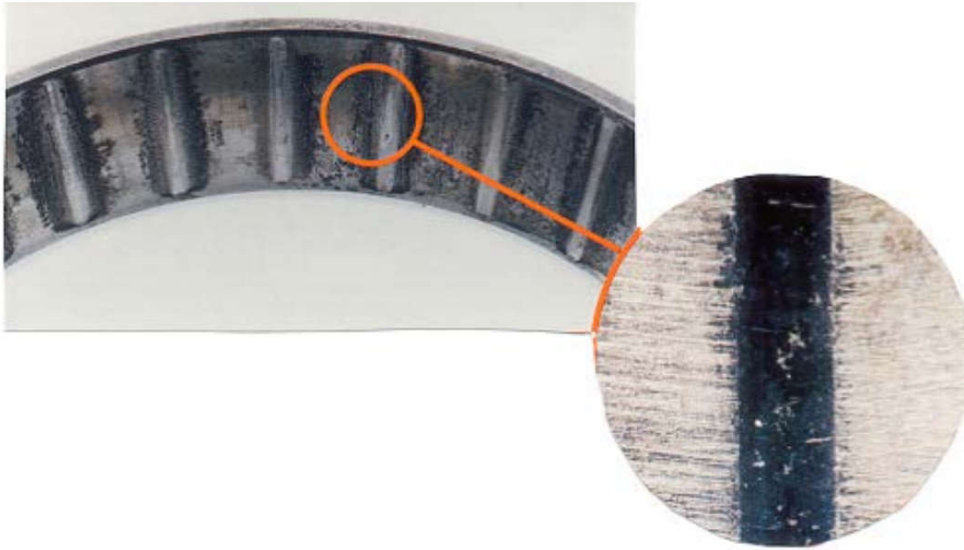


Figure 2.30– False Brinelling on bearing raceway [98]

2.4.3.5 Debris Denting/ True brinelling-plastic flow

This plastic flow failure mode is characterised by the indentation of bearing surface by a harder compound. True brinelling happens when rolling elements indent the raceways, while debris denting can occur when harder debris is pressed into contacting surfaces to produce an indent. Exceeding a bearings static capacity greatly increases the onset of True brinelling. Poor lubricant cleanliness can also contribute to debris denting.

2.4.3.6 Wear- abrasive wear

Abrasive wear is common in many bearings. It happens when a harder material which moves relative to a softer material causes the removal of material from the softer material. In bearings, wear is typically controlled by lubrication which separates the contacting bodies and prevent them from coming into contact. Roller end wear is a common failure mode which is caused by excessive axial load of preload.

2.4.3.7 Other Failure modes

Other failure modes include classical high cycle fatigue fracturing. Cage failure also causes bearing seizure. Moisture corrosion is usually controlled by lubrication; however, lubricant contamination can lead to corrosion and degradation of bearing surfaces.

2.4.3.8 Common Failure modes observed in drivetrains

From reliability analysis of medium sized wind turbines, the most critical components in the drivetrain are the generator and the gearbox. Most failures in the gearbox are found either in the bearing or the gear sets[99]. Details of field data have revealed that bearing failures are prominent at the high speed stages of the gearbox while gear failures are more concentrated on the lower speed planetary stage [100] [101] .

The primary failure mechanisms for gear sets include surface fatigue, wear, plastic flow and breakage. Each mechanism may result in different failure modes. Supposing a gearbox is adequately designed, installed properly and maintained sufficiently, it is expected the gearbox will eventually fail due to fatigue. In general gearbox failures arise as a result of one of, or a combination of misapplication, lubrication error and misalignment[98] 80% of gearbox failures arise from the bearing, which ends up causing secondary damage[102].

Bearing failures are known to lead to secondary failures for example a bearing failure which is caused by wear may increase friction and deteriorate the lubricant quality, due to the increased temperature. The poor lubricant quality will increase the probability of gear pitting or wear. Similarly excessive wear can lead to misalignment or vibration which may adversely influence the lifespan of other components.

Following long surface and/or subsurface fatigue damage, structural cracks begin to develop in bearings. Sub surface cracks present stress concentrations which cause rapid and complete failure of the raceway[103]. Milburn[104] describes such axial cracks in the inner race of bearings in wind turbine drivetrains as a failure of "epidemic proportions ". This type of failure was also reported [101] where bearing

spall and gear pitting are the dominant failure modes of the gearbox sub assembly[102]. For ball bearings localised spalling is a typical failure mode [105].

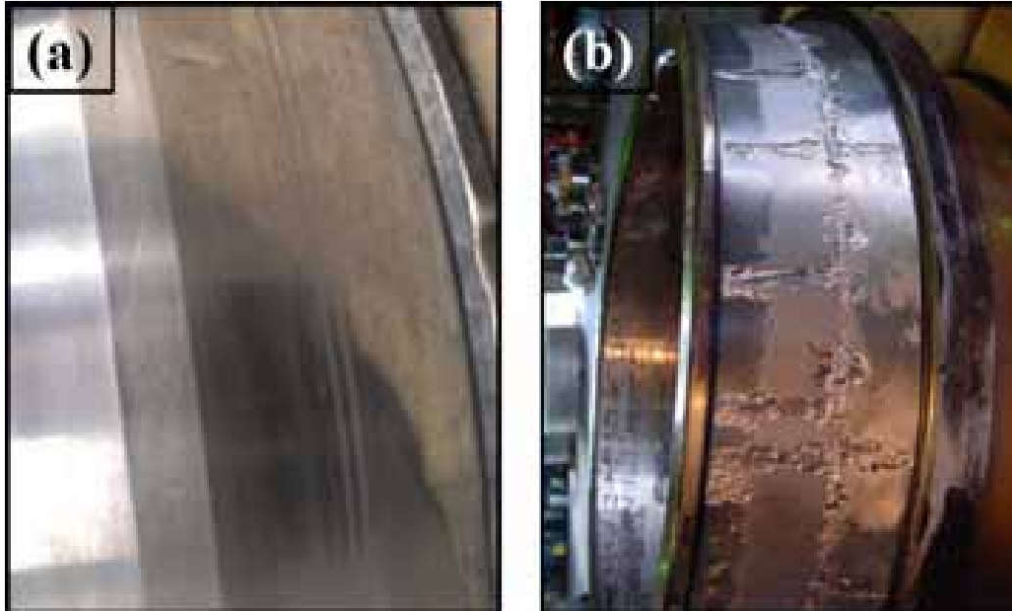


Figure 2.31– Micropitting of a 230/600 series spherical roller main

shaft bearings (a) onset of micropitting (b) Advanced micropitting and spalling [106]

Errichello and Muller [107] inspected a failed gearbox in an 800kW wind turbine. The inspection revealed severe scuffing on the high speed gear set. Scuffing is a type of adhesive wear which manifests itself in the form of scratches in the tooth surface due to wearing and tearing [99]. Lubricant starvation was identified as the possible root cause of this scuffing. The inspection also revealed the presence of a Straw –Yellow temper colour on the high speed shaft bearing which indicates that temperature may have reached 400°F. It is evident that the lubricant starvation which caused scuffing in the high speed gear set may have been initiated by the high temperature in the bearing which caused the lubricant to fall out of specification. Scuffing is prominent in roller bearings with full complement bearing being the most susceptible to this failure. Figure 2.32 below depicts scuffing in a wind turbine gear teeth.



Figure 2.32– scuffing on the high speed stage of wind turbine [107]

Fretting corrosion was the primary failure mode of the sun spline in Errichello and Muller's [107] analysis. This failure mode was also observed on several parts of the sun gear assembly including the bearing retainer, bearing outer ring, sun spherical thrust rings and sun pinion. This type of failure is caused by vibratory movements and occurs on two contacting surfaces which are pressed together and experiencing cyclic loading of small amplitudes. Severe Fretting corrosion was observed on all the teeth of the intermediate stage gears along with some scuffing and polishing wear.

Planetary gears are ideal in many cases where high torque to weight ratios and a compact design are required. For this reason they have been used in industries such as the aerospace, automotive and heavy industries. In a planetary gear box, the load transmitted by the sun gear is shared among the planets. The sun gear is thus subjected to very large loads which makes it susceptible to pitting and cracking and, indeed, these are frequent failure modes of the sun gear [108] [109]

2.4.3.9 Root causes

A root cause of a failure may initialise different failure mechanisms, hence lead to different failure modes. Similarly a failure mode may have numerous root causes. The major causes of bearing failure include wear and fatigue [110]. Wearing is nevertheless reduced significantly when a bearing is well lubricated, well-sealed

and operating at moderate loads. A bearing under this operating condition will inevitably fail due to spalling.

Overloading is one of the major causes of failure in many parts of the drive train. Transient events such as emergency stops apply severe dynamic loads to components of the drive train. Scott et al [111] demonstrated that such transient events can increase loading by a factor of three. In addition overloading at low speeds results in inadequate lubrication which, in turn, may lead to secondary failure modes associated with lubrication failure such as wear. Overloading, for example, is known to affect the planetary stage bearings of a gearbox are not equally shared between planet gears [112] hence planetary bearings may exceed their design load, leading to spalling, which often occurs when design loads are exceeded.

Non torque loads are generated by the hub and blades, tower shadow, wind gusts, control, thrust and other forces. An axial thrust force is also produced as a result of the out of plane component of the aerodynamic forces. The pitching and yawing mechanisms also contribute to imbalances in the load on the rotor, which will apply non torque load on the drivetrain. In typical wind turbine designs the main bearings are designed to transmit axial thrust forces on the main shaft directly to the bedplate, to prevent it from getting to the gearbox. However, the gearbox may be moved by a reversing thrust because bearings are designed to have axial clearance[93].

In addition, bending in the main shaft is also known to adversely impact the planet ring gear meshing pattern and also lead to planet carrier misalignment[93]. The clearance in the planet carrier bearing affects the sensitivity of the gearbox to non-torque loads and may lead to unequal loads on the planet bearings[113].

Moisture ingress in the lubricant is also common in wind turbine applications. An inspection by Errichello and Muller [107] revealed that the seal on the high speed shaft of a gearbox was missing. This led to moisture and dust entering the gearbox and lubrication system. In addition to this, they found some assembly damage on the upwind intermediate bearing. This indicates that installation practices do have an impact and can be improved to increase reliability.

The lubrication systems play a vital role on the reliability of the drivetrains [114]. Lubrication errors do not only affect wear but also have an influence on micropitting and other failure modes. Lubrication error may also be a secondary root cause. It has been observed from experience that most secondary gearbox failures are caused by bearing debris and excess bearing clearance which arises as a result of surface wear and misalignment [102]. The accumulation of debris happens after continuous wear, micropitting, spalling, breakages and failure modes which cause the removal of materials from bearings in the gearbox.

2.4.3.10 Tidal turbines: Applying the wind turbine experience

Although horizontal axis tidal turbine technology is similar to the horizontal axis wind turbines, the two are exposed to very different operating environments. Given that the density of water is much greater than that of air, it is possible to use smaller rotors to extract energy from tidal flow. Tidal velocities, on the other hand are much slower than wind. However, it is common practice to design tidal turbines to operate at tip speed ratios (TSR) which are similar to wind turbine TSR. Tidal turbines are consequently designed to operate at rotational speeds ranging from 10 to 20 revolutions per minute (rpm)[40]. Given that tidal turbine blades rotate at similar rotational speeds to wind turbines, they often use three stage gearboxes incorporating a first stage planetary system with two spur gear stages, [3] just like the ones which are commonly used in the wind industry. MCT's Seagen [115] employs such a gearbox to convert the 12 rpm rotation of the rotor to 1000rpm. The drivetrain components used in wind turbines are, therefore, very similar to those used in tidal turbines, in both technology design and configuration.

Due to the cyclic nature of tidal flows, tidal turbines cut in at speeds circa 0.7m/s [27]. However turbines with pitching capabilities may be left at a standstill or idling at slack water. When the turbine is at a standstill, turbulence structures in the water will apply minute loads on the turbine components. These standstill events have the potential to cause fretting corrosion and false brinelling in tidal drivetrain components, just as experienced in wind turbines.

In contrast to wind flows which are highly stochastic, tidal flows are somewhat deterministic. The oscillatory motion caused by the tide imposes a cut-in for each half tidal cycle. The high transient loads (acceleration) which occurs at cut-in is likely to influence failure mechanisms such as skidding. In addition tidal turbines are subjected to wave loadings and much larger turbulence scales relative to rotor size. McCann[40] has illustrated that there is a correlation between wave loading and fatigue damage, as well as turbulence and fatigue damage on general tidal turbine components. Turbulence length scale in tidal flows can be as high as 16m, which is comparable to a rotor diameter of pre-commercial tidal turbines with rotors about 16-20m. The effects of turbulence on turbine drivetrains may be greater in tidal turbines.

The main failure mode of the main shaft in wind turbines has been identified as high cycle fatigue [85]. The cyclic nature of wave loading and turbulence are likely to increase structural fatigue failure modes in the drive train. The turbulence in the tidal current is likely to accelerate many failure modes such as fretting corrosion at both standstill events and during operation.

The NREL's Gearbox reliability collaborative (GRC) [93] considers non-torque loads as one of the major contributors to the failure of wind turbines. Some sources of non-torque loads in tidal turbines such as hub weight, can be reduced by adjusting the buoyancy of the rotor blades accordingly.

The axial thrust force and gust induced non-torque loads in wind turbines are replicated in tidal turbines. The higher turbulence intensity at low speeds is likely to accelerate failure modes caused by non-torque loads. Given that adhesive wear is caused by high frequency load variation [68] which arises as a result of high turbulence, it is likely that this failure mode will be accelerated. Turbulence from wake effects are avoided in wind farms by appropriately separating wind turbines. However, the bathymetry of a tidal site is a lot difficult to control, but has a significant influence on turbulence in the tidal current.

Finally, marine growth could have an effect on turbine performance and loading. As Musial et al [93] point out, severe non-torque loads are generated by imbalances in the rotor and hub movements. In tidal applications, rotor and hub imbalances may be exacerbated by marine growth and bio fouling.

2.4.3.11 Main Bearing Reliability

Typical ‘drivetrain’ systems as shown in Figure 2.16 consist of the main bearings, shafts and couplings. With the exception of the gearbox, this has the highest downtime per failure as per [43]. The Main bearings are a major component in the drivetrain of tidal turbines. Its primary role is to support non-torque loads that are generated by the rotor, while enabling the torque to be transmitted to the gearbox and then on to the generator to produce electricity.

Guo et al. [116] modelled the influence that gravity and main bearing clearance nonlinearity has on wedging in a wind turbine spur planetary gearbox. They revealed that bearing clearance and gravitational excitation may cause failures in the planetary stage of the gearboxes. Failure of the main bearings to eliminate non torque loads to the gearbox has been shown to influence the gearbox performance and reliability. Park et al [117] established that the presence of non-torque loads modified gearbox mesh misalignment, contact pattern, load distribution, and load sharing [117]. It is clear that the reliable performance of the main bearings is vital to the reliability of the whole nacelle.

2.4.4 Static Load distribution radial roller bearings

In general, the load, Q carried by a single rolling element in a rolling element bearing is proportional to the deformation δ of the rolling element and a constant (K) and is postulated as: [6]

$$Q \sim K\delta^n \quad (\text{EQN 2.30})$$

The exponent n is often 1.5 for ball bearings and 1.11 for roller bearings. For a double row roller bearing in static conditions, the load carried by a rolling element in position ψ on row number i can be expressed as a function of the maximum roller load [118]:

$$Q_{\psi i} = Q_{\max i} \left[1 - \frac{1}{2 \epsilon_i} (1 - \cos \psi) \right]^{1.11} \quad (\text{EQN 2.31})$$

Similarly, the radial force F_r and the axial force F_a are related to the maximum roller load $Q_{max i}$

$$F_r = ZQ_{max i}J_r \cos \alpha \quad (\text{EQN 2.32})$$

$$F_a = ZQ_{max i}J_a \sin \alpha \quad (\text{EQN 2.33})$$

where, J_r and J_a are

$$J_r = J_r(\epsilon_1) + \frac{Q_{max2}}{Q_{max1}}J_r(\epsilon_2) \quad (\text{EQN 2.34})$$

$$J_a = J_a(\epsilon_1) + \frac{Q_{max2}}{Q_{max1}}J_a(\epsilon_2) \quad (\text{EQN 2.35})$$

and $\epsilon_1, \epsilon_2, J_r, J_a$ values can be found in tables such as provided by Harris and Kotzalas [118].

The internal clearance of the bearing plays a critical role in the internal load distribution in the Bearing. Figure 2.33 below shows the effect of bearing clearance on load distribution. When the nominal internal clearance is zero the bearing load is distributed along 180° of the bearing. Conversely, a clearance larger than zero will result in load being distributed in less than 180° leading to the maximum peak load which exceeds the peak load for a bearing with zero clearance. Similarly, preload will result in the load being distributed along a wider section of the bearings. This results in a reduction in peak load. Other factors may play a role in the bearing load distribution such as raceway thickness (rigidity), as well as bearing supports and housing.

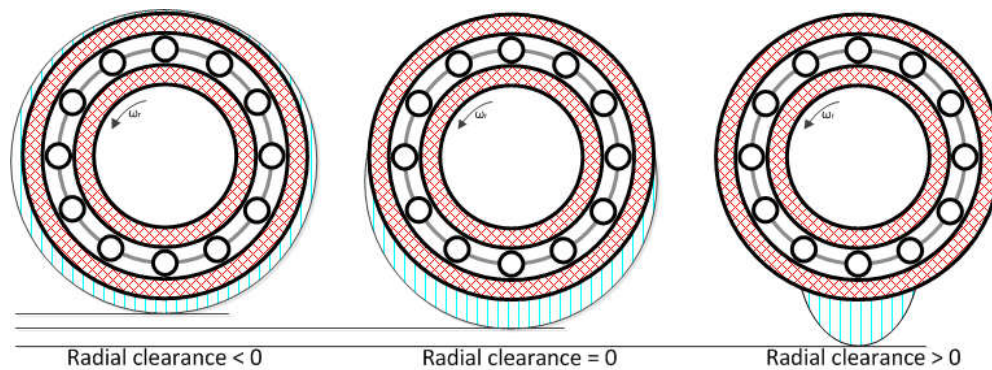


Figure 2.33– Effect of internal clearance on load distribution.

2.4.5 Contact Mechanics

The study of contact between bodies has been the study of many researchers for over a century. Heinrich Hertz first investigated the contact between two elastic bodies by considering contacting bodies as elastic half-space in 1882 [119]. In his analysis which considered contact of curved bodies, the deformation of contacting bodies was defined to be a function of the materials modulus of elasticity and geometry of the contacting bodies. This resulted in an induced normal stress in the bodies.

In developing the theory behind the compressive contact between curved elastic bodies, Hertz assumed that strains caused by the load are small enough that the elastic material under consideration is elastic and does not undergo plastic deformation. The idealised conditions imposed by hertz included the treatment of the surfaces in contact as frictionless and non-conformal.

In the late 1960's experimental observations confirmed that Hertzian theory is not universally applicable because contacting bodies can sometimes support a tensile force. These experiments confirmed that at low loads, the contact area is larger than that predicted by Hertzian theory. In addition, when the load was removed completely, the contact area assumed a non-zero value. A strong adhesive behaviour was observed when the contacting surfaces were clean and dry. This had been investigated by Bradley in the 1930s who explained an effect caused by Van der Waal's forces between spherical bodies which are near each other but not in

contact. Johnson-Kendall-Roberts (JKR) model included the effect of the adhesive van der Waal forces and Hertzian theory to develop the JKR models for adhesive elastic contact of spheres. Similarly, the DMT model [120] was presented by Derjaguin, Muller and Toropov in 1975 which focused on contact where there is a small curvature radius and high stiffness contacting body. This model also assumes the deformed surface geometry takes a similar form as that presented by Hertz. JKR and BMT models appeared to contradict each other because they solve a similar problem and end up with starkly different results. JKR assumes adhesion in the contact area while DMT considered adhesion outside the contact area. Tabor [121] found the DMT and JKR operate within different operating regimes and gave coefficient λ showing the regimes where these models may apply.

$$\mu = \left(\frac{Rw^2}{E^2 z_0^3} \right)^{1/3} \quad (\text{EQN 2.36})$$

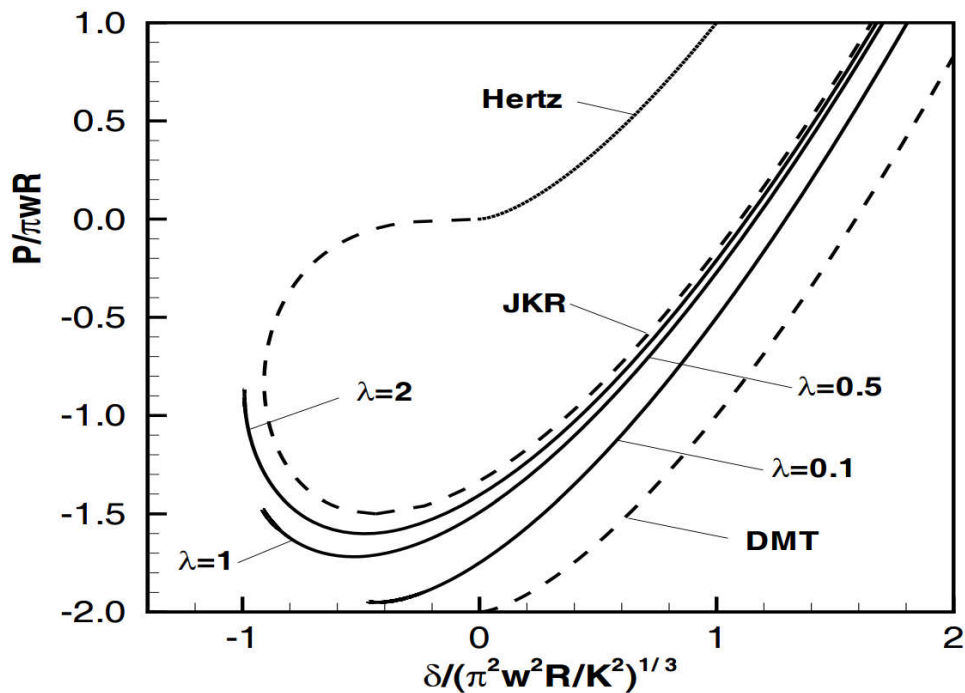


Figure 2.34– Moments on main shaft(output of elastic simulation)

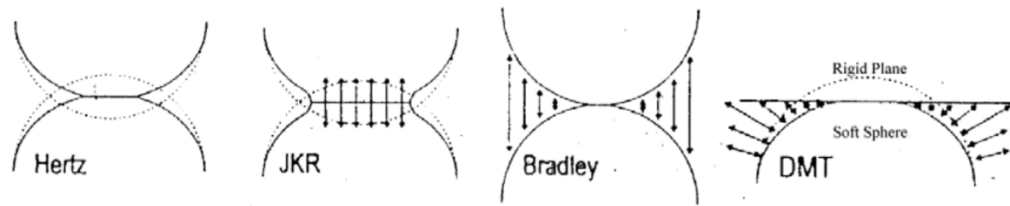


Figure 2.35– Moments on main shaft(output of elastic simulation)

Maugis[122] improved on Tabor's ideas and presented models for the transition between JKR and DMT based on work done by Dugdale [123] to form the Maugis-Dugdale model which is solved iteratively. A closed form approximation of the Maugis-Dugdale model was presented by Carpick et al known as the Carpick-Ogletree-Salmeron (COS) model [124].

The classical Hertzian model considers single contacts. Realistic contacting surfaces are composed of several asperities in contact. To generalise the Hertzian model to reflect contact of rough surfaces, a multi asperity contact model must be applied. Adams and Nosonovsky [125] grouped the multi-asperity contacts into two groups, coupled and uncoupled analysis. Uncoupled analysis treats the roughness as a set of asperities with statistically distribution of contact parameters such as asperity height or summit curvature. Individual asperities are considered to have local effects and the effect of all asperities is analysed by summing up the effect of individual asperities. Conversely, coupled models require solving the whole multi-asperity contact simultaneously. This leads to a mixed boundary value problem which can only be solved analytically for simple geometries.

Greenwood-Williamson theory[126] considered contact between surfaces with randomly varying roughness. Bush, Gibson and Thomas extended this work to include roughness with different length scales. Today many statistical models are available to treat the surface irregularity in contacting bodies. Method such as the one presented by Greenwood and-Williamson considered elastic contacts. Plastic and elastic-plastic contacts which further generalises the contact problem have also been analysed by [127][128] and [129]. Recently, Fractal analysis has been employed for such uncoupled asperity analysis[130].

The problem of the contact between elastic bodies is still under investigation by many researchers. However, for rolling element bearings where the contact force is often large enough, Hertzian theory still delivers a good approximation of the contact problems. In addition, the adhesion force in this case is several orders of magnitude smaller than the gravitational forces and applied loads. Consequently, Hertzian theory forms a major part of many rolling bearing calculations ranging from life evaluation to lubrications analysis.

2.4.5.1 Hertzian contact theory

According to Hertzian theory for an ideal line contact, the maximum contact pressure when a force Q is applied on a cylinder whose length is l , may be evaluated by

$$P_{max} = \frac{2Q}{\pi l b} \quad (\text{EQN 2.37})$$

where b is the half width of the contact area given by

$$b = \left[\frac{4Q}{\pi l \sum \rho} \left(\frac{(1 - \nu_I^2)}{E_I} + \frac{(1 - \nu_{II}^2)}{E_{II}} \right) \right]^{\frac{1}{2}} \quad (\text{EQN 2.38})$$

The sub surface principal stress for this contact is given by

$$\sigma_x = 2\nu P \max \left[\sqrt{1 - \xi_b^2} - |\xi_b| \right] \quad (\text{EQN 2.39})$$

$$\sigma_y = P_{max} \frac{1 + 2\xi_b^2}{\sqrt{1 + \xi_b^2}} \quad 2|\xi_b| \quad (\text{EQN 2.40})$$

$$\sigma_z = P_{max} \frac{1}{\sqrt{1 + \xi_b^2}} \quad (\text{EQN 2.41})$$

$$\xi = z/b \quad (\text{EQN 2.42})$$

Where z is distance below contact surface.

$$\tau_{max} = \tau_{\frac{1}{3}} = \frac{\sigma_z \sigma_x}{2} \text{ for } 0 \leq \xi_b \leq 0.436 \quad (\text{EQN 2.43})$$

$$\tau_{max} = \tau_{\frac{1}{3}} = \frac{\sigma_z \sigma_y}{2} \text{ for } 0.436 \leq \xi_b \quad (\text{EQN 2.44})$$

The von-Mises stress is thus given by

$$\begin{aligned} \sigma_{VM} = \frac{1}{\sqrt{2}} & \left[(\sigma_x - \sigma_y)^2 + (\sigma_y - \sigma_z)^2 + (\sigma_z - \sigma_x)^2 \right. \\ & \left. + 6(\tau_{xy}^2 + \tau_{yx}^2 + \tau_{zx}^2) \right]^{1/2} \end{aligned} \quad (\text{EQN 2.45})$$

No closed form solution exists for the mutual approach of a Hertzian line contact but several approximations can be found in the literature. A common approximation is given by [131]

$$\delta_c = \frac{2F(1 - \nu^2)}{\pi LE} \left(\frac{2}{3} + \ln \frac{4R_1}{b} + \ln \frac{4R_2}{b} \right) \quad (\text{EQN 2.46})$$

2.4.5.2 Frictional Rolling Contacts

Due to the spherical geometry of SRBs, they are subjected to a phenomenon called Heathcoat slip. From Figure 2.17 it can be observed that if the surface velocities between the inner race and the rolling element are equal at locations 1 and 3, then the surface velocities must differ at location 2. It can be concluded from this that there is sliding between the roller and the centre of the raceway. Many researchers[132][133] have pointed to Heathcoat slip a cause of failure in spherical roller bearings.

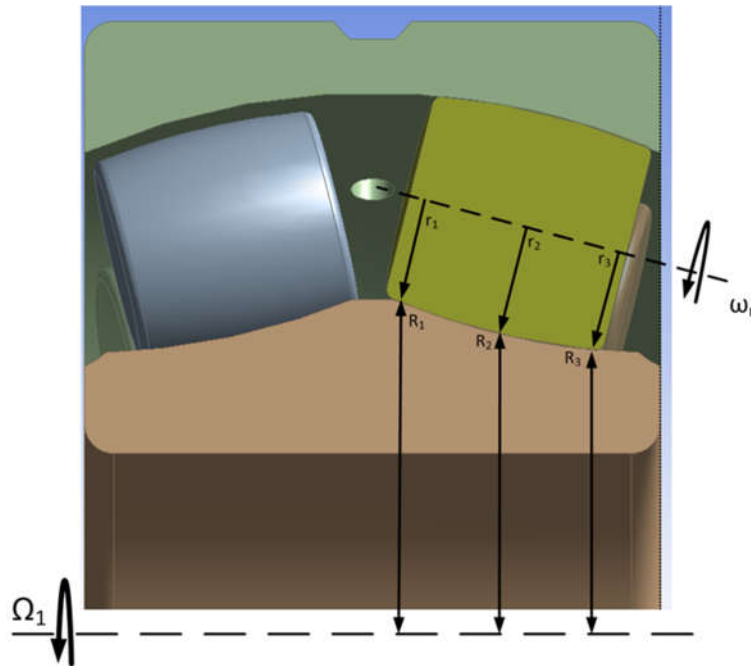


Figure 2.36– Physical description of the source of Heathcoat slip in a spherical roller bearing.

2.4.5.2.1 Two-dimensional rolling

It has been correctly identified that to achieve tractive rolling between two bodies, the rolling contact must not be in pure rolling but must also move relative to each other. A Slip velocity (slip) comprising the rigid body motion and elastic deformation is introduced as the relative velocity between two points from the different bodies in contact. The linear component of slip in the direction of rolling forms the longitudinal creepage while the component in the direction transverse to rolling is the lateral creep. Spin creepage is also present due to the elastic angular component of slip.

In the contact patch formed by two bodies in rolling, sliding exist in the contact patch in an area known as the slip region where limited sliding occur well before the contacting bodies slide over each other. The remaining part of the contact patch is called the stick/adhesion region is indicated in Figure 2.37. In 1926, Cater [134] based his study on a plane strain assumption to reduce the tractive rolling of rail wheels into a two-dimensional problem. This enabled the pure longitudinal contact

problem to be solved. This solution was also later confirmed independently by Fromm[135]. The solution for the 2D problem is written in non-dimensional form as

$$\frac{Q}{\mu N} = \frac{2R}{\mu a} v_x + \frac{R^2}{\mu^2 a^2} v_x |v_x| \quad (\text{EQN 2.47})$$

This arrives at the so called Carter's creep curve which enforces saturation by Coulombs law of friction as shown in Figure 2.39

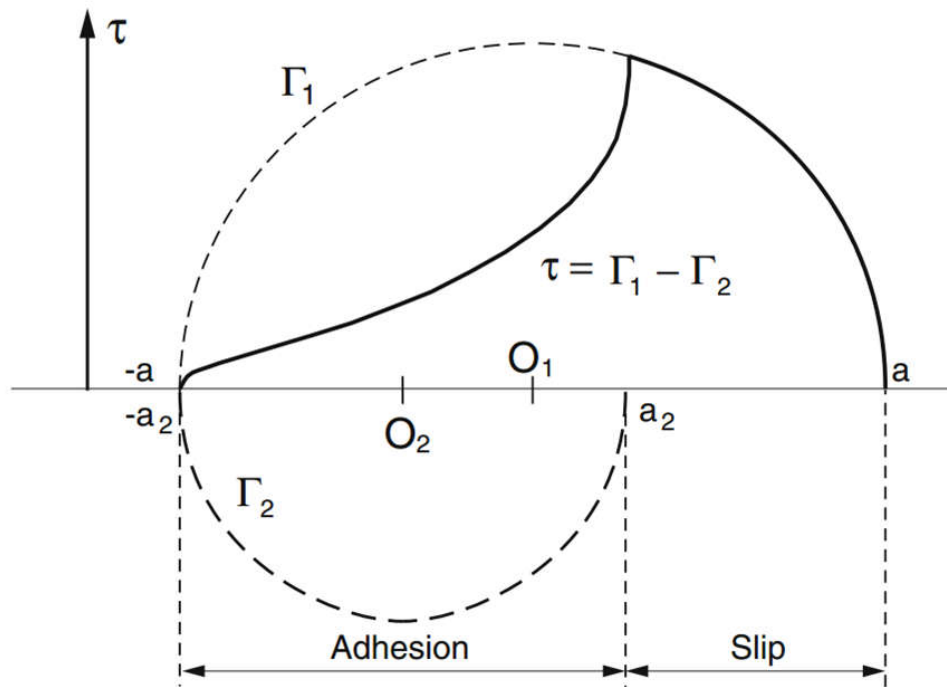


Figure 2.37--:Traction distribution in Carter's theory[136]

2.4.5.2.2 Three dimensional rolling

The problem of three-dimensional rolling contact was treated by Johnson[137] who correctly identified that the spin generates a lateral tangential force which opposes the lateral force created by lateral creepage as well as a moment around the vertical plane. Vermeulen and Johnson [138] extended Jonson's work to include an

elliptical contact where the stick region is smaller but has identical ratios to the original contact patch axis.

Kalker [139] introduced a linear theory which described an exact analytical method to calculate the contact forces in the linear region of the force-creep curve as shown in Figure 2.39. Kalker further developed Haines and Ollerton's [140] model which discretises the contact area into strips which are then solved using Carter's method while ignoring interaction between strips. This generally gives a better result compared to Vermeulen-Johnson theory for small spin values and when the lateral length of the contact area is small.

Kalker later combined spin and creepages in what he called the 'complete theory' for three dimensional rolling contacts. The iterative nature of the so called complete theory increases the computational effort required to solve. Kalker [141] later introduced simplified theory to approximate a parabolic traction bound to solve the tangential problem. He later introduced FASTSIM [142] which implemented the approximate solution in a numerical algorithm that can be used in multibody dynamics packages. Other faster approximations have been developed by Polach [143] which unlike FASTSIM can also deal with non-steady state conditions. Today, these contact models are available in some dynamic simulation packages such as Simpack and ADAMS.

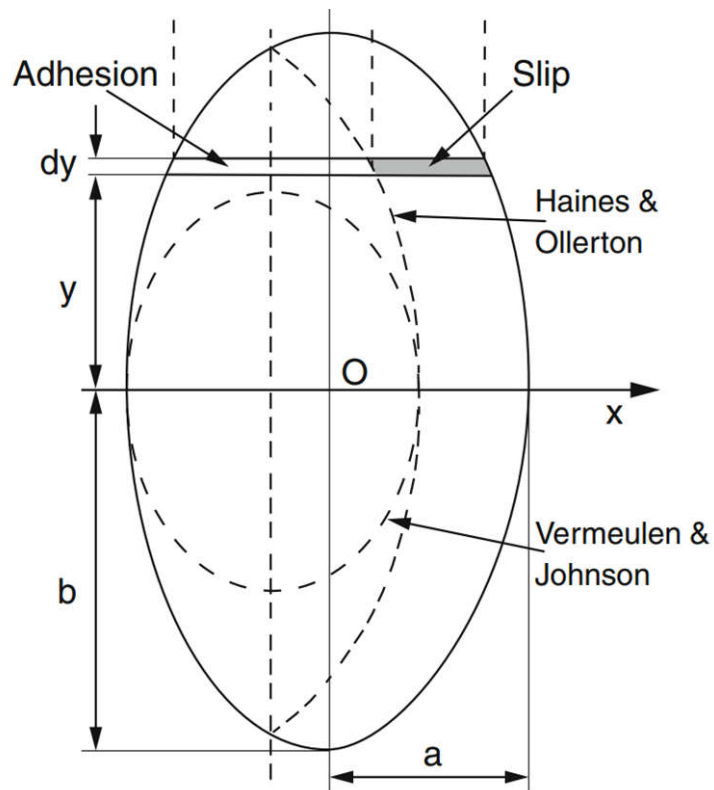


Figure 2.38--:Comparison between the tangential stress distributions for 3D contacts[136]

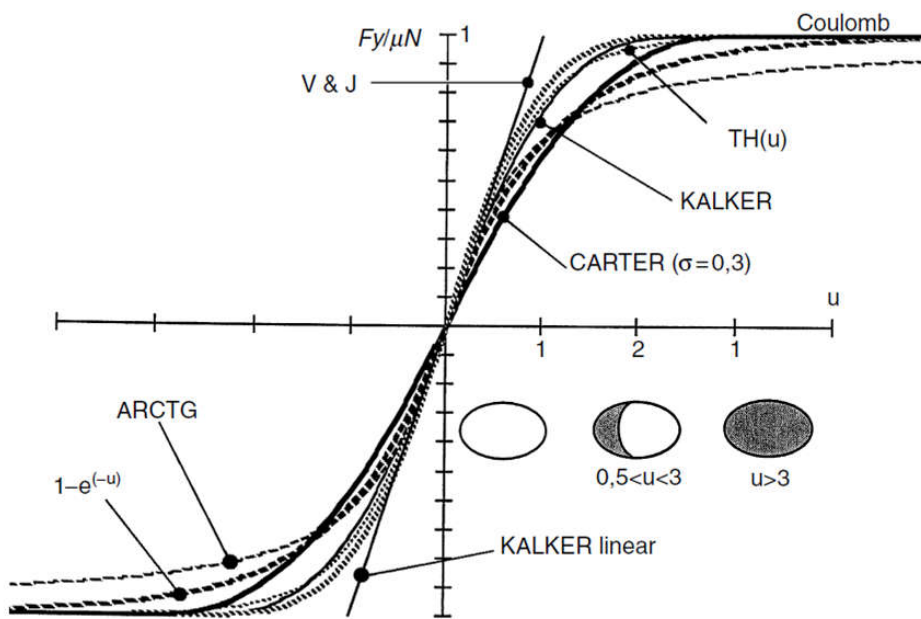


Figure 2.39--:Traction creepage curve for theoretical frictional contacts

2.4.5.3 Elasto-hydrodynamic Lubrication

Lubricant properties have a profound influence on the traction, friction, wear and bearing performance. Commonly, lubricant properties are changed by operating parameter such as temperature and pressure. Four lubrication regimes can be distinguished depending on the effect of effect of pressure on lubricant's viscosity

Isoviscous rigid- As the name implies, the viscosity of the lubricant does not change significantly with pressure. This occurs when the elastic deformation of the contacting bodies is small relative to the lubricant thickness. Intrinsically, this is akin to hydrodynamic lubrication regime.

Piezoviscous Rigid- In this regime, the pressure in the contacting surface is high enough to change the lubricant viscosity even though the elastic deformation of the contacting surfaces is so small that they can be neglected.

Isoviscous elastic- This regime is observed when the elastic deformation of the contacting bodies is influential on the film thickness. However, the pressure is insufficient to cause a significant change in viscosity.

Piezoviscous Elastic- Here, elastic deformation and pressure influence the film thickness. This regime is observed by common machine components which operate by rolling contact such as rolling element bearings and gears. This is often called the EHD regime.

The contact between a rolling element and a bearing race way is a non-conformal contact. The pressure distribution in a static non-conformal contact can be evaluated by Hertzian theory. In the EHD regime, the pressure distribution often takes the shape as shown in Figure 2.40. The spike in EHD pressure has been shown to reduce the fatigue life of bearings[144].

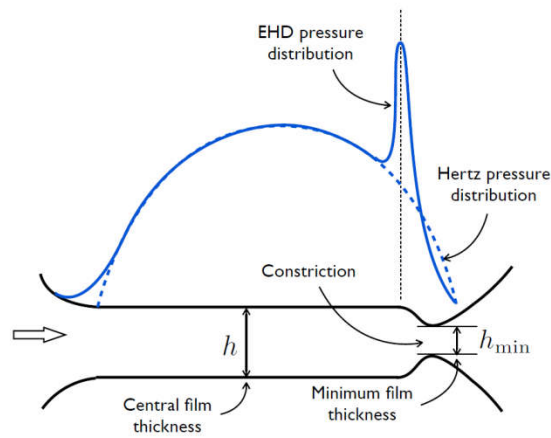


Figure 2.40—:Pressure distribution and film-thickness variation in an EHD contact

General formulation for contacts assumes a smooth surface. In reality, contacting surfaces are full of asperities. The characteristics of the asperities influence the mechanism through which the fluid film is formed. Generally, a film parameter is defined to characterise the influence of asperity on the formation of lubricant film. This dimensionless parameter Λ is used to characterise the lubrication regime as shown in Figure 2.41

$$\Lambda = \frac{1}{(\lambda_A^2 + \lambda_B^2)^{1/2}} \quad (\text{EQN 2.48})$$

In rolling contact, a tangential stress distribution is formed across the contact area due to rolling action which produces traction. To calculate the tractive force in the rolling contact, simple approximations are commonly made by assuming a constant film thickness in the contacting bodies and a Hertzian pressure distribution. Considering the lubricant as a Newtonian fluid, the shear-strain rate is evaluated by

$$\tau = \eta\gamma = \eta \frac{u}{h} \quad (\text{EQN 2.49})$$

Where τ shear stress, γ is a shear strain rate and u/h is the velocity gradient across the fluid film thickness. Combining the shear stress, the applied normal force and the contact area, the traction coefficient μ is defined by:

$$\mu = \frac{\tau A}{F} = \frac{\eta A}{F} u \quad (\text{EQN 2.50})$$

Where u is the slip velocity and h , Film thickness. A general dimensionless method for evaluating the minimum film thickness is given by

$$h_{min} = 3.07 \frac{\alpha^{0.57} R^{0.4} (u \eta \sigma)^{0.71}}{(E')^{0.03} W_z^{0.11}} \quad (\text{EQN 2.51})$$

Rolling element bearings are generally designed to operate in under elastohydrodynamic lubrication regime characterised by the dimensionless film parameter (EQN 2.48). Figure 2.41 shows the different lubrication regimes which may be characterised by the dimensionless film parameter. Due to the low friction in this regime it can be observed that the traction coefficient is low during the elastohydrodynamic lubrication regime where rolling element bearings operate.

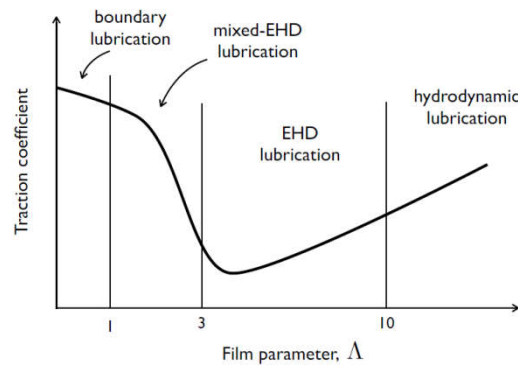


Figure 2.41–: Lubrication regimes

The traction properties of a lubricant as shown in Figure 2.43 and other factors including geometry material finish and normal force affect how the rolling element slips or rolls without slipping or sliding. The occurrence of slipping is highly unlikely in main bearings of tidal turbines because of their low running speed. However the load distribution may affect the normal load hence the traction coefficient.

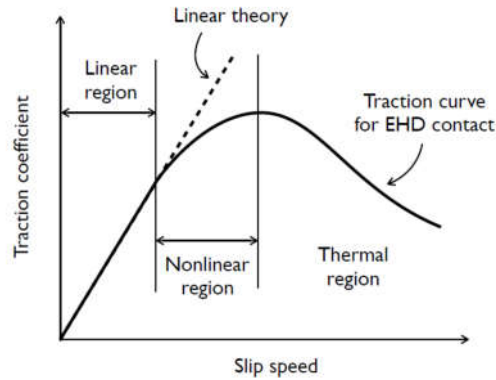


Figure 2.42--: traction properties

2.4.5.4 Bearing Kinematics

The objective of rolling element bearings is to reduce frictional losses. As such pure rolling is of significant importance. Supposing that no gross sliding occurs, there exists a kinematic relationship between the rolling elements bearing components which are dependent on geometry of bearing components. The translational velocities of bearing components is given by

$$v = \omega r \quad (\text{EQN 2.52})$$

The rotational velocity of the inner race v_i is thus given by

$$v_i = \frac{1}{2} \omega_i (d_m - D \cos \alpha) \quad (\text{EQN 2.53})$$

$$v_i = \frac{1}{2} d_m \omega_i (1 + \gamma) \quad (\text{EQN 2.54})$$

Similarly the velocity of the outer race v_o is

$$v_o = \frac{1}{2} d_m \omega_o (1 + \gamma) \quad (\text{EQN 2.55})$$

Considering that

$$\omega = \frac{2\pi n}{60} \quad (\text{EQN 2.56})$$

The cage speed is

$$v_m = \frac{1}{2}(v_i + v_o) \quad (\text{EQN 2.57})$$

$$v_m = \frac{\pi d_m}{120} [n_i(1 - \gamma) + n_o(1 + \gamma)] \quad (\text{EQN 2.58})$$

$$v_m = \frac{1}{2} \omega_m d_m \quad (\text{EQN 2.59})$$

Expressing this in terms of number of inner (n_i) and outer (n_o) race rotations in one cycle yields

$$n_m = \frac{1}{2} [n_i(1 - \gamma) + n_o(1 + \gamma)] \quad (\text{EQN 2.60})$$

where,

- n_m - Cage rotational speed in rpm
- n_i - Inner race rotational speed in rpm
- n_o - Outer race rotational speed in rpm

2.4.1 Dynamic Bearing simulations

Many researchers have investigated the dynamic behaviour of bearings because of its wide spread use. Generally, dynamic modelling tools that have been used to analyse bearing behaviour can be grouped into “independent bearing analysis” tool or “generalised models” which are generated by Multibody Simulation (MBS) tools.

2.4.1.1 Independent bearing analysis tool.

Independent bearing analysis tools have been generated as a tool for analysing single independent bearings on their own. ADORE is one of such bearing simulation tools that can be operated in dynamic and quasi static mode. The

dynamic model solves the a list of differential equations that govern the bearing components to predict bearing life, wear, skidding, etc.

Stacke and Fritzon [145] presented an analysis model they called BEAST. BEAST was developed as an in-house analysis tool by SKF. It allows general loading conditions to be applied when evaluating cage skew, rolling element misalignments etc. Their simulations have been validated using test performed in house. A similar Analysis tool CABA3D was Developed by Schaeffler Group (FAG) which can simulate full complement bearings.

CAGEDYN is an independent tool developed by Houpet to simulating rolling element cage interactions. Houpet's work studied forces such as cage pocket stiffness in detail and change stiffness The performance of CAGEDYN was validated by test in [146][147][148].

A 6DOF tool for modelling cylindrical roller bearings was presented by Ghaisas et al[149]. The tool called DBM focused on cage instability and used the tool to show that cage instability can cause collisions in race-cage contacts. [150]

Recently, Mesys rolling bearing became available for calculating bearing and shaft loads. It considers factors such as Bearing clearance, Centrifugal forces, Roller profile and others to calculate bearing life given a load spectra.

Calyx performs contact analysis of two or three dimensional bodies. Here contacting bodies are modelled using finite element models and stiffness matrices assembled together using a multi-level hierarchy. This has been used to model the stiffness behaviour of a bearing in [151].

2.4.1.2 Generalised MBS models

BearinX- Schaeffler offers online calculation of detailed bearing loads and positions on shaft systems to their customers. The calculation model performs the analysis in a detailed manner including Individual rolling element. In addition to this, their BearinX-Map is a bearing contact model which can be incorporated into multibody simulation packages.

Sakaguchi et al [152] Simulated the behaviour of a cylindrical roller bearing using ADAMS but ignored roller tilting and skewing. Through this, the roller raceway contact force, roller cage pocket force and cage centres were analysed. MBS software ADAMS was used by Fritz [153] who developed a model of a ball bearing model. Hahn investigated the elasticity of the cage in a ball bearing with ADAMS as well included the macro stiffness of the cages. Teutsh [154] proposed an explicit load-deflection relationship for rollers which included the effect of adjacent slice of material thus enabling the roller misalignment to be calculated.

Recently, Qian [155] has used Simpack coupled to a Fortran subroutine to evaluate the dynamic behaviour of a cylindrical roller bearing. The Fortran code evaluated the contact parameters while dynamics was solved using the MBS software.

2.4.1.3 Drawbacks in current packages

Great progress has been made in bearing simulation with a majority of the more sophisticated models being developed in the past decade. Some of the sophisticated bearing simulation programs are dedicated tools for bearing manufactures thus are not commercially available. Some of the other tools are also platform specific while others are more suitable for frequency analysis problems. Some of the software such as CAGEDYN, CABA3D, BEAST and ADORE offer many advantages but the ability to couple them to other components is lacking. Bearinx considers dry contacts and offers static models [155] which can be used in MBS packages.

2.4.2 Rolling Contact Fatigue (RCF analysis)

A comprehensive review on rolling contact fatigue was presented by Sadeghi et al [156]. Empirical methods have been very helpful in giving reliable estimates for reliability but fail to do so through rigorous treatment of the micro structural interactions that lead to rolling contact fatigue. In recent decades more effort has focused on the micro structural alterations that happen at the μm scale, nm scale and even at an atomic level [157]. The various geometric scales at which bearing steels have been studied and some of the common methods used is presented in Figure 2.43 below.

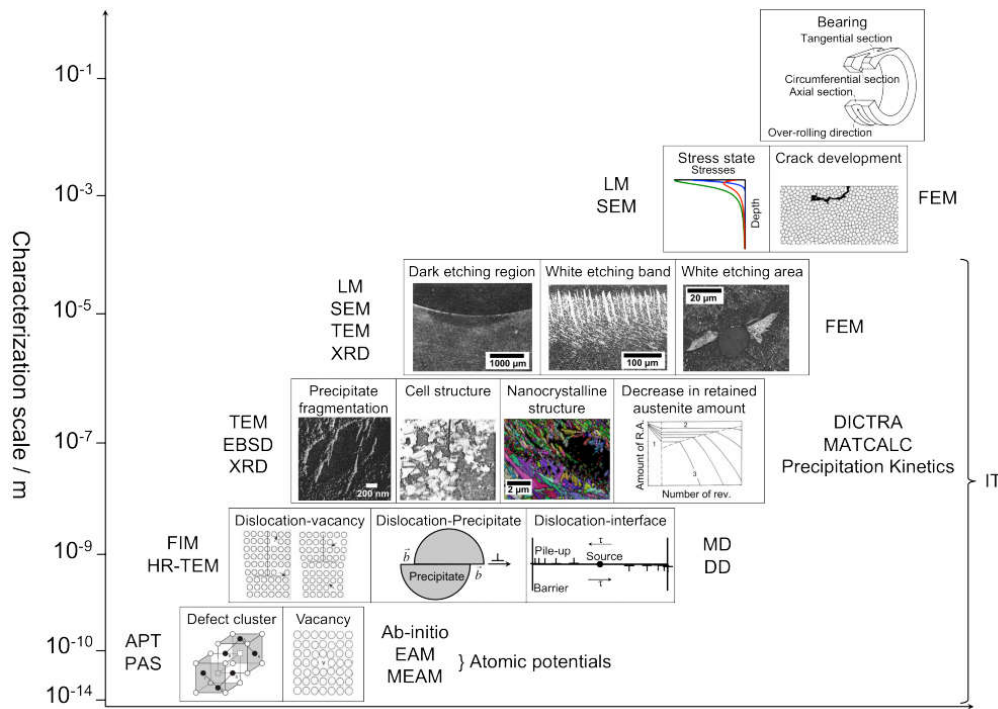


Figure 2.43– Various levels at which rolling contact fatigue has been studied[157] .

2.4.2.1 Life prediction for radial bearings

Endurance testing of rolling element bearings has shown that bearing life is highly probabilistic. For a group of identical bearings tested under similar conditions, there is a wide distribution of life. Consequently the life of bearings is defined based on the probability that they will survive a given load. Following tests carried out by Palmgren (Palmgren 1924) and the work of Weibull in 1939 (Weibull 1939), Lundberg and Palmgren [158] published an equation for evaluating the life of rolling element bearings, which later became the basis for bearing life estimation in ISO standards. The life which 10% of bearings will have failed and 90% will have survived is given by the L_{10} life as:

$$L_{10} = \left(\frac{C}{P}\right)^n \quad \text{(EQN 2.61)}$$

Following Palmgren’s model, several life models for rolling element bearings have been presented. Recently, Zaretsky [159] presented a review of life models for

rolling element bearings. The most accepted life models are semi-empirical in nature, that is, they are based on fitting test data to an assumed theoretical distribution. Similar to methods advocated by British Standard 5760 series, they are dependent on failure rates which are often derived from reliability (endurance) tests. The so called L_{10} life of a bearing is the life that a group of identical bearing operating at a specific load at which 90% of bearings are expected to survive. C is often called the basic load rating and symbolises the purely radial load at which the specified bearing will have an L_{10} life of one million revolutions. P is the equivalent load rating which is pure radial load that represents of the applied radial and axial loads, while n is a life exponent which is 3 for ball bearings and 10/3 for roller bearings.

The L_{10} life forms the basis for bearing selection in many industry approved standards including ISO 281-2007[160] however its strong ties with experimentally derived terms make it difficult to scientifically demonstrate failure mechanism and processes. For roller bearings, many have suggested a life exponent of 5 to account for the improvements in material and processing techniques. ISO 281[160] presents modification factors which may be applied to the basic L_{10} life to attain a more realistic life prediction. From common industrial practice, the equivalent load rating of a bearing is usually evaluated by

$$P_e = X F_r + Y F_a \quad (\text{EQN 2.62})$$

where F_r and F_a are the radial load and axial load respectively. Factors X for radial force and Y for axial force are factors applied to account to the sensitivity of the specific bearing to the applied load. These values may be obtained from manufacturer's catalogue or bearing data books. For bearings with ideal geometries, theoretical values may be obtained for both ball and roller bearing under simple loads. The L_{10} life of the bearing is evaluated based on a strict series reliability of the inner race and outer race contacts.

$$C_{i,0} = 552 \lambda_{i,0} \frac{(1 + \gamma)^{27}}{(1 - \gamma)^4} \gamma^{\frac{2}{9}} D^{\frac{29}{27}} l^{\frac{7}{9}} Z_{i,0}^{(-14)P} = \left(\frac{1}{Z} \sum_{j=1}^{j=Z} Q_j^{4.5} \right)^{\frac{1}{4.5}} \quad (\text{EQN 2.63})$$

$$L_{i,o} = \left(\frac{C_{i,o}}{P_{i,o}} \right)^4 \quad (\text{EQN 2.64})$$

Based on a strict series reliability,

$$L_{10} = \left(L_i^{-\frac{9}{8}} + L_o^{-\frac{9}{8}} \right)^{-\frac{8}{9}} \quad (\text{EQN 2.65})$$

(EQN 2.63) is applicable to bearings with rigid rings which operate at moderate speed. Referring back to (EQN 2.62) it can be observed that the equivalent load rating is dependent on the summation of the load carried by each individual rolling element.

Frequency of occurrence of bearing failure modes

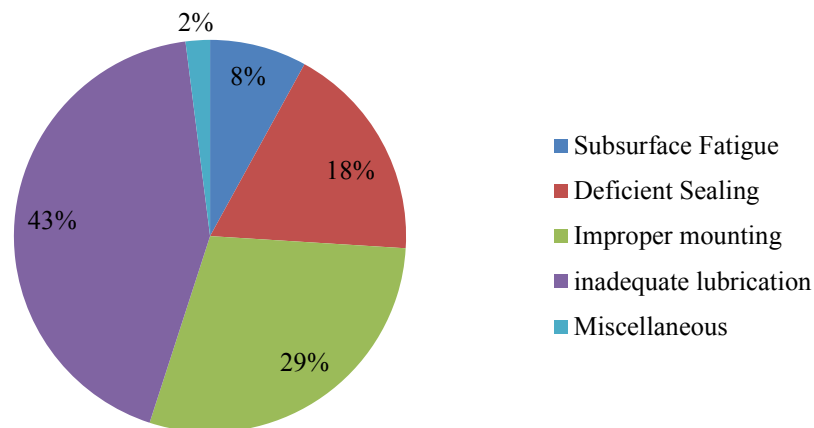


Figure 2.44--: Common Bearing failure causes

2.4.2.2 Bearing steels

There has been a tremendous improvement in bearing performance and longevity since the 60s. Many of this can be attributed to the introduction of new materials, processing techniques and handling methods. Today bearings used in applications

where a high level of reliability is required (Such as the aerospace and automotive industries.) conform to stringent material processing and post processing. Details of general bearing steels can be found on [161] [162] [163].

Many researchers have focused the fatigue properties of these bearing materials. One of the most studied materials is 100Cr6 bearing steel (JIS: SUJ2, AISI/ASM 52100) which is a common steel used in wind turbine drivetrain systems[164] [98].

Shiozawa, Sakai and co-workers [165] [166] [167] [168] [169] have extensively studied the fatigue properties of JIS: SUJ2 . In their investigations, a rotating bending tester used to assess the fatigue properties of the material in the Giga cycle range of on loading cycles. The JIS: SUJ2 exhibited a duplex S_N curve behaviour as shown in Figure 2.45. Two types of failure were distinguished. Surface damage caused by Cristal slip tends to occur at much lower cycles compared to subsurface failures caused by Non-metallic inclusion.

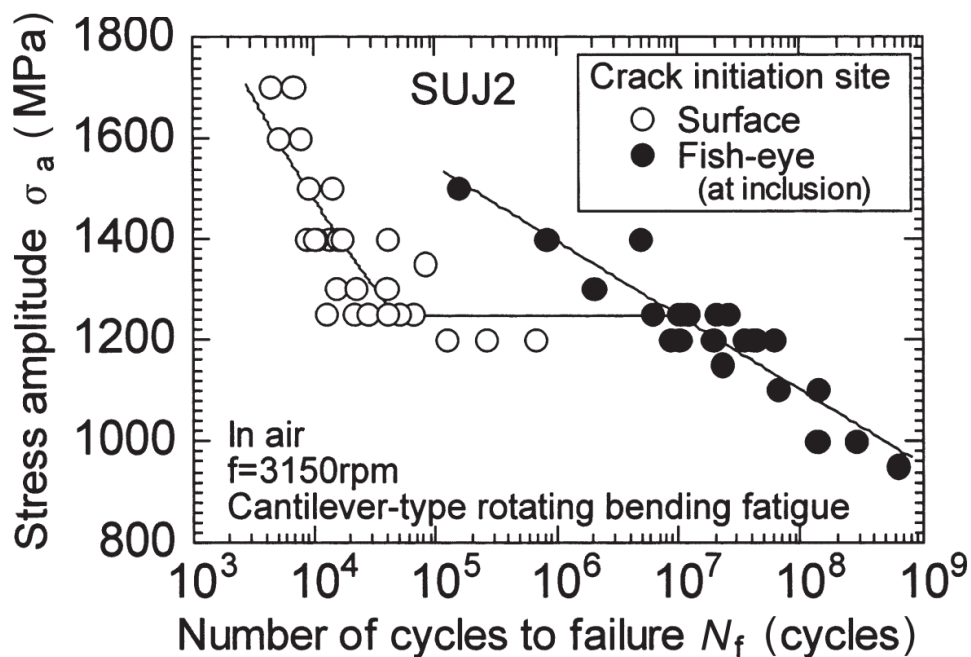


Figure 2.45--: Duplex SN Curve of JIS SUJ2 bearing steel[170]

In their experiments, there was no indication of a fatigue limit for subsurface initiated failures at the gaga cycle range thus tests were right censored. Bathias [171] concluded that there is no fatigue limit in some metallic materials. In his work

[172], he explained with the use of experimentation in the Giga cycle range to show that the use of an asymptotic SN curve by the use of statistics of test specimens in the 10^6 - 10^7 range may not be valid. The S-N curve presented by Battacheriy et al. [173] for M50-Nil bearing steel as shown in Figure 2.46 does not show any indication of endurance even past the Gigacycle region. Gabelli et al. [174] concluded that existence of a horizontal asymptote in the S-N curve of bearing steels is not required or significant for the ISO 281:2007 although from their Monte Carlo analysis the presence of a fatigue limit is possible.

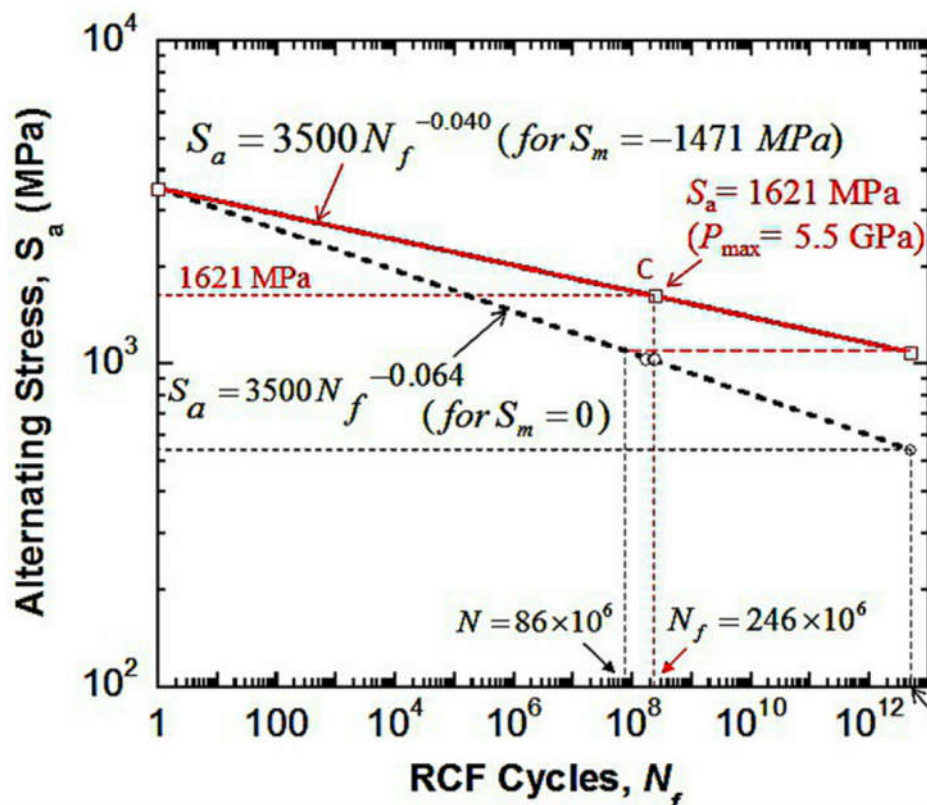


Figure 2.46—: Rolling Contact fatigue SN curve for M50-Nil bearing steel[173]

Nakajima et al [175] revealed that the fatigue behaviour of SUJ2 bearing steel differed based on the experimental setup. In their work, test samples that were tested by axial tension and compression consistently have shorter fatigue life compared to results obtained by rotating bending machine. They also showed that the value of R which is the ratio of the minimum stress to the maximum stress has a

profound influence on the fatigue life. Since bearing materials often encounter non zero means stress, Bhadeshia [176] pointed out test obtained by $R=0.5$ may be better suited as opposed to $R=-1$. Nonetheless, very little data exist for scenarios when $R=0.5$.

For bearings, the propensity for the fatigue spall damage to be caused by surface slip is small since the maximum contact stress often occurs subsurface.

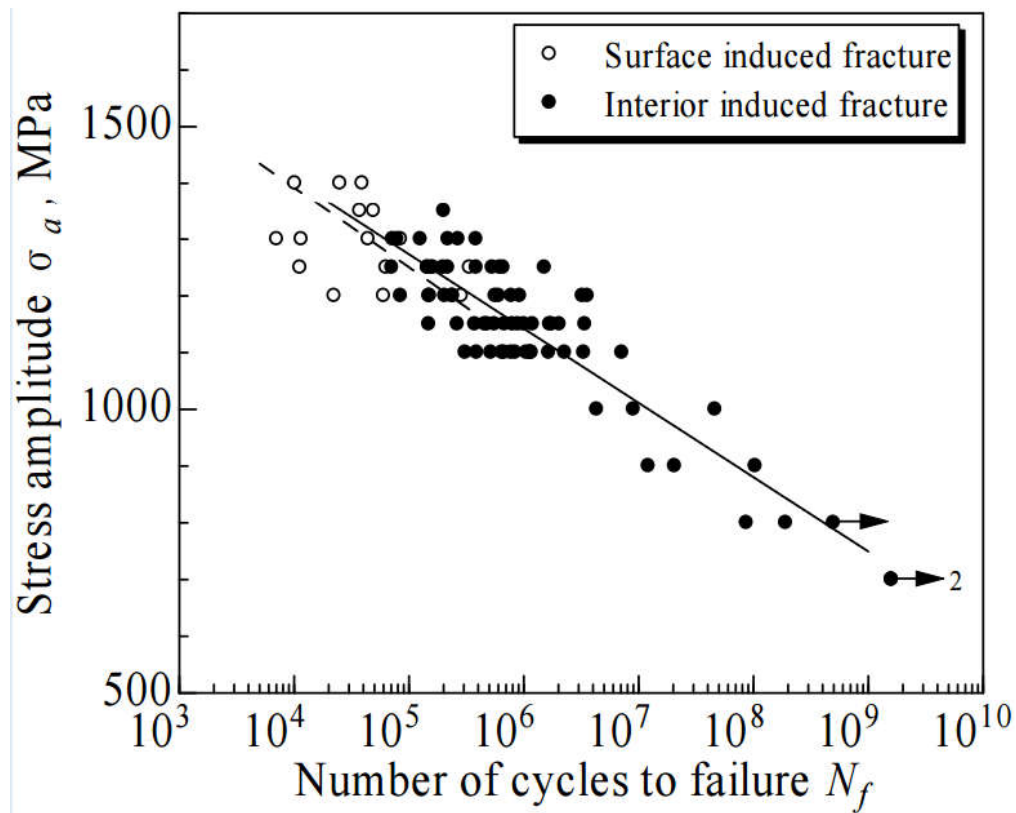


Figure 2.47—: SN Curve for JIS:SUI2 steel in axial loading [177]

2.4.2.3 Bearing Testing Methodologies

Experimentation on full scale bearings has received a lot of attention, even before the days of Palmgren[178] in the 1920s. experimentation aided the formation of empirical formulations such as the one presented by Lundburg and Palmgren [158]

which formed the initial basis for bearing selection in ISO standards. These days, bearing endurance tests remains critical part of the bearing industry.

In general, two experimental setups are used to identify the relevant factors that affect bearing performance and life. Traditionally, full scale testing of bearings is performed to obtain the endurance of bearings. In these tests, failure is judged to have occurred with the observation of the first fatigue spall. The spall phenomenon was load cycle dependent and appeared to occur in a region subsurface of the contact point, particularly where the maximum shearing stress occurred. This delivers the fatigue life given by the basic life equation. An alternative setup uses so called element testers for bench testing which is used in typically to rank parameters such as lubrication surface finish and so on.

Recently, Vlcek and Zaretsky [179] compiled as a comprehensive report on testing of rolling element bearing testing. A summary of this is given below. Hoo [180] catalogued many types of bench type fatigue testers and rolling-element test rigs as a whole. The prominent test rigs among this catalogue utilised automated failure detection and shutdown systems. The superior lubrication mode appears to be that of oil mist in terms of efficiency, having tested oil mist, oil drip, oil jet and oil bath methods.

2.4.2.3.1 Bearing bench testing/element testing

The primary aim of performing bench type tests is to characterise material and lubrication. The results from such testing are critical to establishing adjustment factors for bearings which are applied to the basic L_{10} life as done in ISO 281[181].

Fatigue life of rolling-element bearing often exhibit a high scatter making the testing process costly as large samples must be analysed to accurately represent population. To circumvent this obstacle, bench type rolling-element testers have been engineered which are capable of simulating full-scale bearing in operating conditions. Results of these testers provide more qualitative rather than quantitative insights into rolling-element fatigue. Examples of the data derived from bench type testers include insight into failure trends as well as best materials and lubrication modes to use.

Care must be taken while using bench type test rigs in order to obtain comparable variables and conditions. For example, it is recommended all specimens of the rolling-element be made from the same sheet of material, heat treated to the same hardness. Except when the surface finish is the variable being tested, all the rolling-element specimens must have the same surface finish. The hardness between the contacting test specimens must remain constant. Therefore, the microstructure of the steel, together with the austenite, as well as the residual stress pre- and post-testing must be recorded.

All the contacting elements are cleaned thoroughly with a solvent then wiped dry, then mating elements coated in testing lubricant before fitting into the tester. Lubricant flow, speed and test temperatures are tracked. To prevent damage to the contacting surfaces due to skidding, all specimens are loaded before start-up. All the specimens are inspected and their post testing conditions recorded.

2.4.2.3.2 Bearing Endurance testing

Endurance testers are used to evaluate the underlying fatigue life of bearings. These are often performed so that test data can be fitted to the bearing life equation. Figure 2.48 provides popular configurations for full scale bearing testers.

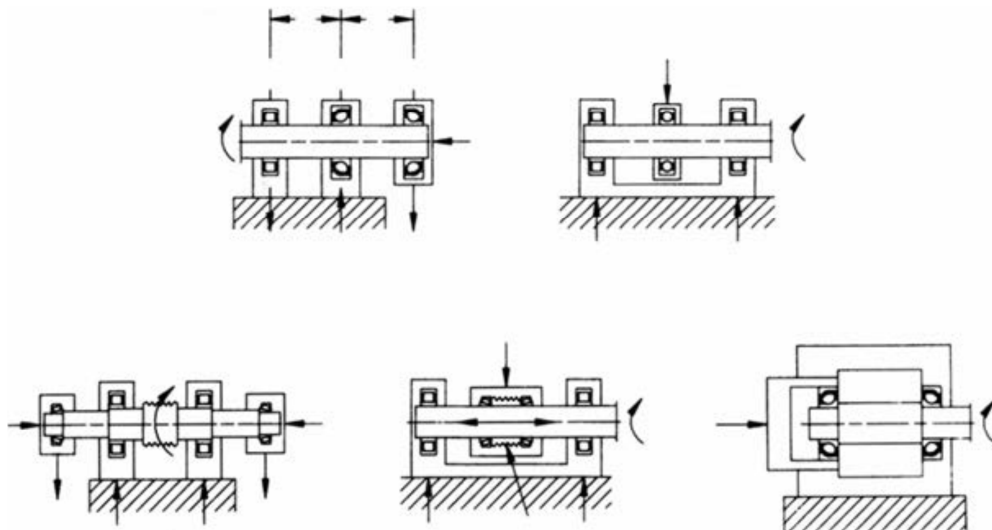


Figure 2.48– Designs for bearing endurance testers[94]

2.4.2.3.3 Testing Methodologies That Reduce Total Test Time

Determining rolling-element bearing life experimentally is complex, time-consuming and can be costly, yet may not deliver a coherent failure pattern, hence crucial importance of finding methods to reduce test times. Leonard G Johnson (1964) presented three methods for reducing test time.

The first method requires that more specimen than is intended to fail is tested simultaneously. For example, the median time to failure in a batch of 10 of 20 samples on a Weibull slope of 1.0 is 76% less than that in batch of 10 of 10 samples. Assuming same testers are used and failed specimens are not replaced.

Alternatively, sequential analysis is performed where test specimens are failed sequentially, one after another until tester decides the bare minimum of test runs to determine improvement or worsening of life is obtained. E V Zaretsky and colleagues have used the 50 Percent Life (L50) estimates to run identical testers on bearing until this life is reached. Samples are removed after failure or suspended at L50 with new samples mounted and tested until L50, until a minimum required sample size established. So improvement or worsening of life is determined using the minimum number of runs.

Finally, the third method, involving sudden death testing reduces accumulated time by not running all specimen to failure, but by dividing total specimens (n) into equal-sized (m) sub-groups r (number of testers), where $n = m \times r$. Similar fatigue tests are the done simultaneously in sub-groups. Specimen m in each subgroup is tested until first failure, the second subgroup m and so on till first failure is reached in each sub group m , so there are r failures generated while $(m-1) \times r$ samples are suspended.

It is acknowledged by Vlcek and Zaretsky [179] that proving these methods accurately predicts bearing fatigue with reduced total test times would require significant and unreasonable experimental data. Vlcek, Hendricks and Zaretsky performed Monte Carlo simulations using Weibull-Johnson.

Chapter 3 Main Shaft Load Case Evaluation

3.1 Introduction

The environment in which a tidal turbine is placed has grave influence on the loading on the turbine components and turbine's reliability as a whole. To evaluate the lifetime damage or reliability one must understand the effect the environmental loads have turbine loads. This chapter discusses how main bearing loads are affected by the tidal environment through analysing the main shaft loads.

The chapter introduces a generic 1MW horizontal axis tidal turbine which is used throughout this work. Through an elastic model of this turbine, the typical loads which will be imparted on to the main shaft are analysed. As such, generating realistic environmental conditions as well as turbine behaviour lies at the heart of this work. An introduction to the design criteria and assumptions are first given then followed by the process of modelling realistic tidal environmental loads. Sensitivity analysis is performed to illustrate the influence of different environmental parameters on turbine behaviour and loads.

Tidal turbines are designed to extract energy from tidal flows by converting the kinetic energy in the tidal stream to electricity. As it follows, the velocity variation at a tidal site is one of the most critical parameters which affect many decisions in tidal projects. Consequently the flow speed variation over the life of the turbine is treated as a basis for grouping turbine loads. The long term flow speed variations are analysed and discussed in addition to other site characteristics such as turbulence, wave loads, velocity shear profile etc. Other factors which may affect the main shaft loads such as cavitation and bio-fouling are briefly discussed.

3.2 Generic Tidal turbine

A generic turbine was developed to aid the computation of main shaft loads on a typical tidal turbine. The model of the turbine was developed using FAST to mimic the behaviour of typical tidal turbines in the mega-watt range.

FAST interfaces with the AeroDyn subroutine which calculates the rotor loads using Blade-Element-Momentum Theory(BEMT). The rotor consist 3 blades who's profile were generated from Naca63_424 aerofoil and a cylindrical cross section at the root. The blade is defined by 75 node points with linear interpolation between nodes. Blade properties including twist, chord length and distributed mass and stiffness properties that were adapted from [182] and can be found in Appendix B.1 . A sample of the Aerodyne file can also be found in Appendix B.2.

The rotor calculations using BEMT interface with the whole turbine model in FAST. Here the rest of the turbine properties are defined including tower properties, nacelle properties and a variable speed controller. These parameters are defined in a “.fst “ file as shown in Appendix B.3.

The turbine's controller is of paramount importance because it directly affects the loading on turbine components. The turbine is controlled by a simple speed controller defined in an input file “pitch .IPT” The controller gains are turned to achieve an effective performance and to operate within control boundaries. The speed set points in the pitch control file sets the required speed to achieve a rotor speed as seen in Figure 3.1.

The turbine possesses yawing capabilities enabling it to face the mean flow direction. As shown from the literature in 2.2.5 above, the flow in many tidal channels are bidirectional. Moreover, changes in direction of mean flow happen at a relatively slow pace therefore it is reasonable to assume the turbine can face the mean flow with very little or no yaw error. With that in mind, turbulence from viscous effect and wave loads cause changes in the instantaneous flow direction and does not necessarily line up with the turbine.

A summary of the properties of the Generic turbine that was developed is given in Table 3.1. Such a turbine yields a power curve as shown in Figure 3.1.

Table 3.1 - Properties of generic 1 MW turbine

Property	Value	Units	Property	Value	Units
Rated Power	1	MW	Gearbox ratio	87.3	
Rated flow speed	2.5	m/s	Number of blades	3	
Rated rotor speed	11.5	rpm	Rotor diameter	20	m
Rated generator torque	10	kN m	Rotor aerofoil sections	Naca 63_424	
Cut in speed	1	m/s	Variable speed control	Yes	
Cut out speed	4	m/s	Pitch regulation	Yes	
Hub height	20	m	Yaw control	Yes	
Water depth	40	m			

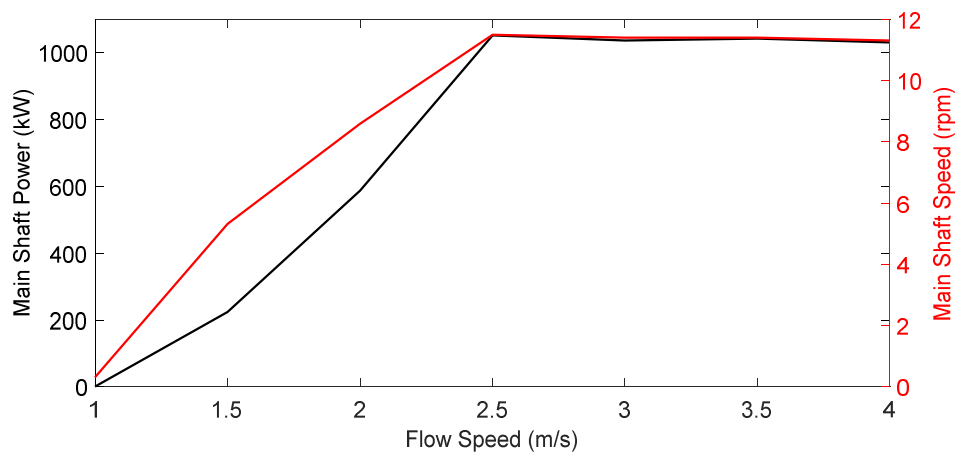


Figure 3.1–: Power curve of generic 1 MW turbine

The primary input to the FAST model as described above is a tidal flow field. Tidal flows exhibit complex flow behaviours due to the bathymetry, wave loads, wind load etc. A study by the Author [183] shows the average tidal velocity is the most influential environmental load on turbine loads. Consequently, the flow fields used as input to the tidal turbine is characterised by the average flow speeds.

3.3 Flow Speed Variation

For turbines to be economically viable they must be placed in a high energy site. An ADCP placed in a tidal site will record the mean velocity at the site as shown in Figure 3.2.

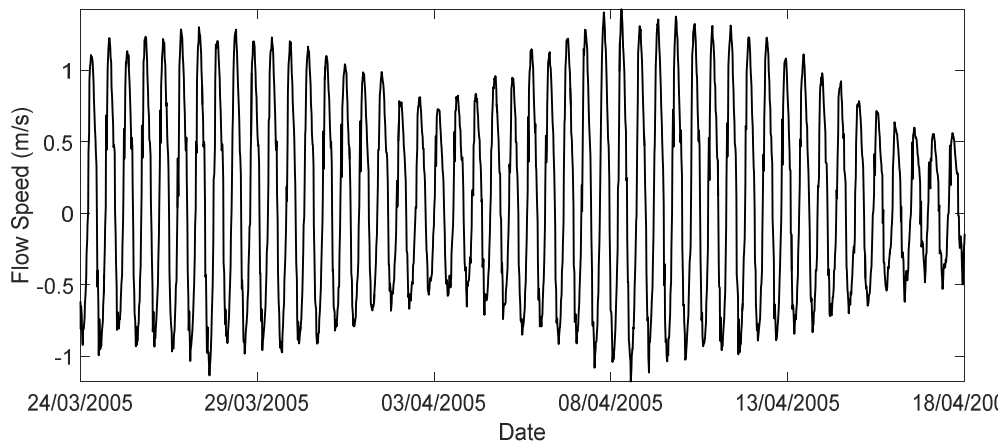


Figure 3.2—: Doppler Current Profiler measurement of tidal Velocity

From such data, harmonics analysis can be performed to hind cast or forecast tidal flow velocities. Harmonics analysis has been used to forecast tidal flow speeds for many years. They employ reliable site measurements over periods typically longer than a month to aid the harmonic analysis. The tidal harmonic analysis software TTide has been employed in this work to forecast flow speeds for the a given ADCP record as shown in Figure 3.2 .

TTide uses measured ADCP records to develop the tidal constituents and their phasing. With the known constituents, the tidal velocities can be forecasted with relative accuracy. Figure 3.3 compares TTide predictions (red line) with ADCP measurement (blue line). Figure 3.4 shows a more detailed view of Figure 3.3. It can be observed the harmonic analysis prediction agrees well with the measured data. The harmonic analysis over predicts the peak flood tides while it under predicts the peak velocity of the ebb tide. In addition, the predicted velocities tend to follow a smooth transition when flow direction changes while the measured data show the high frequency velocity oscillations particularly at the peak ebb or flood velocities in a cycle.

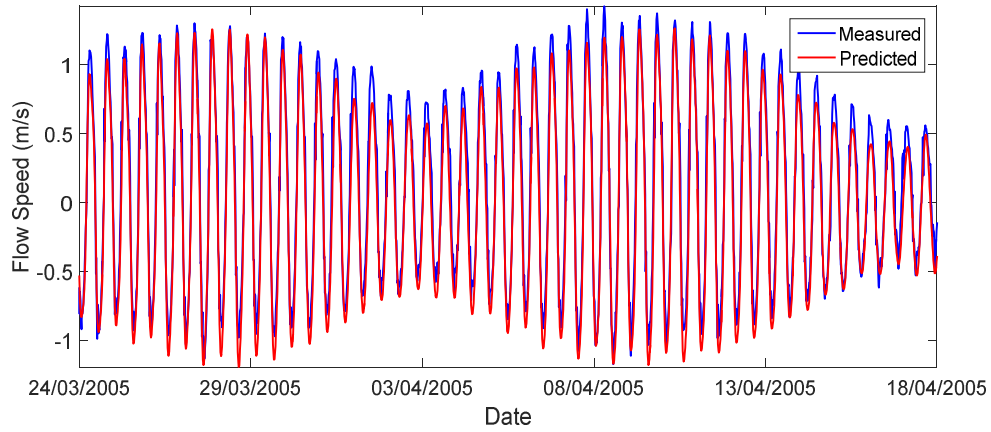


Figure 3.3—: Comparison of measured tidal flow speeds with TTide predicted flow speeds

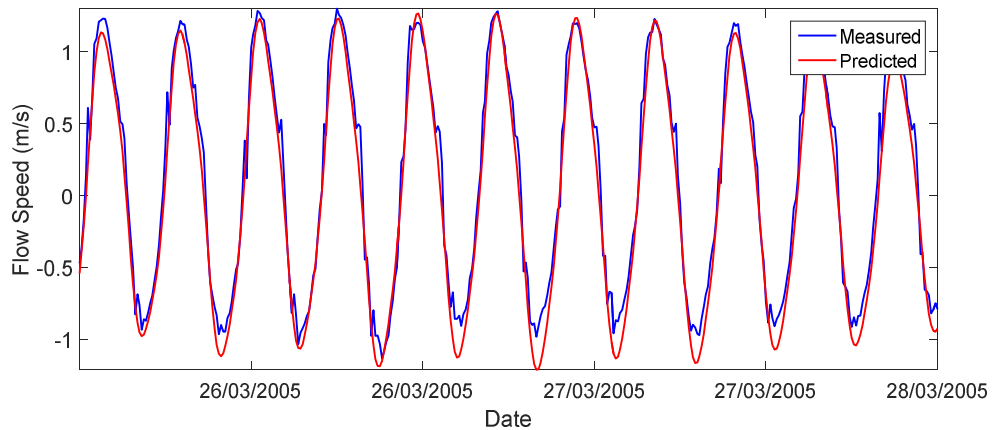


Figure 3.4—: Comparison of measured tidal flow speeds with TTide predicted flow speeds

Following the analysis of the tidal constituents, the flow speeds at the tidal site is predicted for the 20 years a turbine is expected to be in operation. For clarity, Figure 3.5 only shows the predicted velocities for the period between 1st January 2015 and 1st January 2016. Here the monthly and seasonal variation of the tidal flow velocities is clear.

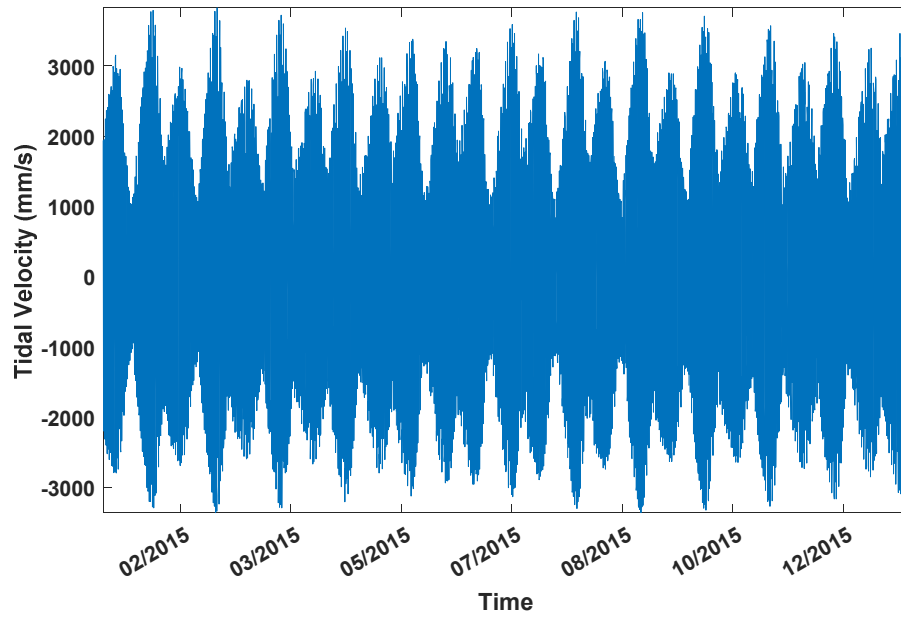


Figure 3.5--: predicted tidal velocities over a year

The flow speeds over the life time can be categorised into velocity bins based on the method of bins as advocated by IEC 61400 for wind turbines.

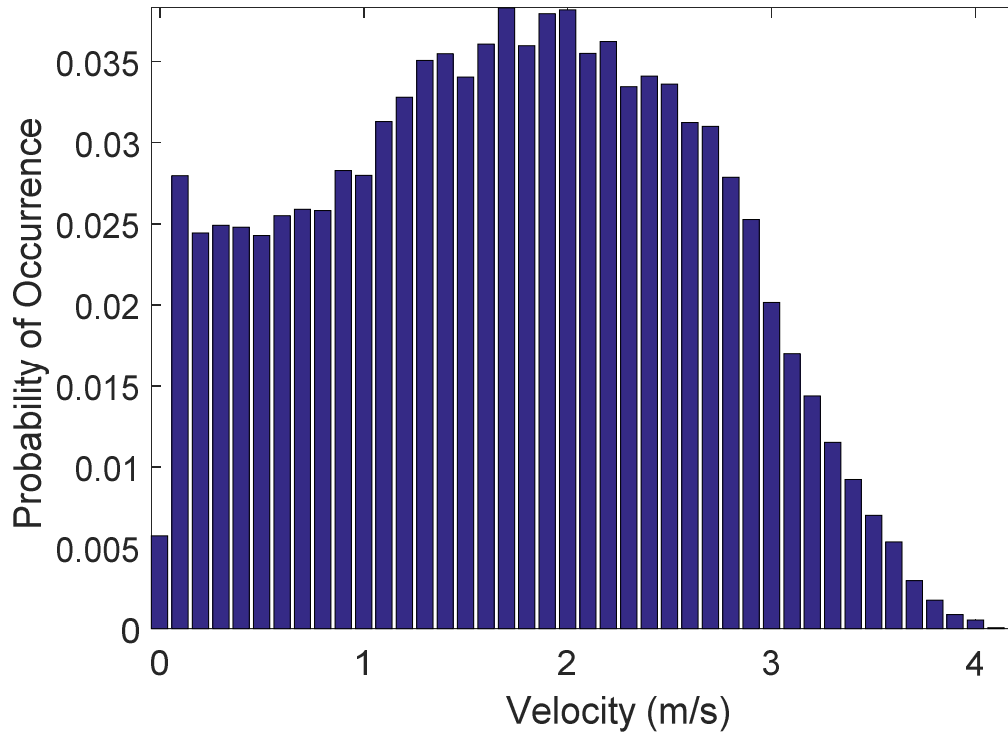


Figure 3.6—: Probability distribution of flow velocities

3.4 Flow field modelling

Figure 3.6 gives the average flow speeds at the tidal site in a twenty year window. Nevertheless, actual flow fields are very complex consisting turbulent eddies caused by wave effects and bottom roughness effects. Stochastic flow field simulators enable some of these effects to be accurately simulated to generate a more realistic flow field while maintaining the average flow speed. Consequently, the tidal module in Turbsim, a stochastic flow field simulator was used to generate a more realistic tidal flow.

The spectral model used for the TIDAL option in Turbsim takes the form of the Risø smooth-terrain model in Olesen et al [184]. Unlike the model presented by [184] which is based on atmospheric boundary layer theory, spectral amplitudes and

shear are scaled directly with empirical data. The empirically calculated factors were obtained from measurements from Marrowstone Island in Puget Sound Washington [25].

$$S_k(f) = \frac{\sigma_k^2 S_{1,K} \left(\frac{\partial u}{\partial z}\right)^{-1}}{1 + S_{2K} \left(\frac{f}{\partial u / \partial z}\right)^{5/3}}$$

$$S_{1,K}, S_{2,K} = \begin{cases} 1.21, 4.30 & K = u \\ 0.33, 0.50 & K = v \\ 0.23, 0.26 & K = w \end{cases}$$

The shear $\partial u / \partial z$ is evaluated by employing a logarithmic shear profile making the shear proportional to u/z . The Turbulent Kinetic Energy (TKE)

σ_k^2 is the evaluated by

$$\sigma_k^2 = UStar^2 \mu_k e^{-2z/refHt}$$

$$\mu_u, \mu_v, \mu_w = (4.5, 2.25, 0.9)$$

This is used to produce a turbulent flow field as shown in Figure 3.7 and Figure 3.8. Figure 3.7 slices the flow field through a plane that lies in the centre of the rotor in the lateral direction to show the axial variation of the axial flow speeds. Likewise, an axial slice of the flow field shows the lateral variations in Figure 3.8.

Generally, lower velocities are expected the closer we get to the seabed due to the shear profile. In Figure 3.7 however, some parts of the lower sections have a higher flow velocity. This can happen because of the random nature of turbulence and also because turbulence intensity tends to be higher the closer we get to the sea bed. This creates periods where the typical vertical flow speed variation differs from what is classically expected. The effect as shown in Figure 3.7 is not experienced all the time but the reproduction of this phenomenon sows the versatility of TurbSim to generate realistic random flow pattern as expected in a high energy tidal site.

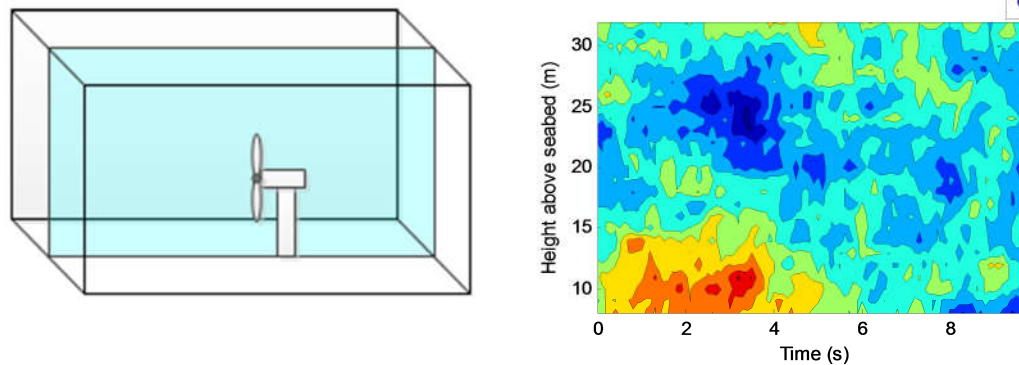


Figure 3.7– Axial variation of flow speeds

Figure 3.8 shows the flow across the turbine in the axial direction of the tidal stream at one point in time. The average velocity across the rotor reduces with water depth as expected due to viscous effects (which cause a shear profile) This flow stream is reminiscent of typical tidal flow in tidal channels.

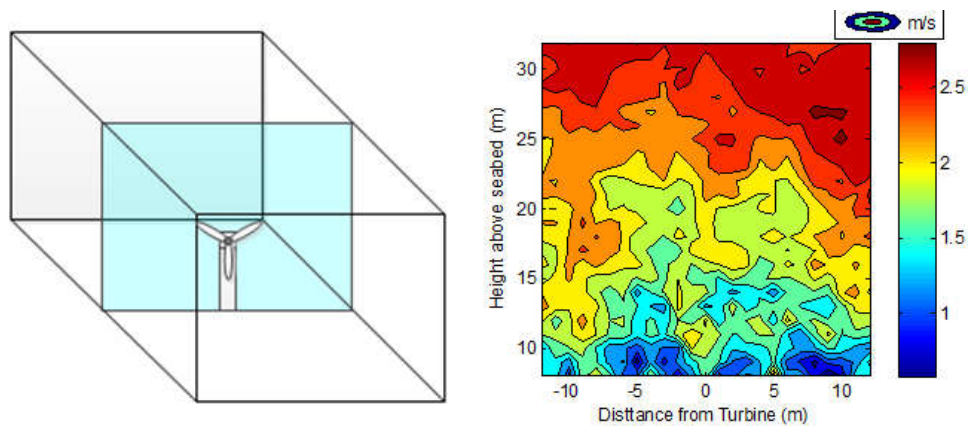


Figure 3.8– Lateral variation of flow speeds

The general components of the turbulence intensity as $(I_U, I_V, I_W) = (1, 0.67, 0.77, 0.42, 0.48)$. These figures are in good agreement with data published in [16]. Unlike for wind applications where the TKE is define in the form of

$$\sigma = c I_{ref} \left(0.072 \left(\frac{V_{ave}}{c} + 3 \right) \left(\frac{\bar{u}_{hub}}{c} - 4 \right) + 10 \right)$$

The measure of turbulence used (i.e. turbulence intensity) is not applied in the TIDAL case when using TurbSim. Consequently, the flow field from TurbSim must

be adjusted to obtain desired turbulence values. The turbulence intensity is adjusted to suit a desired value following equation (EQN 2.4). Figure 3.10 shows the time series data for a single point in a TurbSim generated flow field

To date, the TurbSim simulator does not have a module to include wave induced velocities. Consequently, wave particle orbital velocities are superimposed on the values generated by Turbsim. In addition to this form of turbulence, the turbulence intensity in the flow is modified to a given turbulence level using (EQN 2.4)

3.4.1 Super positioning of Wave orbital velocities

The effect of waves is included by super imposing wave particle orbital velocities on the local flow field generated in TurbSim. It is assumed the flow is homogenous thus the propagation of waves can be evaluated by Linear wave theory (Airy wave theory). Under linear wave theory a variety of orbital velocity patters can be categorised into shallow, intermediate (finite depth) and deep water groups. The finite depth equations are used to analyse the orbital velocities. The horizontal flow is modified to include the horizontal water particle velocity as given by:

$$u = \omega a \frac{\cosh k(z + d)}{\sinh kd} \cos(\omega t - kx) \quad (\text{EQN 3.1})$$

Likewise the vertical variation due to wave motion is included using the vertical water particle velocity given by

$$w = \omega a \frac{\sinh k(z + d)}{\sinh kd} \sin(\omega t - kx) \quad (\text{EQN 3.2})$$

Where x is the coordinate in the direction of wave propagation, z is the coordinate in the vertical direction, t =time, ω =wave frequency, k =wave number and d = water depth. The wave number is defined by (EQN 3.3) where the wavelength (L_w) is solved iteratively from (EQN 3.4)

$$k = \frac{2\pi}{L_w} \quad (\text{EQN 3.3})$$

$$T_p = \frac{4\pi^2}{gk \tanh kd} \quad (\text{EQN 3.4})$$

The superposition of waves on the tidal flow is carried out by a MATLAB program that propagates a single wave over time and includes the orbital velocities by summing up the velocities with ones generated by TurbSim . Supposing a 5 m wave is superimposed of a 3m/s uniform flow, the resulting flow field is as shown in Figure 3.9.

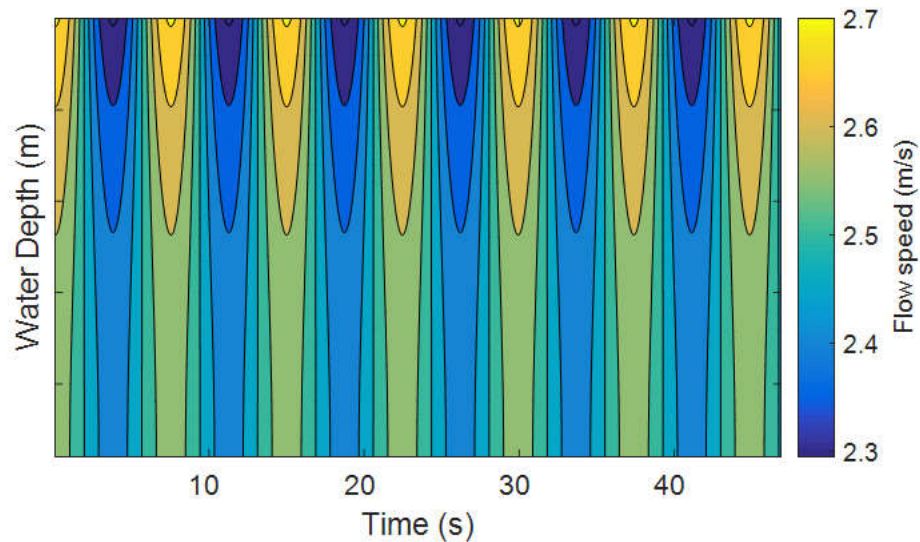


Figure 3.9– Axial flow speeds with a superimposed 1.5m, 7.5 period wave on a 2.5m/s flow speed.

3.5 Influence of Turbulence Drivetrain Loads

The influence of turbulent eddies in a tidal channel on turbine blades and structures have been presented in the literature by many researchers [16] [185] [40]. It is clear that in most cases turbulence contribute to increased damage on a range of turbine components. It is therefore critical that the turbulence in the tidal stream be correctly treated to avoid inaccuracies in expected lifetime damage. Here, turbulence which arises as a result of bottom roughness effect is implied.

(EQN 2.4) shows that turbulence intensity consist of turbulent fluctuations in 3D space. From (EQN 2.4), the axial turbulence I_U intensity relates to axil flow fluctuations(U_i). Similarly, the lateral turbulence intensity I_V relates to the lateral flow variations (V_i).and the vertical turbulence intensity I_W relates to the vertical flow variations(W_i .)

A range of turbulence intensities have been studied to understand their effect on main shaft loads. The range covers some typical values presented in the literature. The influence of the turbulence intensity on stream wise velocity of the flow is shown in Figure 3.10. Each of the axial velocity time series data has a mean of 2.5m/s.

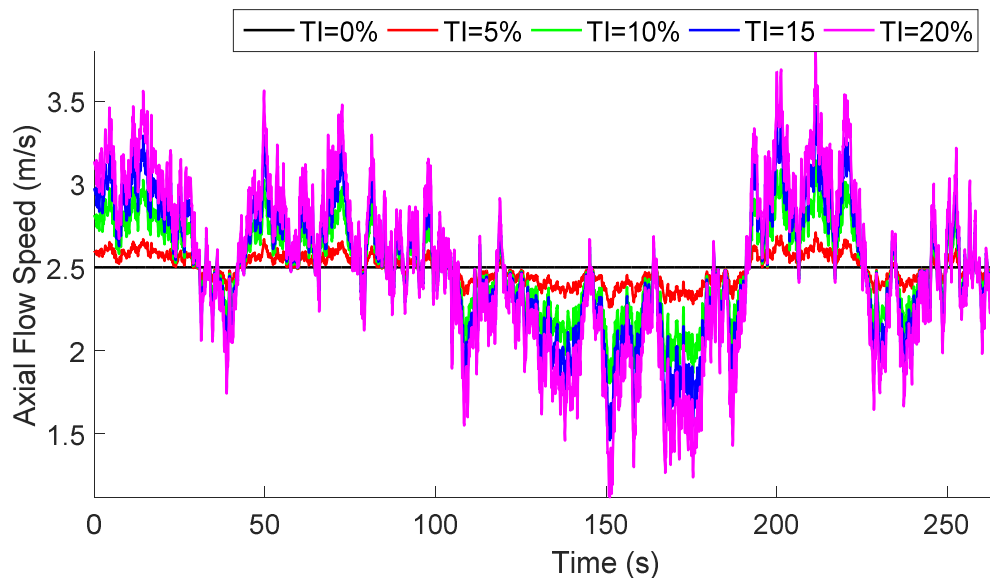


Figure 3.10– Time series of axial flow speeds at hub height for a range of turbulence intensities.

The axial velocity is often of prime interest because it directly relates to the power output thus revenue generated from the turbine. However, from the perspective of main shaft loading and reliability the off axis flow speeds could be of interest. Figure 3.11 shows how the lateral flow speed (V_i) changes with changes in the turbulence intensity.

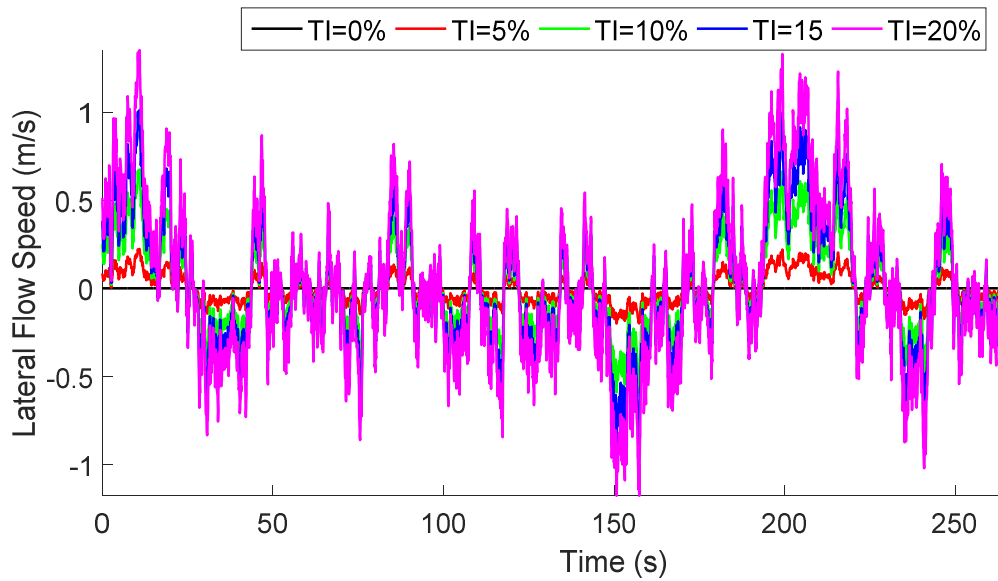


Figure 3.11– Time series of lateral flow speeds at hub height for a range of turbulence intensities.

The 3-D turbulent eddies also create vertical water velocities which are shown in Figure 3.12.

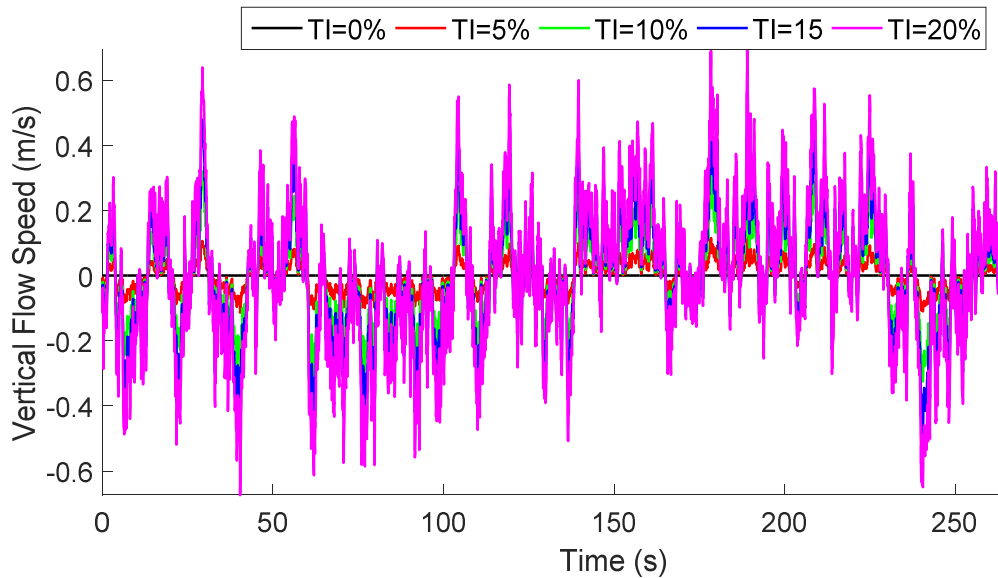


Figure 3.12– Time series of vertical flow speeds at hub height for a range of turbulence intensities.

The loading on the main shaft is directly influenced by the turbulence intensity. The axial force is one of the primary loads which affect the main bearing life. The response of the axial force due to the flow field as described in Figure 3.10 to Figure 3.15 is shown in Figure 3.13. The increased fluctuation in flow speed with increasing turbulence intensity leads to increased fluctuations in the axial thrust load on the main shaft. As can be seen from Figure 3.13, every high turbulence fluctuations lead to lower magnitudes of axial load. This happens because as the fluctuations cause the instantaneous velocities to exceed the rated speed. Consequently, the controller tries to adjust for the increased speed by following the turbine power curve as shown in Figure 3.1. Conversely, the off-axis forces F_Y and F_Z increase in magnitude for increasing turbulence intensity as shown in Figure 3.14 and Figure 3.15 because a major contribution to these are the rotor imbalances.

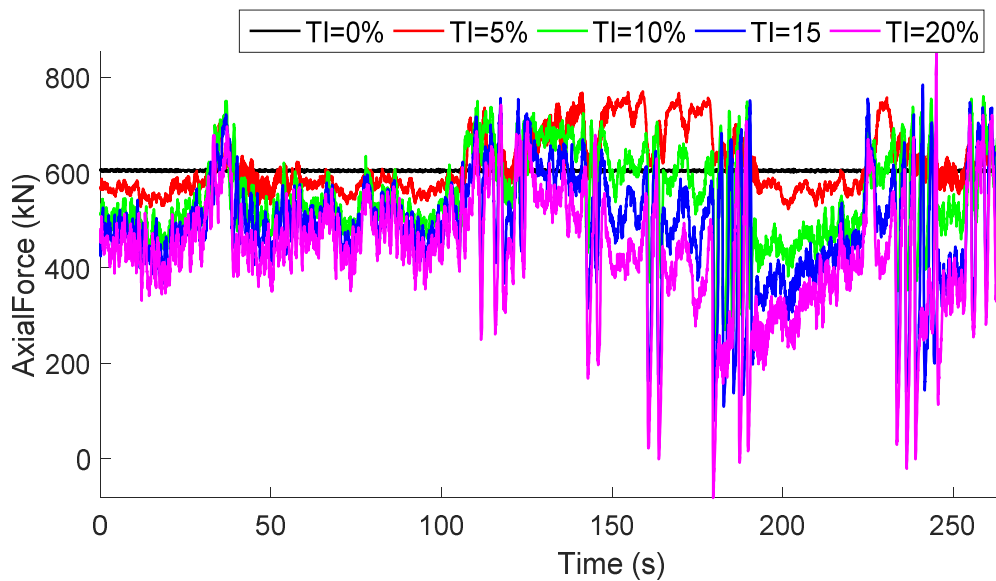


Figure 3.13– Time series of axial thrust force at different turbulence intensity levels.

The mean axial loads may be reduced in a high turbulence case due to the controller. Never the less the standard deviation of the load remains higher for higher turbulence intensities. The huge fluctuations in the turbulent case could potentially have cause failures such as scuffing in some drivetrain components.

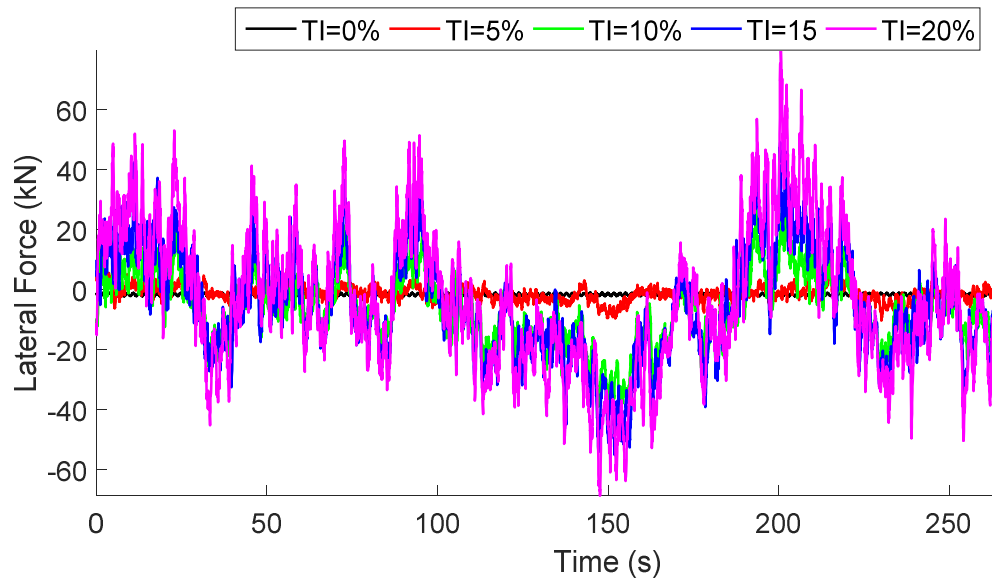


Figure 3.14– Time series of Lateral Shear force at different turbulence intensity levels.

Unlike the axial force, the off axis shears forces increase with increasing turbulence. These directly contribute the main shaft load which is supported by the main bearings.

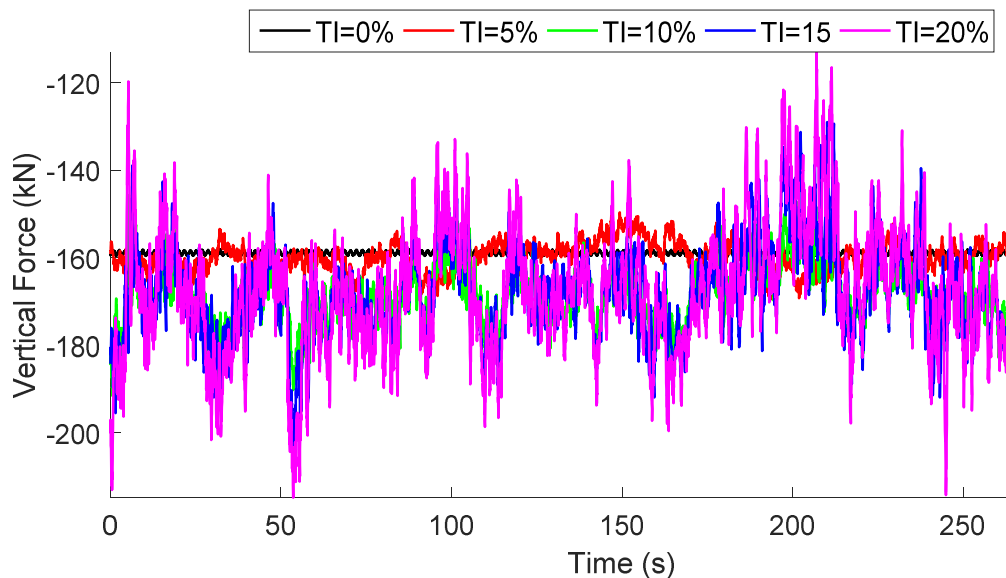


Figure 3.15– Time series of Vertical Shear force at different turbulence intensity levels.

The control goal for the simple speed controller is to achieve the optimum power while controlling speed. At very high turbulence intensities, there are high

fluctuations in torque which may cause rapid increase/reduction of speed. There is evidence that high turbulence can cause torque reversals as shown in Figure 3.16. This sort of high fluctuation is not only detrimental to torque carrying components such as the gearbox and generator but the sudden acceleration/deceleration due to these torque changes affect main bearing speed and can initiate failures such as scuffing.

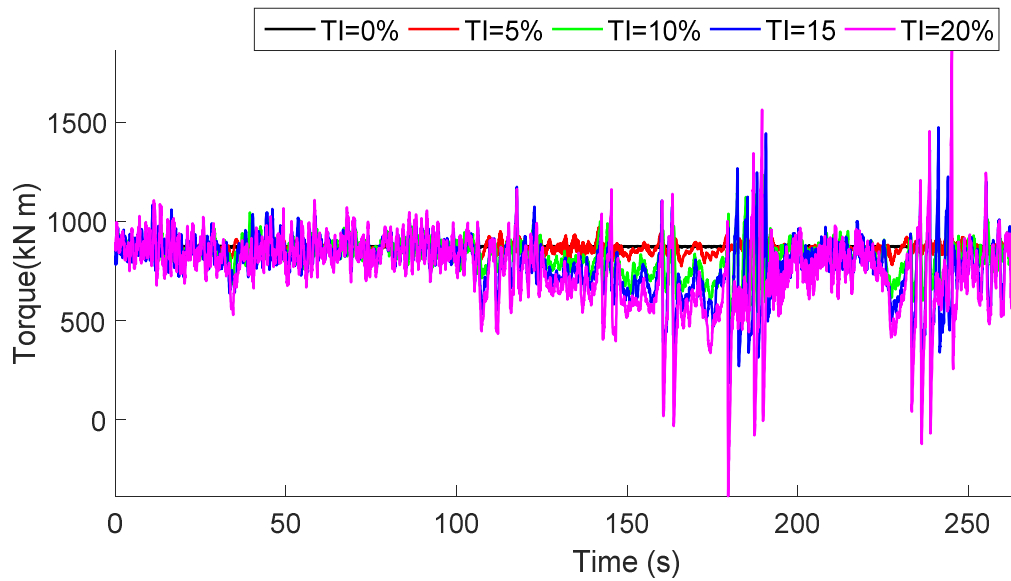


Figure 3.16– Time series of Torque at different turbulence intensity levels.

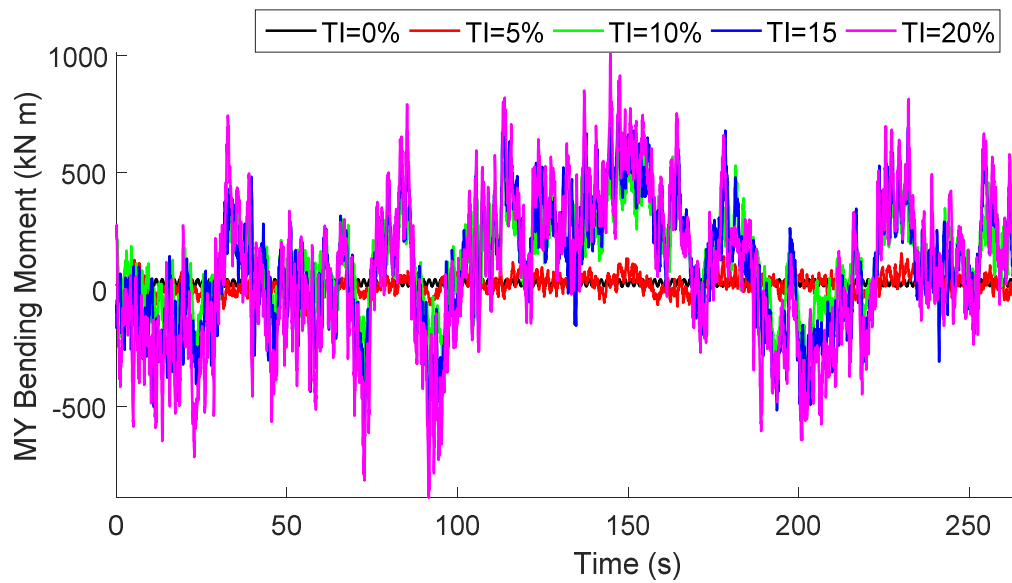


Figure 3.17– Time series of MY bending moment at different turbulence intensity levels.

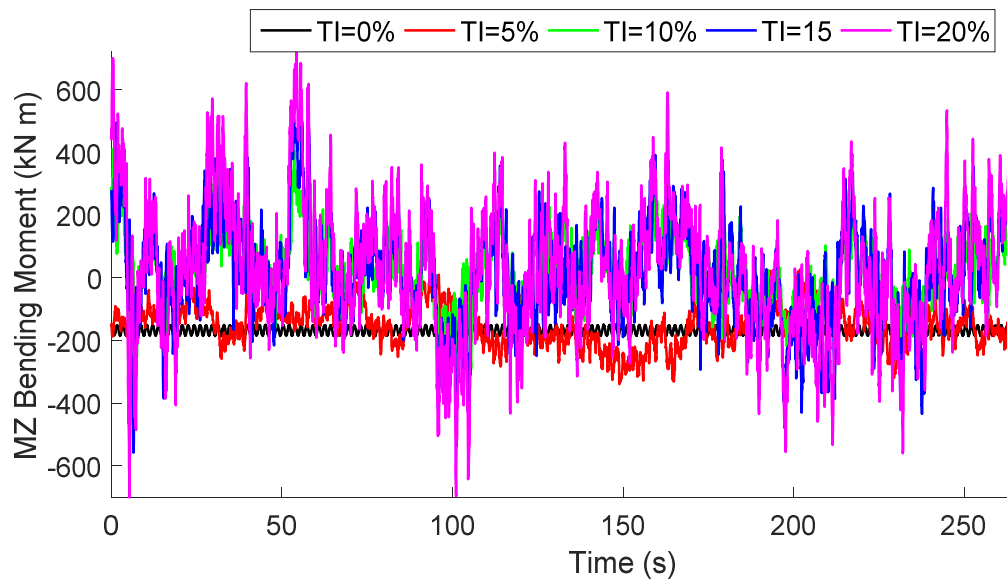


Figure 3.18– Time series of MZ bending moment at different turbulence intensity levels.

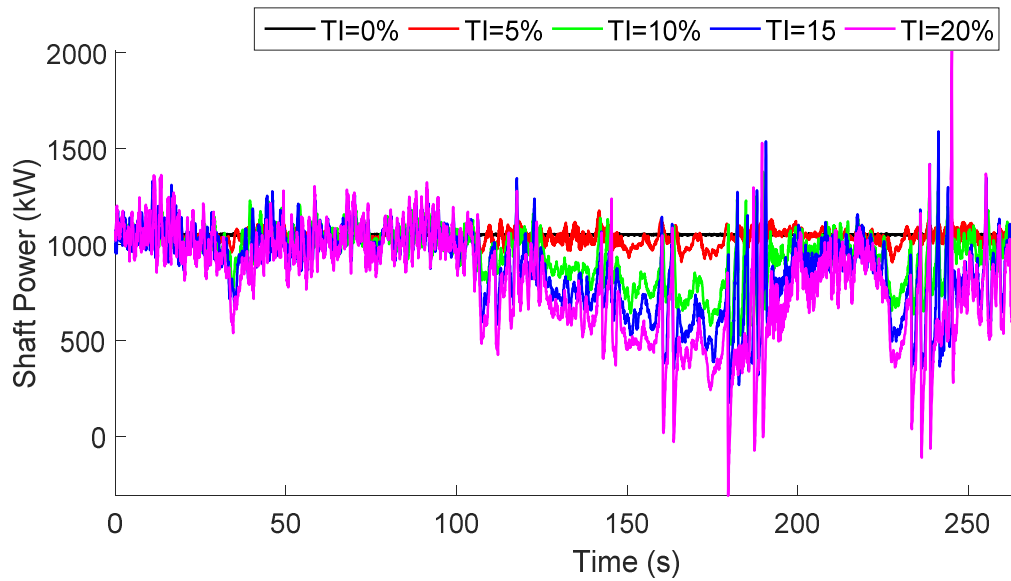


Figure 3.19– Time series of Torque at different turbulence intensity levels.

From Figure 3.19 it may be argued that the controller takes a pessimistic view, optioning for a much reduced load to avoid overloading. Additional energy is not extracted as the turbine goes above rated conditions but when turbulence lead to lower velocities, there isn't as much energy that can be extracted. This truncation at rated speed, caused by design, leads to the lowering of the average power in the more turbulent flow fields.

The effects of turbulence on shaft speed can also be seen in Figure 3.20. At high turbulence intensities, the shaft speed may drop sharply and accelerate back to rated speed in a small time period.

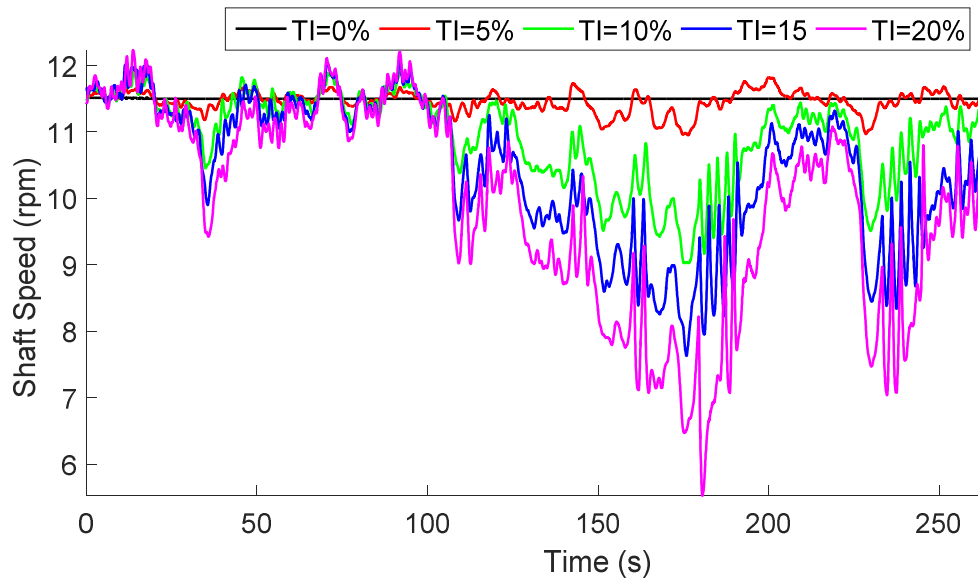


Figure 3.20– Time series of shaft speed at different turbulence intensity levels.

Clearly, the effect of turbulence on shaft loads and turbine performance is not only significant at rated speed as shown above. In the other operating average flow velocities, turbulence plays a critical role. Notice from Figure 3.21 that turbulence generally increases the non-torque loads on the main shaft with the exception of the axial force. As mentioned before, the pitching action has a role to play in the apparent lower axial loads in high turbulence.

Figure 3.22 paints a different picture of the effect of turbulence. It shows that in the operation region, huge standard deviations in the axial load may persist. This has a tremendous effect on drivetrain loads and reliability as bearings are generally selected with their capacity to carry axial loads in mind.

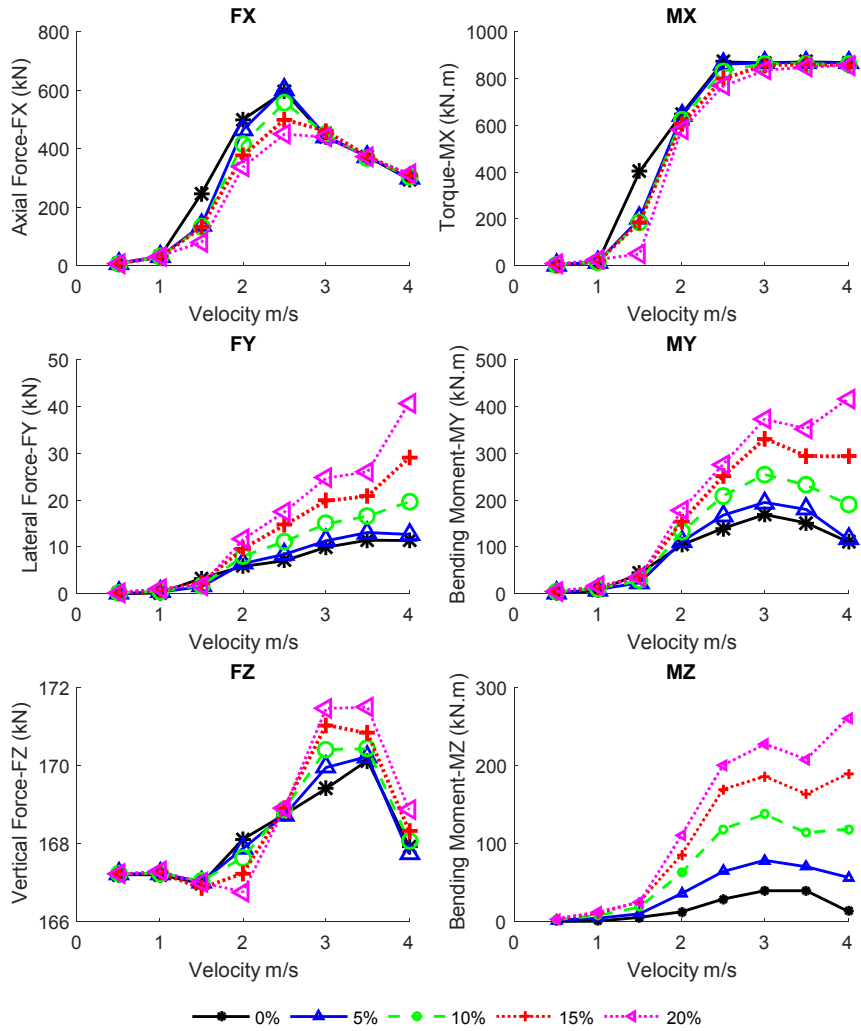


Figure 3.21– Effect of turbulence intensity on RMS shaft loads at expected velocity range

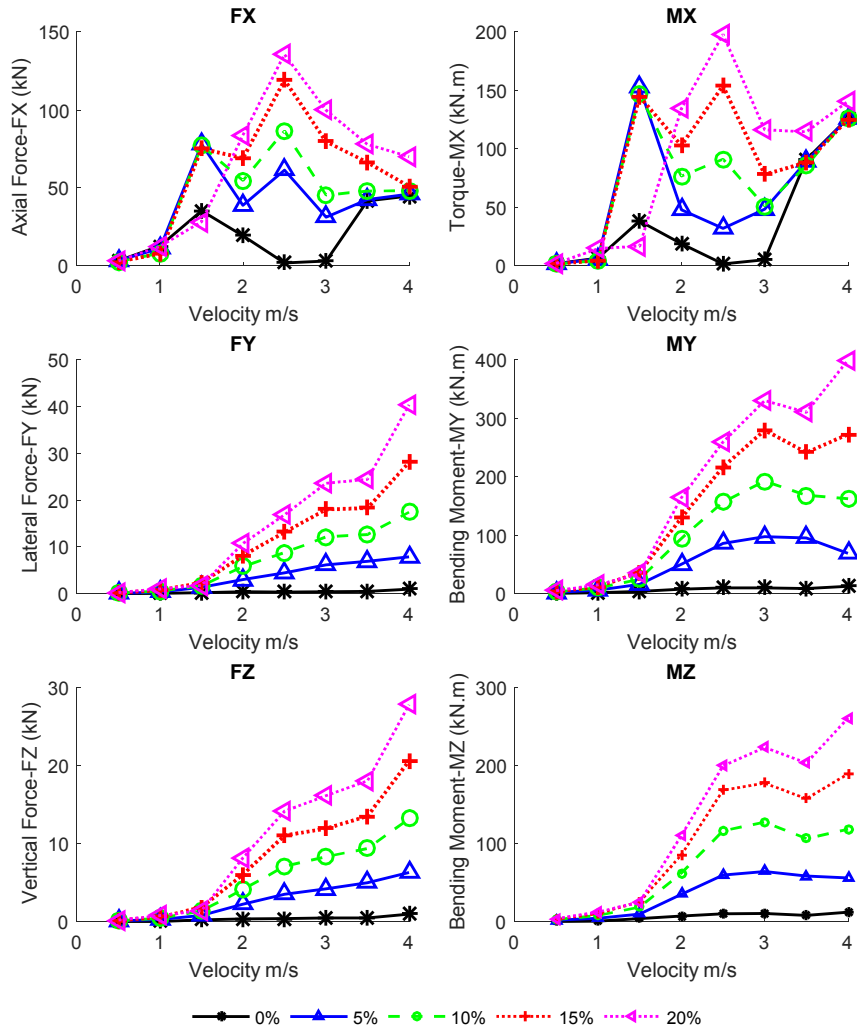


Figure 3.22– Effect of turbulence intensity on standard deviation shaft loads at expected velocity range

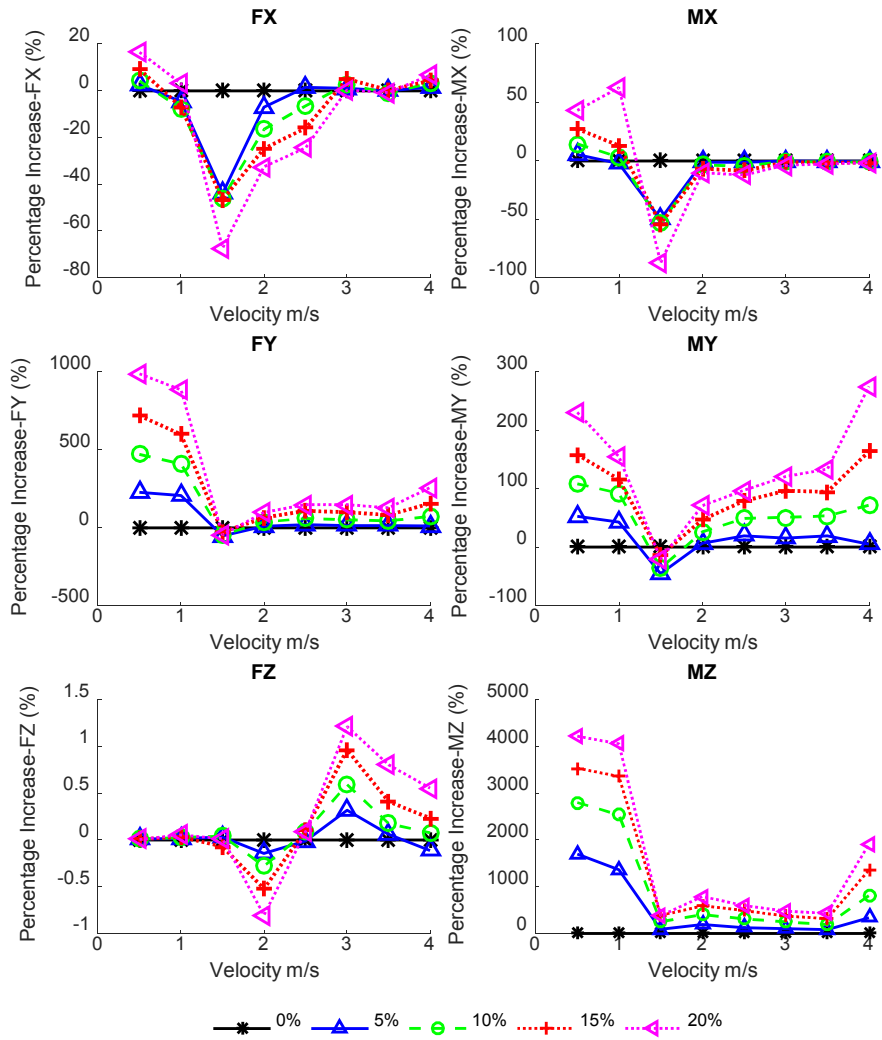


Figure 3.23– Effect of turbulence intensity on percentage increase RMS shaft loads at expected velocity range

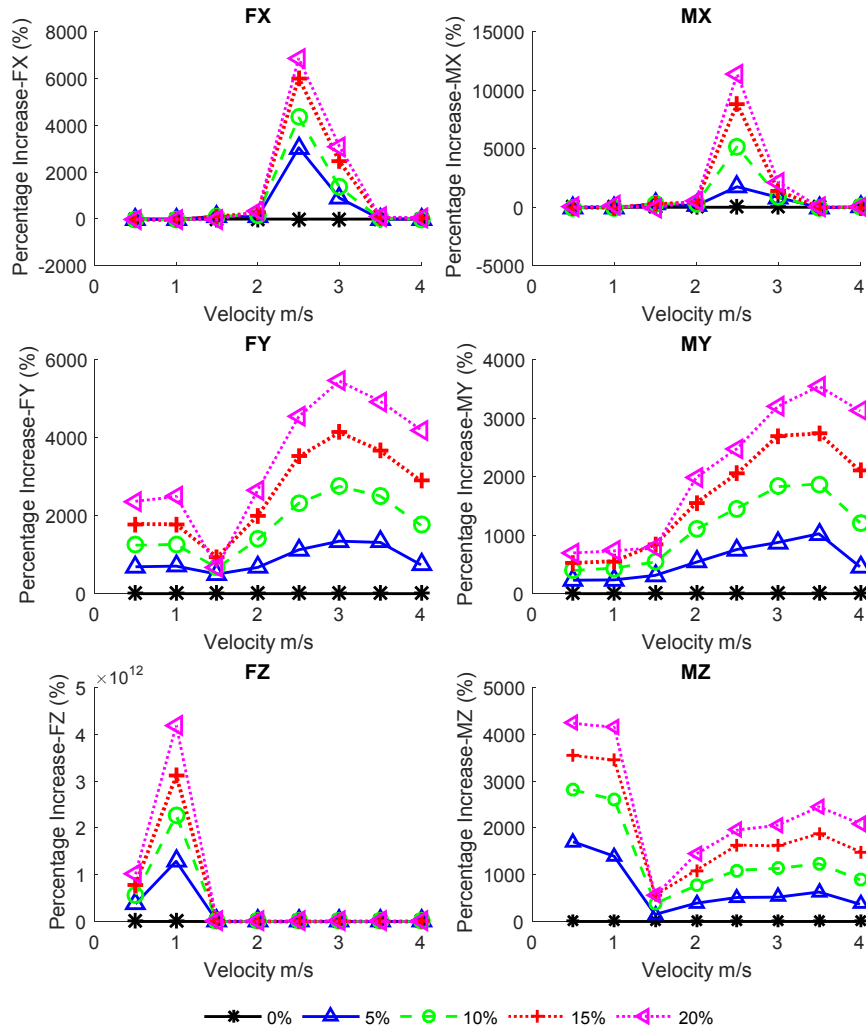


Figure 3.24– Effect of turbulence intensity on increase in standard deviation of shaft loads at expected velocity range

3.5.1 Effect of turbulent eddy components on main shaft loads

Turbulence is a three dimensional phenomenon thus always tend to have eddies in different random directions. Apart from changes in turbulence intensity, the nature of the turbulent eddies may vary from sites to site. Turbulence eddies may be more dominant in a single direction than others. Since turbulence varies both spatially and temporarily, it is important to understand how the eddy structure affects mains shaft loads and drivetrain component damage in the long run.

Figure 3.25 compares the loads on the main shaft of the turbine with components of the turbulence in all three special directions defined as “All ($U_i V_i & W_i$)”. To simulate conditions where the axial component of turbulence is more dominant in general, the line “ U_i ” shows a case where only the axial component of turbulence is present. Similarly, two-dimensional eddies are compared for vertical planer (XZ plane) eddies “ $U_i & V_i$ ”, vertical planner eddies (XY plane) “ $U_i & W_i$ ” and axial planer (YZ plane) “ $V_i & W_i$ ”. Figure 3.25 compares the Root Mean Squared (RMS) values are more indicative of the loading sustained at each velocity. Notice how the FY force has a significant RMS value compared to the mean. Other statistical values which are useful are the extreme values. These are critical for the survivability of the device. Additionally, the standard deviation indicates how variable the loads are over time.

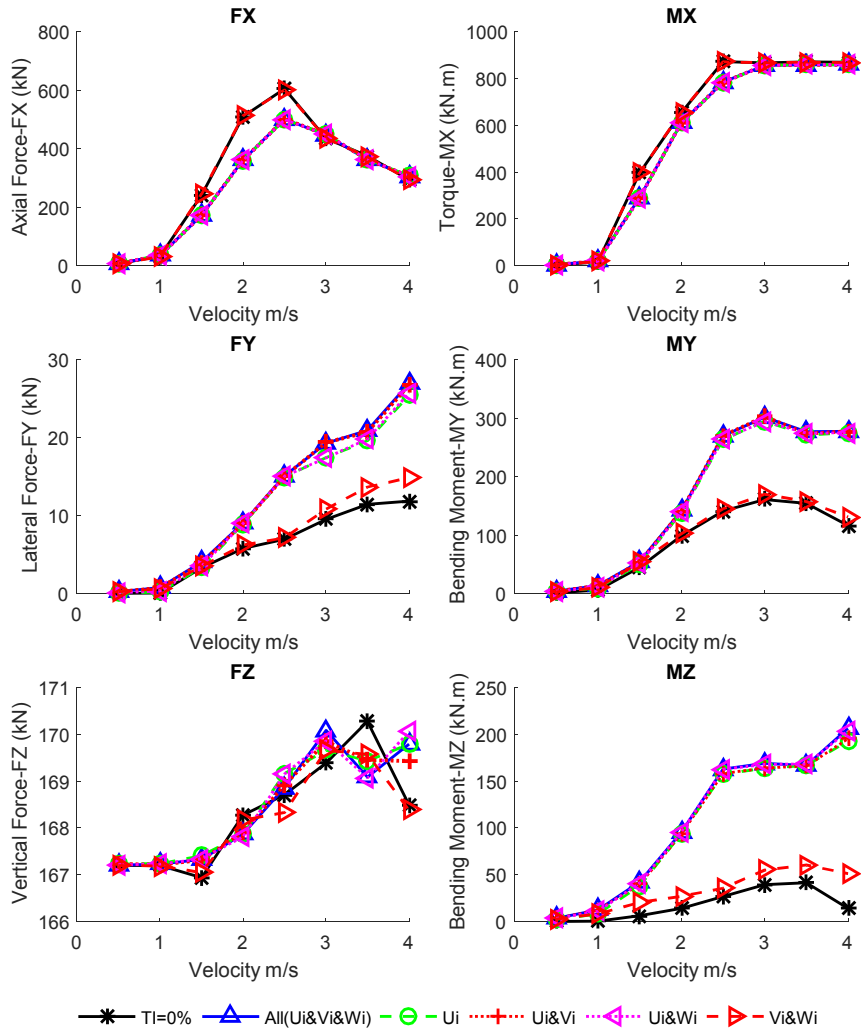


Figure 3.25– Influence of turbulence components on RMS of main shaft Loads.

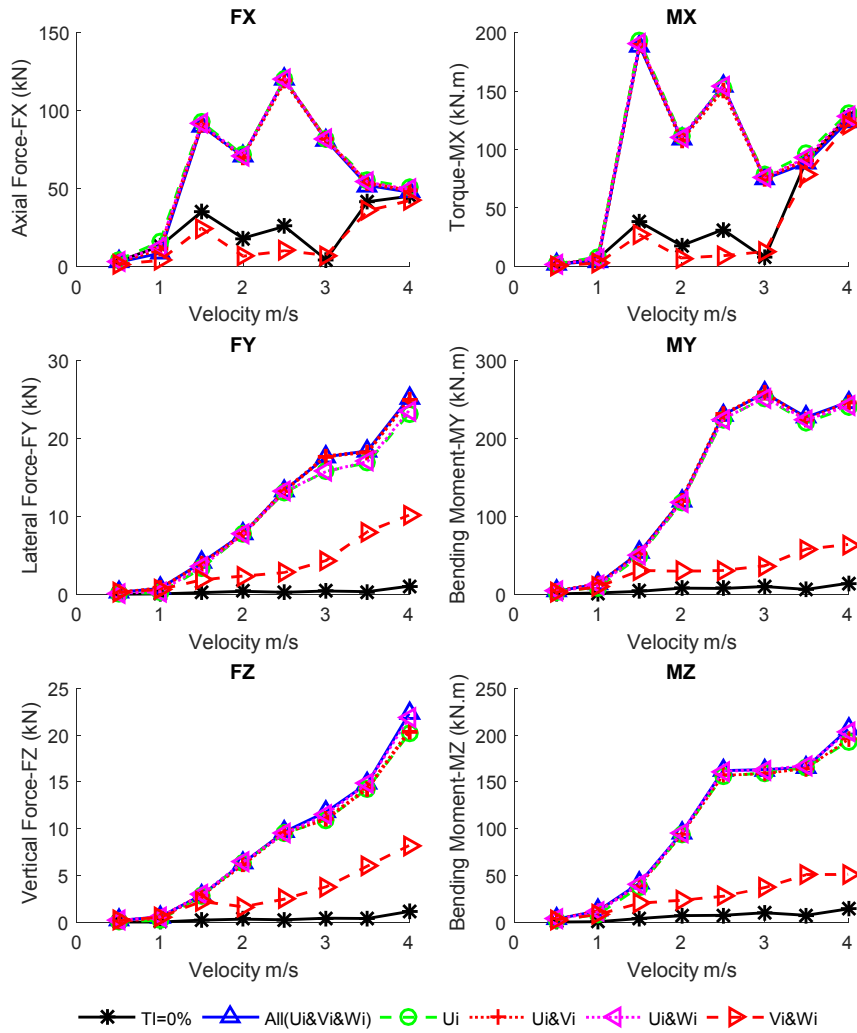


Figure 3.26– Influence of turbulence components on standard deviation of main shaft Loads.

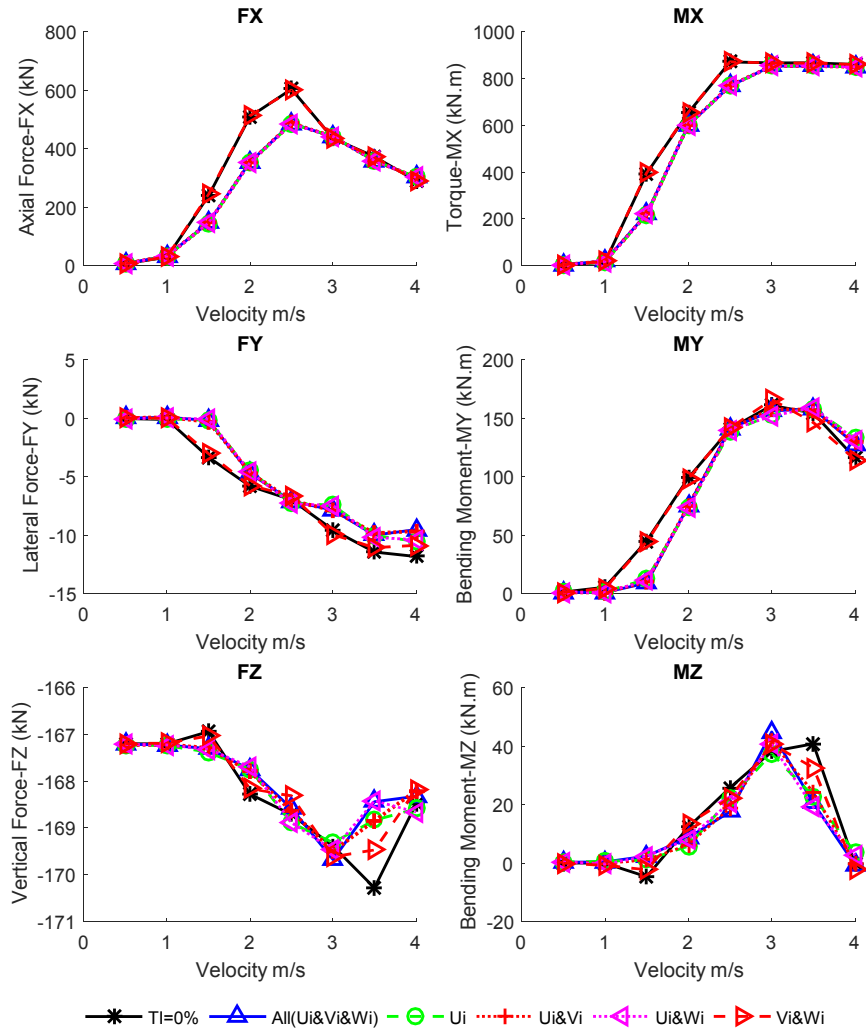


Figure 3.27– Influence of turbulence components on mean of main shaft Loads.

In Figure 3.27, the axial force is most influenced by the axial turbulence. In the cases where the axial turbulence component was present, no noticeable change is observed between the cases where there is off-axis turbulent eddies. Similarly, no noticeable difference is observed for cases where the axial component was present. The same was observed for the torque. This behaviour is expected as these two are derived mainly from the axial flow velocities.

It has been shown here that, the off-axis components of turbulence do in fact contribute to increase in non-torque loading on the main shaft of a tidal turbine. As

such care must be taken to consider them in flow simulations which are subsequently used to analyse main shaft loads.

Despite the off axis velocities contributing to non-torque loading, the influence of the axial component of turbulence was shown to affect the non-torque loads as well. In fact, the effect of the axial component of turbulence is stronger than the effect observed when only off axis components are present. The blade geometries are designed to extract energy from the axial direction thus the blades are more sensitive to the axial flow velocities. The key aspect of turbulence which is of paramount importance is the axial component of the turbulence.

3.6 Influence of Wave action Main Shaft Loads

In addition to turbulence created by the bathymetry, wave action also creates perturbations in the flow field. This is addressed by super imposing wave orbital velocities on the tidal flow field. As explained in Chapter 2.2.5, wave propagation at many tidal sites is often bidirectional because tidal sites are often located in channels or surrounded by a headland.

To this end, a single wave is propagated on to a smooth tidal flow field as described above. This is carried out by the superposition of wave orbital velocities on to a non-turbulent flow field with an average 2.5 m/s flow speed. The temporal flow particle velocity variation is as shown in Figure 3.9. The figure indicates a cross section through time to show the vertical variation over time of the flow speeds change with the wave action.

The wave condition at a site is often characterised by a scatter diagram showing frequency of occurrence of particular waves, grouped by the wave height and periods. The wave conditions at a particular time is characterised by a sea state which consists of many of the different waves in the scatter diagram. Here the effects of these individual waves from the scatter diagram are compared to demonstrate their potential effect. In Figure 3.28 the effects of wave loads on axial force is shown.

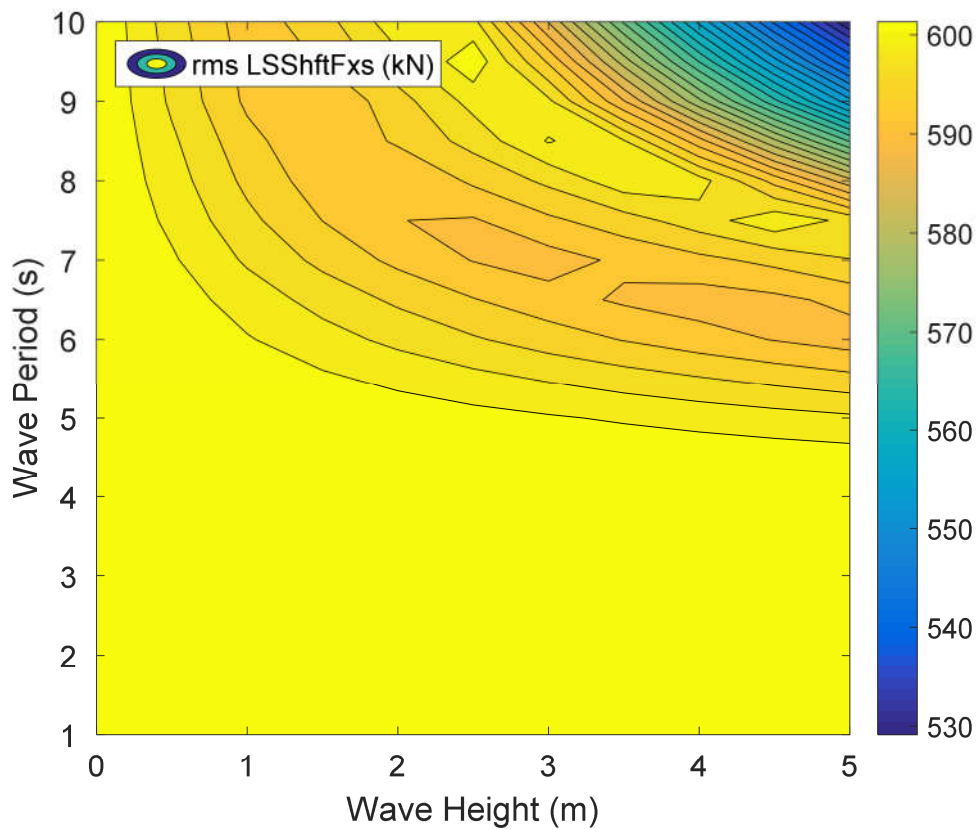


Figure 3.28– RMS of axial force for variation of waves

Among the sweep of wave heights and periods, there is a low probability of encountering large wave heights at low periods or low wave heights at large periods (as shown in Figure 2.12) due to wave breaking. Although these waves are somewhat impossible to produce in real life they are included in the plot for completeness.

Notice the range of the axial force in Figure 3.29 barely changes for lower wave periods and wave heights none the less at high wave heights and periods the range increases. The transient loading induced by wave action could increase the damage on the bearing. The control strategy however has a role to play here since the changing average particle velocity will trigger a response. In realistic sea states which consists various waves the instantaneous flow velocity may be enhanced or curbed by the combination of loads.

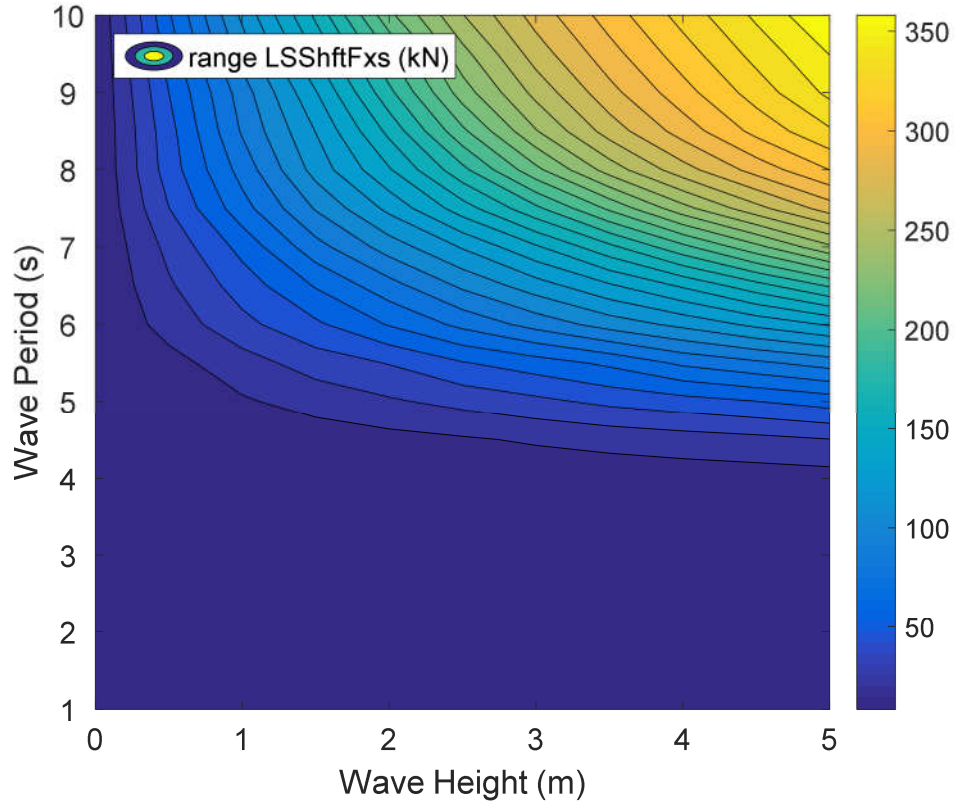


Figure 3.29– range of axial forces for the variation of waves

3.7 Influence of velocity Shear profile.

The shear profile in tidal channels can exhibit complex behaviours. Although the power law profile is generally accepted for modelling the shear profile of tidal flows, it is important to understand the advantage one shear exponent may have over another. The velocity u at a particular height above the seabed D_z is described as a function of the flow speed u_0 a reference height D_0 and a shear exponent κ .

$$u = u_0 \left(\frac{D_z}{D_0} \right)^\kappa \quad (\text{EQN 3.5})$$

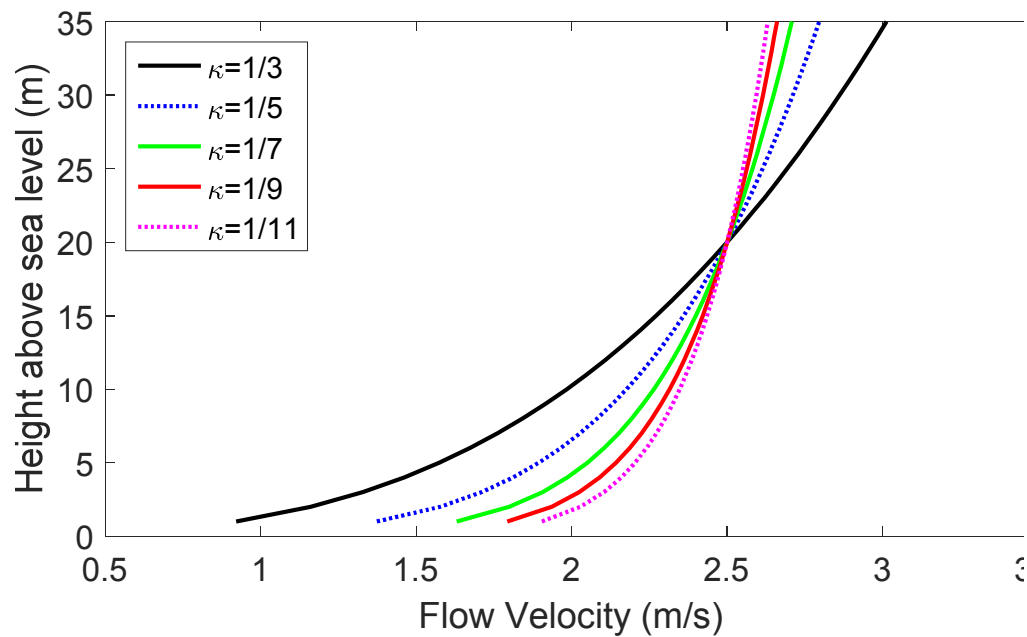


Figure 3.30– Lateral variation of flow speeds

It is clear from Figure 3.31 that the shear profile has little or no impact on the torque and axial thrust force. Never the less it contributes significantly to non-torque loads on the turbine's main shaft. As the power law exponent reduces, the velocities across the turbine are more even in the vertical direction. This clearly will influence the overturning moment (MY) and the vertical shear force (FZ). But as shown in Figure 3.31 and Figure 3.32, the lateral shear force FY and side-to-side bending moment MZ are also influenced by the velocity shear profile of the flow.

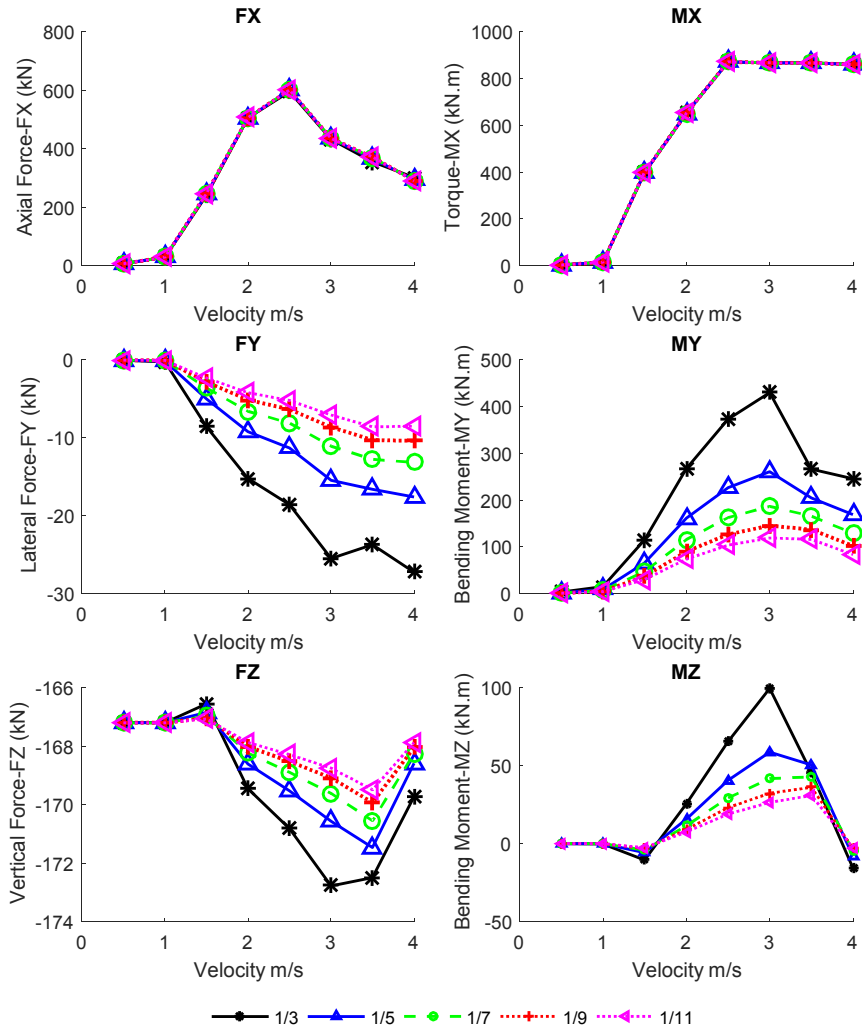


Figure 3.31– Effect of shear profile power exponent on mean drivetrain loads.

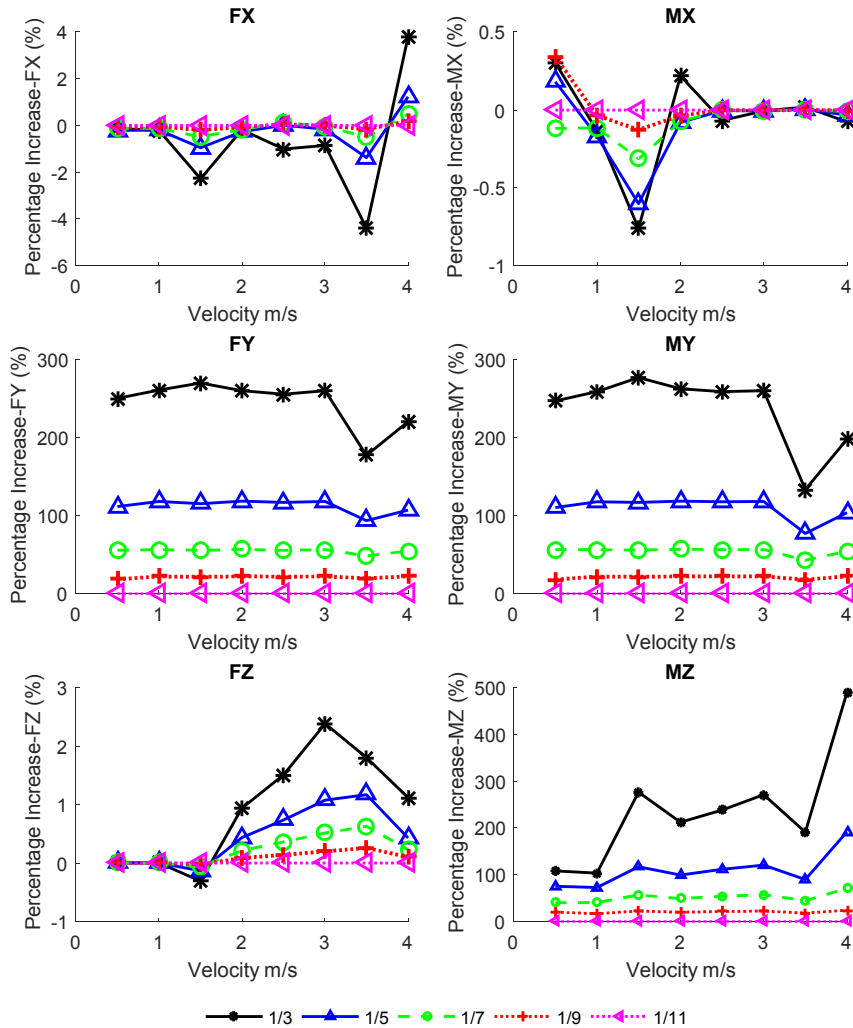


Figure 3.32– Effect of shear profile power exponent on mean drivetrain loads

3.8 Summary of Main Shaft Load characteristics

A range of environmental conditions which affect the drivetrain load has been discussed above. The primary environmental load is the flow mean velocity as it generally defines the magnitude of the average main shaft load. For tidal turbines, unlike wind turbines, small changes in flow velocity lead to a big increases in loading due to the density of water.

3.8.1 F_x-axial thrust force

The axial force on a turbine is strongly dependent on the axial induction factor of the blade section. For pitch regulated turbines, the turbine changes the blade pitches to optimise power. After reaching rated power, typical turbine designs with pitching capabilities pitch out to shed power to avoid over loading. Consequently, the axial thrust force reduces after rated speed is reached just as shown in Figure 3.21.

For a typical design of the horizontal axis tidal turbine a positive axial thrust force is observed for both flood and ebb tides because the turbine is yawed to face the average flow direction.

The average axial load may not necessarily increase with increased turbulence (from waves or bottom roughness), however its variation, characterised by the standard deviation in Figure 3.22 increases thus the axial force assumes a wider range of values. Today, many turbine arrangements employ tapered roller bearings or thrust bearings primarily because of the large variation of axial loads.

The turbines control strategy and control goals have key influences of the turbine loads in general and the axial load in particular. As can be seen Figure 3.25, the turbine sheds load at tidal velocities that are greater than rated speed. Although the average speed across a turbine over a ten minute period may be at the rated speed, turbulent eddies will cause the velocity across the turbine to exceed this amount at some points within the time period. The turbine's response these speeds will be to shed the load.

3.8.2 F_y-lateral force

Unlike the axial thrust load which directly follows the mean flow speed, loading cycle follows the tidal velocity in a cycle to a point, the lateral force may change directions several times in one loading cycle. As such, the primary loading cycle must not be described as a sinusoidal loading which has one cycle per tidal cycle. The cycling rate of the F_y load is however much higher than the tidal cycle. The primary contributor to this is loads such as turbulence which is stochastic in nature. This force is however small compared to the axial force F_x and vertical shear force F_z.

3.8.3 Fz vertical force

The primary contribution to the vertical force on the bearing is from the mass of the shaft, hub and rotor. The overturning moment caused by the velocity profile tends to cause a reduction in this force. The velocity shear profile has a profound influence on this some non-torque Loads.

3.8.4 Mx-torque

The torque is often the primary focus of turbine design because it dictates the power that can be generated ergo revenue. Turbines are designed as a consequence to extract the maximum amount of power from each tidal cycle. Accordingly, the toques increases with velocity until rated flow speeds or cut out speeds are reached.

The shear profile was found to not significantly influence the torque generated assuming the average flow remains the same. However turbulence created by waves or bottom friction influences the generated torque to an extent.

At high turbulence intensities, the mean torque may be reduced due to controller performance however the range and standard deviations increase with increasing turbulence intensities. Fluctuation in torque will lead to fluctuations in speed which could have a detrimental effect several components of the drivetrain.

3.8.5 My- bending moment about lateral plane

The primary contribution to the My bending moment about lateral plane is turbulence and shear profile. As the rotor rotates imbalances are caused by uneven flow field because of an increase in non-torque loads.

3.8.6 Mz- Bending moment about vertical plane

Turbulence has a profound impact on the magnitude and variability of the Mz bending moment. The impact is not only created by off-axis turbulence eddies but also the axial component of turbulence.

Wave action can also have a significant impact on the M_z loads. In this work however, actual sea states were not used but single waves were superimposed in the direction of the flow. Consequently, the impact of wave loads on the M_y moment is not as prominent as it could be. The velocity shear profile also has some influence on the M_z bending moment although it is quite limited for low velocity shear cases.

3.9 Potential effect of Cavitation

Cavitation may occur around a tidal turbine blade when the localised pressure falls below the vapour pressure of the local water. The likelihood of cavitation is dependent on many things including the shape of the aerofoil. Generally, aerofoils with bigger cambers tend to have stronger low pressure regions above the stagnation point. This gives rise to the possibility of cavitation.

Due to the vertical flow profile of tidal flows, more energy can be extracted from areas closer to the surface than at the bottom due to viscous effects. Several tidal device concepts aim to extract energy in this region to maximise the energy yield. The potential for cavitation in these situations is thus increased.

According to [59], cavitation can be avoided by keeping rotor tip velocities at 10-15 m/s. Batten et al [60], pointed out the level of occurrence of cavitation in tidal turbines is not yet understood. This gives rise to the need to further study the phenomenon. Cavitation is characterised by the cavitation number σ given in (EQN 2.6).. The critical cavitation number for cavitation inception depends on the minimum pressure coefficient around the aerofoil. Cavitation happens when

$$\sigma = CP \quad (\text{EQN 3.6})$$

As lift and pressure drag are derived from the integral pressure distribution around the aerofoil, the lift and drag coefficients are altered by cavitation. Figure 3.33 shows the difference between the pressure distribution around an s1012 aerofoil for a non-cavitating case and cavitating case with $\sigma = 1$.

A model of a generic tidal turbine operating at a hub depth of 15m, rotor diameter of 10m and tip speed ratio of 7 has been modelled using BEM formulation. The

rotor blade is formed from S1012 profile and the tidal velocity is specified as 3m/s. The cavitation number is calculated for each 1m blade annulus. An adjustment factor is then applied to the lift coefficient in the BEM formulation depending on cavitation number and angle of attack.

The pressure distribution around the S1012 aerofoil was determined using the subsonic 2-dmventional aerofoil analysis software XFOil [186]. The lift coefficient was calculated for the angle of attack between 0 and 15 degrees. The lift coefficient was also calculated for the different angles of attack and cavitation number from 0.5 to 5. Combining the two gave a model which maps an angle of attack, cavitation number and lift coefficient. Figure 3.34 presents how cavitation number and angle of attack influence the loss in lift.

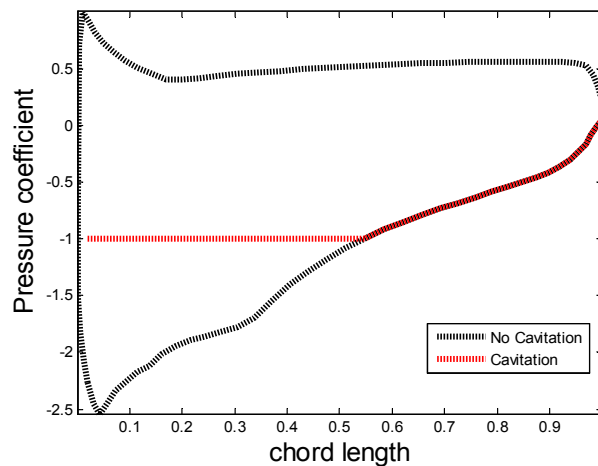


Figure 3.33– Variation of pressure along the chord of an S1012 aerofoil at a 6° angle of attack

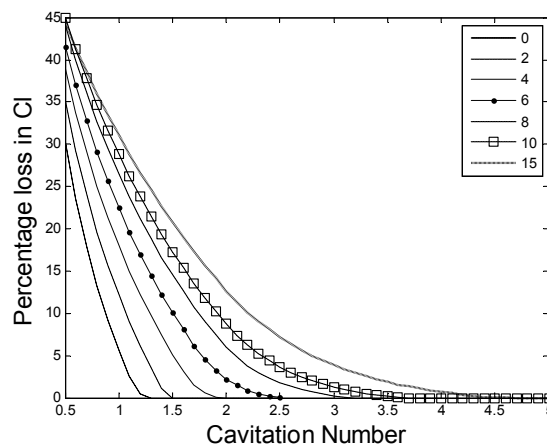


Figure 3.34: Loss of coefficient of lift with cavitation number for different angles of attack

Along the length of the blade, the cavitation number changes as the water depth changes as well as the blade twist and the magnitude of the incident flow velocity. Due to this, the cavitation number is very low at the tip of the blade as shown in Figure 3.35.

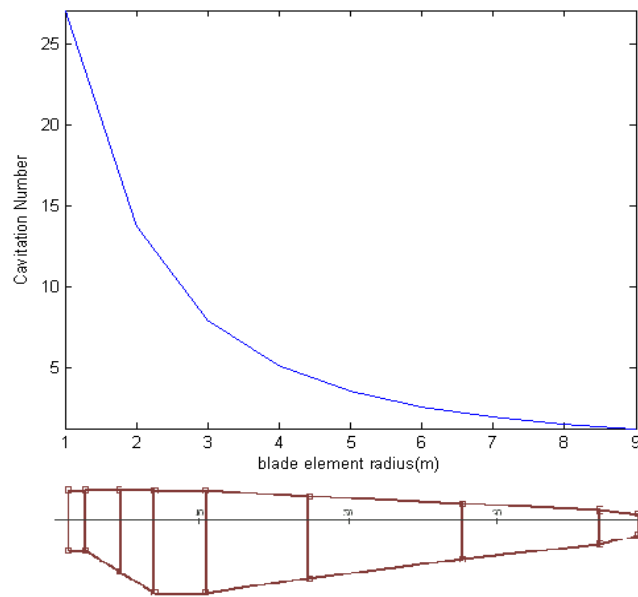


Figure 3.35– Variation of cavitation number along blade annuli

Figure 3.36 shows the power generated by a single rotor in one revolution calculated by the BETM model. The loss in performance peaks when turbine blade is at 90° (vertically upwards). In this position, 4% of power/torque is lost to cavitation effects. As a percentage of the total power this represents a small effect even in a turbine which is not made from an anti-cavitation hydrofoil, which is also operating close to the water surface. In ideally designed turbines which operate in even deeper water, the effect of cavitation on drivetrain loads is likely to be very small. All the same, cavitation could degrade rotor performance leading to unbalanced loading on the main shaft. This is, of course, very difficult to predict and account for. It is conclude that for well-designed turbines in appropriate sites cavitation is unlikely. The effect of cavitation (even when it does append) on drivetrain loads is small and can be neglected in further analysis.

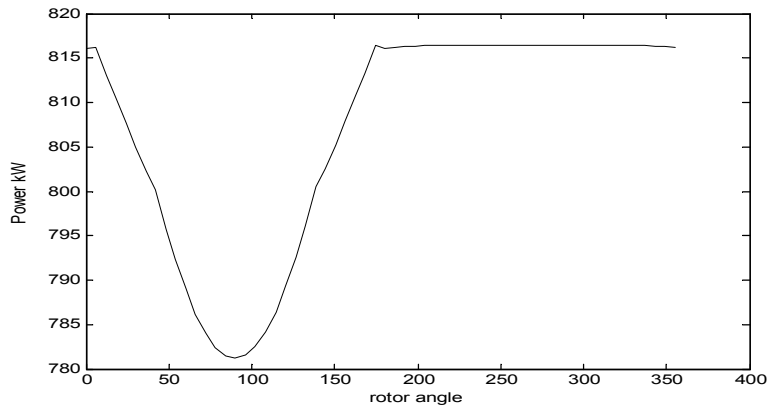


Figure 3.36– Power generated by a single blade under cavitation

3.10 Conclusions

It has been shown that the primary source of loading on the main shaft and therefore main bearing is the tidal flow velocity. While higher flow velocities lead to higher non torque loads in general, the axial load may be reduced due to power shedding after rated speed is reached.

Another major environmental factor that affects the main shaft non-torque loads is the velocity shear profile. In the work, the seventh power law profile which has been used by many researchers was adopted. The shear profile was found to affect the main shaft loads thus should be considered carefully when analysing turbine loads, hence life.

The wave climate within which a turbine is located will have an impact on turbine loads. In this work, single waves were superimposed on a tidal flow field instead of a spectrum of waves. Consequently, the influence of wave spectra and directionality has not been studied exhaustively. Nevertheless, it is clear that the wave climate must be considered for assessing turbine life and whole as well as component lives.

While cavitation can have severe impact on turbine performance and loading, proper blade design and submersion can eliminate the problem in tidal turbines. On the other hand, bio-fouling cannot be avoided. It is expected that bio-fouling can degrade turbine performance and change turbine dynamics but quantifying its effect is challenging due to the variety of factors which affect the bio fouling rate.

Chapter 4 Bearing Component Load Assessment

4.1 Introduction

This chapter tackles the process of evaluating bearing damage given shaft loads such as presented in chapter 3. A short description of a generic tidal turbine main bearing system is initially presented. The formulation of a rigid dynamics model is presented. The model aims to convert the integral bearing load into component loads on the bearing. The numerical time domain analysis delivers the time history of loads on the individual components as well as their displacement, velocities and accelerations.

In order to use the Stress-Life method for fatigue damage analysis, a finite element model whose results contribute to a force stress look up table is presented. Subsequently, section 4.5 brings its preceding sections together to develop a damage calculation method that delivers the damage on the inner race of the roller bearing.

4.2 Main Shaft bearing system

The main shaft system consists of two spherical roller bearings as shown in Figure 4.3. Spherical roller bearings are used in the main bearings of turbine drivetrains because of their tolerance to misalignment. Spherical roller bearing cannot support any moment loads in their own thus must be used in combination with other bearings as shown in section Figure 4.2 to support a moment.

The shear forces F_y and F_z are distributed along the length of the shaft thus it is assumed to take effect at the centre of mass of the shaft, which is 0.612m from rotor apex if the shaft is assumed to have a shape as shown in Figure 4.1. Generally, the bearing system is statically indeterminate. The system reduces to a statically determinate system when the shaft stiffness approaches infinity. The shaft can be selected such that it exhibits high stiffness by ensuring it is not hollow or has a sufficiently small inside diameter if it is hollow. Consequently, the bearing system may be depicted as shown in Figure 4.2. As shown below, the bearing reaction forces F_1 , and F_2 are evaluated according to (EQN 4.1) and (EQN 4.2). Notice that as the distance a remains greater than $l/2$, the primary bearing is subjected to more load. As the geometries are fixed in the bearing system, the primary bearing is subjected to the majority of the load for all values of p . Consequently, this is the focus of further work carried out in this chapter.

$$F_1 = p\left(1 + \frac{a}{l}\right) \quad (\text{EQN 4.1})$$

$$F_2 = p\frac{a}{l} \quad (\text{EQN 4.2})$$

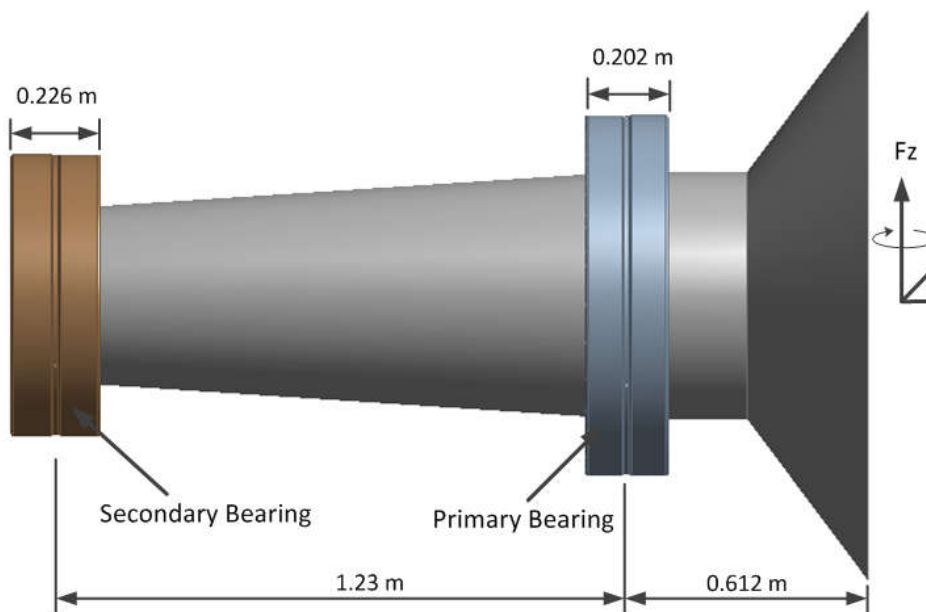


Figure 4.1- CAD Rendering of main bearing system

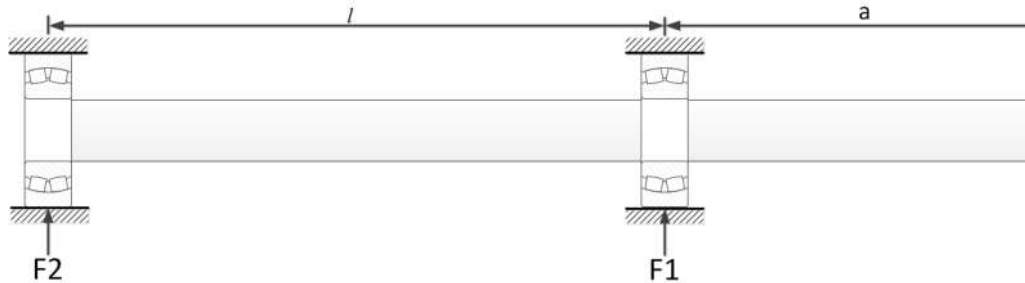


Figure 4.2- Static representation of moment load on bearing system

4.2.1 Bearing geometry

The primary main bearing used in this work is a 230/630-w33 series spherical roller bearing. As shown in Figure 4.3 the bearing consists two rows enabling it to carry additional radial load.

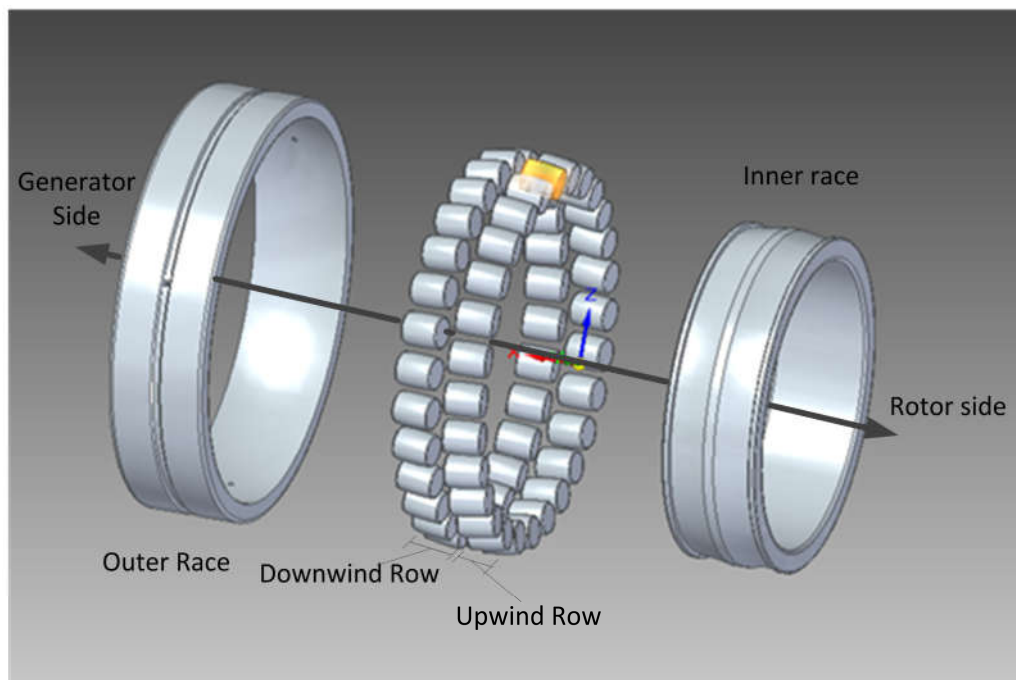


Figure 4.3- Rendering of the components of the 230/630- w33 series bearing

4.3 Numerical modelling

4.3.1 Rigid dynamics modelling

Rigid Body Simulation (RBS) packages evaluate forces, displacements, velocities and accelerations on a system with relatively low resource compared to FE models. A RBS system reduces the number of DOFs of an entire system by representing each component by a rigid body.

Many RBS models of similar (wind turbine) drivetrains have focused on the torsional dynamics of the system. In these cases, the main bearing is represented by a stiffness matrix. With this approach, the integral load on the main bearing can be evaluated. Following this approach, the loading on the bearing components can be evaluated using FE models. This approach can be time consuming and expensive due to the computational resource required to perform dynamic FE analysis.

4.3.2 Rigid Dynamics Bearing model.

Using the rigid dynamics formulation, each rolling element of the bearing is represented by a 6 DOF spring and damper as show in Figure 4.4

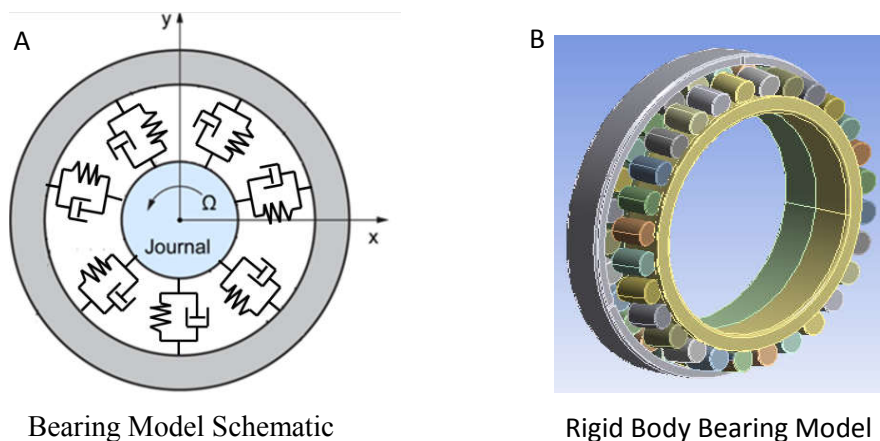


Figure 4.4- A) schematic of bearing model B) Rendering Rigid body simulation of bearing

The stiffness is aligned to the bearing centre to reflect the geometry of the spherical roller bearings. To correctly evaluate the load carried by individual rolling elements, the nonlinear stiffness of both the inner race contact and outer race contact must be

representative. The total stiffness of the rolling element k_{total} is therefore given as a function of the outer race contact stiffness k_{OR} and the inner race contact stiffness k_{IR} .

$$\frac{1}{k_{total}} = \frac{1}{k_{IR}} + \frac{1}{k_{OR}}$$

It is assumed the bearing has a perfectly stiff cage and the rolling element does not slip. The inner race is fixed to the main shaft therefore rotates at the same speed.

4.3.2.1 Contact Points

ANSYS rigid dynamics enable one to create joints between rigid bodies. This ranges from 1DOF joints to 6DOF joints. The solution to the set of rigid dynamics equations is solved over time using a Runge-Kutta time marching algorithm.

To enable the creation of two contact surfaces, two contact points are generated on each rolling element. These contact points are defined as very small Rigid bodies with their coordinate system placed on the surface of the rolling element where there is a contact between a rolling element and race way as shown in Figure 4.5.

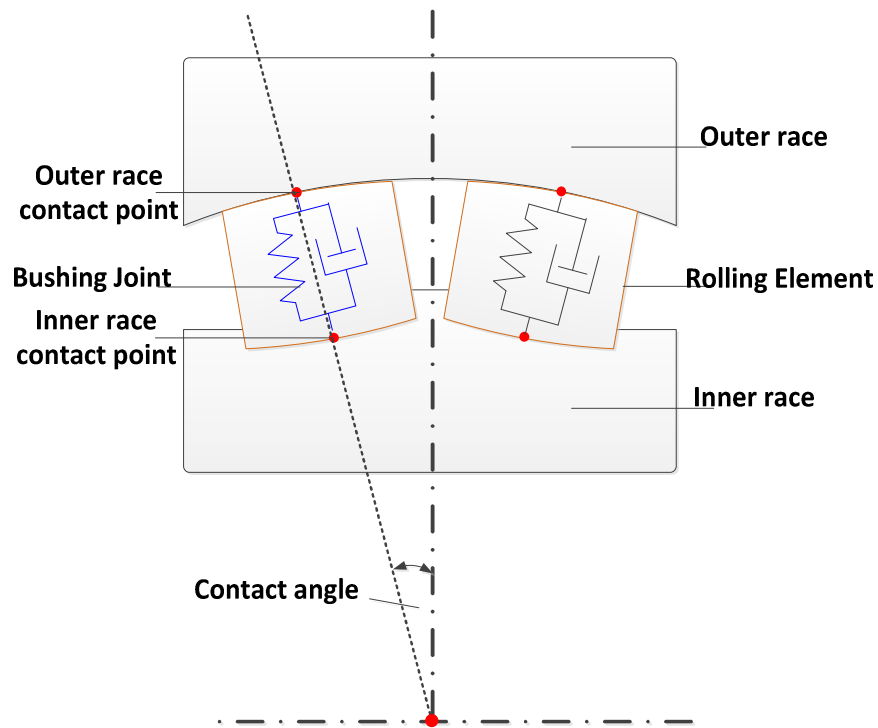


Figure 4.5- Schematic of rolling element representation

The contact point is modelled as a General Joint (with restricted translational motion). To enable independent raceway data extraction for both rows, the bearing is sliced through a central plane as shown in Figure 4.6.

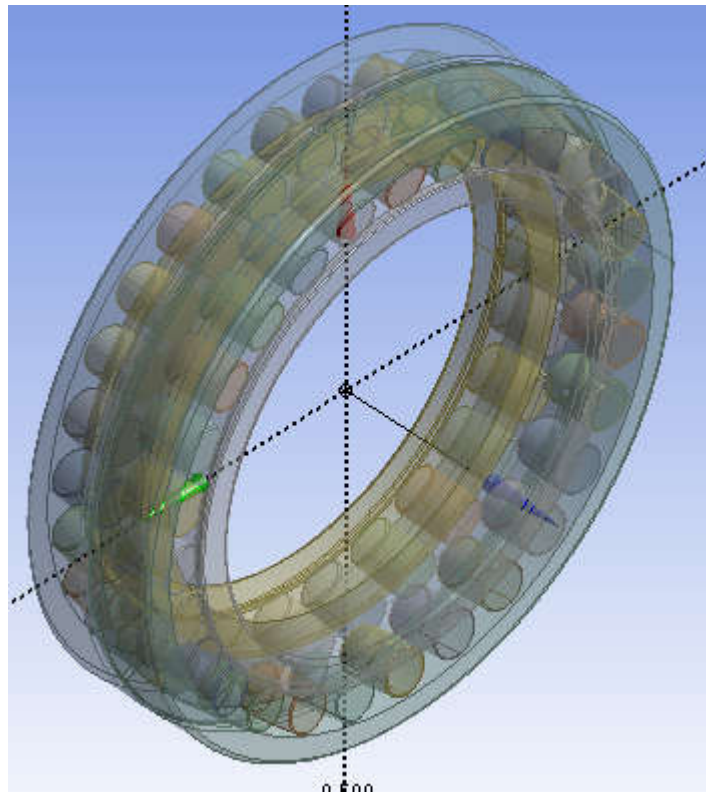


Figure 4.6-Bearing model

4.3.2.2 Bushing joints

The dynamic characteristics (stiffness and damping) of the bushing joint can be entered into a 6x6 stiffness and damping matrices as shown in Figure 4.7.

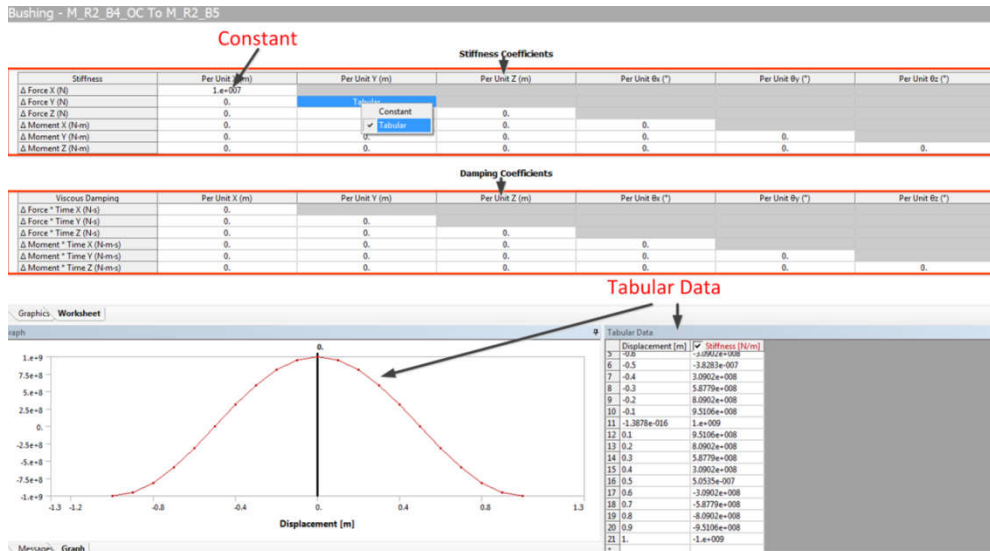


Figure 4.7–Bushing Joint Stiffness and Damping

The diagonal terms of the stiffness matrix can be defined in a tabular form thus enabling non-constant stiffness values to be entered. Nonlinear behaviour is enforced by defining nonlinear stiffness characteristics.

4.3.2.2.1 Basis matrix

The Bushing Joint is defined as an element between defined coordinate systems. Intrinsically, it is critical that these coordinate systems are defined in the correct position and orientation to each other. The orientation of each coordinate system is controlled by a 6x6 basis matrix. These can be defined in relative to a Global Coordinate System(GCS). The relative rotation about the x-axis is given by

$$R_x(\alpha) = \begin{bmatrix} 1 & 0 & 0 \\ 0 & \cos \alpha & \sin \alpha \\ 0 & \sin \alpha & \cos \alpha \end{bmatrix}$$

$$R_y(\beta) = \begin{bmatrix} \cos \beta & 0 & \sin \beta \\ 0 & 1 & 0 \\ \sin \beta & 0 & \cos \beta \end{bmatrix}$$

$$R_z(\gamma) = \begin{bmatrix} \cos \gamma & \sin \gamma & 0 \\ \sin \gamma & \cos \gamma & 0 \\ 0 & 0 & 1 \end{bmatrix}$$

The coordinate transformation matrix for rotational axis is therefore given by

$$R_x R_y R_z = \begin{bmatrix} \cos \beta \cos \gamma & \cos \beta \sin \gamma & \sin \beta \\ \cos \alpha \sin \gamma + \sin \alpha \sin \beta \cos \gamma & \cos \alpha \sin \gamma & \sin \alpha \sin \beta \cos \gamma \\ \sin \alpha \sin \gamma & \cos \alpha \sin \beta \cos \gamma & \sin \alpha \cos \gamma + \cos \alpha \sin \beta \sin \gamma \\ \sin \alpha \cos \gamma & \cos \alpha \cos \beta & \cos \alpha \cos \beta \end{bmatrix}$$

4.3.2.2.2 Command snippets

The procedure as defined above can be carried out manually. However, the model consists 112 contact points and 56 bushing hence manual definitions of these joints can be tedious and time consuming. ANSYS rigid dynamic enable the use of a command snippet (which operate in Iron-python programming language) to control aspects of defined model. This was utilised to automate the generation of joint basis matrices and update nonlinear stiffness behaviour of the rolling elements. In addition, they are used to read csv files which contain the loading on the bearings. The Iron-python code that was implemented can be found in Appendix C

4.3.2.3 Bearing kinematics

As the bearing components are represented by coordinate systems their rotations are described relative to each other. The rolling element rotations are describes relative to the race ways. The inner race contact is defined relative to the inner race while the outer race contact is defined relative to the outer race. These contacts are assumed to rolling without slipping. To enforce rolling without slipping, the tangential force F_t must not exceed the frictional force.

$$F_t < \mu F_N$$

It is thus reasonable to assume no slipping occurs between the rolling element and the raceways to enable quicker computation. As such the kinematic relationship between bearing components is described by (EQN 2.60).

4.3.3 Rigid dynamics Results.

4.3.3.1 Static Force on stationary bearing

For a static spherical roller bearing, Harris [118] summarised a theoretical approach to calculating the force on each rolling element. The performance of the Rigid Dynamics model has been compared to theoretical predictions given by (EQN 2.37). Figure 4.8 shows the comparison between theoretical prediction of the bearing load distribution across the rolling element. Figure 4.9 compares the load distribution between the upwind row of the bearing and the downwind row. The two rows have an identical load distribution since no axial load is applied. The loads are however not necessarily equal as because the two rows are 6.428° out of phase with each other.

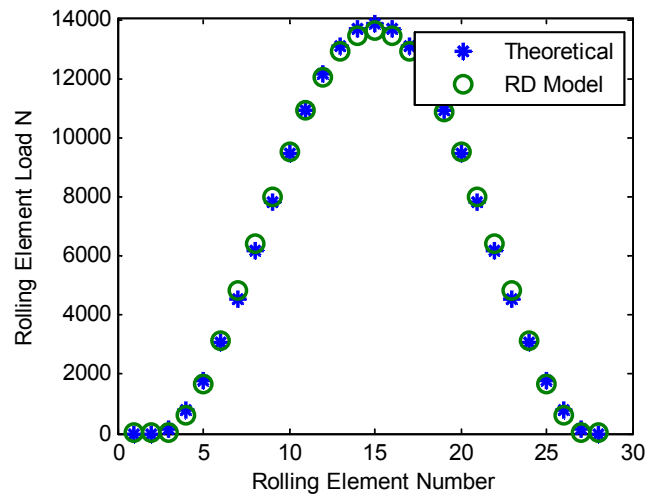


Figure 4.8–Variation of rolling element load when subjected to 200kN of radial load

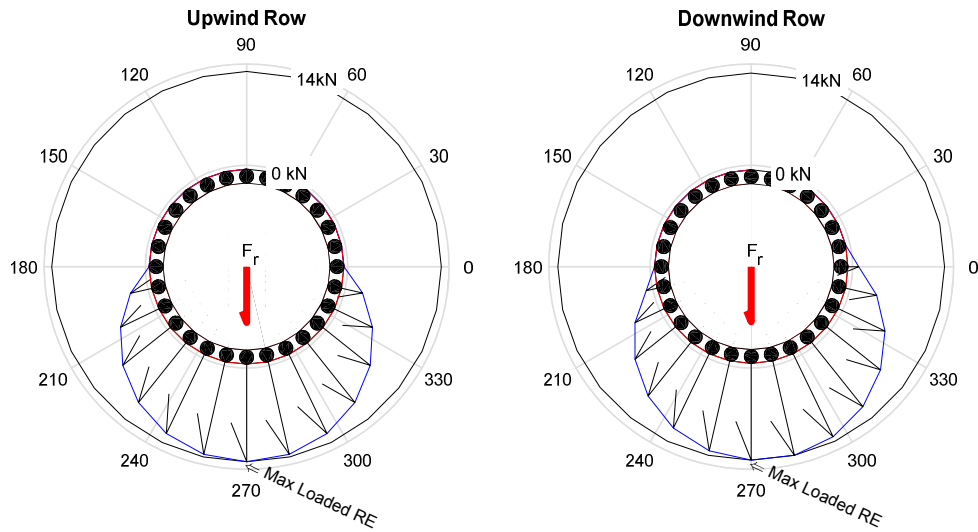


Figure 4.9–Variation of rolling element load when subjected to 200kN of radial load

Figure 4.10–Figure 4.15 below show the evolution of the load distribution in the bearing as the axial force is increased. In each of the figures, a radial load F_r of 100 kN is applied. From Figure 4.10 it can be seen that the small ratio of axial to radial force leads to an even load distribution between the bearing rows.

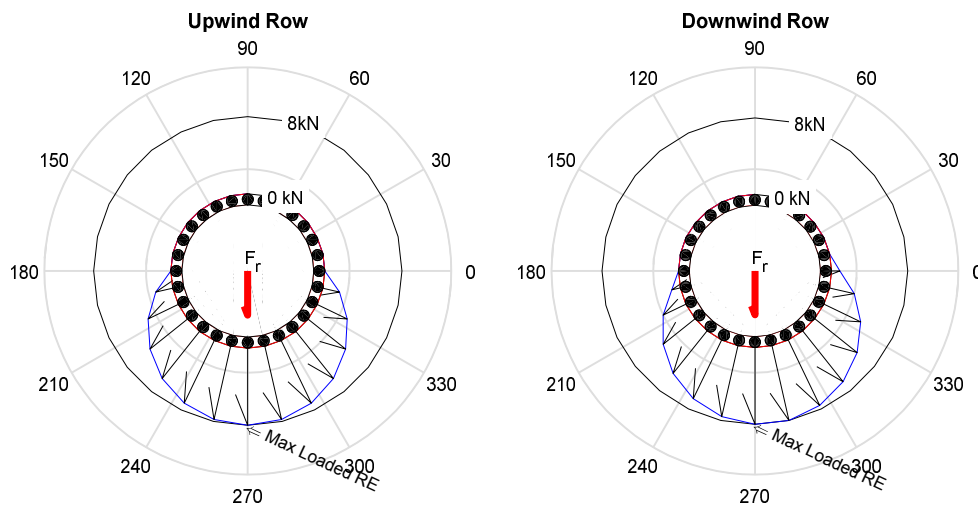


Figure 4.10–Variation of rolling element load when subjected to 100kN of radial load and 5kN axial force

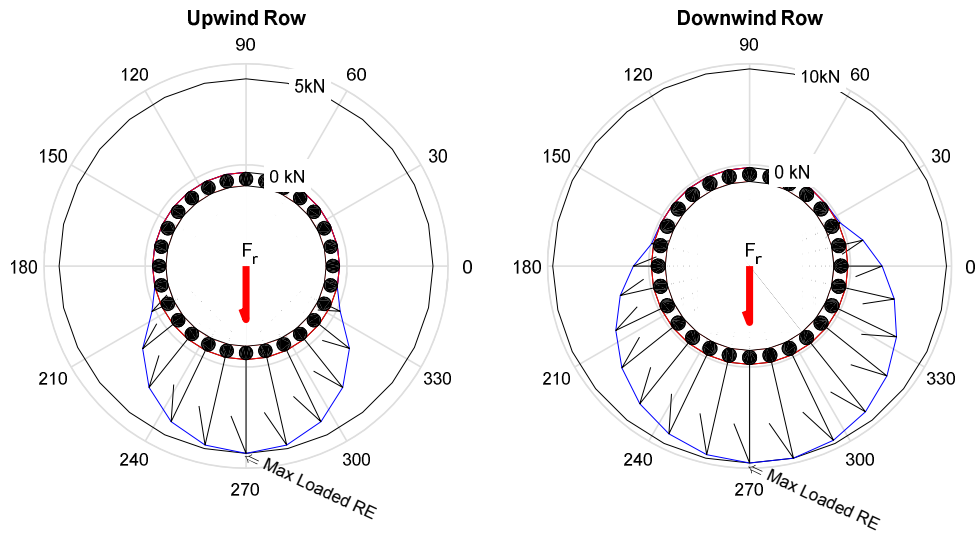


Figure 4.11– Variation of rolling element load when subjected to 100kN of radial load and 10kN axial force

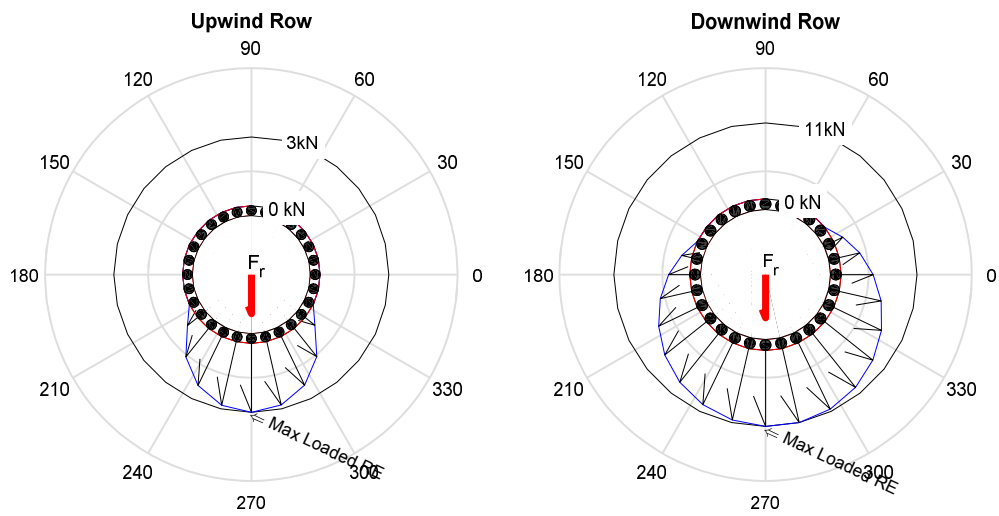


Figure 4.12– Variation of rolling element load when subjected to 100kN of radial load and 15kN axial force

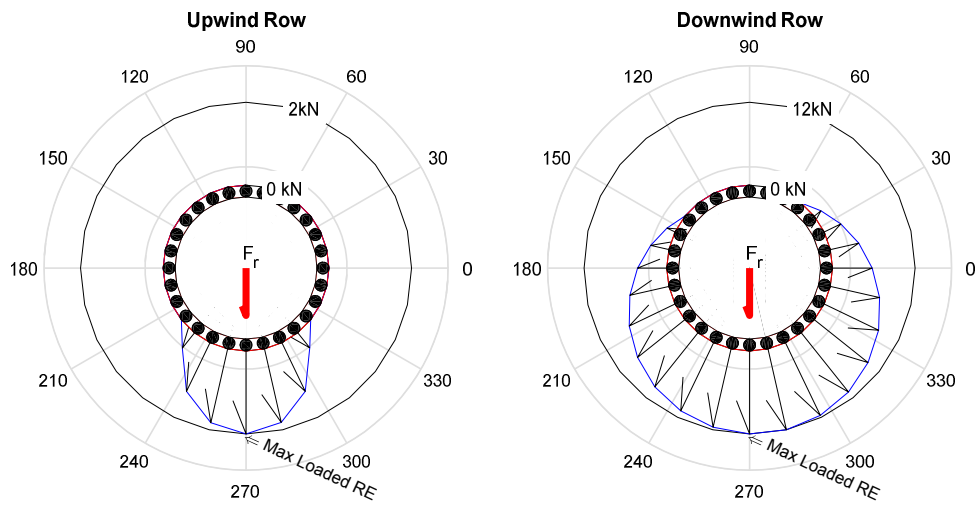


Figure 4.13– Variation of rolling element load when subjected to 100kN of radial load and 20kN axial force

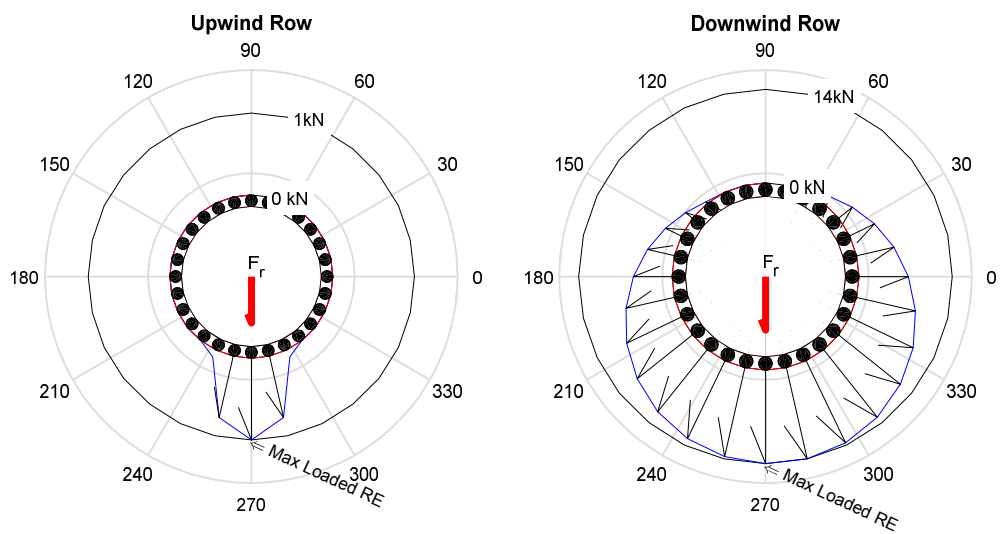


Figure 4.14– Variation of rolling element load when subjected to 100kN of radial load and 25kN axial force

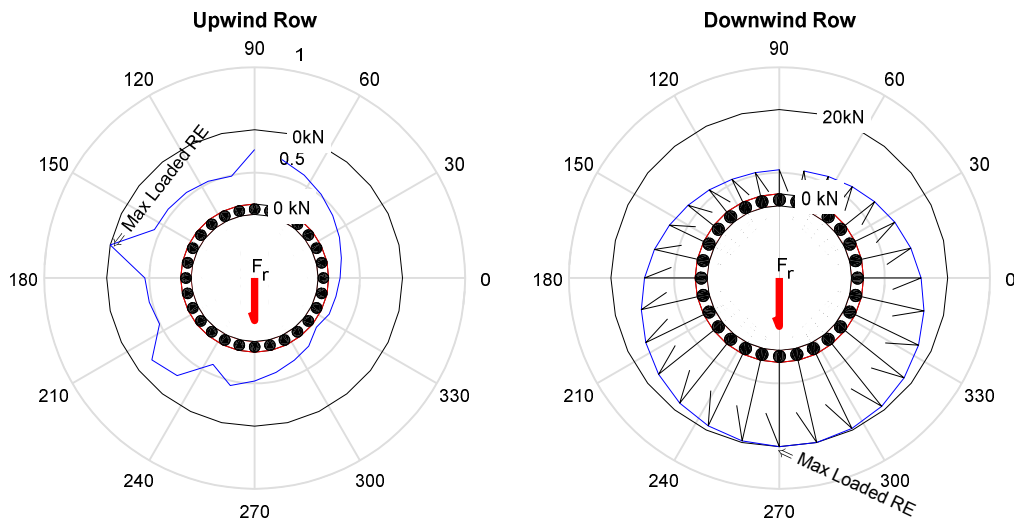


Figure 4.15– Variation of rolling element load when subjected to 100kN of radial load and 50kN axial force

In a situation when there is a static force, on a static bearing, Figure 4.9 to Figure 4.15 show a snapshot of the bearing load distribution in time. Given that this is representative of static conditions the load remains constant through time. In such conditions, the time history of a 200kN load applied on the bearing can be seen in Figure 4.16 . The resulting bearing load history is shown in Figure 4.17.

In Figure 4.17, the colour map indicates the relative angle between a rolling element and the resultant radial load which is indicated by ψ in (EQN 2.31). The Rolling elements which lie between $-\pi/2$ and $\pi/2$ are loaded while rolling elements which fall outside this range remain unloaded. It must be reiterated that this loading distribution is modified by the axial load. However, with a purely radial load the load distributions within the two rows remain identical.

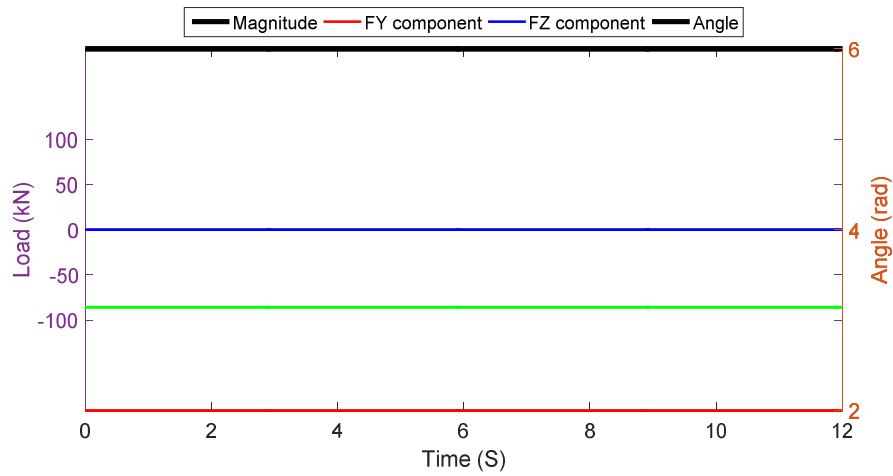


Figure 4.16–Specified bearing loads is static conditions

Over time, the load carried by each roller remains constant since the bearing is not rotating.

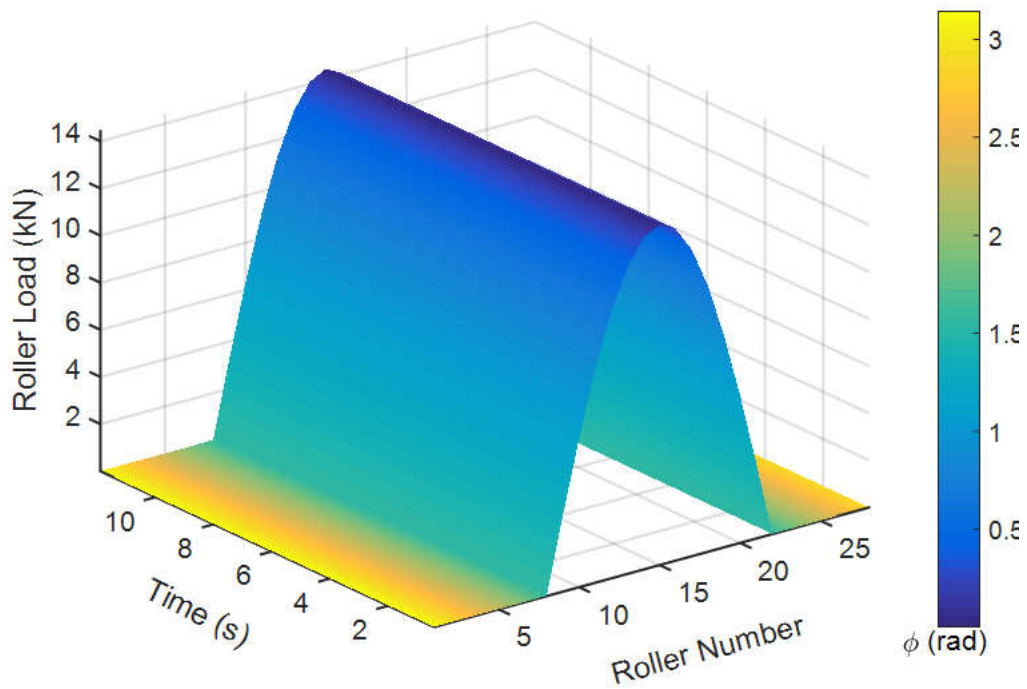


Figure 4.17–Dynamic force on static rolling element bearing at a static load

4.3.3.2 Static force on rotating bearing

When a torque greater than the starting torque of a bearing is applied, it accelerates thus its rotational speed increases. With the onset of rotation, the loading distribution within the bearing changes to reflect the new relative angle ψ between the load and the rollers. For simplicity, the case where the bearing rotates at a constant speed of 11.5 rpm is considered in Figure 4.18.

The loading on the bearing whose results are shown in Figure 4.18 matches the loads in Figure 4.16. However, due to rotation, specific rollers become loaded or unloaded as they enter or leave the loading zone respectively. This is still dictated by the angle ψ .

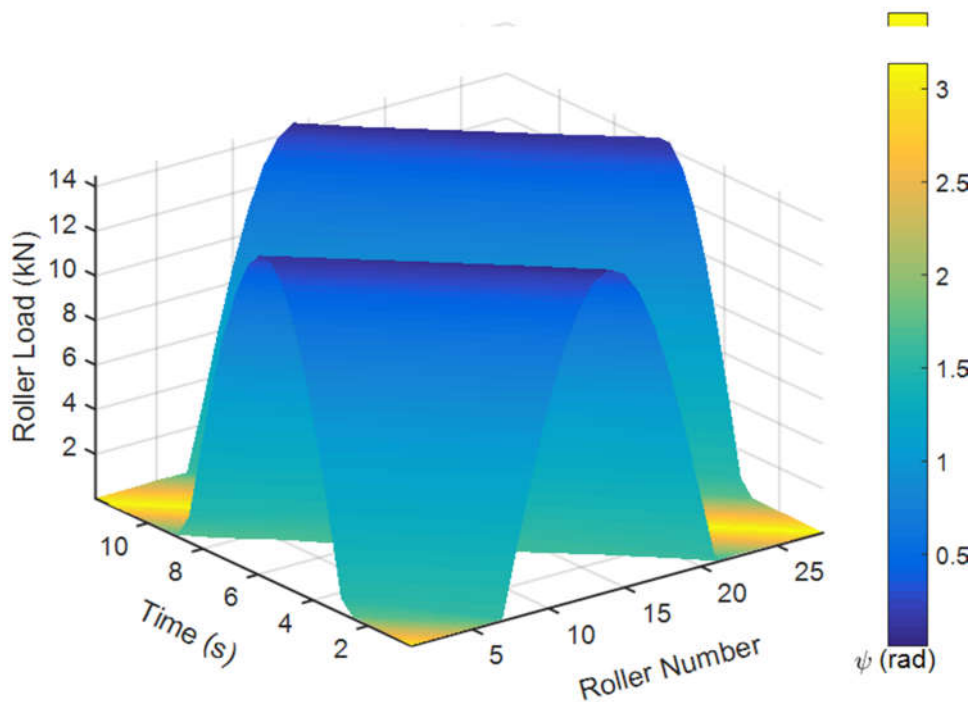


Figure 4.18—Dynamic force on rollers when bearing is subjected to a 200 kN static load and a constant rotational speed

Notice that in the 12 second period, each roller is subjected to just a single load cycle. This is due to the fact that the rollers rotate round the central axis of the bearing at a much slower speed than the inner race.

4.3.3.2.1 Constant speed -Dynamic force on rotating bearing

In practice, the bearing load is dynamic as well as the bearing itself. The dynamic radial load may vary both in terms of magnitude and direction. Since the relative angle between a roller and the resultant radial force is critical to the roller loads, the direction of the dynamic radial load is critical.

Supposing a bearing is subjected to a 200 kN load in keeping with the analysed scenarios above, with the exception of changing the direction of the radial load, the loading on the rollers will be modified. Figure 4.19 presents the loading on a bearing in such a scenario where the radial load is rotated round in circles while Figure 4.20 presents the loading on the individual rollers over time.

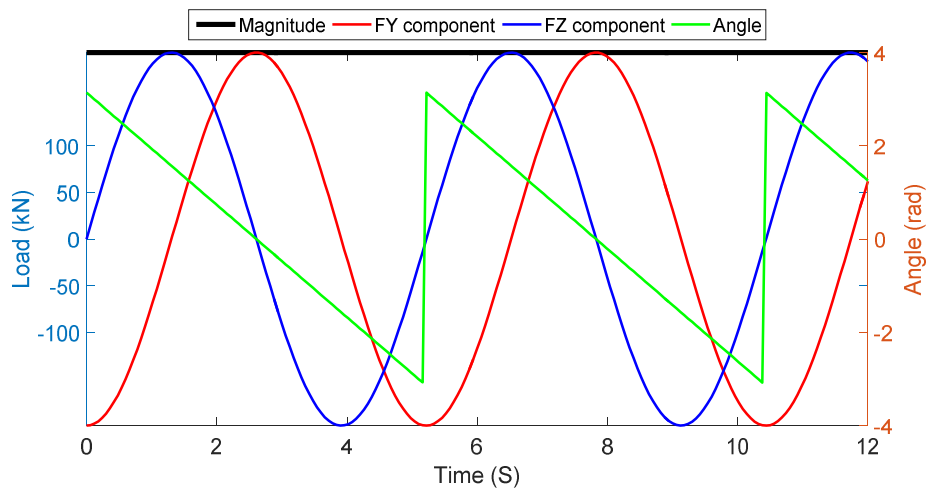


Figure 4.19–Loads on a bearing rotating at constant speed with constant rotation of radial load

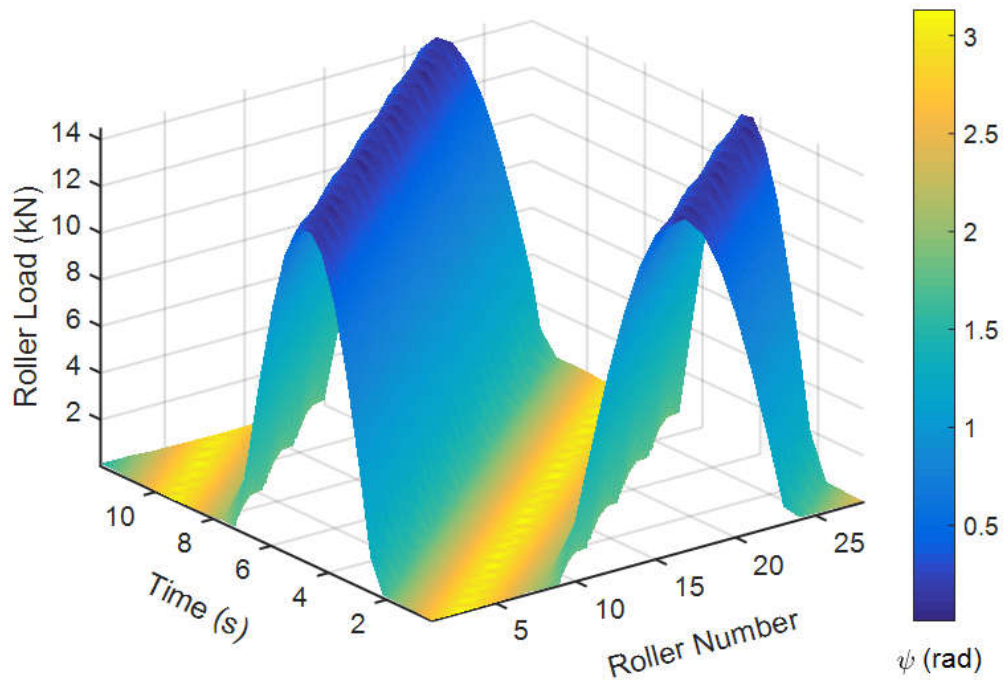


Figure 4.20–Variation of roller loads when subjected to 200kN rotating radial load on a stationary bearing.

Equally, Figure 4.21 shows the bearing load when the direction of rotation is reversed and Figure 4.22 shows the roller loads as a result of this loading condition. As expected, when the rotational direction of the load opposes the direction of the bearing rotation the loading cycles on the rolling easement are increased. That is, this condition is likely to degrade rollers performance quicker than when the load and bearing directions are in unison due to the higher number of load cycles.

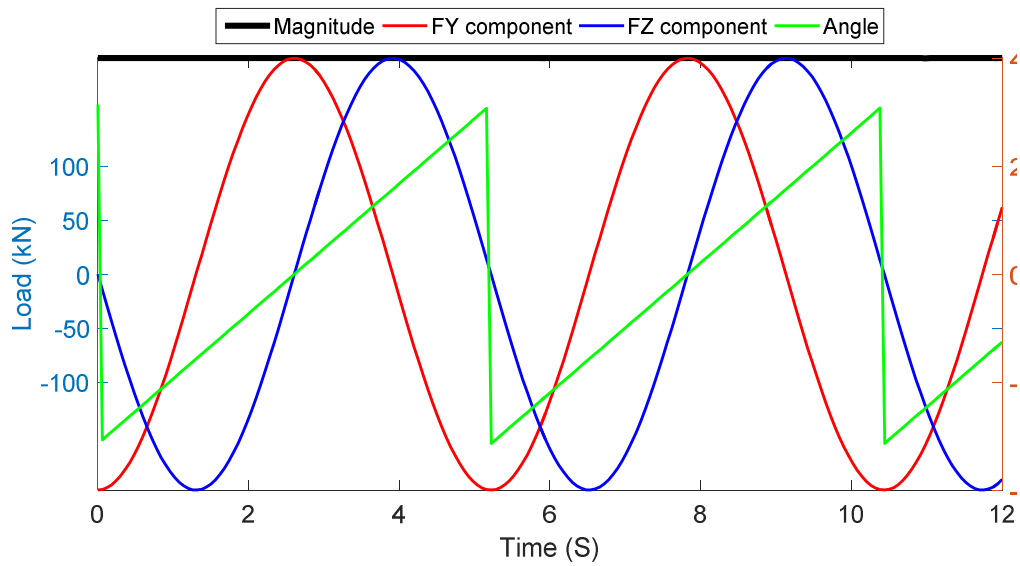


Figure 4.21– Loads on a bearing rotating at constant speed(reverse direction to Figure 4.19)
with constant rotation of radial load

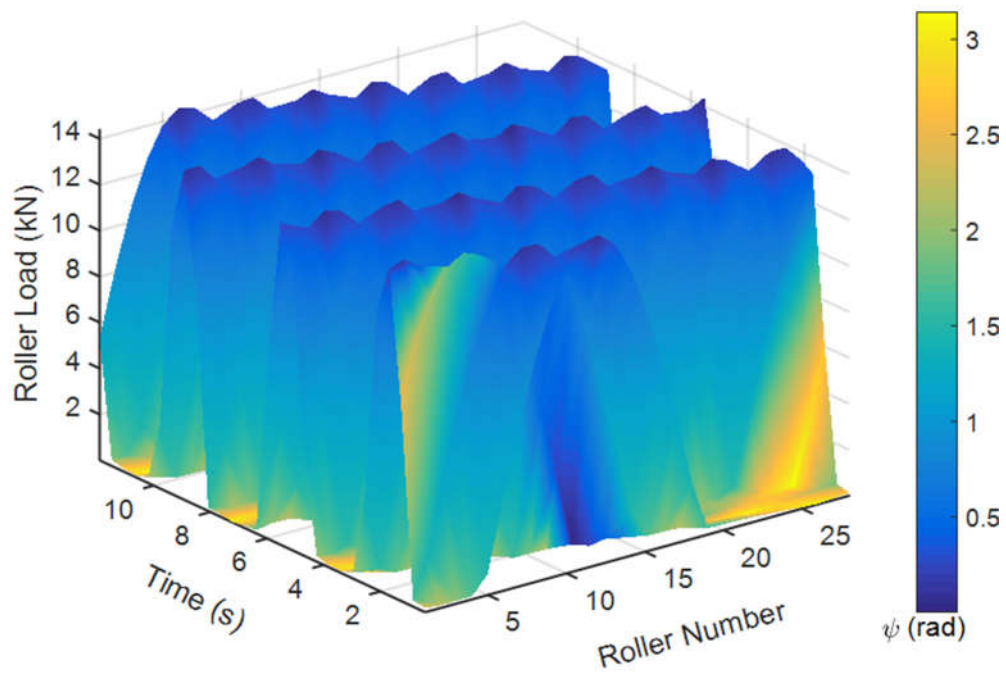


Figure 4.22–Variation of rolling element load when subjected to 200kN of radial load and
5kN axial force

Race rotation and load rotation in opposite direction results in a higher frequency which is akin to when the rotational direction of the load is in the same direction as the raceway but at a higher rotational speed.

Where the rotation speed is twice the rotational speed of the inner race and is in the same direction as shown in Figure 2.23 there is an increased number of load cycles per roller in the given time as shown in Figure 4.24. Consequently, a higher number of roller load cycles can be achieved with a smaller frequency if the rotations are in opposite directions.

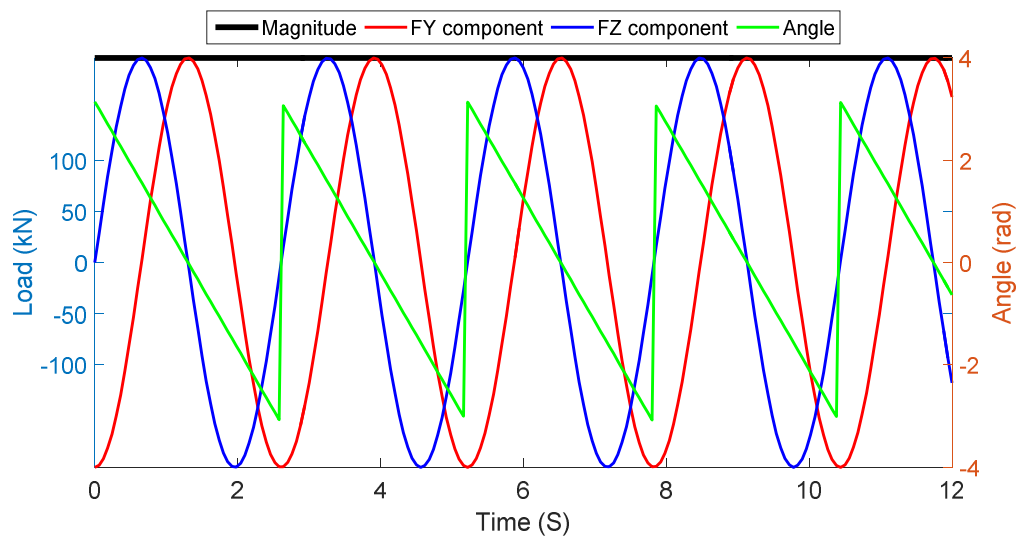


Figure 4.23– Loads on a bearing rotating at constant speed(twice the speed of Figure 4.19) with constant rotation of radial load

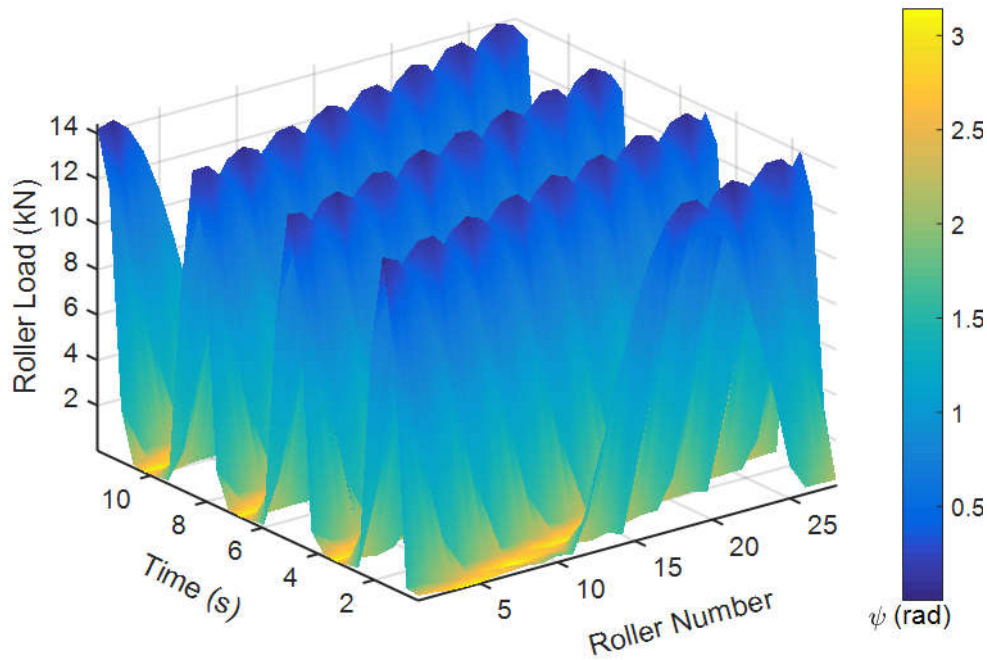


Figure 4.24–Variation of rolling element load when subjected to 200kN rotating radial load and twice the rotating frequency

4.3.3.3 Dynamic forces on rotating bearing

The control goal of many tidal turbines is to maintain a constant torque. The fluctuation in the flow field causes fluctuating in main bearing speed as well as the bearing's load. Unlike the scenarios shown above, the rotational speed in tidal turbines varies temporally just as much as the load it carries.

Figure 4.25 shows a randomly generated bearing load. The load varies both in terms of magnitude and direction and these values change rapidly over time.

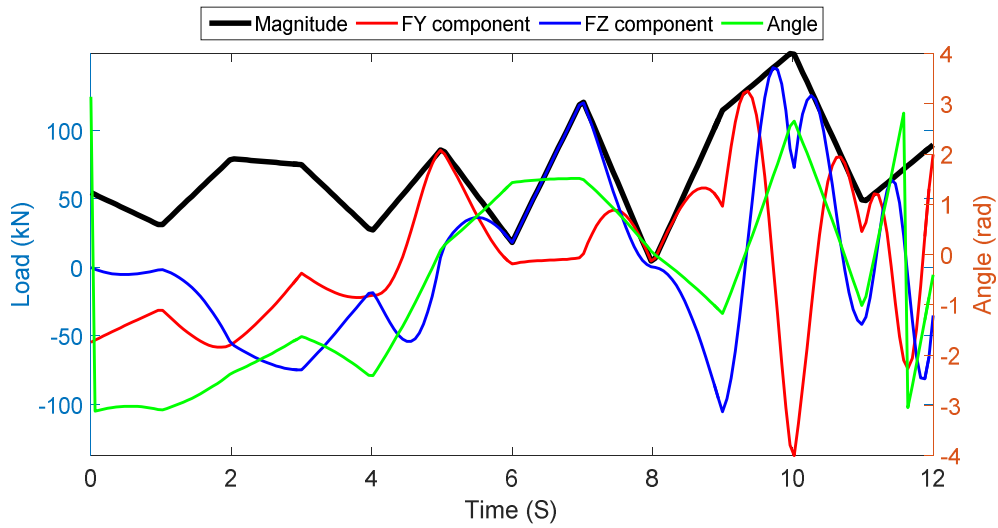


Figure 4.25–Random dynamic bearing load

As the bearing rotates and the loading directions and magnitude behaves in a random fashion there is no clear method to establish the load carried by a roller in time. Consequently a time domain analysis is needed to resolve the roller loads over time.

As shown in Figure 4.26 a complex surface is formed by the roller loads under the loading the loading conditions in Figure 4.25. As expected, at each point in time, the maximum load is carried by the roller located closest to the direction of the resultant radial load.

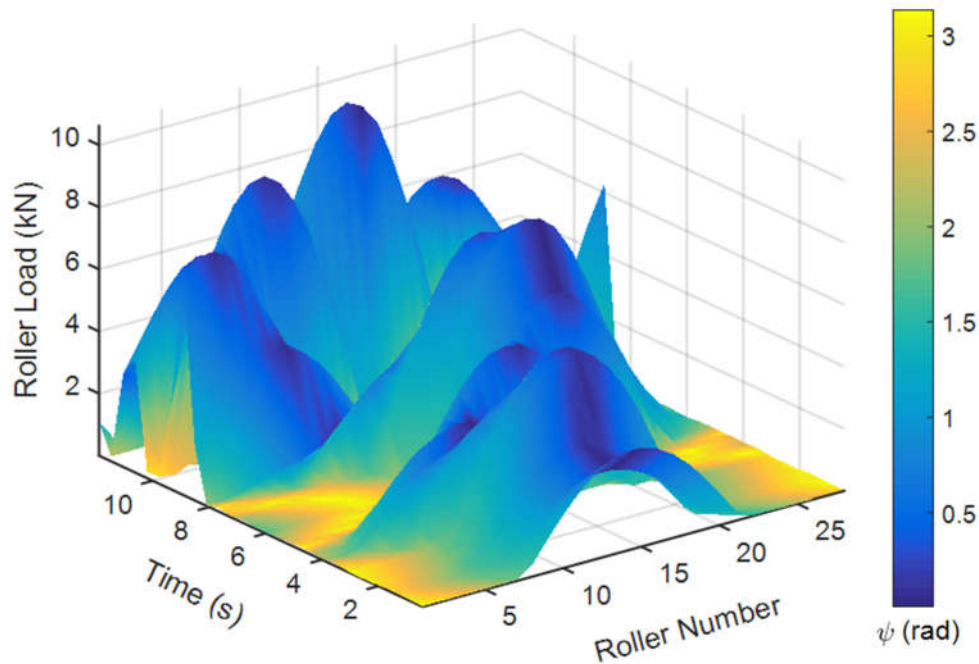


Figure 4.26–roller loads under random dynamic loads

Tidal turbine bearing loads are more akin to this type of highly dynamic load as shown in Chapter 3. In this case the rotation speed of the bearing may also fluctuate resulting in a more complex roller load over time. In addition to load (Force) information, the dynamic model delivers the displacements, velocities and acceleration of all the bearing components in a timely manner.

4.4 Particulate modelling

Table JIS SUJ2 Materials properties

property	Value	unit
Young's Modulus strength	210	GPa
Poisson ratio	0.3	-
density	7850	Kg/m ³
Yield stress	2.5	GPa
UTS	3.1	GPa

4.4.1 Contact modelling

Common Finite Element (FE) analysis packages solve equations of the form

$$[K]\{D\} = \{R\}$$

to determine deformations caused by a force or vice-versa. In some situations the equations may deviate from a set of linear equations into a set of non-linear equations of the form

$$[K(D)]\{D\} = \{R(D)\}$$

The primary causes of nonlinearity in FE models are either from Geometric or material nonlinearities. Force or displacement nonlinearities can also be achieved if a force is dependent on displacement or vice versa. Non linearity may exist in an FE model primarily due to material or structural nonlinearity. Material non-linearity effects are present in nonlinear elastic materials, viscoelastic materials, plastic region of linear elastic materials or due to creep.

A common problem where geometric nonlinearity plays a critical role is in the modelling of contacting bodies. Here the geometry of the bodies change as it displaces hence introducing geometric nonlinearity.

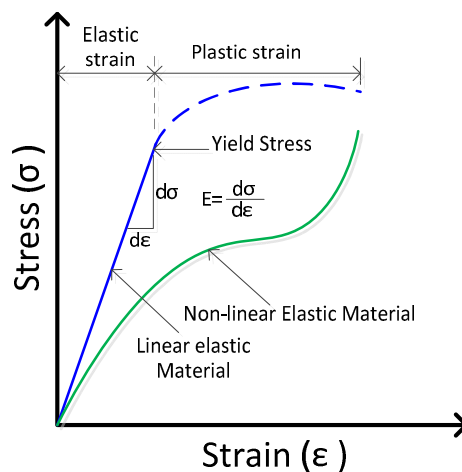


Figure 4.27– Stress-strain relationship of materials

While modelling the contact between a rolling element and a raceway, geometric nonlinearities are present but material nonlinearity is not expected. The JIS SUJ2 bearing steel is modelled as a linear elastic material thus stresses above its yield point will result in plastic deformation.

ANSYS Mechanical offers a range of contact models varying from penalty based to LaGrange and Augmented LaGrange.

The penalty based formulation resolves the contact forces as composed of a contact stiffness k_{normal} and displacement x_{normal} .

$$F_{normal} = k_{normal}x_{normal} \quad \text{pure penalty}$$

$$F_{normal} = k_{normal}x_{normal} + \lambda \quad \text{Augmented LaGrange}$$

The augmented LaGrange is less sensitive to the contact stiffness k_{normal} because of λ , however still allows the penetration of contacting bodies. The normal LaGrange method introduces a DOF for the contact and explicitly solves for the contact force F_{normal} .

$$F_{normal} = DOF$$

It achieves a better accuracy by enforcing a near zero penetration and thus achieves a more accurate contact force. The LaGrange method was used in this work because it offers more accurate results although it can be computationally more expensive.

The contact surface is given an asymmetric behaviour. This means contact surface is constrained from penetrating the target surface which is a requirement for the normal LaGrange method. The rolling element is set as the contact while the raceway is set as the target. A pinball region is defined to help establish the near and far regions of the contacting surfaces. In this work, the pinball radius was set to 1mm.

A common setup for FE models is aimed at finding the displacements (hence stress) caused as a result of an applied force. The nonlinear nature of contact problems however makes it challenging for the solution to converge when a force is applied.

To aid convergence, a displacement was specified instead force. The force reaction to the displacement is then analysed by the FE model.

Overall, to enable efficient use of computational results, the geometric symmetries of the roller bearing are exploited to reduce contacting bodies and the contact problem as a whole. Due to the symmetry between the two rows of the bearing, the contact solution for a single row is required. Similarly, the bearing exhibits circumferential symmetry which enables a single roller raceway contact to be analysed as shown in Figure 4.28. In a similar fashion, the single roller-raceways model, is symmetric about the centre of the contact. Since the inner race –roller contact is being investigated, this section of the contact is selected and analysed further. In this model, the high stresses area forms a small part of model where the contacting bodies meet.

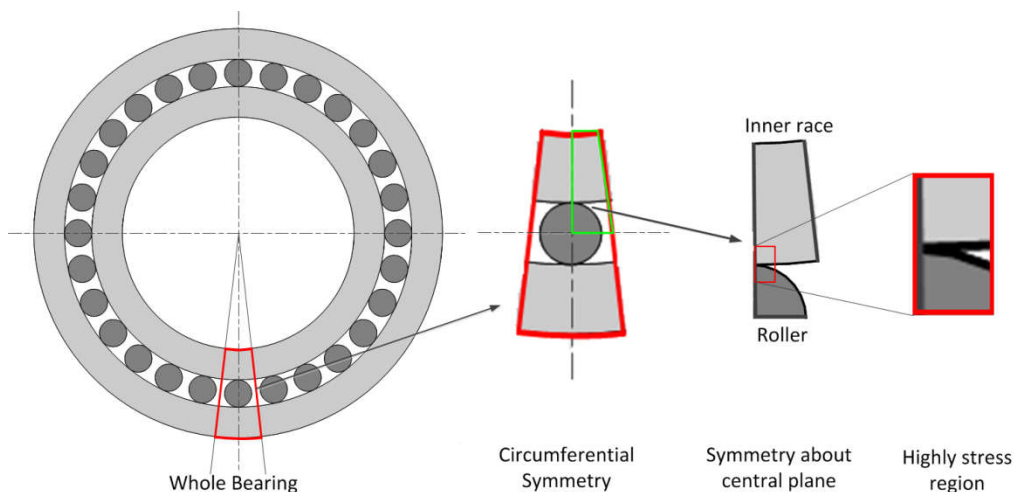


Figure 4.28– Symmetries of Finite Element Model of Contact

To achieve a more accurate result, the meshing of the contact focuses in achieving a high mesh density at the contact point and the area of highly stressed material. Applying symmetry to the model significantly reduces the number of mesh nodes/elements required. Figure 4.29 shows an inner race-roller contact models. In Model A-1toA-5 the whole contact is modelled while B-1 to B-3 was modelled by enforcing a symmetry boundary condition about the centre.

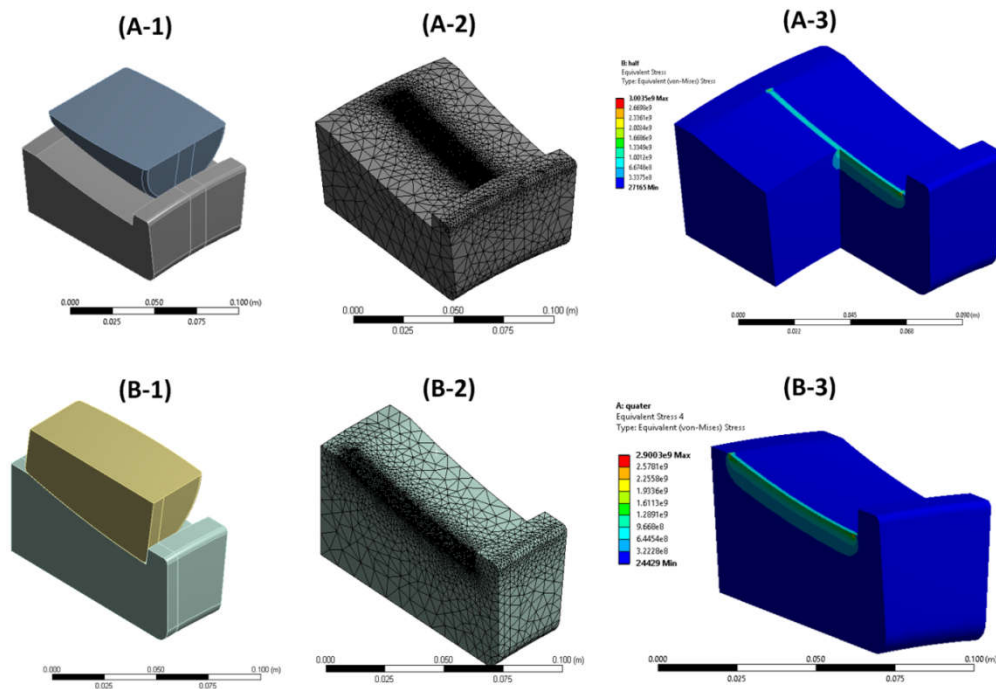


Figure 4.29– Symmetries of Finite Element Model of Contact

A comparison of the force response due to the displacement of the roller is shown in Figure 4.31. As the symmetric model contains half the contact the force response is multiplied by 2. This shows good agreement with the model of the whole contact model.

4.4.1.1 General model boundary conditions

The primary objective of this model is to analyse the contact problem to obtain a force-stress relationship. As such, the contact conditions have been described in more detail above. In addition to these contact conditions, additional Boundary Conditions (BC) have been imposed to ensure proper behaviour of the model.

A General joint is placed between the roller and Ground Figure 4.30-a. This allows loads to be applied uniformly across the highlighted face (shown as green) in Figure 4.30-a. A symmetrical boundary condition is also imposed along the length of the roller and raceway to enforce the geometric symmetry. Finally, a zero displacement condition is enforced at the inner races as shown in Figure 4.30-c. Figure 4.30-d shows where the frictionless contact elements were applied.

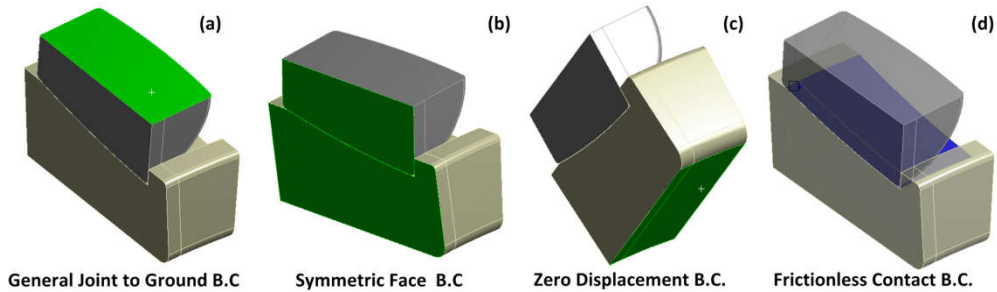


Figure 4.30– Summary of applied Boundary Conditions (B.C.)

The general Joint applied on roller enables 6 DOF loads or displacements to be applied to the roller. The rotational degrees of freedom of the general joint were constrained such that only the translational DOFs are activated. To improve the computation of the contact problem, contact displacements were specified rather than the contact force. Figure 4.31 shows the force response as a result to the applied displacement.

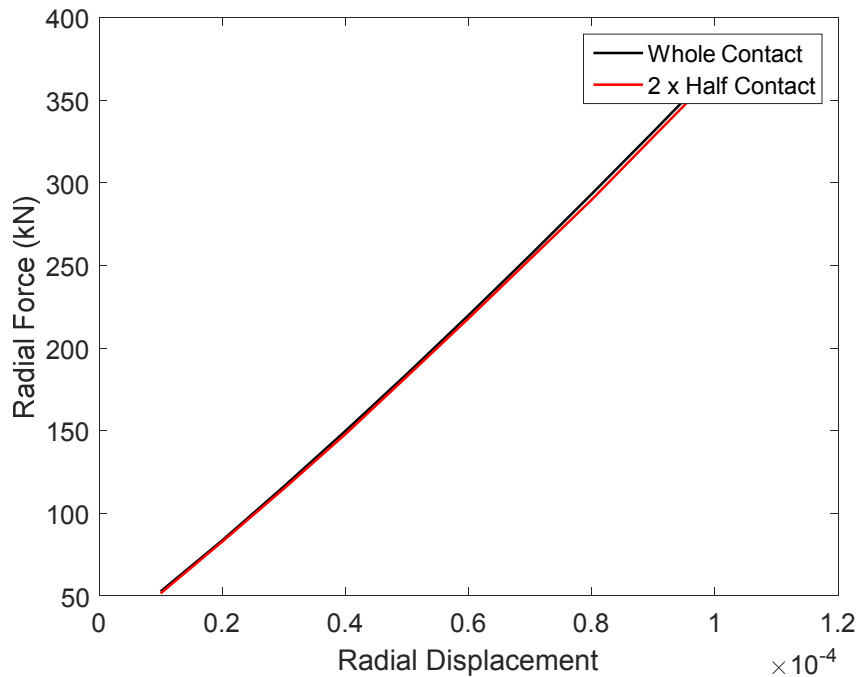


Figure 4.31– Comparison of roller loads in whole contact model and half contact model

4.4.2 Contact modelling results

The contact between the rolling element and the race way is modelled as a frictionless contact as described in section 4.3.1 . With the frictional coefficient $\mu = 0$, the tangential force reduces to zero and the whole contact area is sliding. Figure 4.32 shows the contact condition of a rolling element inner race way contact, showing a fully sliding contact. The frictionless contact conditions make the model more akin to Hertzian contact conditions.

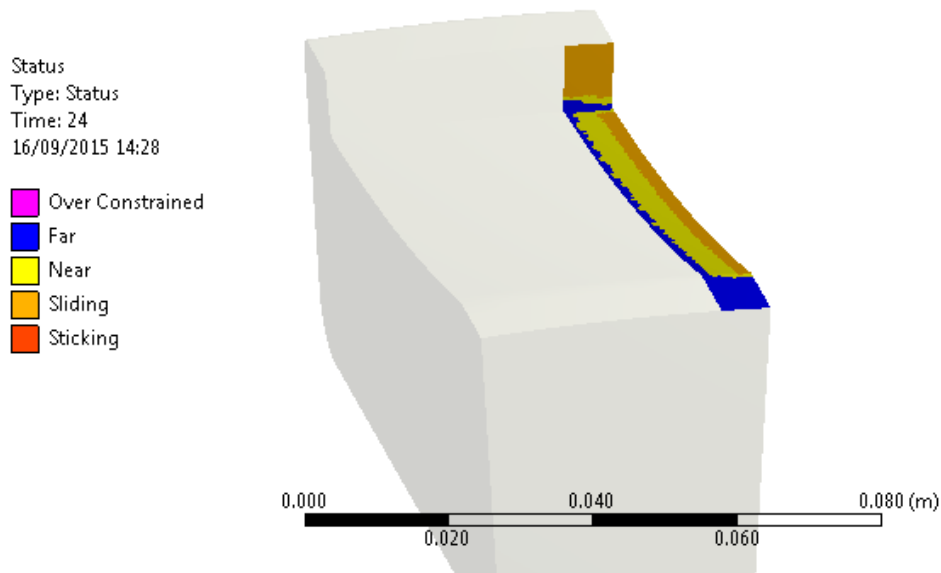


Figure 4.32–Contact implementation

The load distribution along a typical spherical roller bearing contact is expected to follow a progression as shown in Figure 4.33. Due to the geometry of the 230/630-W33 series bearing the contact area is akin to Figure 4.33b because both contact surfaces have the same curvature. Figure 4.33c is also difficult to reproduce in a self-aligning bearing unless the bearing is severely misaligned.

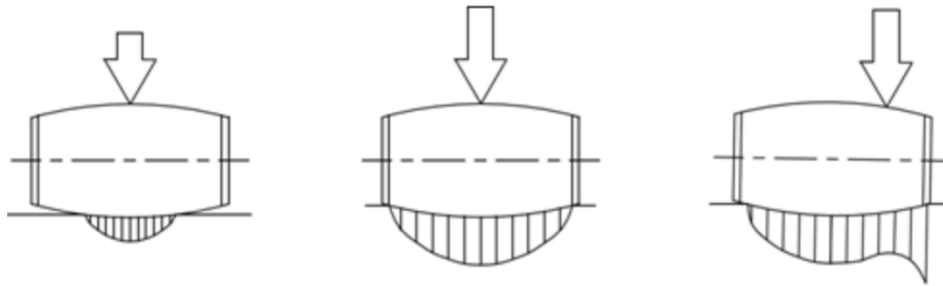


Figure 4.33–Increase of contact length with roller load

4.4.2.1.1 Stiffness evaluation

The applied displacement of the roller causes a force reaction. This force is distributed along the length of the roller and is dependent on the geometry of the contacting bodies. The contact stiffness is defined from the mutual approach δ and the applied force F_N by

$$k_c = \frac{F_N}{\delta}$$

The force stress relationship was analysed for the bearing using a finite element code. A comparison of the contact stiffness of the FE model and Hertzian approximation of the contact stiffness obtained by (EQN 2.48) is shown in Figure 4.34. In general, the Hertzian contact stiffness equation is approximate for ideal line contacts. The complex geometry of the roller and raceway curvatures is such that the contact of the roller and the inner race can be elliptical at low forces and progress to a full line contact at higher loads.

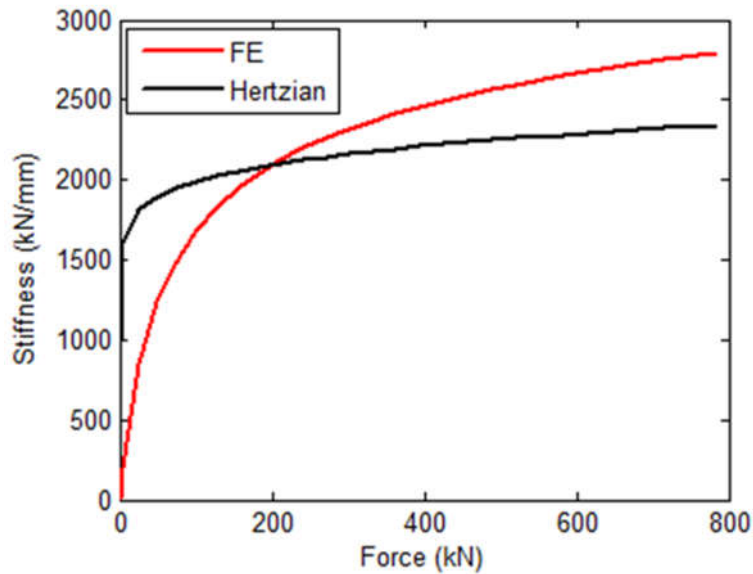


Figure 4.34–Variation of roller contact stiffness with applied force

The contact stiffness is vastly influenced by the size of the contact area. In the Hertzian case deflections along the line contact are assumed to be equal due to the elastic half space assumption. However in the Finite Element case, there is a clear variation of deformation along the length of the roller. Edge loading also plays a vital role here too but Hertzian theory ignores this phenomenon.

The stiffness of the rolling element inner race contact is highly nonlinear just as expected. For most loads however, Hertzian contact stiffness approximation differs significantly from the FE results. The Hertzian case assumes an evenly distributed load along the length of the contact. In the finite element case however, the deformations of the contacting bodies lead to a big variation in the lengthwise load distribution along the length of the roller.

Hertzian theory assumes elastic deformation occurs in the contacting zone while other parts of the body remains unreformed. Conversely, it is observed from the finite element model that far field regions undergo deformations due to the contact as shown in Figure 4.35. The resistance of these contribute to the higher stiffness for the FE model compared to the Hertzian approximation.

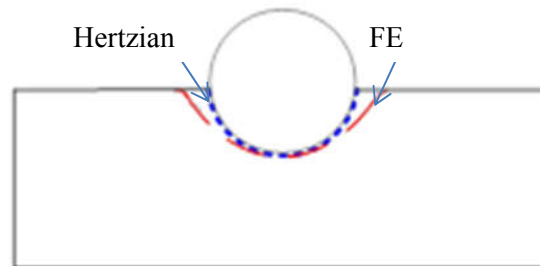


Figure 4.35–Hertzian vs FE contact deformation

4.4.2.1.2 Contact stress evaluation

The key aspect for performing an FE modelling is to evaluate the potential stresses which occur in a rolling element due to the rolling contact. Hertzian theory can be obtained for 2-dimensional approximations, however a 3D model of the contact delivers the solution to phenomena such as edge loading which may be detrimental to bearing life. The stress can be easily compared to the 2-D Hertzian approximations by considering the contact can be divided into annuli as shown in Figure 4.36. Figure 4.36 A-1 to C-1 show the locations of the considered annulus in the lengthwise direction. Figure 4.36 A-2 to C-2 show the 3D view of the contact annulus and Figure 4.36 A-3 to C-3 show the highly stressed area which is of interest in this work. In the lengthwise direction of the contact, the maximum stress in each annulus is considered.

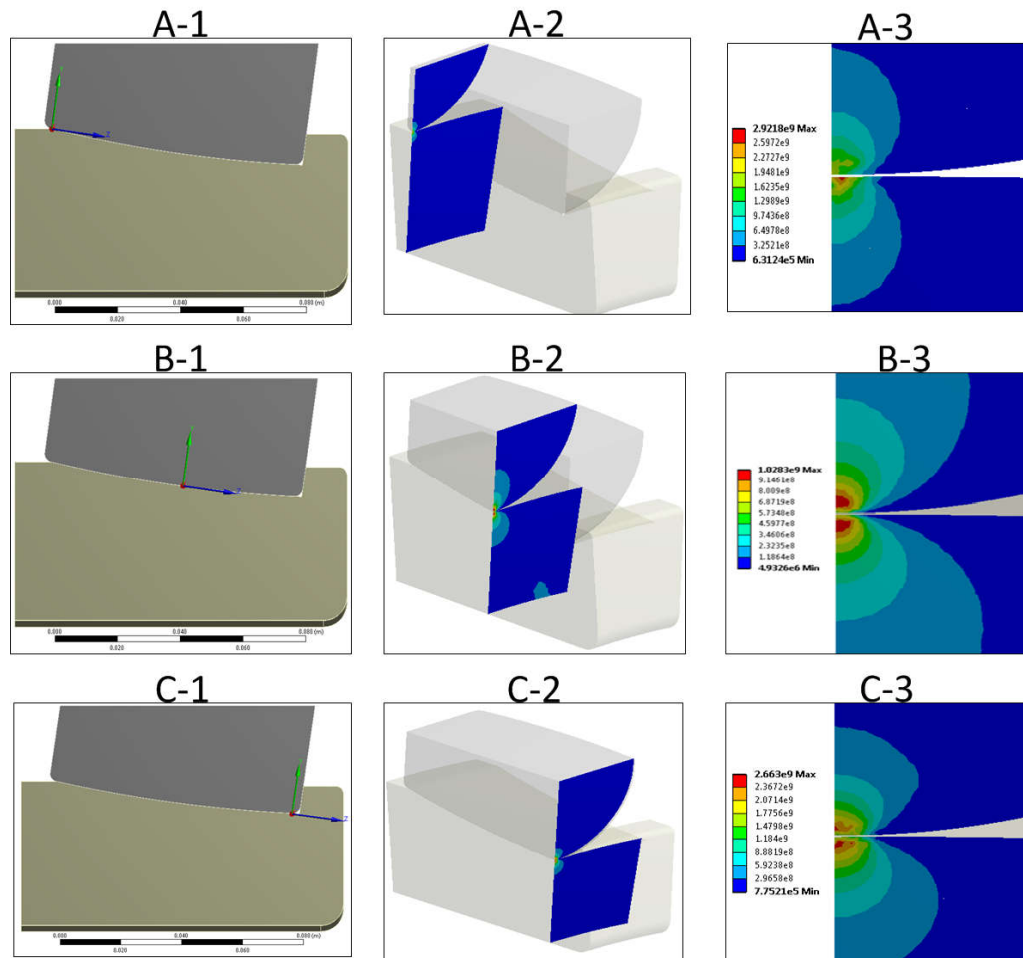


Figure 4.36–Contact Annuli

Due to the small contact area, an immense contact pressure is induced in contact area even for small loads. Unlike the 2D Hertzian predictions, the pressure in the contact surface changes in the lengthwise direction as shown in Figure 4.37. Here the contact pressure also peaks at the edges because of edge loading. Along the length of the roller, one might expect the contact pressure in each annulus to occur in the middle of the contact. Although this was generally true in the middle of the roller as shown in Figure 4.37b, there are some regions where the maximum pressure in an annulus deviates due to deformation of the material

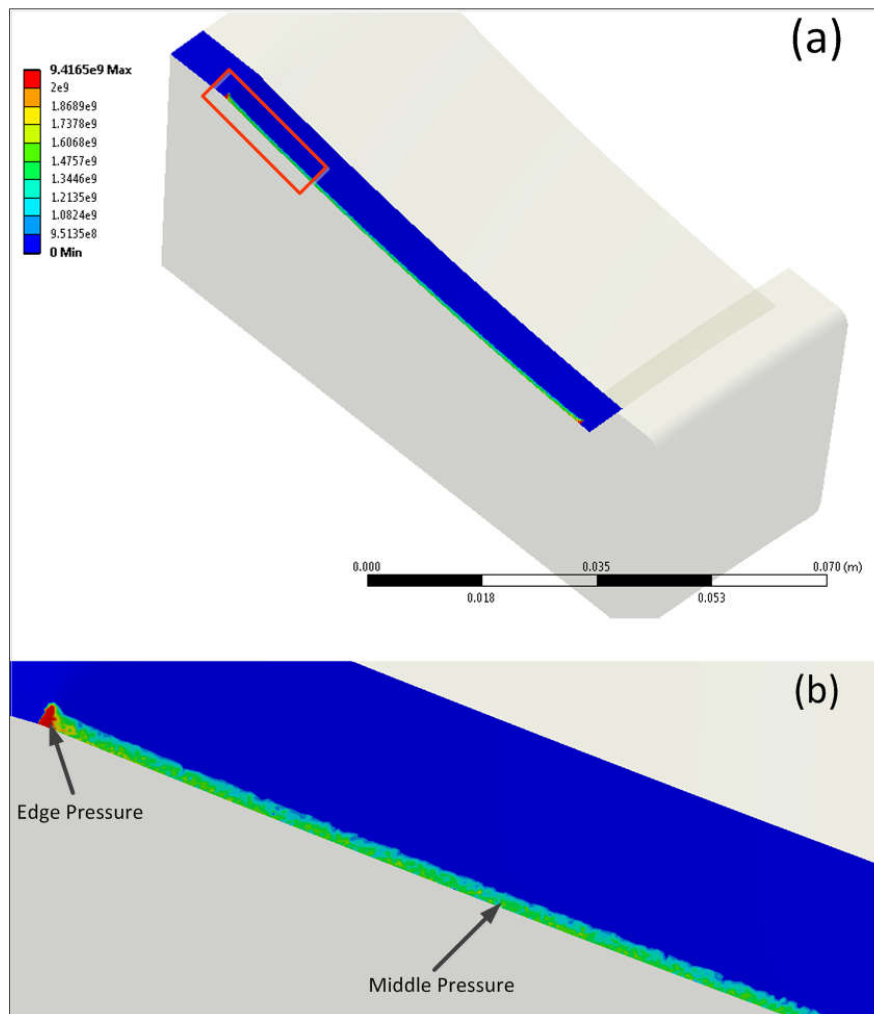


Figure 4.37—Contact pressure at 160 kN roller load

The stress state in the middle parts of the contact agrees well with Hertzian approximations. In general practice the maximum shear stress and the depth at which this occurs is a figure of interest as this is where failure is most likely to occur. This has been shown to also agree well with theoretical predictions as shown in Figure 4.38 when a fine FE mesh is used.

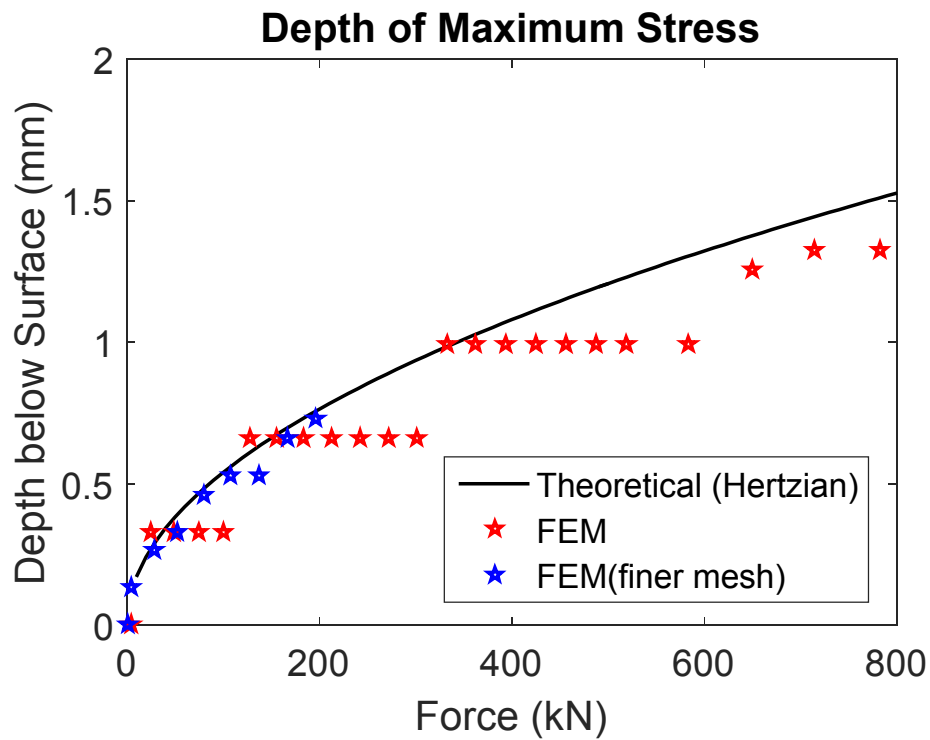


Figure 4.38– Location of the Maximum Stress

The normal stress in the circumferential direction as shown in Figure 4.39a. Figure 4.39b shows the variation of the Normal stress across the surface of the inner race in the circumferential direction. As shown in Figure 4.39, the normal stress peaks at the centre of the contact and reduces down till it reaches areas which are not in contact.

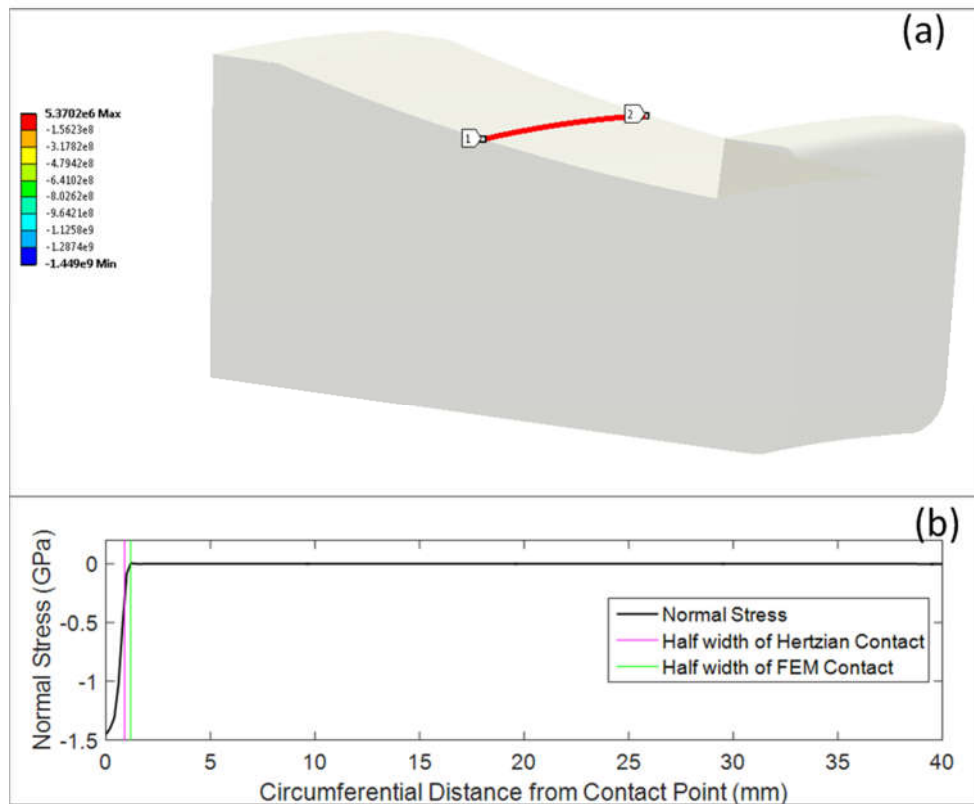


Figure 4.39–Normal stress on an annulus of the inner race surface when under a 160 kN load

While Hertzian contact theory assumes the infinite half space assumption leading to plane stresses, the FE model includes a lengthwise variation of stresses. The lengthwise variation of stresses is presented in Figure 4.40 to Figure 4.43. The von-Mises equivalent stresses at the middle of the roller are shown in Figure 4.40. A comparison of the normal stresses in the middle of the roller is also provided in Figure 4.41. When compared to Figure 4.42 (edge A) and Figure 4.43 (edge b) which shows the von-Mises stress at the edges, it can be observed that the maximum stress is closer to the surface due to edge loading. This may result in the initiation of surface initiated failure modes.

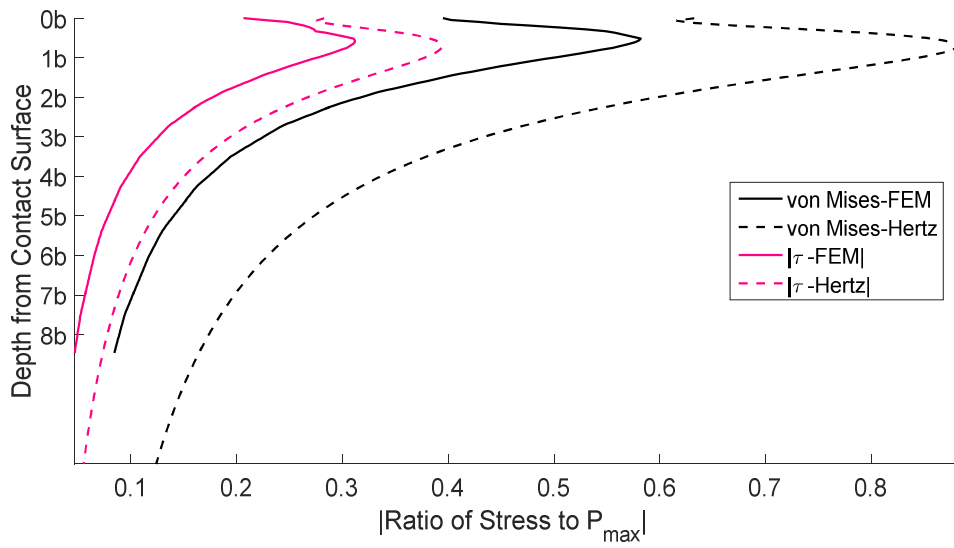


Figure 4.40–Comparison of FEM and Hertzian predictions of subsurface stresses at the middle of a roller

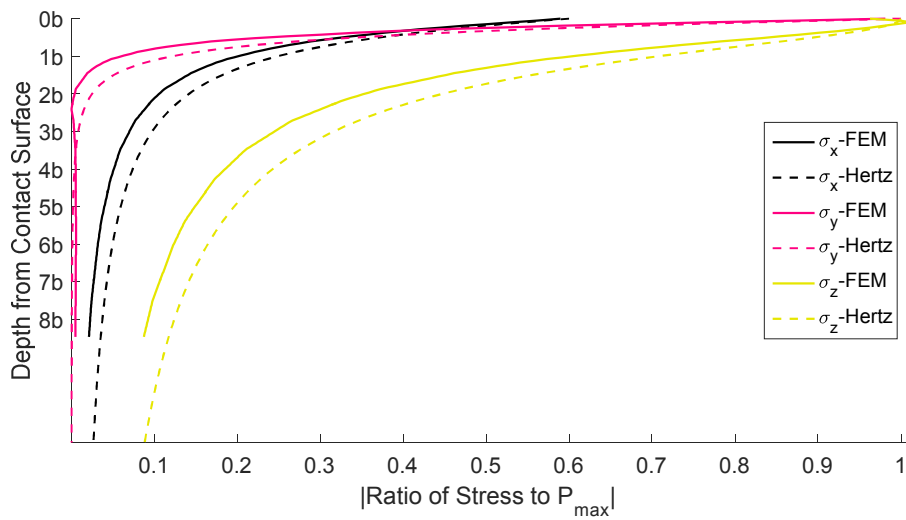


Figure 4.41– Comparison of FEM and Hertzian predictions of subsurface plane stresses at the middle of a roller

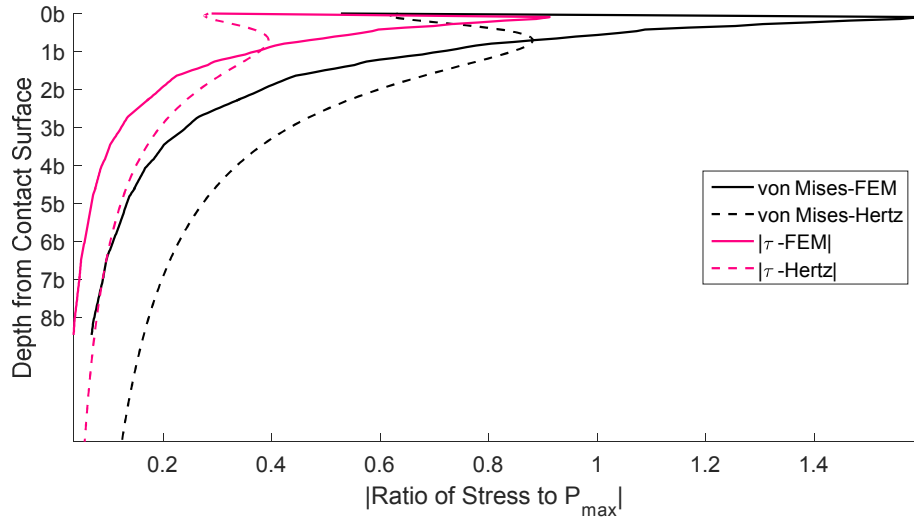


Figure 4.42– Comparison of FEM and Hertzian predictions of subsurface stresses at edge A of a roller

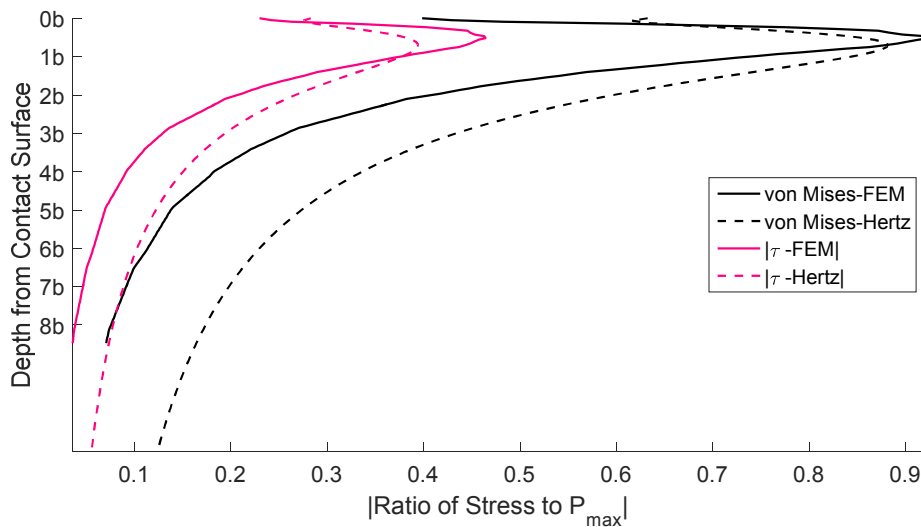


Figure 4.43– Comparison of FEM and Hertzian predictions of subsurface stresses at edge B of a roller

Figure 4.45 shows the lengthwise stress variation in the rolling element when subjected to 390kN load. The highest stresses are located in the positions A and B as shown in the aforementioned figure. These are located at the edges of the roller-

raceway contact. Clearly, despite the roller being crowned, edge loading has not been avoided. From Figure 4.44 it can be seen that the maximum stress at edge A occurs at the surface of the inner race while the maximum stress is subsurface for edge B. This arises as the sharp edge (highlighted in green box) causes a stress concentration. In practice this edge will have a fillet to avoid stress concentration. On edge B, the maximum stress is located subsurface within a region of highly stressed material. Unlike the other edge of the contact, the inner race surface is flat at edge B thus the expected contact conditions are met.

Figure 4.44, compares the stress in the edge A vicinity to the edge B vicinity to Hertzian approximation and the stress which occurs in the middle of the roller. In addition the stress histories of a points A_i in the edge A region and B_i in the edge B region have been compared.

The stress in points A_i and B_i agree well with each other and the maximum load in the edge B area. The maximum stress in the 'edge A' area far exceeds the other stresses due to the stress concentration brought about by having a sharp edge in contact. The maximum stress in the middle annulus of the roller is well below the stress at the edges and what is predicted by Hertzian approximations. This arises because the contact load is not distributed evenly along the length of the roller but has higher concentration around the edge and lower concentration in the middle. On the other hand, the Hertzian approximation uses approximate geometry as well as assumes the contact is symmetrical in the lengthwise direction and infinitely long thus avoids edge loading.

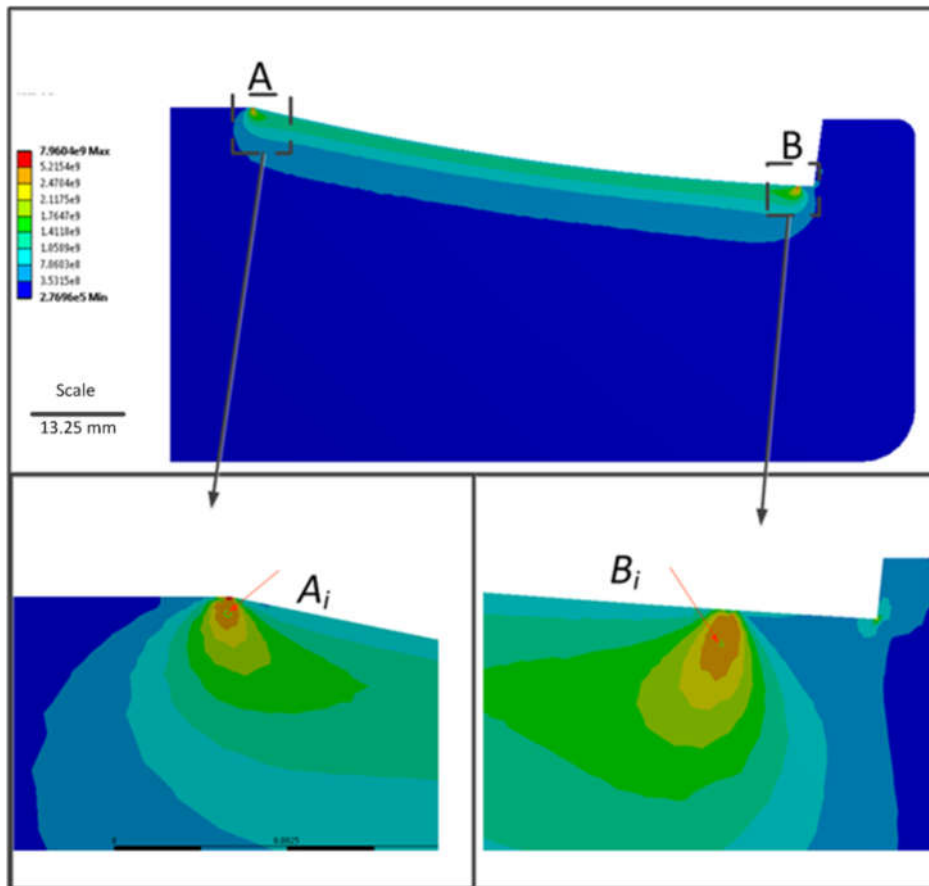


Figure 4.44—von-Mises stress variation along the length of the roller. This shows there is a very high stress concentration at both ends of the roller (i.e edge loading).

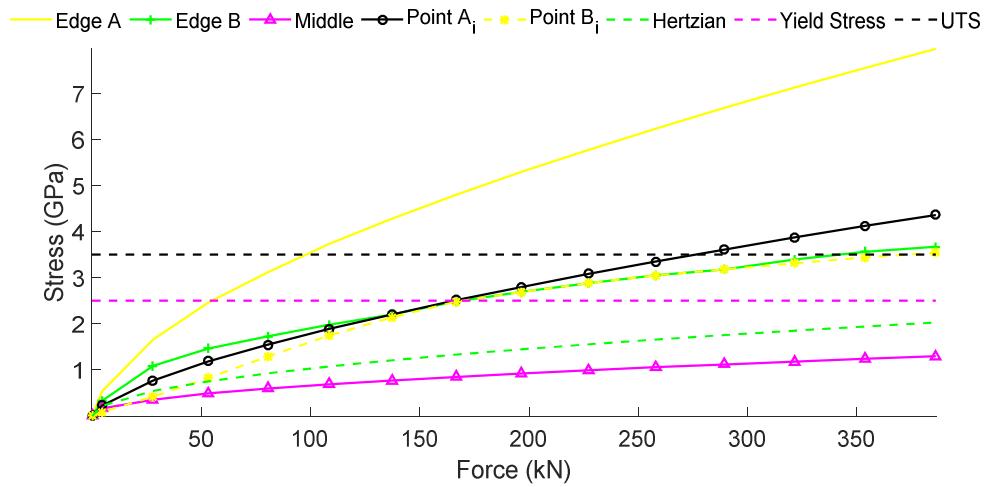


Figure 4.45– Comparison of force stress relationship (FE-mid: stress at middle of rolling element, FE- edge: edge loading, Hertzian: stress as calculated by (EQN 2.37)

In practice, bearing micro-geometry modifications are performed by bearing manufacturers with the aim of reducing the edge. In a specialised application such bearings used in main bearings, bearing manufactures will apply these modifications which are commercially sensitive and therefore, not available for this analysis. Never the less, there is no clear process to proving that the edge loading stresses will be reduced for general applications. Consequently, the limiting stress is taken to be the maximum von-misses stress seen at the edge B side of the bearing.

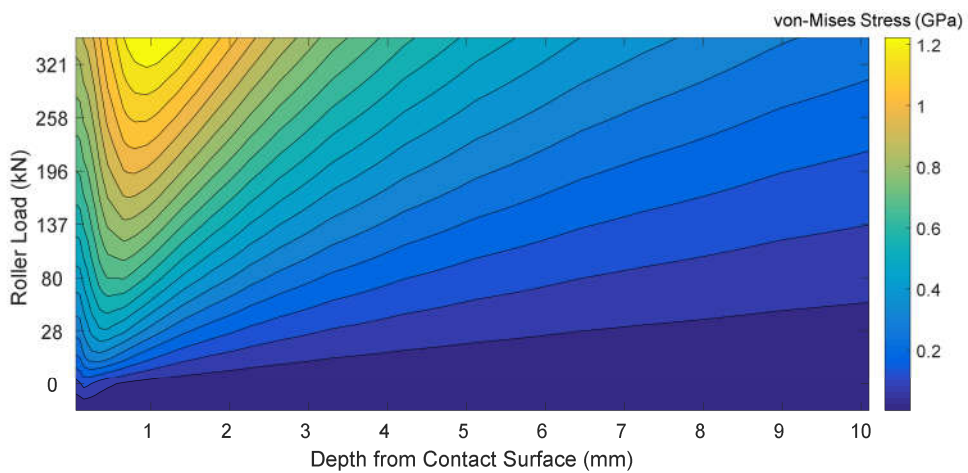


Figure 4.46–stress changes with load and distance from contact point

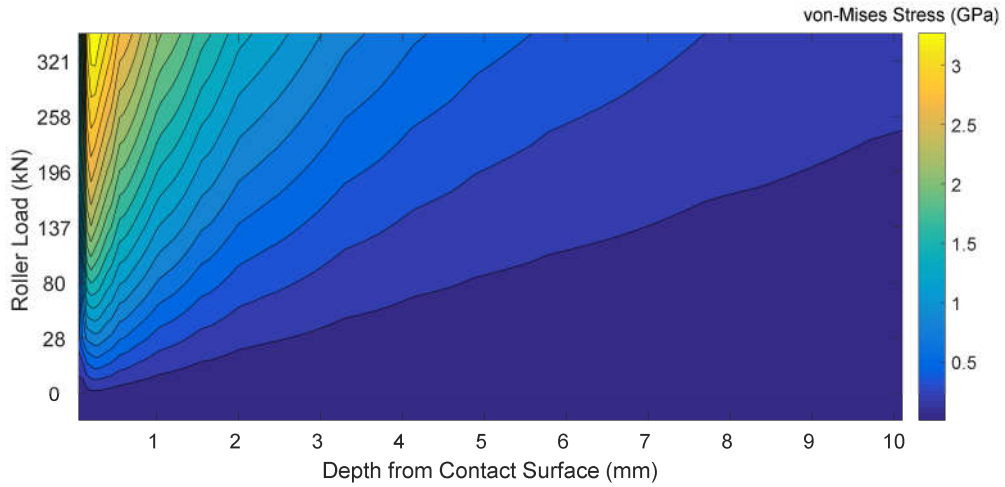


Figure 4.47–stress changes with load and distance from contact point

4.5 Bearing Damage Assessment

Lundberg and Palmgren[158] considered the probability failure of bearing rings subjected to a number of repeated loading cycles N , is given by

$$\ln\left(\frac{1}{S}\right) \propto \frac{N^e \tau_0^c V}{z_0^h} \quad (\text{EQN 4.3})$$

Later, Ioannides and Harris [187] proposed a model for evaluating bearing life which takes the same approach Lundberg and Palmgren however considers the bearing to consist discrete material volumes which have their own probability of survival. The probability of survival of the whole bearing thus can be evaluated by:

$$\ln\left(\frac{1}{S}\right) \approx \bar{A} N^e \int_R \frac{(\sigma - \sigma_u)^c}{z^h} dV, \quad \sigma > \sigma_u \quad (\text{EQN 4.4})$$

Here, σ is the stress that depth z . While σ_u is a fatigue limit stress and A and c are empirical constants. With this development, the stress is not limited to the orthogonal shear stress but can be another stress measure such as the equivalent von Mises stress.

This work aims to analyse the damage caused by loading on bearing inner race by using the von-Mises stress. The inner Race is considered to be made of elemental volumes which have their own probability of failure which can be obtained by a strict series reliability model. As it follows, the inner race of the main bearing in question is divided into elemental volumes as shown in Figure 4.48.

The inner race is discretised by dividing the surface of the inner race in the circumferential direction (from 0 to 2π). That is, the inner race is discretised into elemental volumes, defined by the width of the strip in the circumferential direction, the length of the raceway in the lengthwise direction and the thickness of the raceway in the radial direction. For simplicity this volume is called strip from here on.

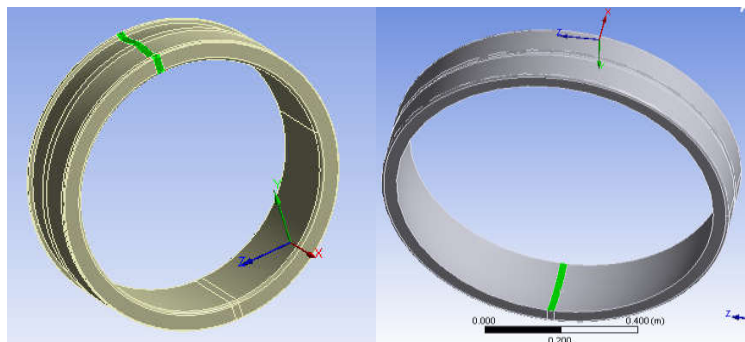


Figure 4.48: division of components into sections

The stress history for each strip is of interest as the stress history will lead to eventual failure. As the rolling motion is observed, individual strips encounter different stresses caused by the applied load. The rigid dynamics model as described in 4.3.1 determines the load on bearing components as well as their location in space. This enables the contact points to be traced through time along with the contact load. The loading history on each section can therefore be analysed to determine the damage on the individual section.

At a constant speed and load, the variation of load thus stress is constant and the frequency of the loading can be determined by the so called ball pass frequency. The stochastic nature of the tidal turbine loads however lead to uneven loads and

speeds on the bearing. Consequently it is impossible to evaluate the loading histories on each strip based on simple geometrical relationship.

Section 4.3 discussed how the loads on a spherical roller bearing used in a configuration as discussed in chapter 4.2 can be analysed using a rigid dynamics model. Chapter 4.4 discussed how the loads from Section 4.3 can be converted into stress in the bearings. The final step required is to identify a mechanism through which the stress induced on each strip by each roller-raceway contact can be identified and aggregated.

4.5.1 Stress aggregation in elemental bearing inner race volumes

The raceway-roller contact induces stress in the vicinity of the contact area. As seen from Figure 4.50 the stress changes both in the circumferential and radial directions defines as per Figure 4.49. The discretisation of the inner race into strips is performed in the circumferential direction. As it follows, the stress induced by a contact whose contact area falls within one strip will influence the stress on other strips.

It is clear and consistent that the stress induced in each strip peaks when the strip and the roller are directly in line as seen in Figure 4.50 for a roller load of 160 kN and for all load levels in Figure 4.38. The stress in each strip is considered to be the maximum under the contact surface as illustrated in Figure 4.46 and Figure 4.47. The maximum stress is located at different depths below the contact surface for each force.

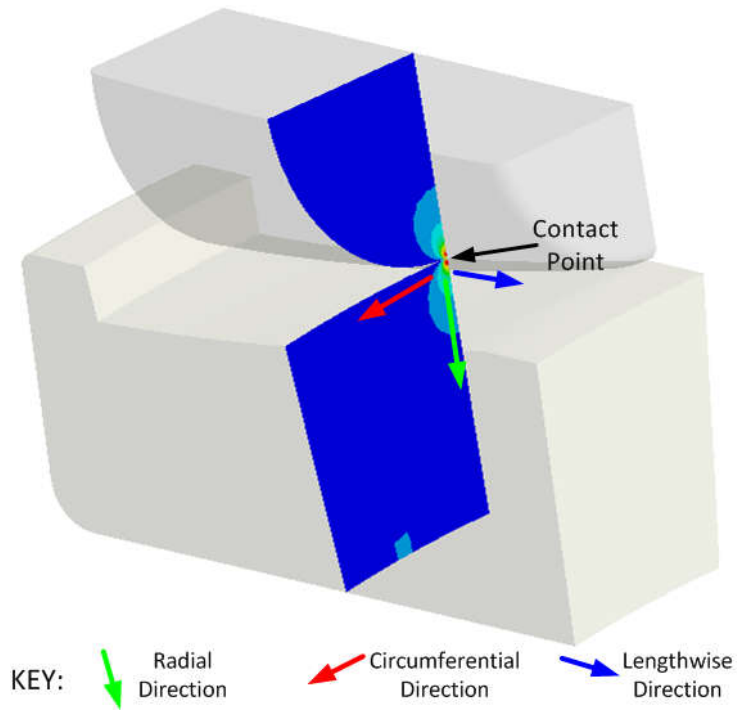


Figure 4.49–Coordinate system definition for roller raceway contact

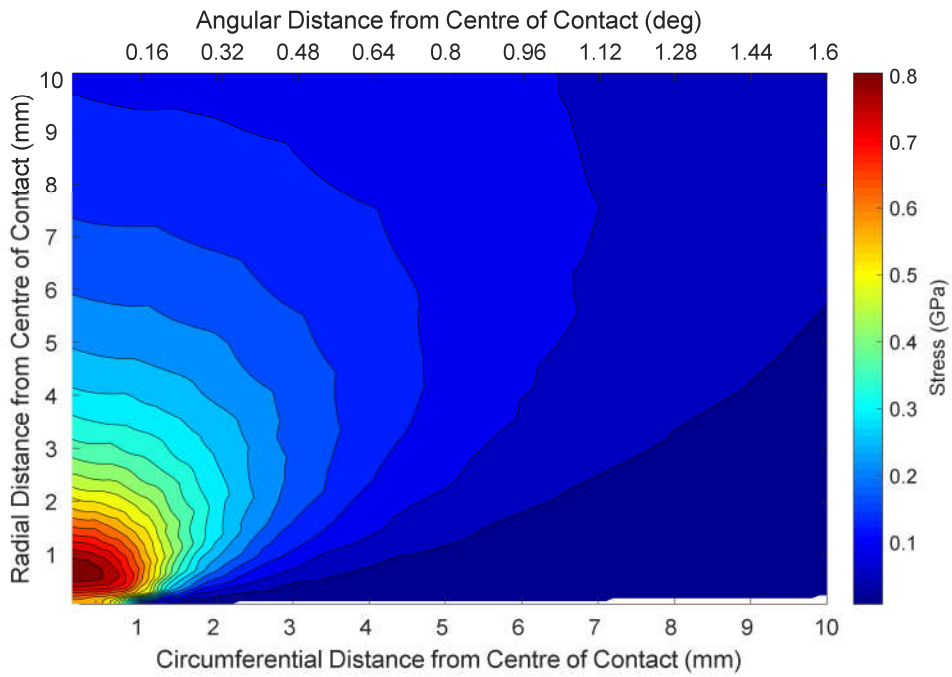


Figure 4.50–Variation of stress across contact showing the maximum stress is located subsurface and the high stress region is much smaller compared to the overall geometry

Notice that on the surface, the stress is very high at the contact point and rapidly drops off to a low stress state in the circumferential direction. Conversely, the circumferential stress variation from a much lower radius (i.e. subsurface of the contact) decays at a slower pace as illustrated Figure 4.51.

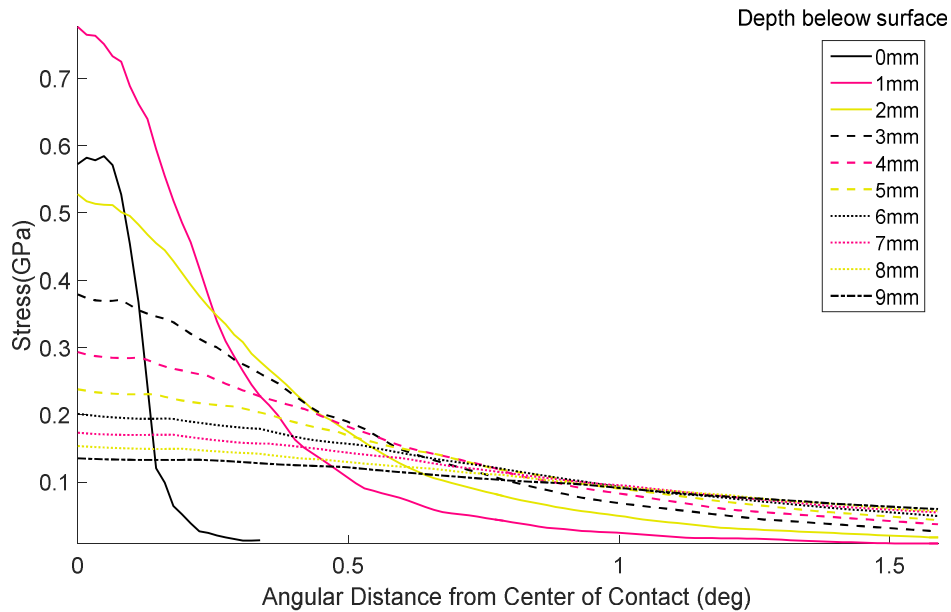


Figure 4.51–Variation of stress in circumferential direction for different depths when rolling element is subjected to 270 kN for force

Clearly, the stress variation in the radial direction of each strip is non-constant. In the interest of being conservative, the stress in each strip is assumed to take the value of the maximum stress in that volume bounded by the width (circumferential direction) of the strip, depth (radial direction) and the length of the strip (lengthwise direction). This maximum stress in each volume is shown by the blue stars in Figure 4.52 for a strip.

The near surface area experiences a higher stress range over a short angle distance as seen in Figure 4.51. Nonetheless in a far enough angular distance, the stress at higher depth also reaches near zero conditions. That is, the stress induced by a contact on distant strip is nearly homogenous across its depth and remains very low. As it follows, by considering the maximum stress induced on each strip the maximum range of the stress which is critical for fatigue life estimation is captured.

The circumferential variation of maximum stress (shown in blue stars in Figure 4.52) also changes with the applied load. This variation is depicted in Figure 4.53 for a range of roller loads. Increasing loads lead to increasing peak stresses as expected which then decay the farther away from the contact point.

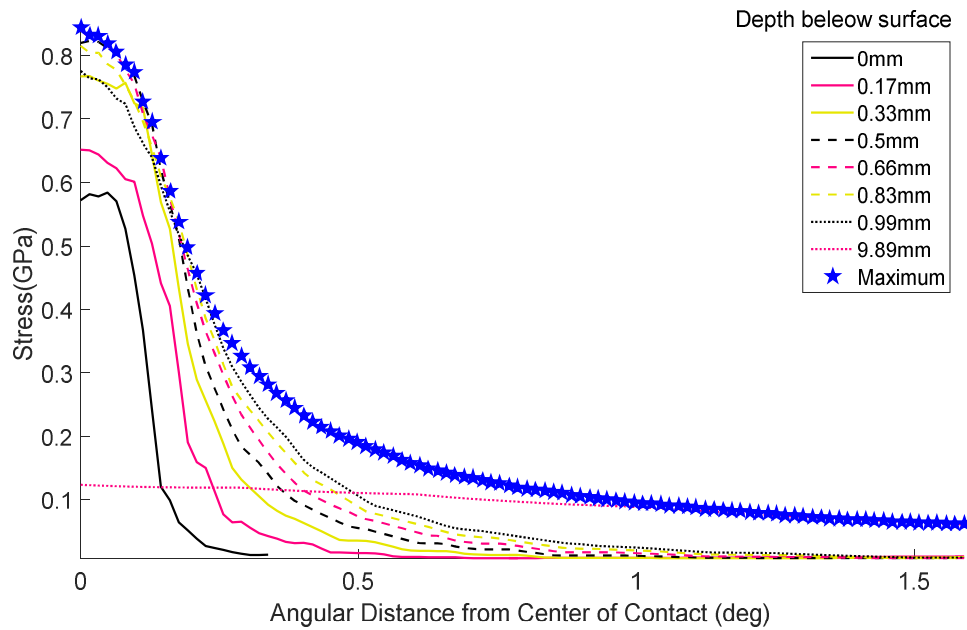


Figure 4.52–Variation of stress in the circumferential direction for different depths when rolling element is subjected to a variation of forces

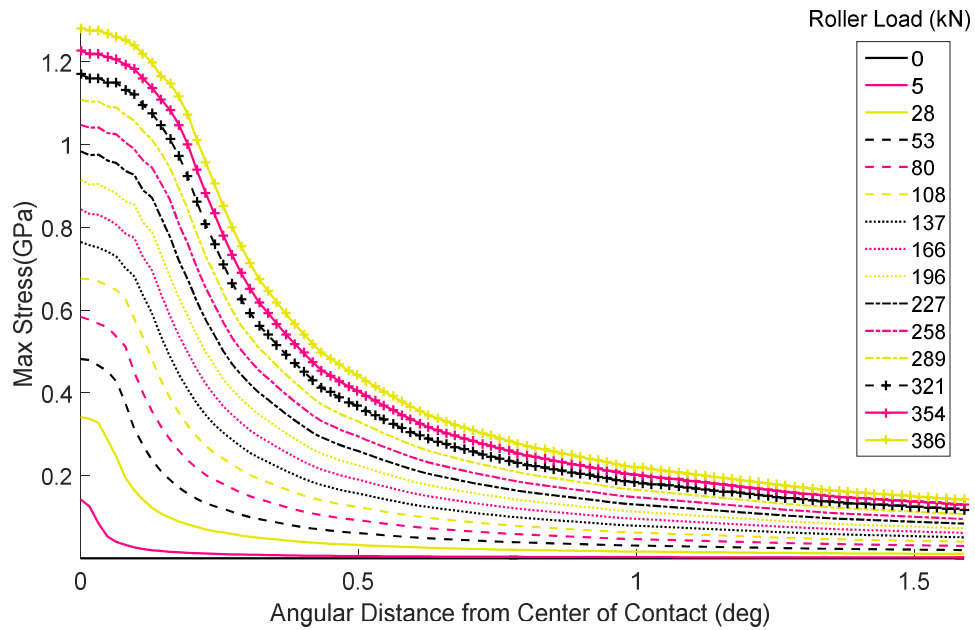


Figure 4.53–Variation of stress in circumferential direction for different depths when rolling element is subjected to 270 kN for force

To obtain a circumferential stress variation which generally describes the variation of the circumferential stress variation for all loads, Figure 4.53 is normalised. The stress is normalised with the maximum stress in each load level. Similarly, the circumferential angular distance is normalised by the depth of the maximum stress expressed as a quotient of the central circumference of the roller raceway. This leads a normalised stress as shown in Figure 4.54. Accordingly, the stress variation in each strip in the circumferential direction can be described by Figure 4.54.

Due to the complex shape of the stress profile in Figure 4.54, fitting a single equation to it remains very challenging. Consequently the shape is divided into two depending on the normalised angle. For normalised angles exceeding 1800, the stress variation is modelled by a two term exponential model given by:

$$\sigma_{Norm} = 1.209e^{(-0.0007293 \theta_{norm})} + 0.2762e^{(-0.0001279 \theta_{norm})} \quad (\text{EQN 4.5})$$

$$\sigma_{Norm} = 1.401e^{-0.07 \theta_{norm}^2} + 1.587e^{-0.05 \theta_{norm}} + 1.003 \quad (\text{EQN 4.6})$$

This enables the complex stress variations in the circumferential direction of the inner races to be modelled accurately with (EQN 4.5) and (EQN 4.6) as shown in Figure 4.55.

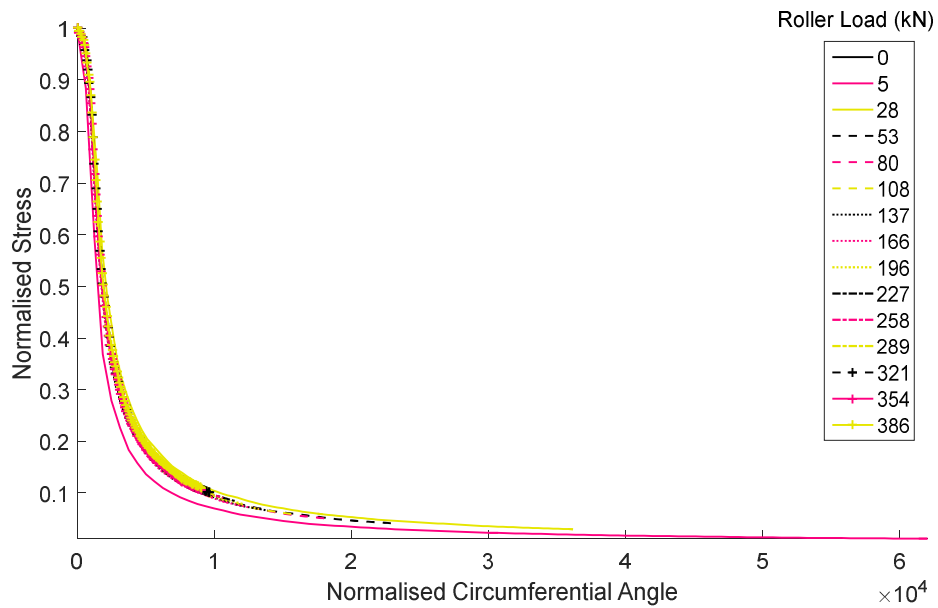


Figure 4.54–Variation of stress in circumferential direction for different depths when rolling element is subjected to 270 kN for force

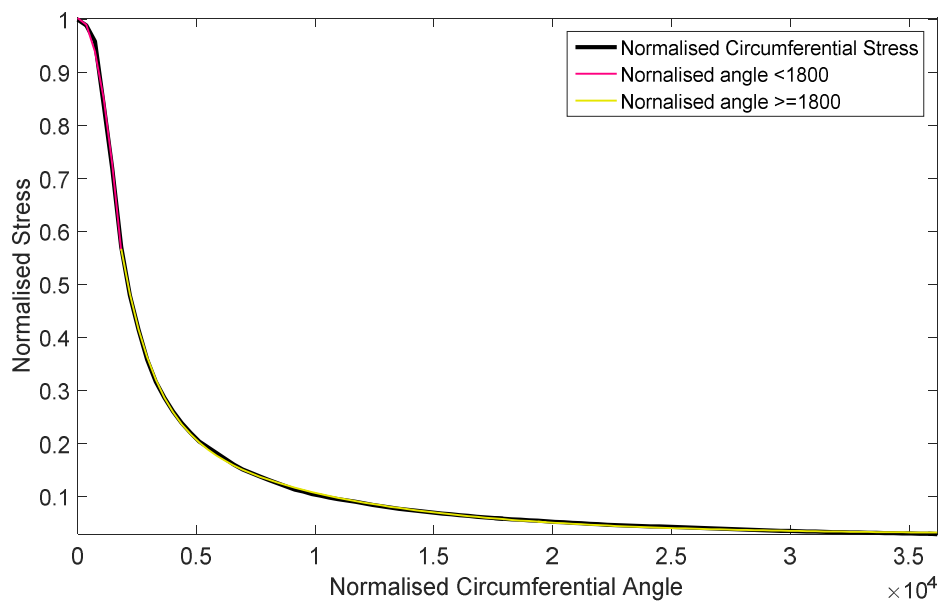


Figure 4.55–Modelling of circumferential stress variation with polinomial and exponential equations

The stress induced by a single roller (roller 15 shown in Figure 4.56(a)) can therefore be superimposed on the various strips around the whole circumference of the roller as shown in Figure 4.56-b. Notice that the stress peaks in the vicinity of the roller-raceway contact and reduces to near zero conditions at angular distances further away. Figure-c shows an expanded view of the stresses. As can be seen the shape of the stress profile changes with the applied radial load just as expected.

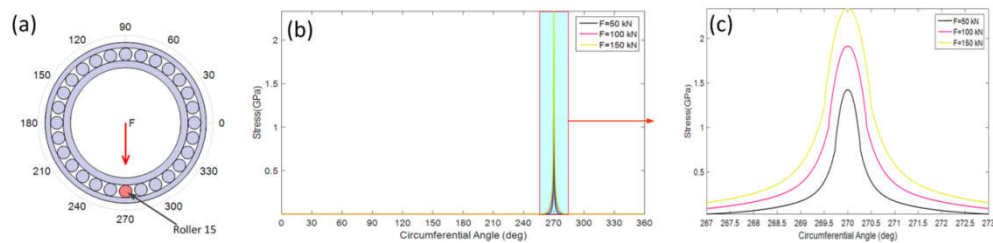


Figure 4.56–Variation of stress in circumferential direction for different depths

At each instant, the stress distribution across the bearing can be evaluated by superimposing the stresses induced by the load in each roller across the entire range of rollers in each row of the bearing as shown in Figure 4.58. By superimposing the stress created by all the rolling elements the stress across all the circumferential strips is obtained as shown in Figure 4.57. Figure 4.59 zooms in on the contact on roller 15. It can be seen that the stress affects a small region around the contact point and retreats to a low stress not far from the contact point just as expected.

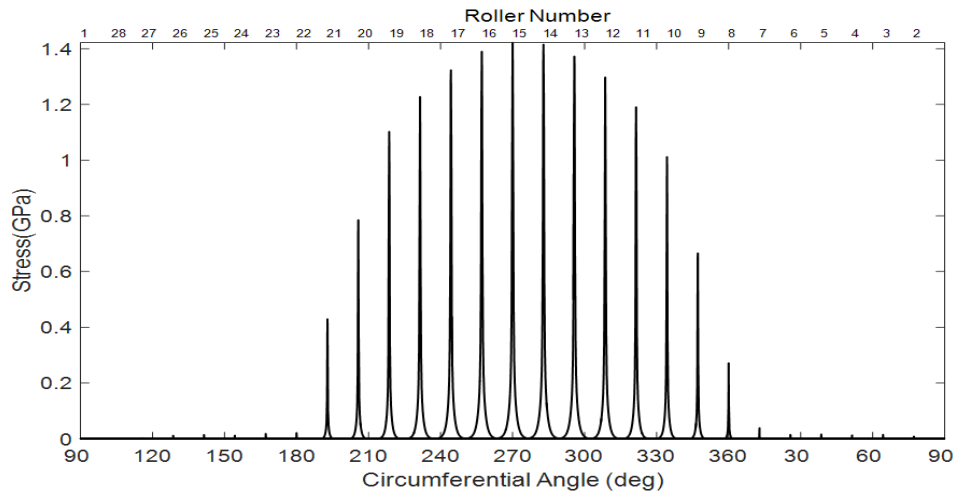


Figure 4.57–stress variation in all the circumferential strips of the bearing (all strips in the circumferential direction).

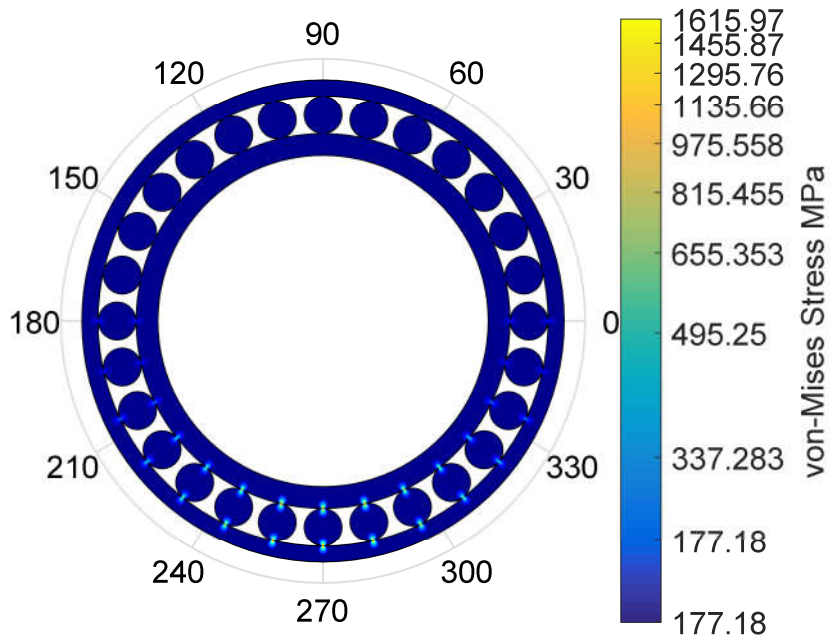


Figure 4.58– Stress variation in roller bearing

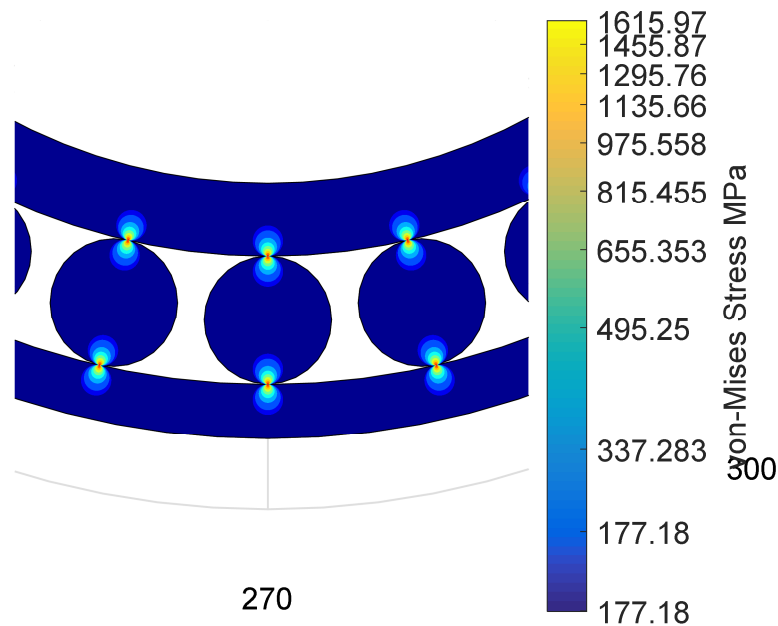


Figure 4.59–Enlarged view of Stress Variation in roller bearing

For a selected strip the loading history is determined using the location of the bearing component as given by the rigid dynamics model and finite element model. While the roller goes past a selected section, this induces a high stress as the rolling element approaches the section till such time when the roller and the section lie in the same plane. Here the maximum stress for the applied force is induced. As the roller goes away from the section, this reduces to the smallest level. This type of stress history for a single strip is shown in Figure 4.60. Here one peak to another represents a single rotation of the inner race. Each peak to peak section contains the stress induced by several rollers as shown in Figure 4.61.

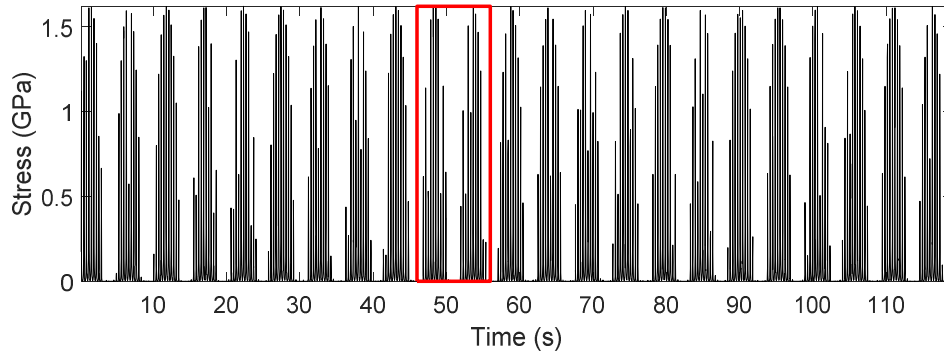


Figure 4.60– stress history of single strip of inner race

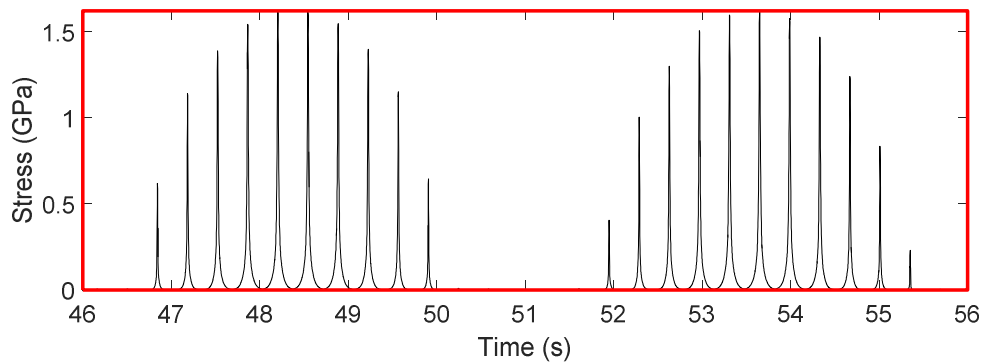


Figure 4.61– load history on single strip of inner race

4.5.2 Linear Damage Accumulation

The Stress Life method is employed to calculate the damage on each individual strip. To commence this process, the ASTM E 1049-85 (2005) Rainflow Counting Method is used to analyse stress history of the strip (egg. Figure 4.60) The rainflow analysis results in a rainflow matrix as shown in Figure 4.62. This indicates, several stress amplitudes with different mean stresses. The majority of the stress cycles are in the very low amplitude and mean stress region. Nevertheless, other stress amplitudes record a few number of cycles, particularly the highest stress amplitudes.

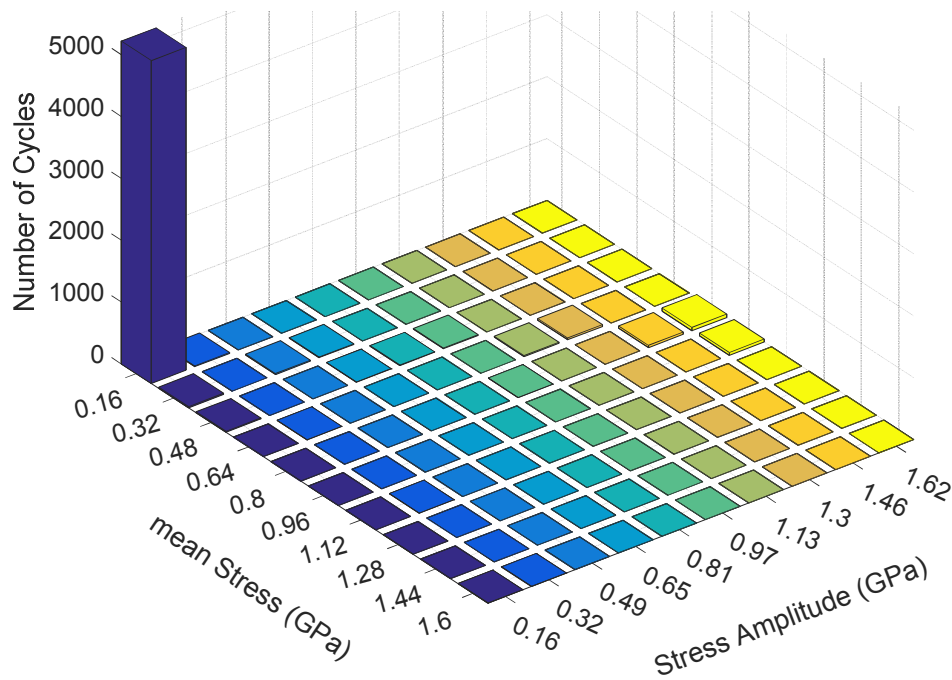


Figure 4.62– Rainflow cycle count matrix

4.5.2.1 Bearing Material properties.

Typical S-N curves for metals present the median number of cycles to failure of test specimens at specific loads. With the interest of achieving a higher than average level of reliability the basic bearings lives are given in terms of number of cycles at which 10% will have failed and 90 percent will have survived. To achieve this, a probabilistic S-N curve is needed. In the absence of readily available probabilistic S-N curve, the probability distribution for M50-NiL from the literature is fitted to an S-N curve. Failure probability of M50-NiL as shown in Figure 4.63 was given by Braza and Pearson [188]

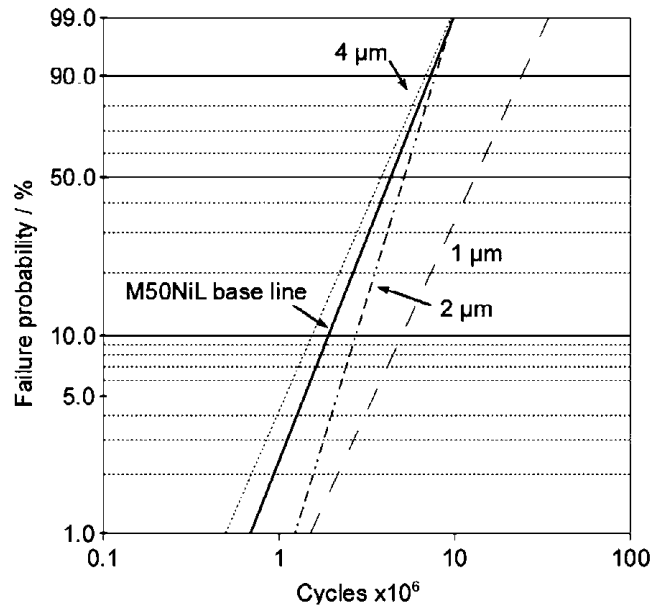


Figure 4.63– Probability of failure of M50-Nil steel [188]

Based on, Figure 4.63, the cumulative frequency distribution and probability density function were generated. A 3 parameter Weibull distribution was fitted to the curve as shown in Figure 4.64

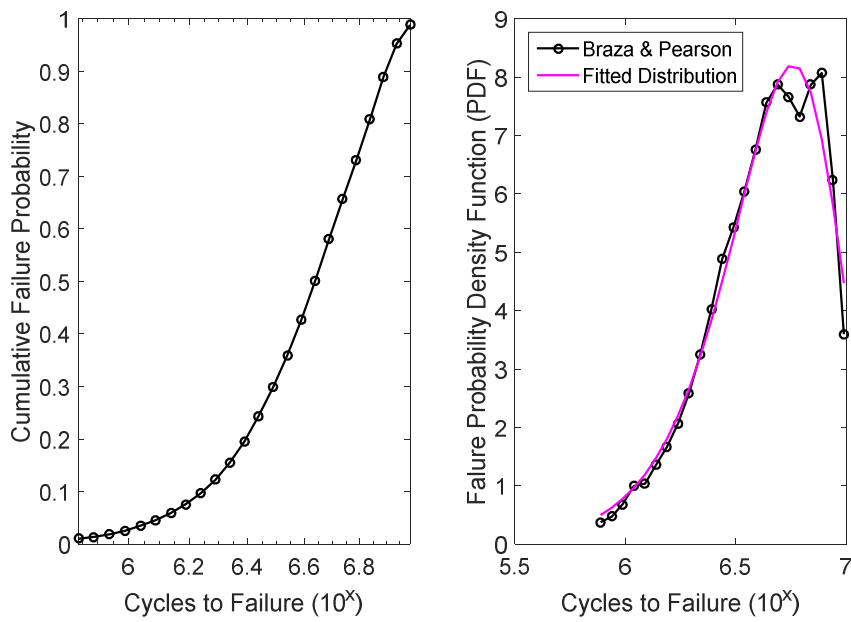


Figure 4.64– Probability of failure of M50-Nil steel [188]

The S-N Curve for the SUJ2 was assumed to be median values thus the 90th and 10th percentiles were established based on the fitted distribution above. Just as in the Basic bearing life (L10) equation, the probability at which 10% of the material will have failed and 90% will have survived is of interest. Consequently, the Lower 10th percentile as shown in Figure 4.65 was used as the failure point for the bearing material.

The S-N curve, as shown in Figure 4.65 was generated using a rotating bending machine and thus have a zero mean stress per cycle. The Goodman's mean stress correction given by (EQN 2.15) was applied to correct the mean stress of each stress cycle. The damage for each stress cycle consisting a mean stress and amplitude are evaluated to achieve a rainflow damage matrix as shown in Figure 4.66

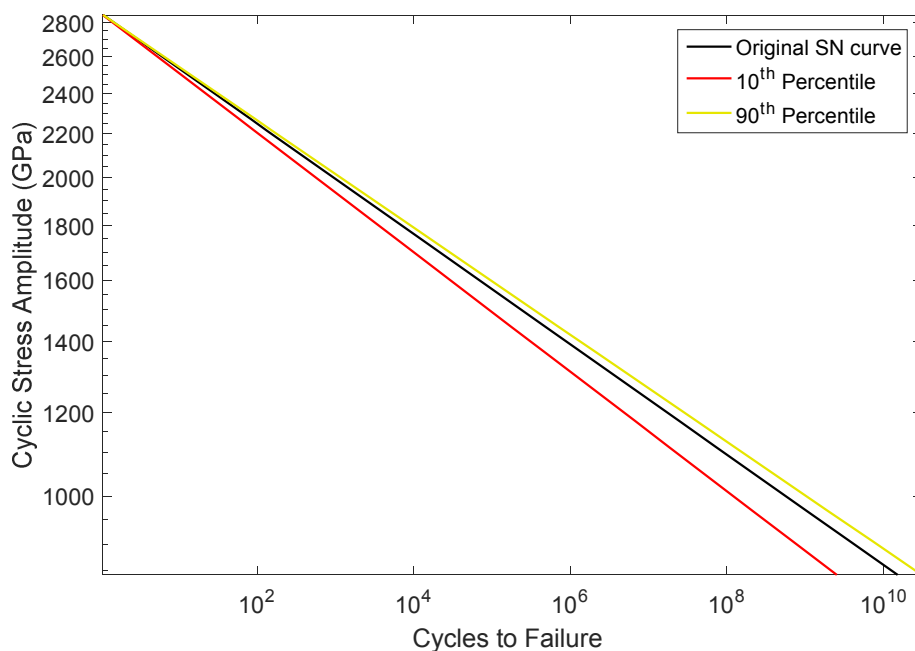


Figure 4.65– Probabilistic S-N curve for JIS SUJ2 bearing steel

The damage caused by each stress cycle is evaluated by the use of the 10th percentile S-N line as illustrated in Figure 4.66. Miner's linear damage accumulation is applied to aggregate the damage from the various stress cycle shown in Figure 4.66. For all the circumferential strips which have their stress histories, the rainflow analysis is carried out on their stress histories, the mean stress

is corrected using Goodman's relation and miner's linear damage accumulation is applied to achieve an aggregate damage.

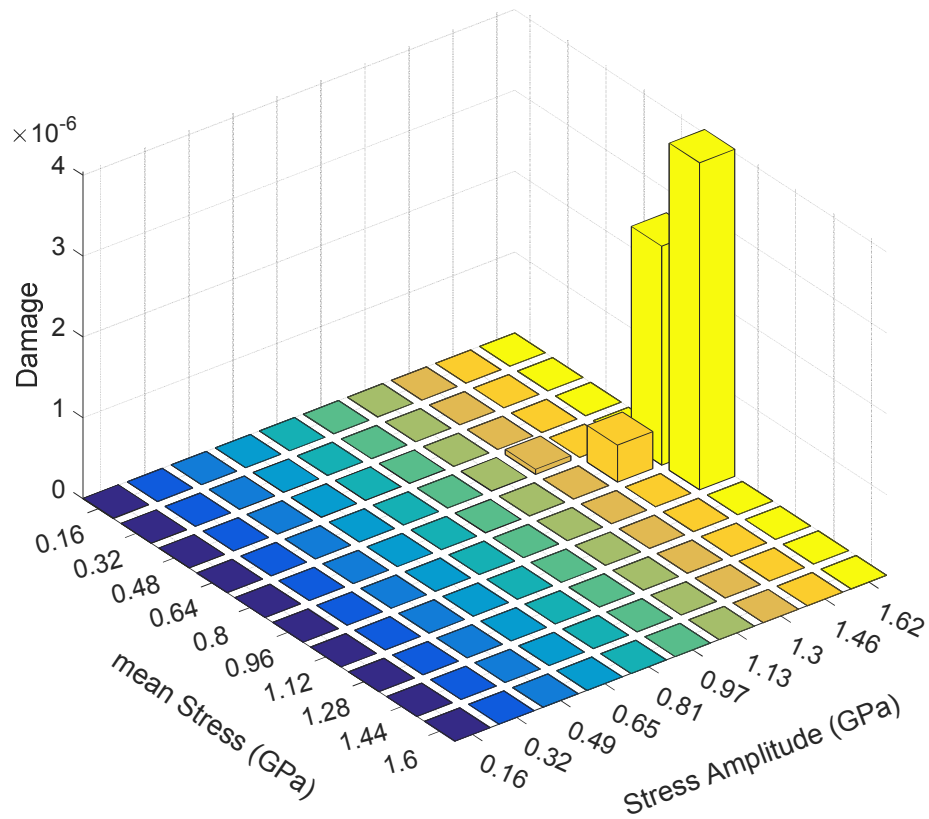


Figure 4.66– Rain flow damage matrix

Figure 4.67 shows the accumulated damage for each strip over a day of the bearing's operation. As failure is assumed to have occurred when damage reaches unity, the time to failure for the bearing can be obtained as shown in Figure 4.68 by

$$TTF = 1/(damage/time) \quad (EQN 4.7)$$

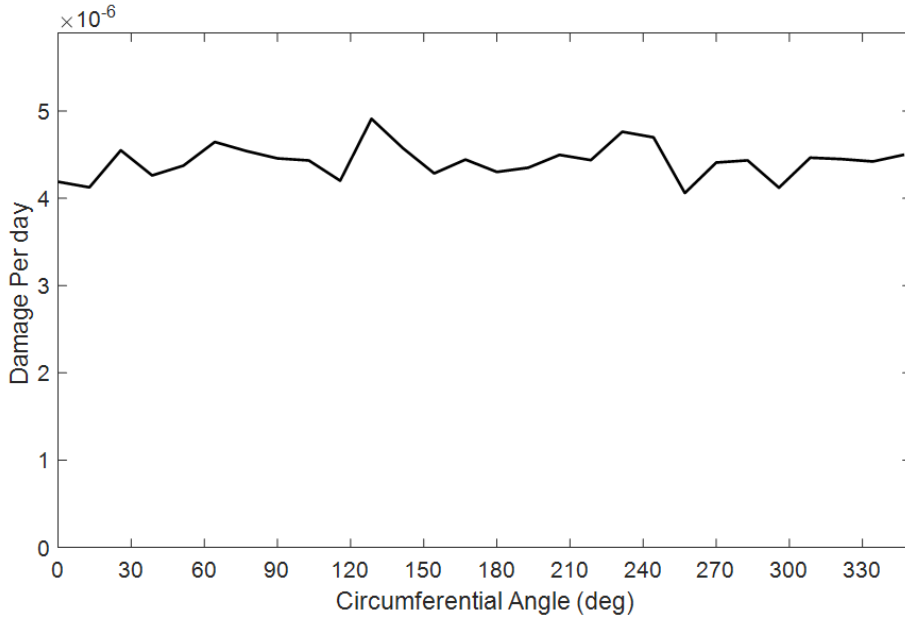


Figure 4.67– Calculated bearing strip damage per day

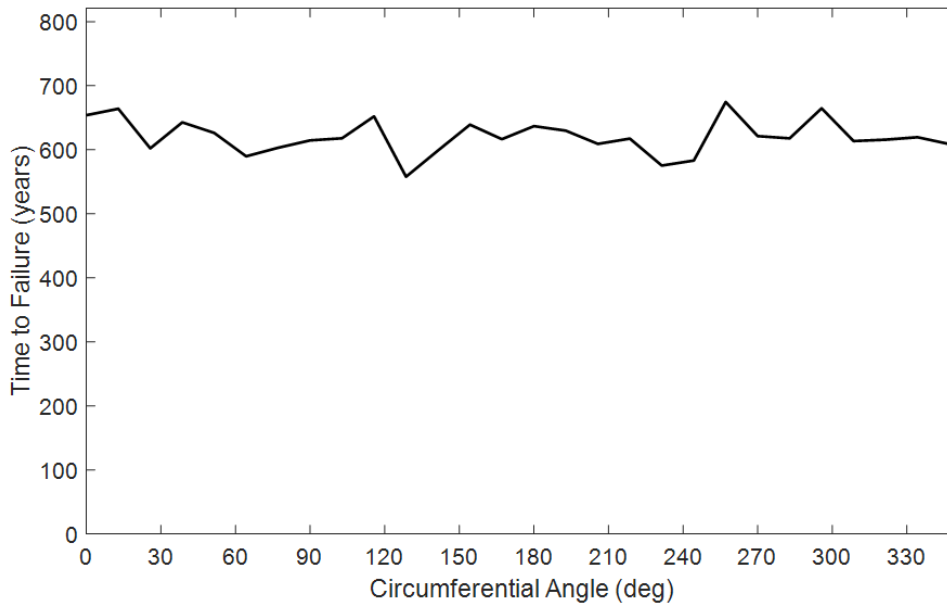


Figure 4.68– Sample time to failure of bearing inner race

4.6 Stress life method

The stress life method is generally accepted for predicting fatigue life of metals in high cycle fatigue. Its application here is quite valid but as pointed out by a few researchers including Bhadeshia [189] the SN curve produced by normal tension compression/rotation bending machines often deviate from rolling contact fatigue process. In general, rolling contact fatigue is highly dependent on impurities in the metal matrix ergo the much improved bearing life from introducing new cleanliness regimes. A better approach is to assess potential bearing life through the use of fracture mechanics.

A problem particular to spherical roller bearings is the occurrence of Heathcoat slip. This causes sliding of the contacting surface hence failures which are induced by increased surface shear can be enhanced.

It must be reiterated that the expected Stress-Life approach incorporating SN curves has shown significant deviation from fatigue spall initiation due to the different conditions in which these spall formation occur. It has been suggested that liner elastic fracture mechanics and continuum damage mechanics may yield better results for spall formation.

4.7 Conclusion

This chapter has presented a methodology for assessing the fatigue damage on a bearing system. The chapter commenced with the description of a potential main bearing arrangement for a tidal turbine. A dynamic model was developed which delivers the time varying roller loads and positions using rigid dynamics formulation. As the components of the dynamic model are considered rigid, they only yield integral loads on each component.

A FE model is used to evaluate the effect of this integral load on stresses in the bearing. Unlike the popular Hertzian theory used to analyse many bearing contact, the FE model illustrated the presence of edge loading. The von-Mises equivalent

stresses produced by the edge loading are generally the maximum thus are assumed to be the life limiting stress.

The stress life method is adopted to calculate the fatigue damage on the inner race of a bearing. The raceway was discretised into elemental volumes called strips whose stress history was analysed by performing rainflow cycle counting. Finally, fatigue damage is calculated by the stress-life method using a linear damage accumulation law via rainflow counting and Goodman's mean stress correction for each inner race strip.

Chapter 5 Accelerated Test Planning

5.1 Introduction

Accelerated tests are used to obtain timely information about products or components which have long service lives. As discussed in chapter 2, the most common approaches used include acceleration by increasing load magnitude or loading frequency. To accurately accelerate the damage caused over the life of the bearing in a shorter period, one must accurately replicate the loading as well as the loading cycles.

Chapter 4 presented a methodology of assessing the damage on the inner race of a main bearing given a main shaft load and speed as described in Chapter 3. This chapter discusses how the evaluated damage in Chapter 4 can be replicated in a full scale nacelle test rig.

The ability to replicate the damage depends on the capabilities of the test rig. As such a dedicated tidal turbine nacelle test rig is described. This is followed by a description and analysis of popular techniques employed to accelerate testing of tidal turbine drivetrains and some potential shortfall they present.

A more robust approach to applying an equivalent amount of damage on bearings is presented in section 5.4. Subsequently, a different approach is presented which can further accelerate testing while keeping within typical constraints. This is followed by the demonstration of the performance of this technique. Finally a conclusion is drawn highlighting some challenges and limitations of the discussed approaches.

5.2 Full Scale Marine Drivetrain Test Rig

To reduce risks associated with tidal energy, the ORE Catapult's National Renewable Energy Centre has developed a marine turbine test rig (i.e. Nautilus). In addition to the dynamometer feature that allows controlled torque and speed to be applied to the test turbine, the test rig with its bespoke Force Application System (FAS) is able to replicate non-torque loads on the tidal turbine drivetrains in all 6 Degrees of Freedom (DoF). The test rig aims to demonstrate the reliability, functionality and performance of tidal turbines through full scale testing.

The primary components of the test rig are as shown in Figure 5.1. The variable speed motor is rated at 3.4 MW and operates at speeds of ± 600 rpm. It is coupled to a split torque speed reducing gearbox through a torque limiting couple. The 20:1 gear ratio gearbox outputs a maximum speed of ± 30 rpm. The gearbox is coupled to the FAS (Non torque Loading Machine) via a flexible coupling. On the other side of the FAS, a 6 axis transducer monitors and records the loading applied to the test piece. The final part of the test set up is the test piece. The spacious 22x12 m test piece area of the facility enables testing of fully assembled full scale nacelles as well as nacelle components. The General parameters of the test rig are as shown in Table 5.1.

Table 5.1: Parameters of Nautilus Marine Test Rig

Parameter	Value
Maximum input power to test piece	3 MW
Maximum torque	5 MNm
Maximum instantaneous torque	10 MNm
Facility crane capacity	125 tonnes
Recirculation voltage	11kV
Customer data acquisition system	400 channels

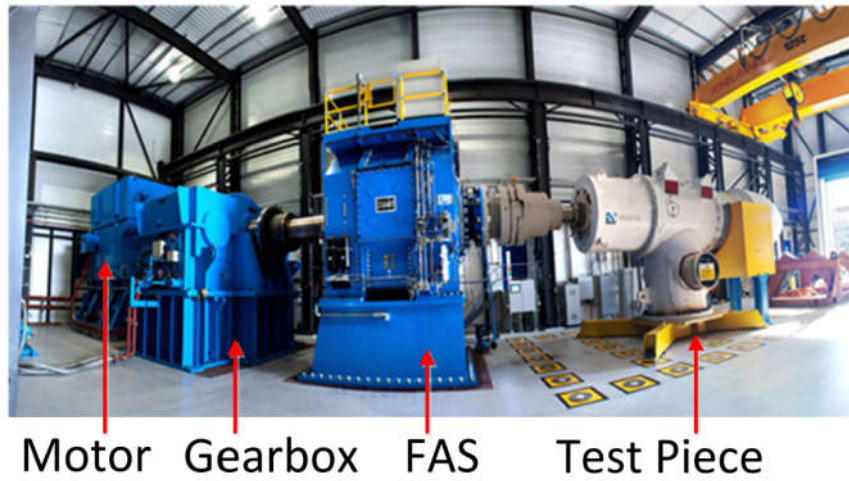


Figure 5.1– Test Setup at Nautilus Test Rig

The highly versatile design of the test rig allows it to perform mechanical as well as electrical tests. One of the key features in the test setup is the FAS(Non Torque Loading -NTL machine). This facilitates the application of highly dynamic loading conditions on the main shaft just as experienced in field. In general, the operating window of the FAS is described in Table 5.2.

Table 5.2: NTL Operating Window

Description	Operating Ranges	Units	Dynamic Range
Axial Load on Nacelle Shaft (F_{XN})	+/- 4	MN	
Radial Load on Nacelle Shaft (F_{YN})	+/- 4	MN	
Radial Load on Nacelle Shaft (F_{ZN})	+/- 4	MN	
Torque Load on Nacelle Shaft (M_{XN})	+/- 5	MNm	
Bending Moment on Nacelle Shaft (M_{YN})	+/- 15	MNm	
Bending Moment on Nacelle Shaft (M_{ZN})	+/- 15	MNm	
Operating Speed (N_L)	+/-30	rpm	
Axial motion (x-direction)	+/-30	mm	
Radial motion (from x-axis)	+/-45	mm	
Angular motion (from y-z plane)	+/-1.6	°	

The capabilities of this test rig makes it ideal for obtaining reliability data on full scale nacelles or component in a timely manner via accelerated testing. Full-scale drivetrain test facilities for renewable energy nacelles can perform tests of assembled Nacelles as well as single components. Independent test facilities offer a great opportunity to demonstrate the reliability of devices before they are deployed. To date, testing of full scale nacelles is quite popular because in most cases, device developers possess a single prototype. Testing full scale nacelles as opposed to nacelle components present many challenges. Even so, laboratory testing offers many advantages as testing needs not focus on reliability demonstration only but can aid other activities such as controller tuning. Device developers are offered opportunities to perform other tests and optimisation using realistic operating condition. Consequently, endurance testing tends to be the last of many tests carried out. In most cases, test to failure is not an option since device developers possess a single prototype.

Typically, for tidal turbines, main bearing will not be tested in isolation but as part of a nacelle test. It is critical the equivalent damage is applied on all nacelle components without enhancing impractical failure modes. However, tidal turbine nacelles are complex and exhibit coupled loading and damage between many components. While replicating the load, a number of parameters must be changed to tune the damage on the bearing such that a representative damage is encountered.

In addition, the typical drivetrain which undergoes testing is a prototype and may differ from production machines but testing provides reassuring estimates of reliability. To make the tested machine suitable for all potential sites, the turbine must be tested under truly extreme flow fields

5.3 Popular Accelerated Test Plan for Tidal Turbine Drivetrains

The 20 year expected lifetime of a typical tidal turbines necessitates the use of accelerated testing methods to obtain lifetime reliability information. A common approach employed to accelerate testing of tidal turbine drivetrains involves applying loads at a much higher frequency than they are subjected to in regular

operation. Typically, this has been done by assuming tidal oscillations lead to a sinusoidal flow speed variation over each tidal cycle as shown in Figure 5.2a. It is assumed that the load on turbine components is dependent on the tidal velocities, thus follow the sinusoidal variation of the flow speeds. In this case, the frequency of this sinusoidal variation can be increased in a testing environment to accelerate the degradation on turbine components. The concept of this method is shown in Figure 5.2 where an acceleration factor of 6 has been applied to a normal semidiurnal tidal flow speed (a), to achieve an accelerated case (b), where the flow variations are assumed to occur at a much faster rate. Here, the loadings on the main shaft are assumed to follow the sinusoidal pattern. The amplitude of this pattern is often taken as the maximum load in the one tidal cycle.

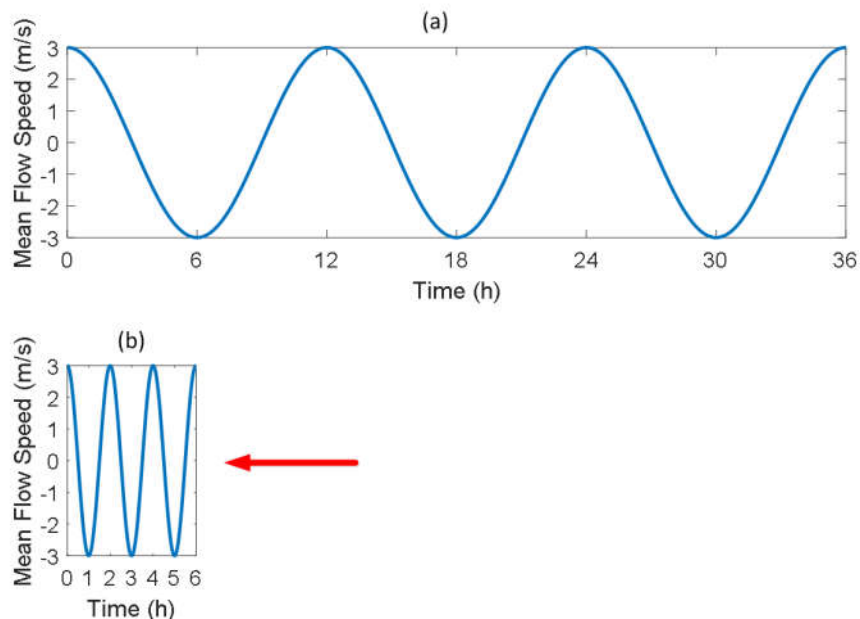


Figure 5.2– Common method of accelerating testing of tidal turbines

This approach to accelerating testing, however, has several drawbacks which simply makes it inaccurate in terms of applying representative damage to drivetrain components and also makes it somewhat impractical.

Generally tidal flow speeds are often composed of several harmonics constituents which make the variation of each tidal cycle different from the other. In general the tidal cycles do not form perfect sinusoidal wave form. In addition, the amplitude of

most tidal cycles vary from tide to tide. This is clear in the more representative tidal site flow conditions presented in Figure 3.3.

Focusing on the amplitude of the flow speed rather than the frequency, the analysis in Chapter 3 showed that the main shaft loads are strongly influenced by the magnitude of the average velocity. It is not necessary that the highest flow velocity inflicts the highest damage on drivetrain components. In fact, the height amount of loading on the main shaft is often recorded at rated speed because power is shed after rated speed is reached

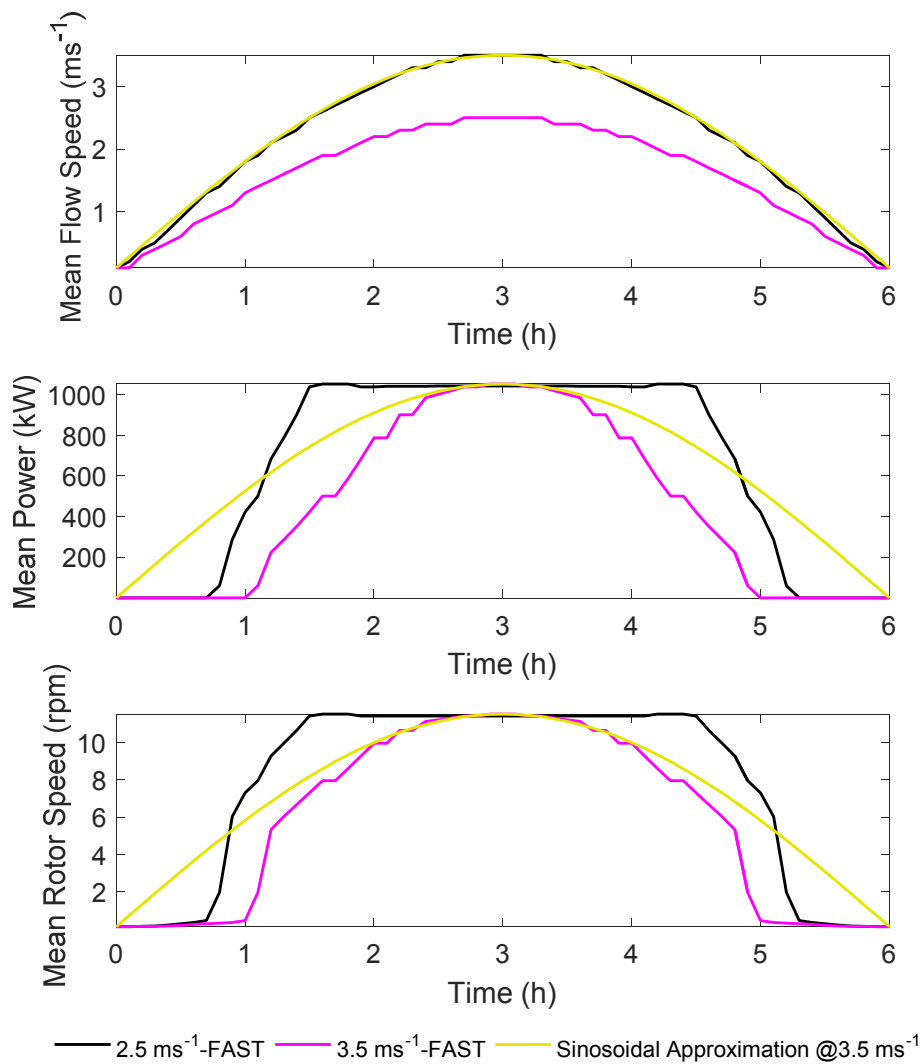


Figure 5.3– Sinusoidal half cycle of a semidiurnal tide with a peak of 2.5 m/s and 3.5 m/s

Supposing one were to simulate the tide through this method, the amplitude of each cycle must be correctly represented. The differences introduced by the magnitude of the flow speed are not necessarily linked to changes in the amplitude of the shaft loading but also affects loading pattern.

A perfectly sinusoidal tidal cycle with peak velocity of 3.5 m/s introduces very different loading on the turbine compared to a similar flow with a peak velocity of 2.5m/s. This is illustrated by the black (2.5 m/s) and magenta (3.5 m/s) lines in Figure 5.4.

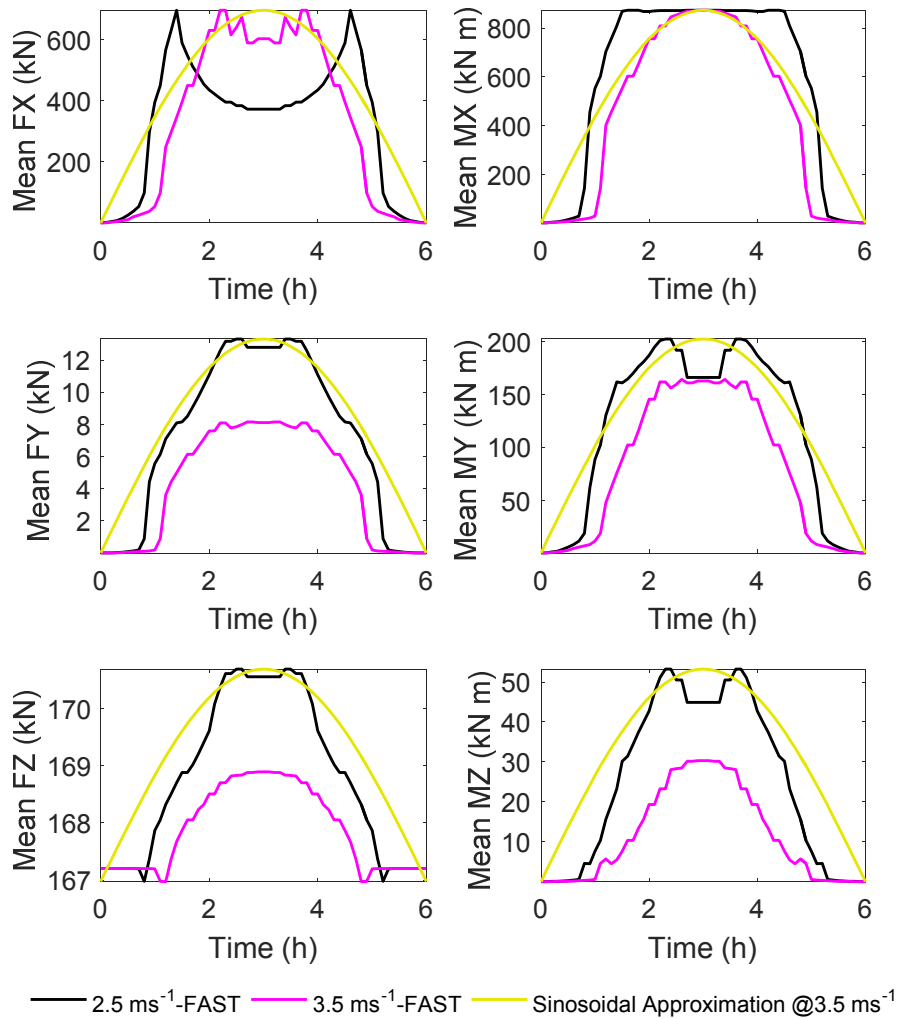


Figure 5.4— Sinusoidal half cycle of a semidiurnal tide with a peak of 2.5 m/s and 3.5 m/s

The variation of the shaft loads for the three cases are shown in Figure 5.4. It indicates the shaft loads in a sinusoidal tidal flow will not necessarily follow a sinusoidal pattern. In addition, the magnitude of the maximum flow speed in each cycle influences not only the maximum loads but may drastically alter the shape of the loading pattern. Also turbulence and low periodic change in flow are not captured by this process since a mean value is obtained at each tidal speed.

The more pressing reason why the discussed approach may incur unequal damage arises from the unrepresentative number of loading cycles on some of the components of the drivetrain. This arises due to the rotational motion of these components rather than the amplitude or the frequency of the tidal speeds. In a single semidurnal tidal cycle the main bearings for the simulated (FAST) cases rotate 2651(2.5m/s) and 2782(3.5m/s) times. Since the life of a bearing is strongly dependent on the number of rotations, the simulated number of rotations must be matched for each accelerated cycle. This can be achieved by increasing the rotational speed of the bearing by multiplying by an acceleration factor, A_f in the form of (EQN 5.1) to achieve a representative number of loading cycles.

$$rpm_{acc} = A_f rpm_{field} \quad (\text{EQN 5.1})$$

5.4 Damage acceleration

In an ideally designed drivetrain system, the main bearing supports all the non-torque loads allowing the gearbox to transmit torque loads only. Although the magnitude of the non-torque loadings may correlate with the tidal velocities in a cycle, the proportion of damage on elemental components of the bearing is dictated by the rotational speed of the turbine. To ideally replicate the loads on the main bearing the number of loads cycles must be accurately replicated as well as the load it carries.

Depending on the bearing type and arrangement, the second row of each bearing will be subjected to the axial load while the first is subjected to the reversing axial load. The design of the spherical roller bearing is such that the thrust carrying row tends to be seated while the other row is relatively unloaded when the axial load

exceeds approximately 25% of the radial load. This sensitivity to thrust loads can be harnessed to increase damage on a bearing by ensuring damage on a particular row is accelerated.

5.4.1 Damage acceleration by increase in load magnitude

Lundberg and Palmgren's equation for bearing life (EQN 2.61) computes the life of a bearing in millions of rotations. For a given rotational speed rpm_b , the time to failure of a bearing in seconds (L_{10s}) is estimated by

$$L_{10s} = \frac{60}{rpm_b} \times \left(\frac{C}{P_{eq}} \right)^p \quad (\text{EQN 5.2})$$

Given that the basic dynamic load rating and the life exponent remain constant, while the rotational speed and loading vary, the life of a bearing can be consumed at an accelerated rate by using two complete sets of speeds and loads. In this case, the life of a bearing operating at a load P_1 (corresponding to P_{eq1} when factors X and Y also remain constant) and speed of Rpm_1 will be reduced by a factor F_{rf} if it is operated at load P_2 and speed Rpm_2 .

$$\frac{60}{Rpm_2} \times \left(\frac{C}{P_2} \right)^p = \frac{60}{Rpm_1} \times \left(\frac{C}{P_1} \right)^p \times F_{rf} \quad (\text{EQN 5.3})$$

$$F_{rf} = \frac{RPM_1}{RPM_2} \left(\frac{P_1}{P_2} \right)^{3.33} \quad (\text{EQN 5.4})$$

Here, the acceleration factor A_f may be defined as $1/F_{rf}$. Notice the ratio between the rotational speeds and acceleration factor A_f has a linear relationship while the ratio of equivalent load ratings has a power law relationship. That is, the reduction in number of load cycles to failure scale with a 3.33 power law for radial roller bearings. For a radial roller bearing, doubling the radial load will result in reduction of operational life by a factor of 10.0561 for the same L10 life. In practice however, the turbine specification loads are often close to the design limit such that additional load increases for test acceleration are mostly limited to about 150% of

specification loads to avoid unexpected or impractical failures. This is to avoid changing the root or failure mode.

5.4.2 Damage acceleration by changing load signal

Increasing the non-torque loading on a tidal turbine main bearing to accelerate its damage while testing may be insufficient to shorten testing to practical and commercially viable periods. Furthermore, rotational speed increases cannot achieve a satisfactory level of acceleration without severe over loading of some other drivetrain components when the whole powertrain is tested. As a result, new approaches needed to enable testing in which the damage on each component can be accurately reproduced yet avoid risking other components.

Classical bearing endurance testing has focused on evaluating life of bearings under specific conditions. This has generally been achieved through endurance testing machines. Such designs are displayed in Figure 2.48. These designs often apply static radial and axial bearing loads. Testing in these types of rigs often achieve test acceleration through increases in magnitude load and rotational speed.

The introduction of the Non-Torque-Load (NTL) application machines in turbine drivetrain tests enables the application of dynamic loading on bearings in a test rig. Unlike conventional machines, the bearing loads can be dynamically applied while keeping within the constraints of maximum load and speed.

The equivalent dynamic load P_{eq} is recalled from (EQN 2.62)

$$P_{eq} = XF_r + YF_a \quad (\text{EQN 5.5})$$

The radial force F_r can be expressed in terms of its constituent forces which are the vertical force, F_z and lateral force, F_y . Such that

$$F_r = \sqrt{F_y^2 + F_z^2} \quad (\text{EQN 5.6})$$

meaning

$$F_y = F_r \sin \theta \quad (\text{EQN 5.7})$$

$$F_z = F_r \cos \theta \quad (\text{EQN } 5.8)$$

Recall that the load carried by a roller in single row of bearing can be expressed by:

$$Q_\psi = Q_{max} \left[1 - \frac{1}{2 \epsilon_{it}} (1 - \cos \Psi) \right]^{1.11} \quad (\text{EQN } 5.9)$$

Where Ψ is the relative position of the rolling element from the radial load defined as:

$$\Psi = \theta \quad (\text{EQN } 5.10)$$

θ is the angle of the resultant radial load and it is often defined as 0° for a vertical radial force and ψ is the radial position of the roller. For a bearing with a constant magnitude radial load, Q_{max} and ϵ_{it} remain constant. Also, for a bearing with nominal clearance of 0, ϵ_{it} reduces to 0.5.

$$Q_\psi = Q_{max} [1 - \cos \Psi]^{1.11} \quad (\text{EQN } 5.11)$$

As it follows

$$Q_\psi = Q_{max} \text{ for } \theta = 0 \quad (\text{EQN } 5.12)$$

That is, the load carried by a rolling element when diametral clearance is 0 mm is given by the relative angular position of the rolling element in the bearing Ψ . Figure 5.5, highlights the strip which is subjected to the highest load for the given direction of radial load. A single loading cycle is observed by a roller when its Ψ goes from $-\pi$ to π . The variation of Ψ over time is therefore critical to bearing performance and long term reliability.

From (EQN 5.11), the load on a rolling element i , Q_{ψ_i} is related to its position Ψ . Consequently this may be exploited in an effort to accelerate the damage on a bearing component. The angular velocity of the radial force ω_r , can therefore be defined by:

$$\frac{d\theta}{dt} = \omega_r \quad (\text{EQN 5.13})$$

The Selection of ω_r determines the load distribution on the bearing thus can be used to accelerate the degradation process. The components of the radial force become:

$$F_y(t) = F_r \cos(\omega_r t + \theta_a) \quad (\text{EQN 5.14})$$

$$F_z(t) = F_r \sin(\omega_r t + \theta_a) \quad (\text{EQN 5.15})$$

Where θ_a is an additional phase terms

Figure 5.5 shows the maximum stressed strip in the inner race due to the applied force. The radial force can be manipulated by (EQN 5.15) to stress different strips in the inner race of the bearing.

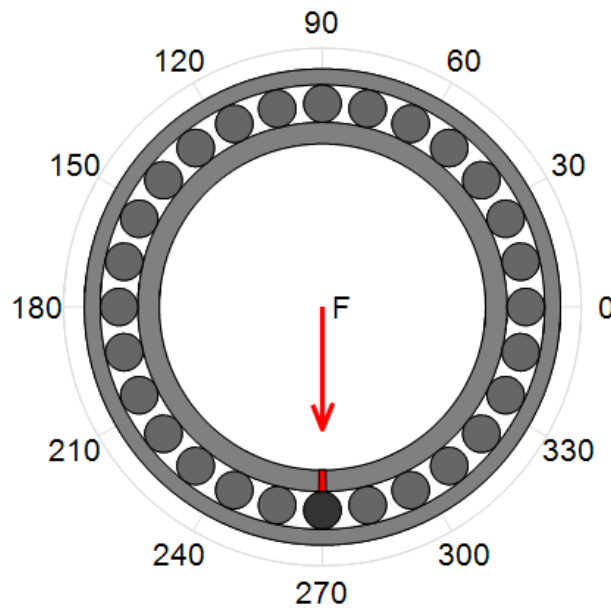


Figure 5.5–Maximum loaded strip as a result of the resultant radial load direction.

Similarly, the phase term θ_a may be defined as a time varying phase term

$$\theta_a = \theta_r + (\theta_g \cos(\omega_g t)) \quad (\text{EQN 5.16})$$

Such that θ_r remains constant over time and θ_g changes according to rotational speed ω_g

Ideally, to avoid unrepresentative damage while testing, a bearing must be operated as close to normal conditions as possible. As has been highlighted, the relative angle between the resultant applied radial load and the radial position of a rolling element determines the proportion of the entire load by the specific rolling element. In an attempt to increase the loading cycles on bearing components per revolution, the phasing of the radial load may be manipulated such that the maximum load is always encountered at particular position of the inner race. Here the phase lag or lead θ_p is defined as a sinusoidal function with a maximum value of θ_g the frequency ω_g . The components of the radial load are therefore defined as:

$$F_y(t) = F_{r \max} \cos(\omega_r t + [\theta_r + \theta_g \cos(\omega_g t)]) \quad (\text{EQN 5.17})$$

$$F_z(t) = F_{r \max} \sin(\omega_r t + [\theta_r + \theta_g \cos(\omega_g t)]) \quad (\text{EQN 5.18})$$

This approach inherently implies the bearing material is considered to be homogenous and the probability of failure of a point (Sp), subjected to a loading has the same probability of failure as all other points on the inner race surface subjected to the same load history.

5.4.2.1 Effect of AbP parameters

The parameters of the ABP method enable dynamic positioning of the resultant radial force to impart the highest loading on a specific rolling elements or portion of a raceway. Since the inner race is the component of interest, the method is used to apply the maximum load on a specific inner race strip. This is achieved by careful selection of parameters in (EQN 5.17) and (EQN 5.18).

The parameters of AbP method can be arbitrarily chosen to suit the specific strip loading history requirements. To demonstrate the influence of these parameters, A range of ω_r are simulated to demonstrate its effect on the damage of the inner race. The effects of a range of values of ω_r are shown in Figure 5.7. To demonstrate the effect of this process on the different strips of the inner race, the stress history of the

strips A ,B ,C and D as defined in Figure 5.6 are extracted for comparison. The stress histories show how the damage on some strips is accelerated by the selection of ω_r .

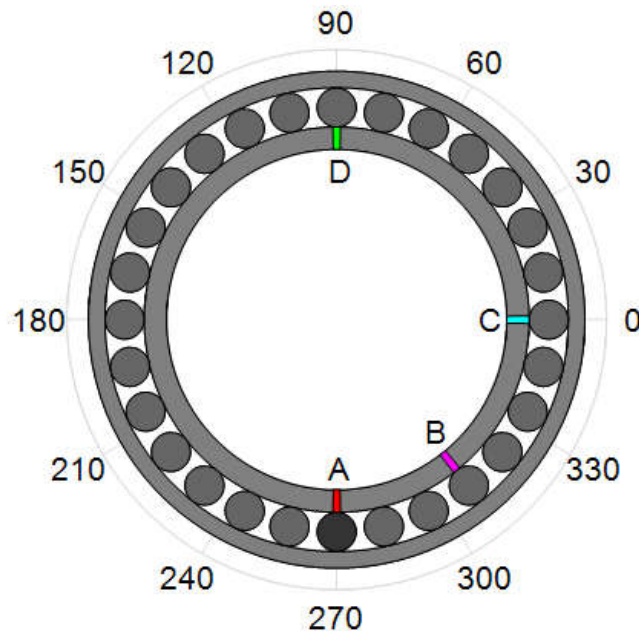


Figure 5.6–Definition of strips A-D in Figure 5.7

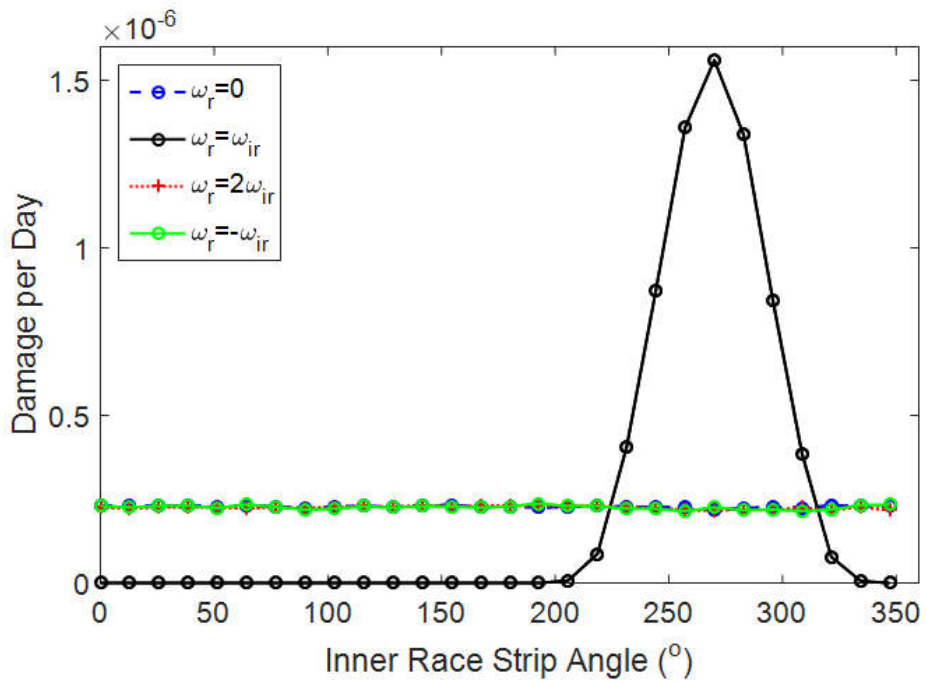


Figure 5.7–Calculated inner race damage for a range of ω_r

In the case where $\omega_r = \omega_{IR}$ the parts of the bearing which is subjected to the maximum radial load remains constant throughout the rotation of the inner race. As seen from Figure 5.7 this results in damage being concentrated in a region of the inner race while in the other scenarios, the damage is spread across all the surfaces of the inner race.

Generally, with an increasing ω_r (from $\omega_r = 0$), the damage on parts of the inner race increases till ω_{IR}/ω_r reaches unity. The maximum damage then declines with further increases in ω_r . Notice that the maximum damage occurs on a single point and tails away the further away from the maximum strip

With $\omega_R = 0$, the loading history of the various strips are identical but with a phase shift. While the inner race rotates, and a strip fall in line with a roller, the peak stress is induced on the strip. However, since the roller load reduces at the phase angle between the roller and resultant radial load increases there is considerable reduction in the load hence stress.

Conversely, enforcing $\omega_r = \omega_{ir}$ while the bearing starts from stating positions as show in Figure 5.6, Strip A encounters the maximum stress induced by each roller each time it falls in line with one. Hence the stress history of Strip A and shown in Figure 5.8 for $\omega_R = \omega_{ir}$ shows the maximum stress for the load is induced by each roller. This happens as the loading distribution is constantly shifted such that the selected inner race strip will be subjected to the same maximum load. For the same case when $\omega_R = \omega_{ir}$, Strip B is also subjected to its initial stress at each roller so this is repeated over time. Strip C and Strip D are barely loaded initially therefore maintain this low loading history. Consequently, there is a drastic variation in stress history across the strips of the inner race for when $\omega_R = \omega_{ir}$ than $\omega_R = 0$. This leads to the difference in time to failure for the different strips.

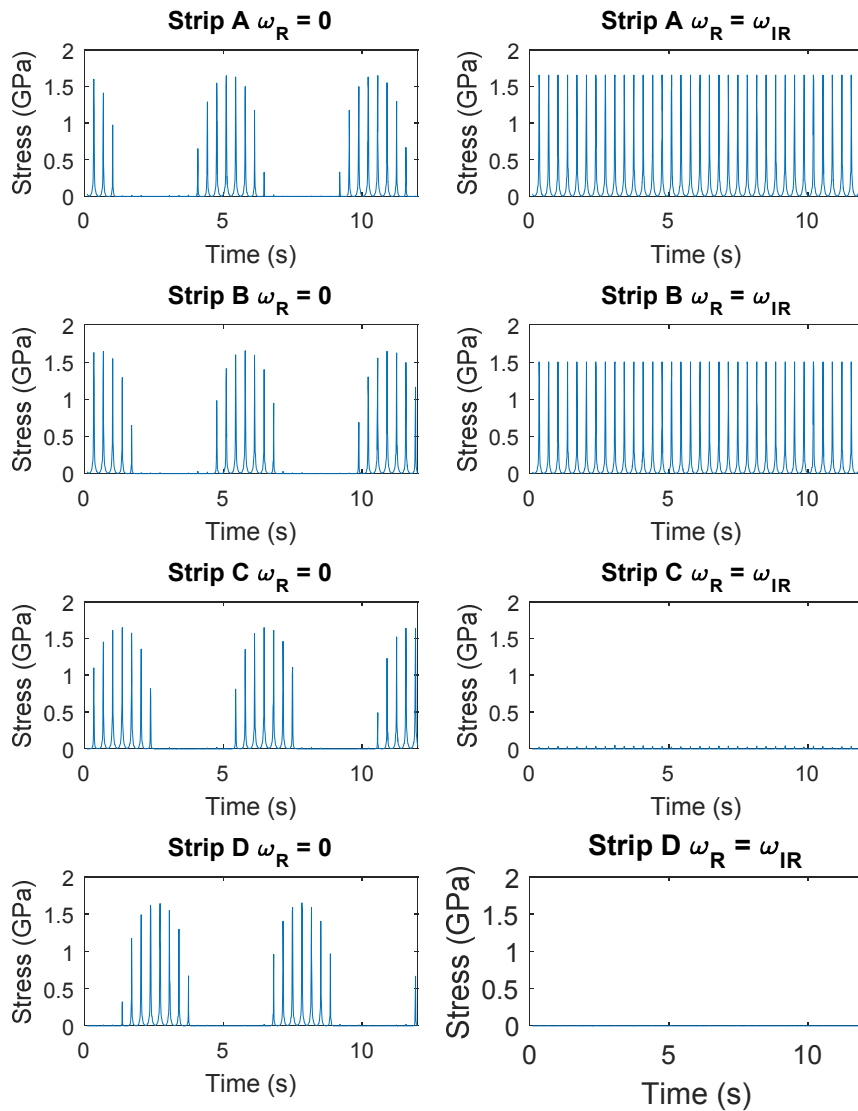


Figure 5.8—Inner race stress history for a range of ω_r

The parameter θ_r changes the initial angular position of the resultant radial force. Consequently, the phasing of the load distribution is shifted to concentrate the maximum load on a different strip. Consequently, selecting $\omega_r = \omega_{ir}$ and including only a range of phase term θ_r yield different inner race damage as shown in Figure 5.9.

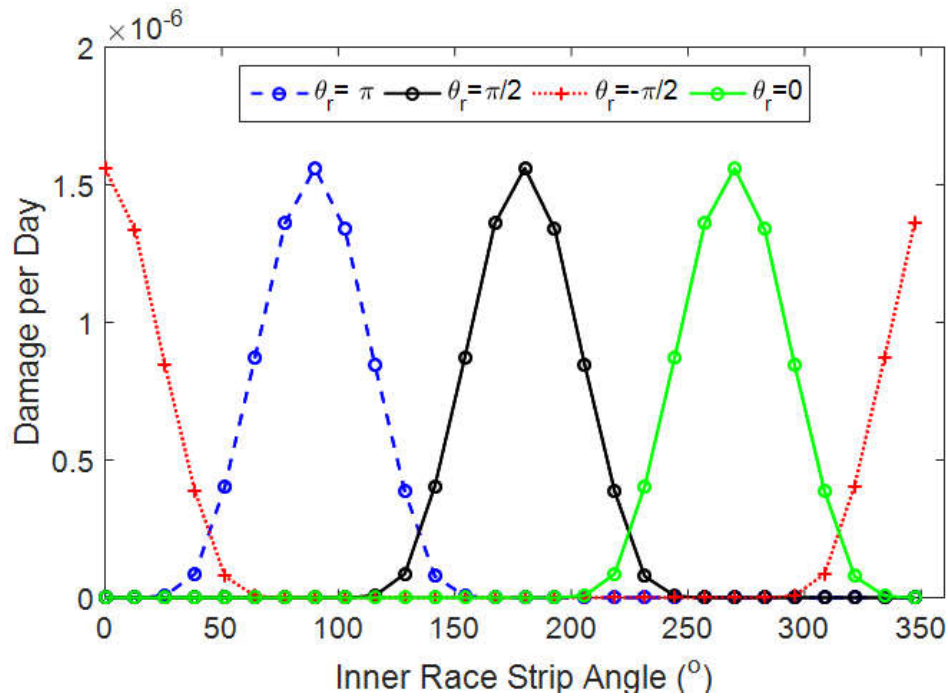


Figure 5.9—Influence of parameter θ_r in bearing inner race damage

When ω_r lightly deviates from ω_{ir} , the region subjected to the maximum stress at each roller shifts over time. In this case a single strip may not be subjected to the maximum load all the time but the maximum loaded strip may change. By introducing the time varying phase parameter as $\theta_g \cos(\omega_g t)$ from (EQN 5.17) this additional term can be controlled.

The effect of changing the amplitude of this additional oscillatory phase term is shown in Figure 5.10 where $\omega_g = \omega_r$. At high absolute values of ω_g (i.e. $|\omega_g| \geq \omega_r$), Figure 5.11 shows its effect is practically negligible

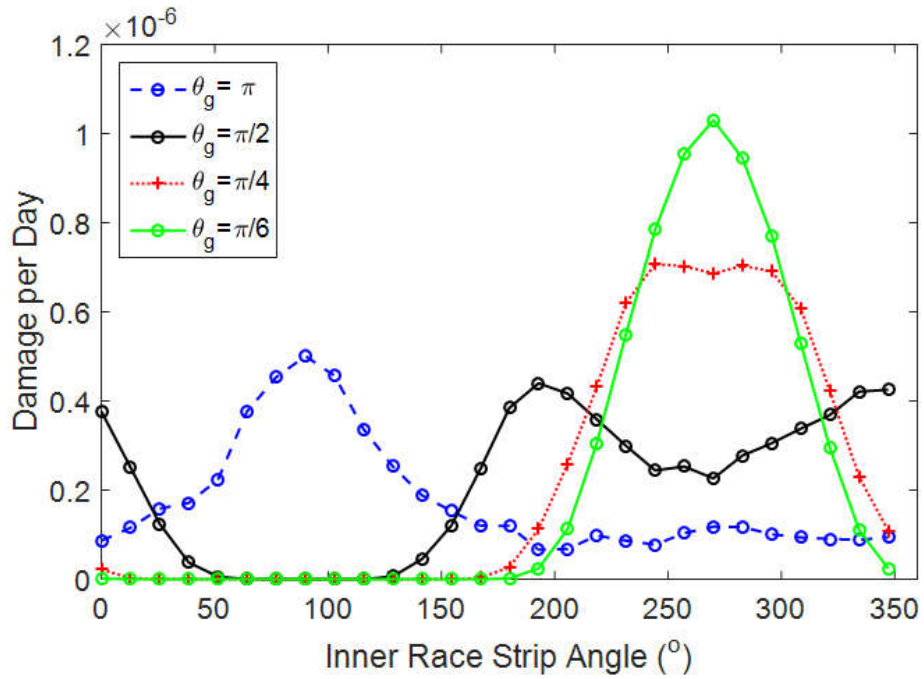


Figure 5.10–: Influence of parameter θ_g in bearing inner race damage

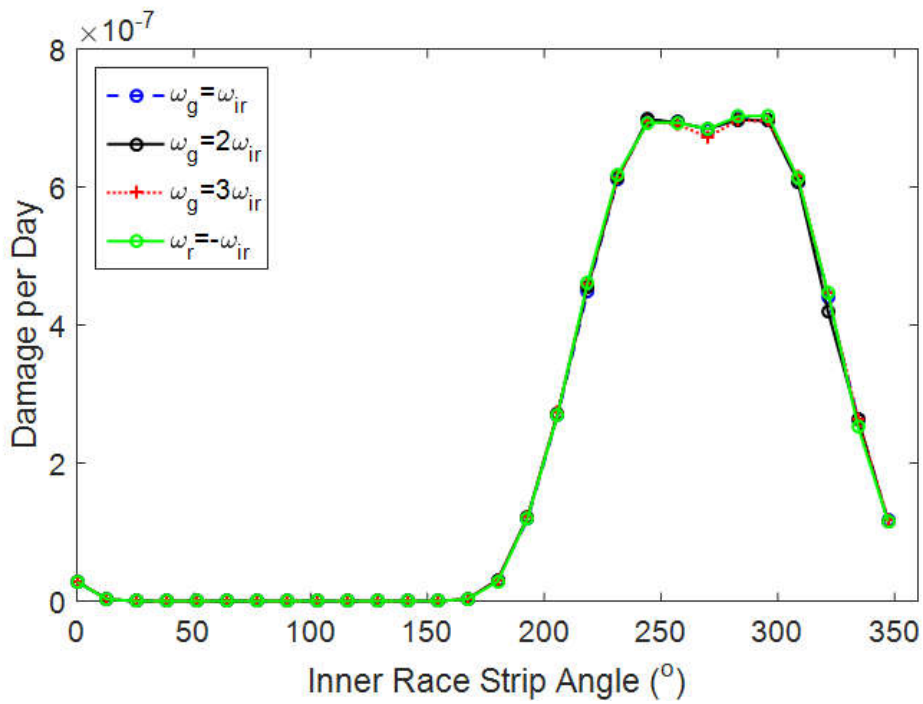


Figure 5.11– Influence of parameter ω_g in bearing inner race damage

5.4.3 Influence of axial load.

Bearings which are designed to support little axial loads have high coefficient of the axial force Y , in (EQN 5.5) thus make the life very sensitive to the applied axial load. For typical spherical roller bearing, excessive trust loads will cause one row to be seated while the other is relatively unloaded. The relationship between the axial load F_a , the radial load F_r and the contact angle of the rollers α is related to the maximum loads on the first row Q_{max1} and the second row Q_{max2} as follows:

$$\frac{F_r \tan \alpha}{F_a} \rightarrow (0,0.5238) \rightarrow \frac{Q_{max2}}{Q_{max1}} \rightarrow (1,0) \quad (\text{EQN 5.19})$$

Higher axial loads also result in a more even load distribution among the rolling elements in the seated row as axial load is shared across the rollers. In general, this increases loads on the seated bearing. Consequently, specific axial loads may be applied to accelerate the degradation of the bearing. It is necessary to select the parameters of the test load conditions such that testing is accelerated without impractical failure modes developing. It is general practice that SRB are not used in applications where the axial load exceeds 25% of the radial load. High axial load can also lead to roller end wear which is an undesirable failure mode in this instance. It is recommended therefore the axial load must not exceed 25% of the radial load.

5.5 Limitations of acceleration methods

Very few drivetrains for tidal turbines have been tested in a laboratory environment. For assembled turbines, testing has generally focused on components which are deemed critical. In geared turbines, the gearbox is often highlighted as the most critical component because of its complexity, cost and general repercussions of its failure. These tests have generally focused on the gearbox load cycles. This is primarily defined in terms of rotational speed and torque. In the case of main

bearings however, primary loads of interest include the rotational speed and Non-Torque loads.

Unlike testing individual components, testing assembled components requires consideration of the failure mechanisms of all the components. In a Tidal turbine's nacelle, the generator has many failure modes which may be triggered by the pulsating torque that is used in many test conditions. From the perspective of the generator, the maximum torque that can be absorbed by the generator is of great importance. In addition, the maximum short term peak torque is also critical. Similarly, by focusing on the Gearbox damage alone, the damage on other components of the drivetrain is often not representative of the true lifetime damage.

To adequately represent the damage caused by non-torque loading, the damage sustained over each tidal cycle must be appropriately matched during testing. However, increasing the rotational speed while holding the torque constant increases the total power required. This will lead to unexpected failures in generator, power electronics and other components due to over loading.

Typically, endurance testing for bearings often isolate the bearings in dedicated test rigs where the rotational speeds can be increased to achieve an equal number of loading cycles in a shorter time. However, spherical roller bearings are not suitable for high speeds. Moreover, full scale test rigs tend to operate at low speeds (below 30 rpm) so considerable levels of acceleration cannot be achieved. To compound the aforementioned challenges, the increase in power requirement for increase in speed for full-scale nacelles make this process impractical.

In presenting methods which replicate damage by applying accelerated loads, it is indicative that components may not necessarily be exposed to the same loading conditions as factors such as lubrication, temperatures; surface finish etc may yet play a vital role in component loads distribution and eventual life. By accelerating damage through loading, it is assumed these factors remain constant as when being used infield. Thus if loading is accurately represented, the damage caused will be accurately represented. Thus one must understand the influence accelerated loads have on different other parameters which are assumed constant.

Testing bearing in an accelerated manner could have a profound influence on bearing ancillaries. By increased rotational speed the fluid film thickness is also increased thus enhancing life of the bearing. Increasing bearing loading cycles through increased rotational speeds also have many drawbacks. The increased friction may degrade lubricant in an unrealistic manner. In some occasions, insufficient cooling may lead to the creation of thermal gradients across bearings which may alter the clearance at specific locations leading to excessive loading and wear.

Typically, accelerated tests are carried out on bearings to determine the bearing life. This is then used in conjunction with tests carried out on element testing machines to evaluate the life of a bearing in its operational condition. This process is repeated using many samples and conditions such that the bearing life can be generalised for many applications. Unlike the generalised approach, here the bearing is defined for a specific use and will often have specific operating conditions. Consequently, the bearing must be tested as close to the operating conditions to ensure correct life is reached.

5.6 Conclusion

The traditional method which has been used to accelerate testing of tidal turbines by assuming load cycles follow each tidal cycle can be misleading. As such a different approach has been presented for accelerated testing of tidal turbine main bearings. The utilisation of the empirical formulation given by Lundberg and Palmgren doesn't give much insight into the damage process and is generally limited by the maximum load and rotational speeds that can be applied.

A new method has therefore been suggested for accelerating the damage on main bearings in a full scale test rig. The method focuses damage on particular sections of the inner race of the bearing. The level of damage can be controlled by parameters as well as the location at which damage is focussed.

Chapter 6 Accelerated testing –a case study

6.1 Introduction

A methodology for accelerated testing of main bearings in a tidal turbine has been presented in chapter 1. Chapter 3 explained how the environmental loads affect the global turbine loads and the loads on the main bearings of a tidal turbine. Chapter 4 illustrated a process for converting the global bearing loads into component stresses enabling the stress-life method to be used to evaluate potential damage on the bearing. Chapter 5 discussed methodologies for replicating the damage on a bearing and introduced a new method to accelerate the damage on main bearings Called ABP. This chapter combines the methodologies presented in the aforementioned chapters to illustrate how the methodology presented in chapter 1 is utilised to develop an accelerated test plan for tidal turbine main bearings.

6.2 Damage evaluation

The methodology highlighted in chapter 1 is implemented to analyse the lifetime damage on a main shaft bearing. This involves analysing the main shaft loading history for a given tidal site as described in Chapter 3. The methodology for analysing bearing component load as shown in Chapter 4 is used to analyse roller loads. Subsequently, the stress history is derived. Finally, the method of bins approach is used to evaluate the damage on the inner race of the bearing material. The total damage is then calculated by summing up the maximum damage in each velocity bin.

6.2.1 Design load cases

The velocity variation was generated for a potential tidal site through tidal harmonic analysis. The so called ‘method of bins’ recommended by IEC 61400 for wind turbines was used to capture the velocity variations in incremental bin sizes of 0.5 m/s. This bins contained standard, normalised 10 minute contiguous data. IEC 61400 standards also recommend that bins are centred in multiples of 0.5m/s. for most wind turbines which operate form 5m/s to about 25m/s average wind speeds this leads to at least 41 samples in the operation range.

The flow conditions at the assumed tidal energy site have been discussed in Chapter 3.3. The velocity distribution is grouped into a velocity distribution curve with bin size of 0.5m/s as shown in Figure 6.1.

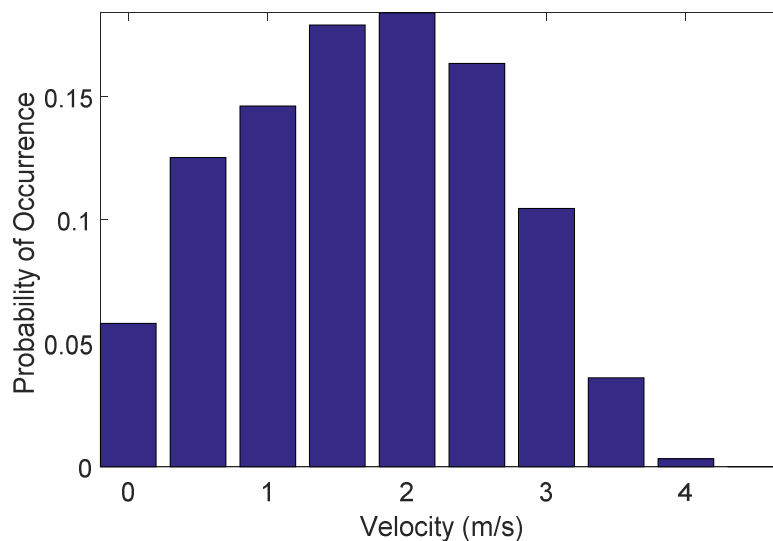


Figure 6.1–Velocity probability density function at the chosen tidal site

For each of the central velocities in the velocity distribution bins (Figure 6.1), a realistic flow field is generated using Turbsim. The generated flow field has a 1.5 m linear wave with a period of 8s superimposed on it by the use of wave orbital velocities. At the turbine’s rated speed (2.5m/s), Figure 6.2 shows the components of the flow field at hub height. The Main shaft loads as per FAST model described in Chapter 3.2 for this flow field is shown in Figure 6.3 and Figure 6.4.

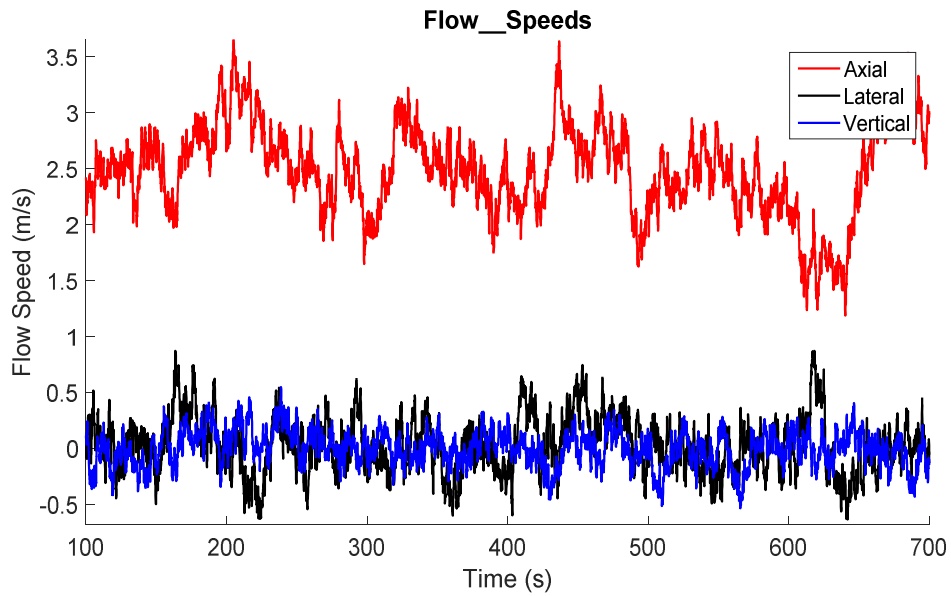


Figure 6.2–Hub Height flow speeds at rated conditions(average 2.5m/s)

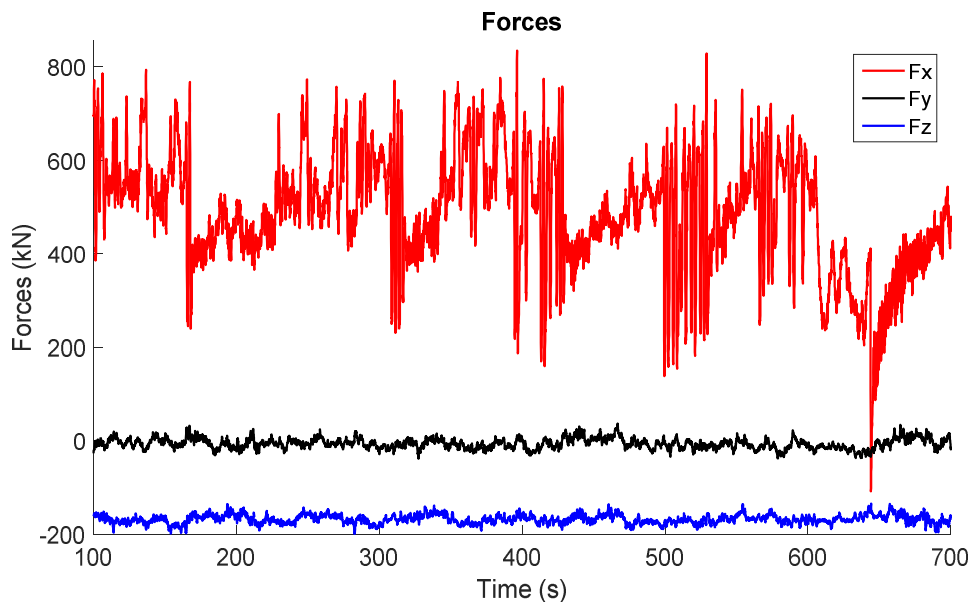


Figure 6.3– Low Speed Shaft Forces at rated speed(2.5 m/s)

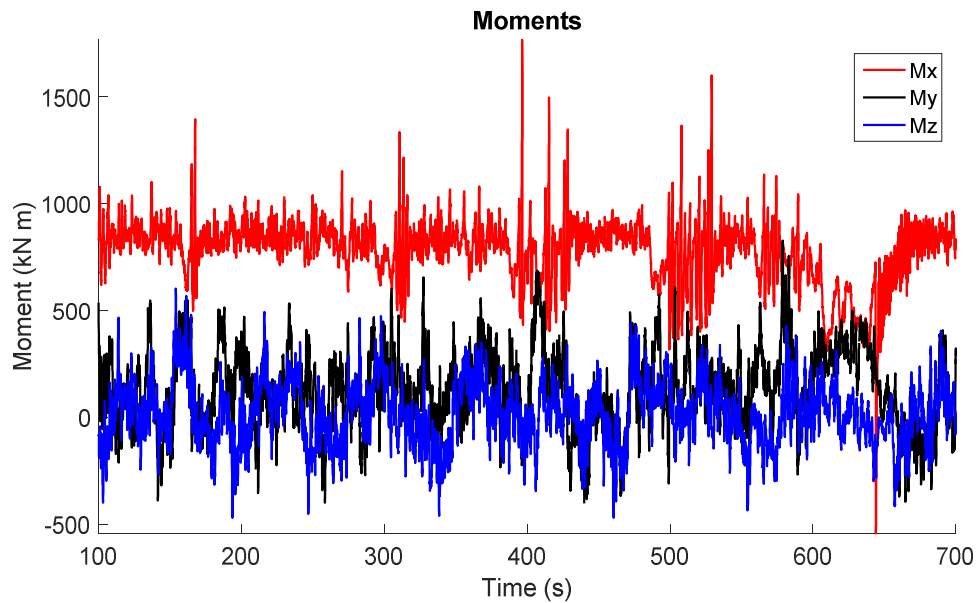


Figure 6.4–Low Speed Shaft Moments at rated speed(2.5 m/s)

To determine the ultimate potential design load cases 10 ten-minute simulations were carried out for each discrete average tidal flow speeds in the operation velocity region(0.5-4.5) in intervals of 0.5 m/s. Figure 6.5 shows the variation of shaft loads with shaft rotational speed and the frequency of occurrence for all flow velocities in the operational region.

One could categorise the loading conditions in terms of the occurrence of loads often called the ‘Time At Load’ method as shown in Figure 6.5 . In that case the damage is evaluated for discrete loading combination and summed together. This presents many challenges with the least being the large number of discrete load combinations considering all 6 DOF.

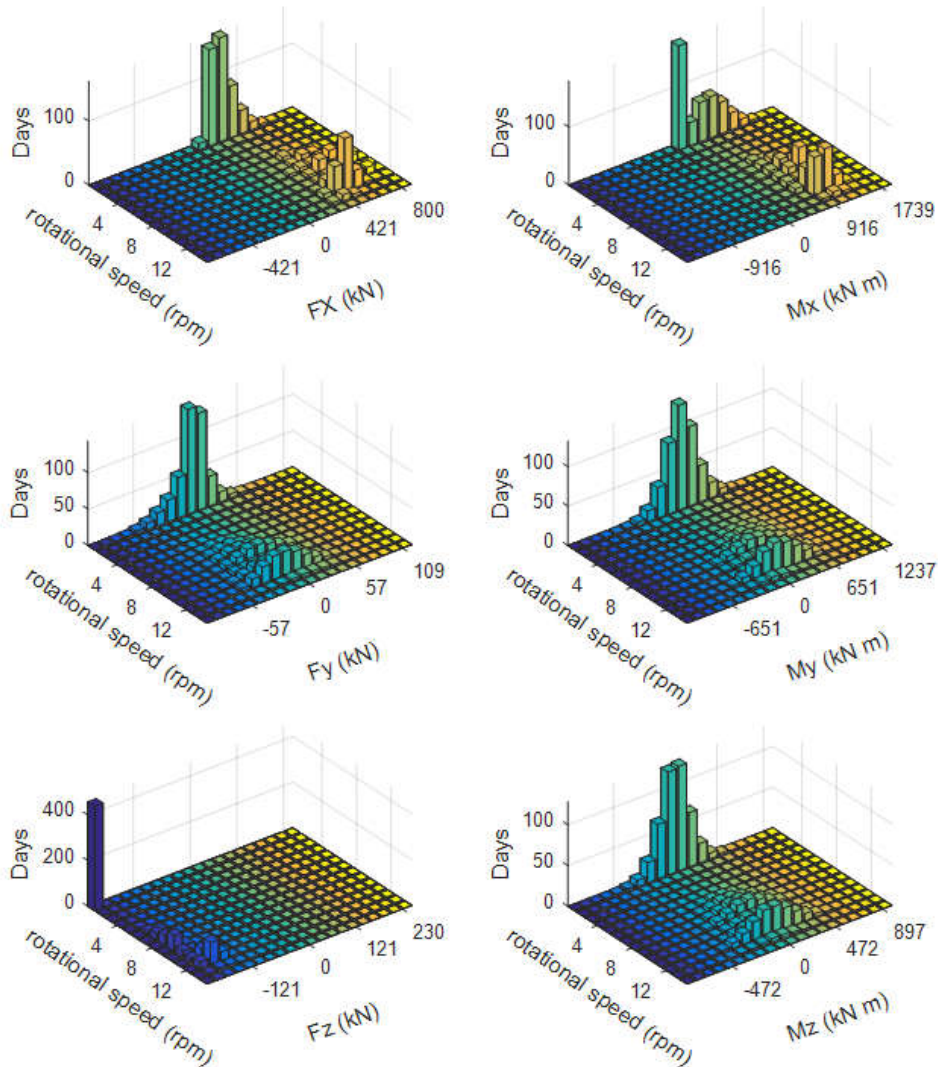


Figure 6.5– Distribution of drivetrain loads and their frequency of occurrence

6.2.2 Bearing component Loads

By considering the main shaft is very stiff and the main bearing configuration is just as described in Chapter 4.2, the loads on the main bearing applied by the loading in Figure 6.3 and Figure 6.4 reduces to Figure 6.6 . The Lateral and vertical forces form the radial component of the bearing load. Figure 6.7 shows the magnitude of the radial load and its direction. As observed from the angle of the radial load, the radial load is highly dynamic in terms of both magnitude and direction. The

dynamic nature of the bearing load leads to a highly dynamic variation in the rolling element load.

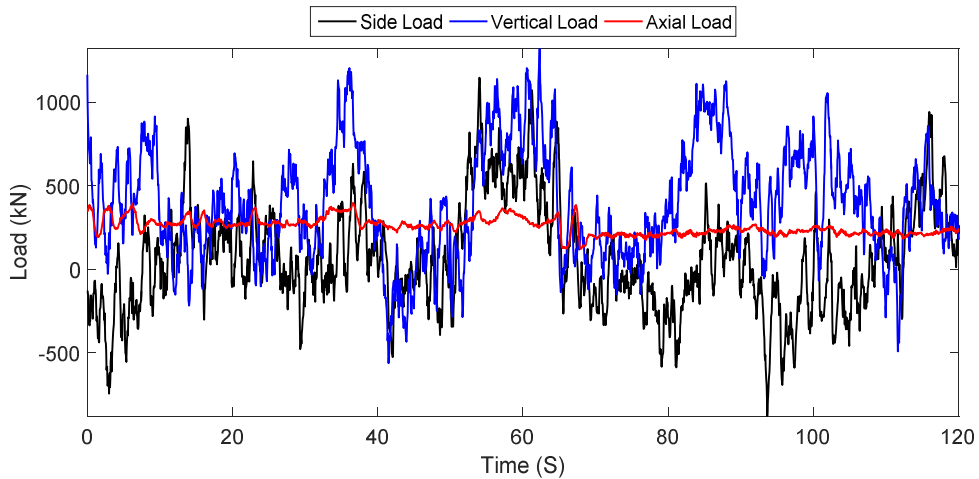


Figure 6.6–Low Speed Shaft loads at rated speed(2.5 m/s)

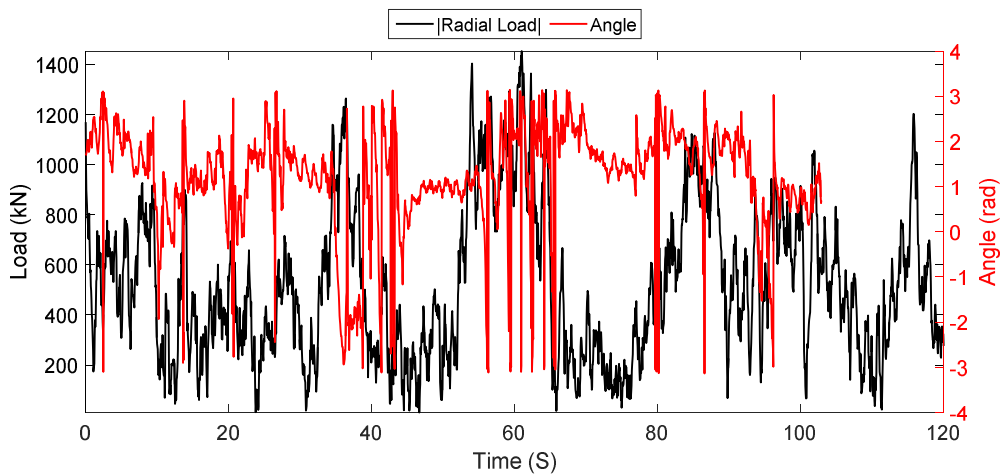


Figure 6.7–Low Speed shaft moments at rated speed(2.5 m/s)

A visual representation of the rolling element loading over time is shown in Figure 6.8 and Figure 6.9. The colours of the figure indicate the magnitude of the load the roller carries. Notice that the upwind roller sees very little load just as expected due to the axial force.

The loads carried by the rollers may be visualised with a 2d contour plot showing time on the horizontal axis and roller number on the vertical axis. The time varying

load on rollers in the upwind row is shown in while the loads on the downwind row are shown in Figure 6.8. Here, the influence of the axial load is evident as most of the load is carried by the downwind row. At low tidal velocities, the axial load remains small in comparison with the radial load. At a flow speed below 1 m/s, the bearing load is more evenly distributed between the two rows of the bearing.

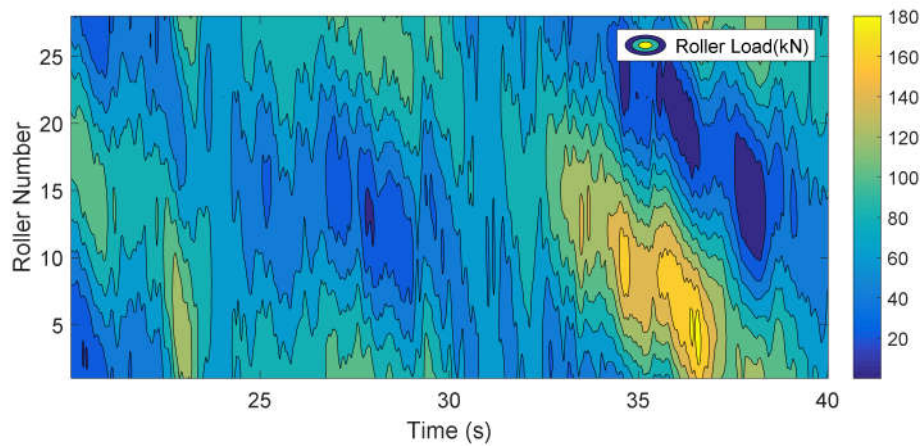


Figure 6.8–Bearing downwind Row Roller load

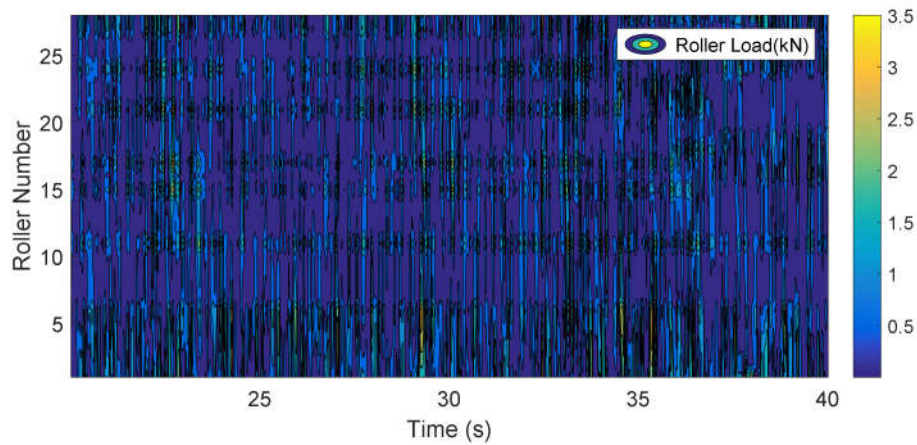


Figure 6.9–Upwind Row Roller load

The loading distribution changes rapidly with the dynamic loading conditions. Although the instantaneous load distribution changes rapidly, general trends can be observed from one flow velocity condition to the other. Figure 6.10 to Figure 6.14 show the loading distribution in the bearing for a variety of flow speeds. In these figures, the maximum load magnitude over time is shown by the magenta line. The

maximum instantaneous load is shown by the black line and the location at which it occurs is shown by the green dot. The relative magnitude of the roller loads are shown by the thin red arrows while the bold red arrow indicates the instantaneous direction of the radial load. The instantaneous axial and radial force are also given at the bottom of each figure.

At low speeds, the axial velocity remains very low, particularly in comparison to the radial load. Consequently, the main shaft load is relatively evenly distributed among the 2 rows of the bearing. This is evident in Figure 6.10, where the axial load is relatively low and the bearing load is distributed among the rollers whose angular location in the circumferential direction is $\pm 90^\circ$ from the direction of the resultant radial load.

An increase in axial force is observed with increasing flow speed, however, there is no great effect observed before cut-in speed. The increased axial force influences the axial load just as shown in Figure 6.11. The difference between the maximum load seen by the downwind row and upwind row is increased.

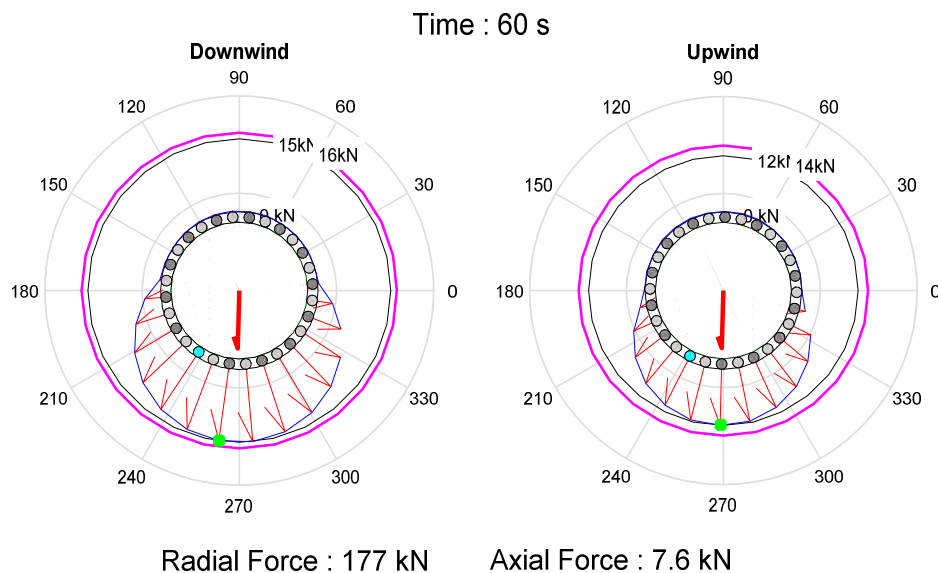


Figure 6.10–Bearing Load distribution at 60s at average speed of 0.5 m/s

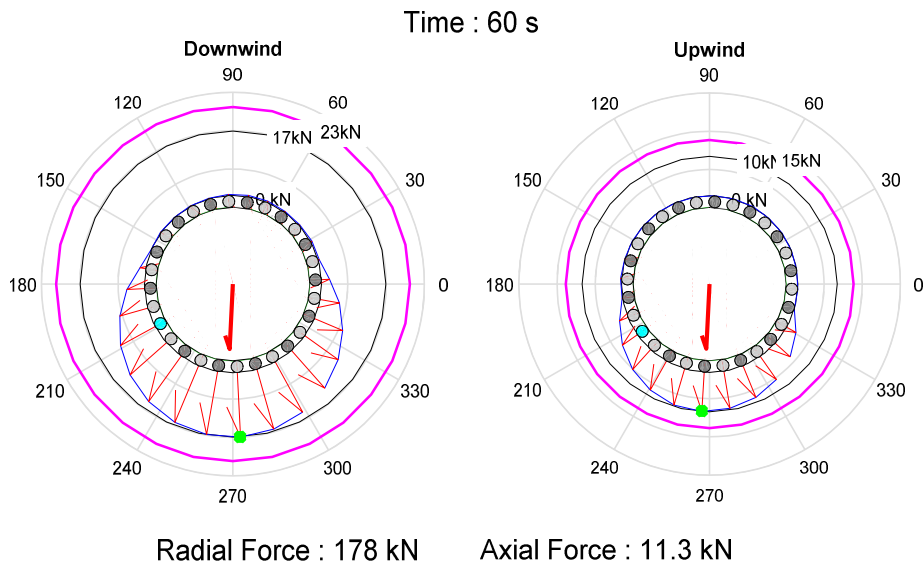


Figure 6.11–Bearing Load distribution at 60s at average speed of 1 m/s

A significant increase in axial load is observed at cut in speed. As the blades in the variable speed turbine pitch to extract energy from the flow field efficiently, the axial load increases leading to an unseated upwind row of the spherical roller bearing. Notice that the relative magnitudes of the axial and radial loads lead to a more even distribution of the load between the rollers of the downwind row.

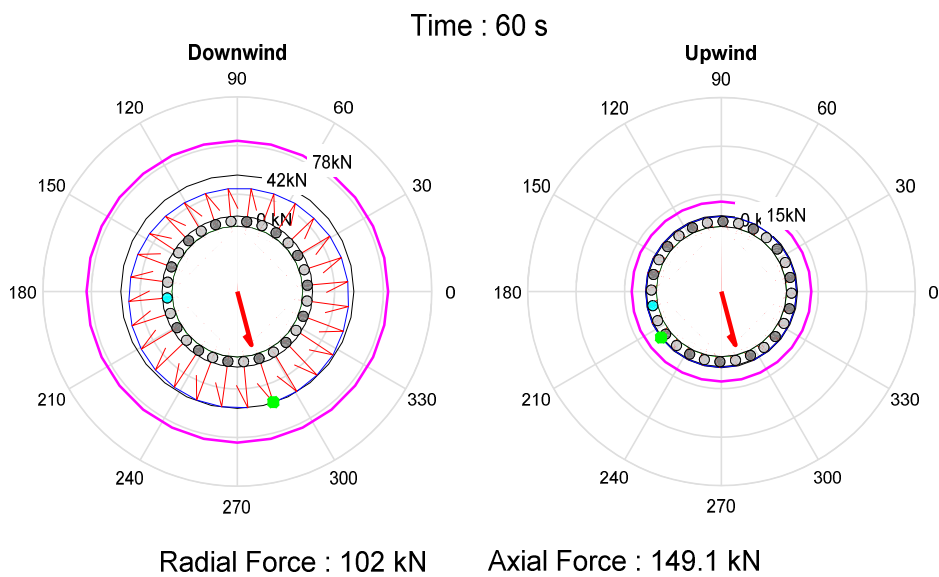


Figure 6.12–Bearing Load distribution at 60s at average speed of 1.5 m/s

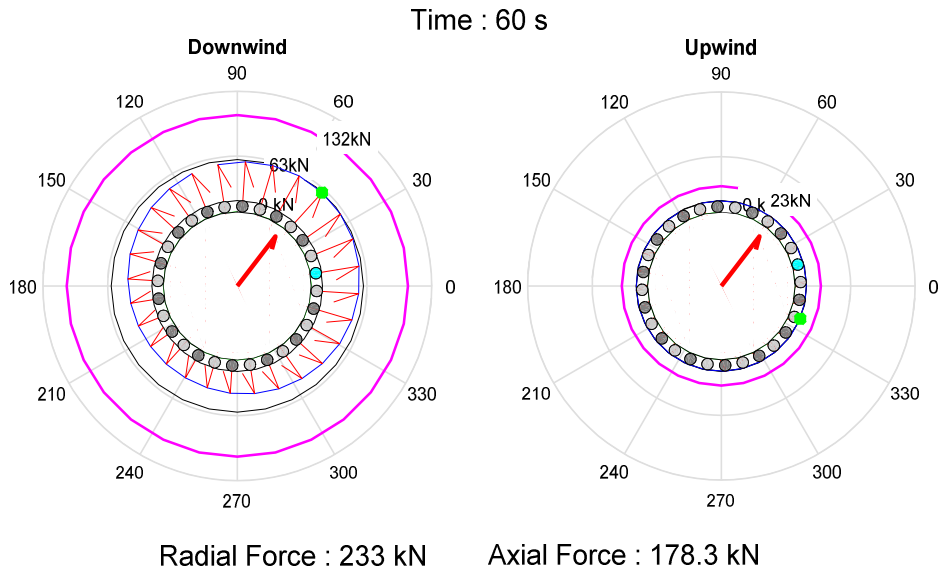


Figure 6.13–Bearing Load distribution at 60s at average speed of 2 m/s

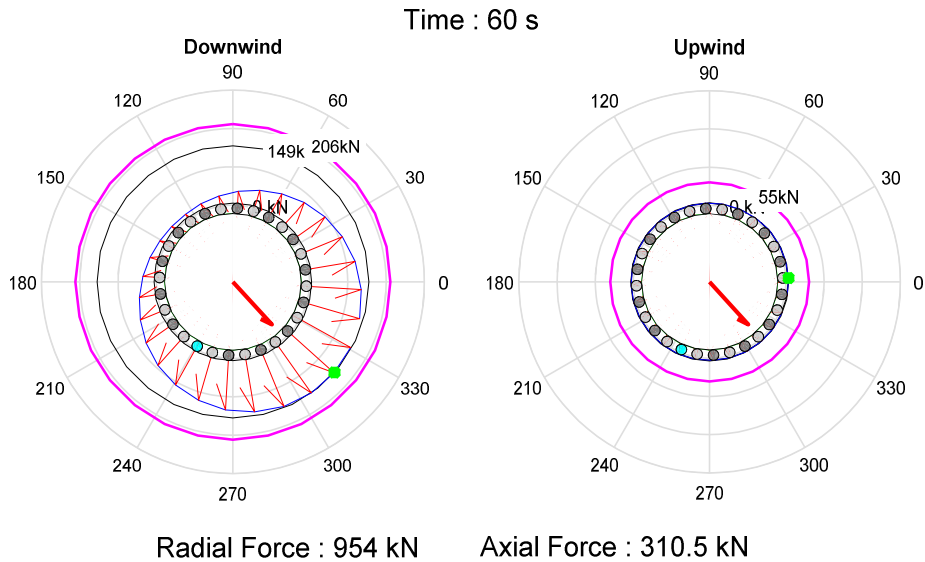


Figure 6.14–Bearing Load distribution at 60s at average speed of 2.5 m/s

Due to the axial load, the total load is mainly carried by the downwind row while the upwind row remains relatively unloaded. This can be seen in Figure 6.14 where

the instantaneous load distribution is shown. Figure 6.8 shows the time history of the load carried by each roller for the case where there is an average tidal velocity of 2.5 m/s. Similarly, Figure 6.9 shows the load carried by the upwind row. It is clear the downwind row of the bearing is subjected to the most loading hence it is the focus of further study.

6.2.3 Bearing component stresses

The bearing loads as shown above impart stresses on the bearing components. As discussed above the inner race is the component being analysed and is discretised into small strips whose stress history is derived and analysed.

For the 230/630-w33 series bearing which has 28 rolling elements, it is reasonable to subdivide the inner race into 28 equally spaced sections or multiples of 28 to maintain equal spacing. The inner race is divided into 112 equally spaced sections each considered to have an angular width of 3.2° .

The stress history of a single section is obtained as shown in Figure 6.15. A more detailed view of the stress history is shown in Figure 6.16. As a roller which carries a load comes across the strip, the strip's stress increases until the strip is directly in line with the roller load. Here, the strip stress registers the maximum stress for the particular roller load. The stress is then reduced as the roller moves away from the strip.

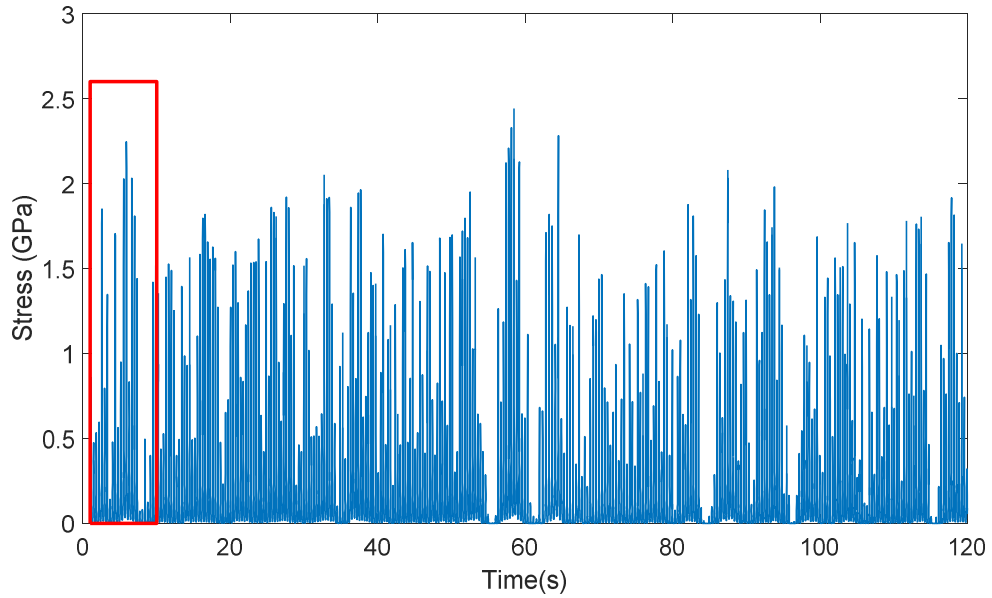


Figure 6.15–Stress History of a single strip at 2.5 m/s tidal speed

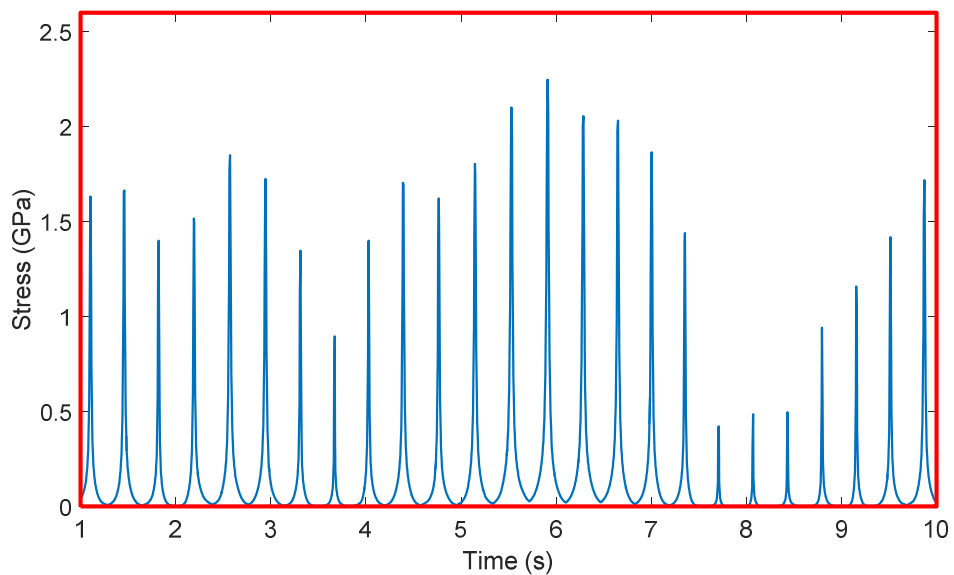


Figure 6.16–Expanded view of stress history of inner race sections

The ASTM rainflow counting algorithm is used to disentangle the stress history of the load into cyclic loads at different stress amplitudes in the stress history. Here the

stresses are grouped by dividing the maximum stress amplitude into a 100 subdivision.

The rainflow matrix for the inner race section with a stress history shown in Figure 6.16 produces a rainflow matrix as shown in Figure 6.17. This shows the stress ranges in the particular strips' stress history and the number of cycles there are in the load signal.

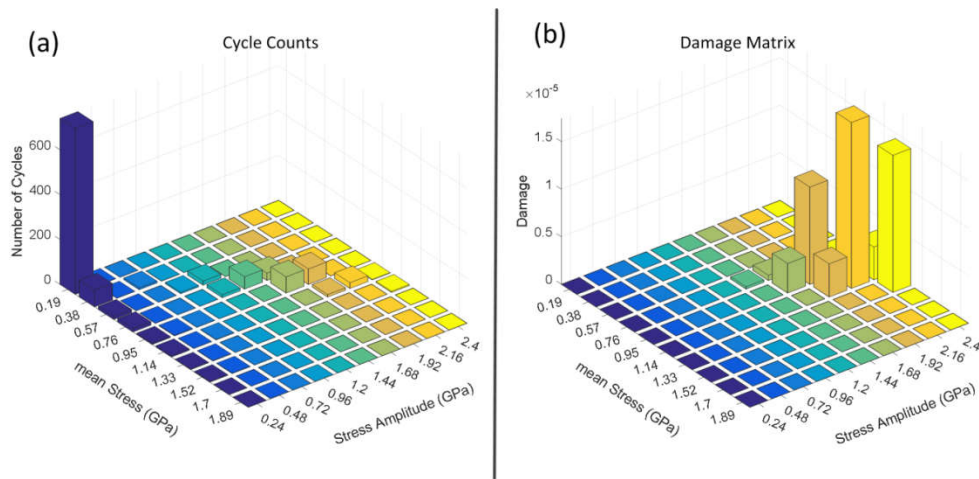


Figure 6.17–Rainflow counting of stress history

6.2.4 Inner race damage profile.

For each strip of the inner race, a damage profile as shown in Figure 6.17 is obtained. Miners linear damage accumulation rule is used to sum up the damage in each strip. Performing this for all strips in the inner race and for all the tidal velocity bins results in Figure 6.18.

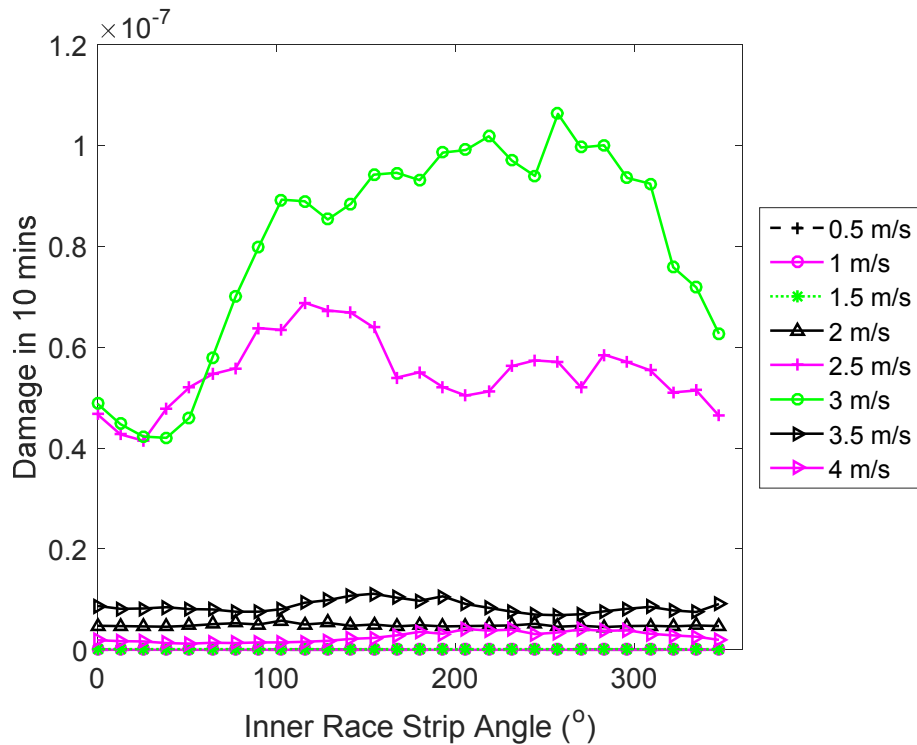


Figure 6.18–Accumulated damage in 10 minutes for different operating speeds)

Generally, there is increased damage around rated speed. This is in part to do with the axial loading which causes the downwind row to be seated while the upwind row is relatively unloaded. There is also increased loading due to the tidal velocity increase.

Figure 6.19 shows the damage accumulated by the inner race in each velocity bin. Here it can be seen that the damage in each section varies significantly. This is mainly due to the dynamic loading condition. It may be argued that over long periods of time the variations due to the dynamic load will average itself out. However, in the interest of being conservative, the highest damage is selected for each bin. Consequently, the lifetime damage obtained from Figure 6.19, by summing up the damages is 0.0251. Assuming the turbine is designed for a safety factor of 2 hence failure is assumed to occur if damage reaches 0.5, the time to failure of the bearing is nearly 400 years.

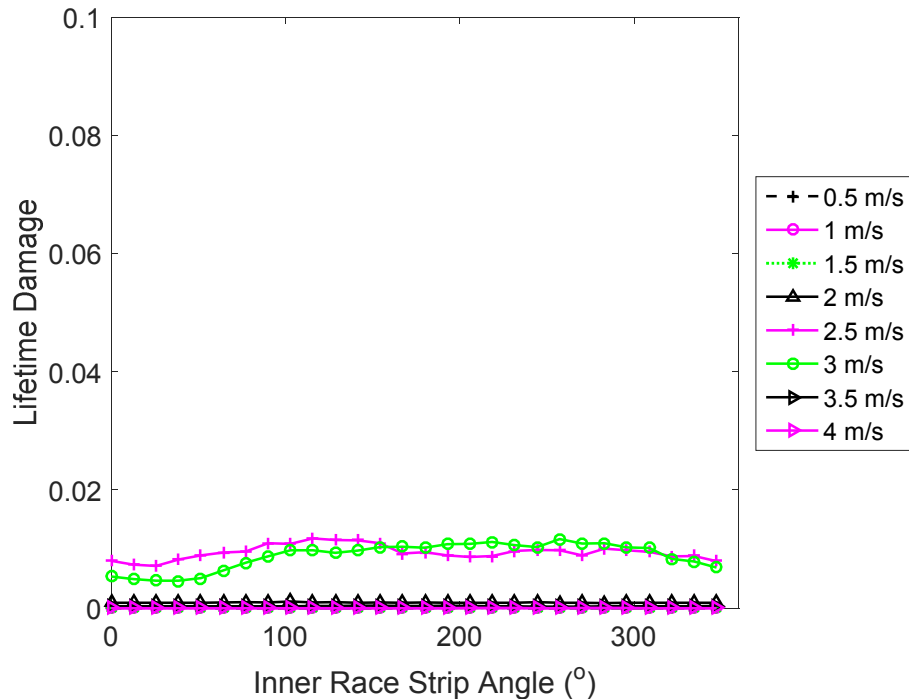


Figure 6.19–Predicted lifetime damage at individual average flow speed bins.

6.2.5 Velocity bin size sensitivity analysis

The velocity range experienced by tidal turbines is limited compared to what is experienced in the wind industry. Consequently using the popular method of bins approach which is common for the wind turbines industry may not necessarily lead to representative conditions in the tidal industry. This is because the 0.5m/s bin size could potentially smear out some of the differences velocity variations may present.

A sensitivity analysis has been performed to investigate the role velocity bin sizes may play when analysing bearing fatigue. This was carried out with the intention of identifying a resolution at which relatively accurate levels of damage can be analysed.

Figure 6.1 shows the velocity probability density function at the chosen site with a bin resolution of 0.5m/s. This resolution is advocated by international standards such as IEC 61400 for wind turbine applications. The operating velocity for wind turbines range from 5-25 m/s. On the contrary, tidal turbines operate at speeds far

less than this. It is, therefore, critical that the velocity distribution is defined with a fine enough resolution to capture the effect of the velocity changes on the calculated life.

A comparative study has been performed to analyse the influence of Velocity PDF bin size on the predicted life of rolling element bearings by using a smaller bin size of 0.1m/s. The PDF for the tidal flow speeds for this bin size is shown in Figure 3.6.

Using the model described earlier in this chapter, bearing loads were evaluated using the elastic model and further analysis conducted to determine component loads. The expected damage caused by all the times the mean flow velocity lied between 2.3 and 2.7 m/s were analysed.

The first instance represented the velocity range by a single bin which has the average of the range of velocities under consideration (i.e. 2.5m/s) . The second case considers the velocity range by dividing them into 5 bins with an average of 2.3m/s, 2.4m/s, 2.5m/s, 2.6m/s and 2.7m/s. Table 6.1 lists the number of seconds spent at each velocity over the 20 year life of a turbine.

Table 6.1: Tabulated values of flow speed probabilities

Velocity(m/s)	Time(s)
2.3	696628
2.4	683563
2.5	663984
2.6	629687
2.7	583921

For each velocity, a velocity flow field is generated with the same random seeds for the flow field calculations. As such the damage calculated is expected to be identical. From Figure 6.20, notice that the average of the two is very similar. Nevertheless, there are big differences between the individual strips of the inner race. The error between the two averages is 1.5408% . On the other hand, the error for various parts of the race way is much larger.

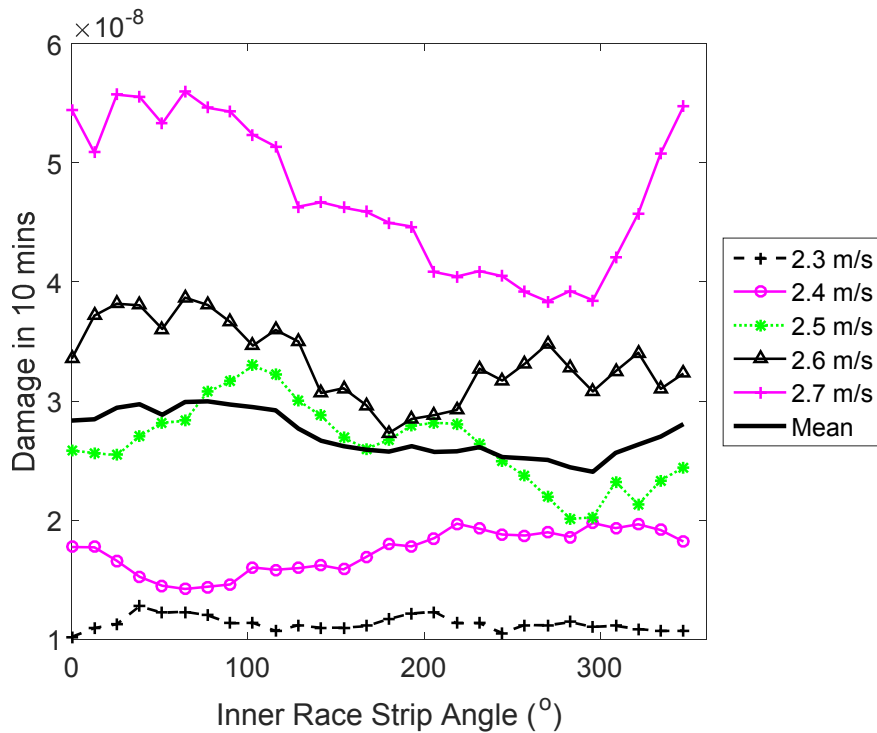


Figure 6.20–Predicted Damage for smaller tidal velocity bins

It is clear from that using a single velocity bin of size 0.5 m/s could lead to over prediction or under prediction of lifetime damage. It is shown above, however, that the average effect of both methods is similar. The discrepancy between the two is most likely caused by the fact that the analysis is performed for a short time period. Longer simulations are likely to lead to an averaging of the calculated damage of each strip.

The average error as seen from is 3.8 %. Consequently, it is concluded that the use of bin size of 0.5 sufficiently captures the average damage caused with little error.

6.3 An accelerated test plan for tidal turbine main bearings

Chapter 6.2 has focused on evaluating the 20 year lifetime damage on the inner race of a tidal turbine main bearing. The next phase is to replicate this damage on the inner race of the bearing in a test rig to demonstrate its resistance to such damage.

Typical testing activity need not just focus on time to failure but practical bearing tests often collect a variety of data, many for design validation. To conduct a typical tidal turbine endurance test, several prerequisite tests must be conducted. In a typical test program, many types of tests may be carried out according to a customer's preference. In this work, however, a test plan is designed to establish the long term performance of a bearing by an accelerated test. The tests to be conducted are as follows

1. Functional test
2. Static test(radial load)
3. Static test(axial load)
4. Bearing characterisation tests (Vibration and temperature)
5. Dynamic test-Transient
6. Dynamic test –Fatigue
7. Extreme load test.

Before testing commences, setting up the bearing could take weeks. Typically, no additional setup activities are required while testing. Each test is, however, followed by inspections to verify the condition of the bearing before the next test. Set up procedures include checking misalignment internal clearance and so on. A summary of the test plan is provided in Figure 6.21.

Test Types	Objective	Process	Axial force	Radial Force	Shaft speed	Duration
Functional Test	Identify manufacturing, handling and installation defect	Confirm bearing and all ancillaries operate as expected	Yes	Yes	Yes	
Static test(Radial force)	Static Design Verification	Measure deflections and strains and compare with design model	No	Yes	No	
Static test	Static Design Verification	Measure deflections and strains and compare with design model	Yes	Yes	No	
Temperature & Vibration Test	Establish baseline thermal and vibration characteristics	Measure Steady state condition conditions under loads	Yes	Yes	Yes	
Dynamic test (Transient)	Verify dynamic design performance	Measure and Compare dynamic behaviour to design models	Yes	Yes	Yes	
Dynamic test (Fatigue)	Verify long term design performance	Apply loads for long periods of time until 20 year damage is reached	Yes	Yes	Yes	
Extreme Loads	Verify survivability of the bearing	Confirm bearing functionality after extreme loads are applied	Yes	Yes	Yes	

Force Key: ≤25% ≤ 50% >50%

Duration Key: Weeks Hours Seconds

Figure 6.21–Summary of test procedure

6.3.1 Maximum test load & design load

It is possible to impose the maximum design load as a fundamental limit which must not be exceeded while testing. However, the maximum design loads as tabulated in Table 6.2 are rarely encountered by the turbine as seen from Figure 6.5. These loads are, therefore, likely to cause impractical failure modes if applied to replicate fatigue damage.

Table 6.2: Maximum design loads

Parameter	Value	Units
Radial force	3.4	MN

Axial Force	420.9	kN
Speed	13.3404	rpm

Notice from Figure 6.16 that when this maximum load is applied to the bearing, the stress history shows regions where the instantaneous stress exceeds the yield point of the material. The stress does not exceed the UTS of the material. However, encroaching into the plastic zone leaves a lot to be desired. There is a potential for plastic strain hardening which could in the long run make the material stronger. On the other hand the occurrence of plasticity could lead to a weakening of the material and acceleration damage in an unexpected manner. Be it to the detriment or improvement of material strength, the occurrence of plasticity introduces uncertainties which are difficult to account for.

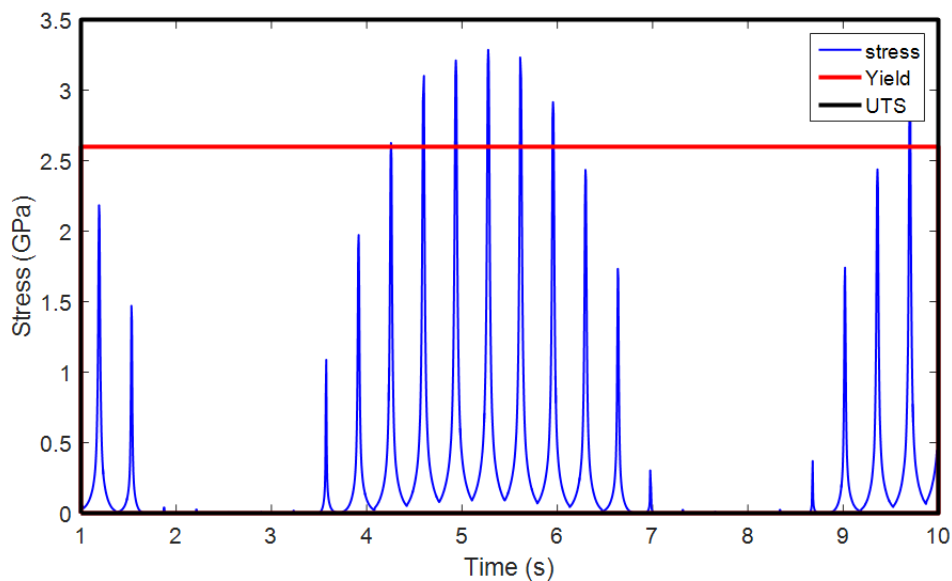


Figure 6.22–Expanded view of stress history of inner race sections

General recommendation for testing full scale bearings have been discussed in Chapter 2.4.2.3, with more details provided in [179]. To avoid unrepresentative damage it is generally recommended the maximum Hertz stress during testing must not exceed 2.4 Gpa [179]. To avoid exceeding the bearing material yield limit, roller loads must not exceed 170kN. This corresponds to a maximum 1.2MN of radial load with a 25% axial load limit (as discussed in Chapter 5.4.3) of 300 kN.

The maximum speed of 11.5 rpm (rated shaft speed) is imposed as in full scales nacelles operating above rated speed for long periods is undesirable.

Table 6.3: Maximum Test loads

Parameter	Value	Units
Radial force	1.2	MN
Axial Force	300	kN
Speed	11.5	rpm

6.3.2 Fatigue test plan development

All tests to be conducted are defined with reference to the test load as listed in Table 6.3. Further description of the tests to be carried out is detailed below.

6.3.2.1 Functional test specifications

A functional test is often the first test to be performed. The main aim for this test is confirm the conformity of the bearing to correct installation procedures and identify potential manufacturing defects. The process of analysing damage assumes a specific design and correct operation of all ancillaries. This must be confirmed before further testing can commence.

For functional test, relatively low loads and speeds are applied over short periods to confirm the bearing does perform its function under these conditions. Two tests are conducted under functional testing, each for 10 minutes. Within this time potential defects such as lubricant leakage and misalignment can be detected and corrected before further testing.

The functional test is initiated without any axial loads because purely radial loads represent ideal operating conditions which should not cause any unexpected behaviour. The application of axial load changes the loads on the bearing rows. In a single cage design this might cause skidding in the unseated row. At this stage the functionality of the bearing both under purely radial and axial loadings confirmed

along with the functionality of all bearing ancillaries. Figure 6.23 shows an example of a recommended test load profile for carrying out functional testing under radial and axial load for the main bearing in this thesis.

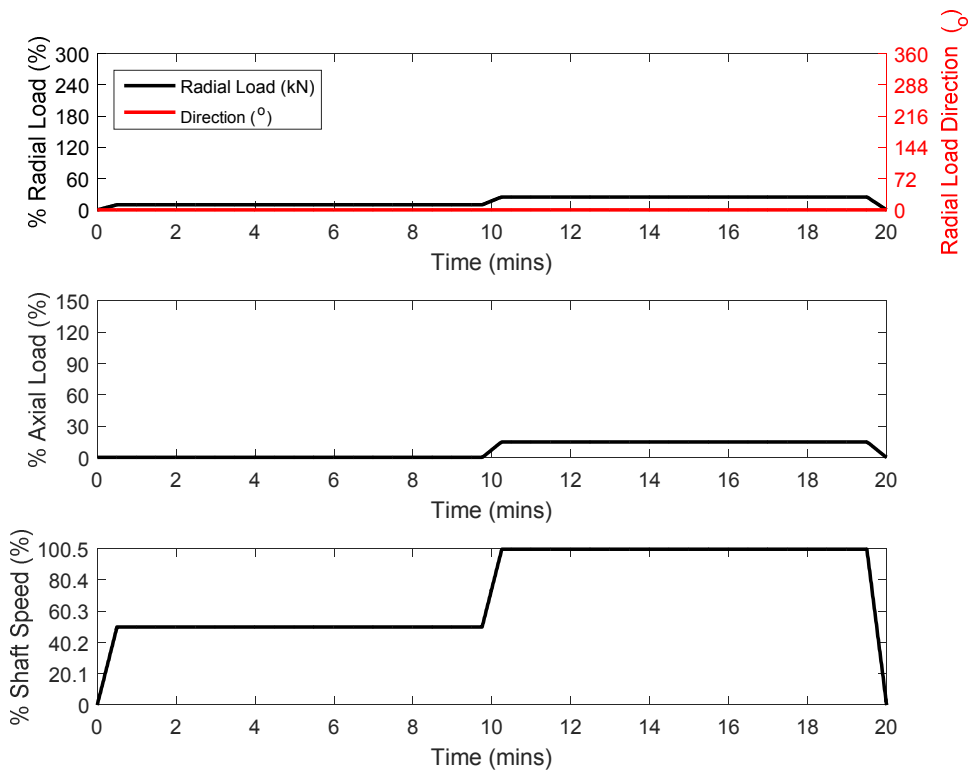


Figure 6.23–Functional test profile showing loads as a percentage of device specification loads

6.3.2.2 Static test (radial force only) specifications

This test confirms the static performance of the bearing under a purely radial load. This will enable engineers to compare the bearing's static behaviour to its expected design. These tests are akin to simulations of standstill conditions; where there is a radial load applied by the hub mass but very little axial loading is present. From the perspective of the test piece performance, the maximum possible displacement and resolution of load application is established by confirmation of the test piece stiffness characteristics.

Proper instrumentation of the bearing will enable static design of the bearing to be confirmed. The radial deformation can be measured by feeler gauges or more sophisticated techniques such as Optical Deformation and Strain Measurement techniques at this stage. The design of the bearing is confirmed when the measured displacements agree well with design models. A profile for carrying out static testing is shown in Figure 6.24. At this stage each load is applied and held for a short time such that the measured displacements can reach a steady figure.

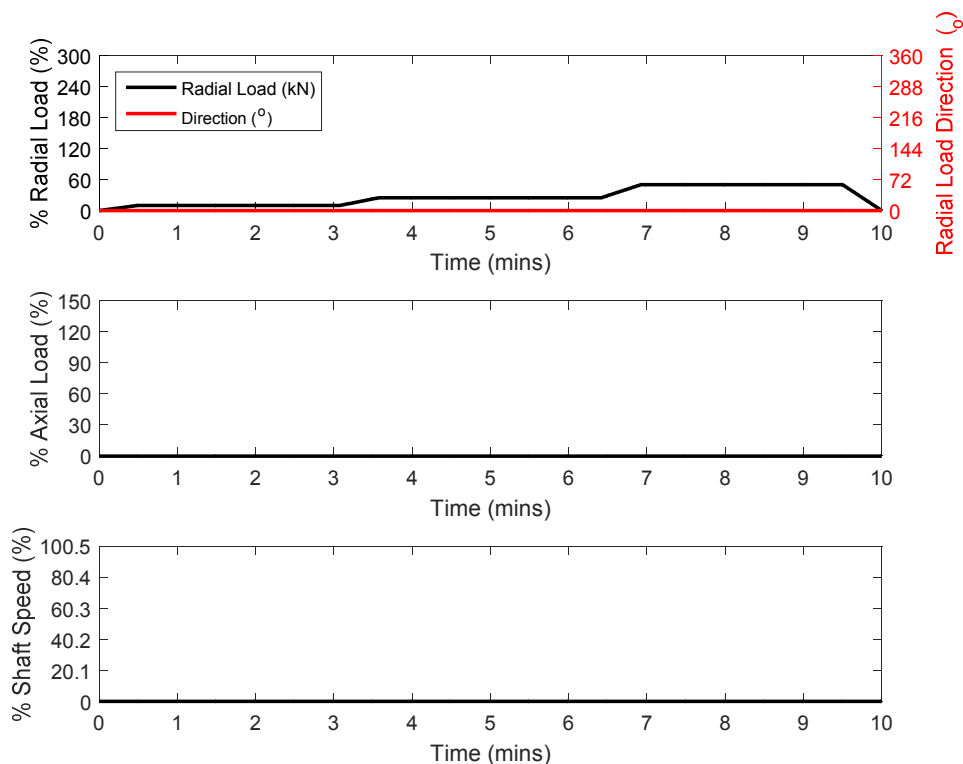


Figure 6.24—Static radial force test profile 50% test radial load

6.3.2.3 Static test (radial and axial loading)

The bearing will carry substantial axial loads at times. Spherical roller bearing is generally very sensitive to axial load. At high axial force the upwind row becomes un-seated. This might cause rollers on the un-seated row to skid, supposing a single cage design is applicable. This test verifies the effect of axial loads on bearing performance. Measured deflections and loading will enable design verification of the bearing under axial load. This follows the process as above with the exception

of the application of axial loads. The loading profile for this test is thus shown in Figure 6.25.

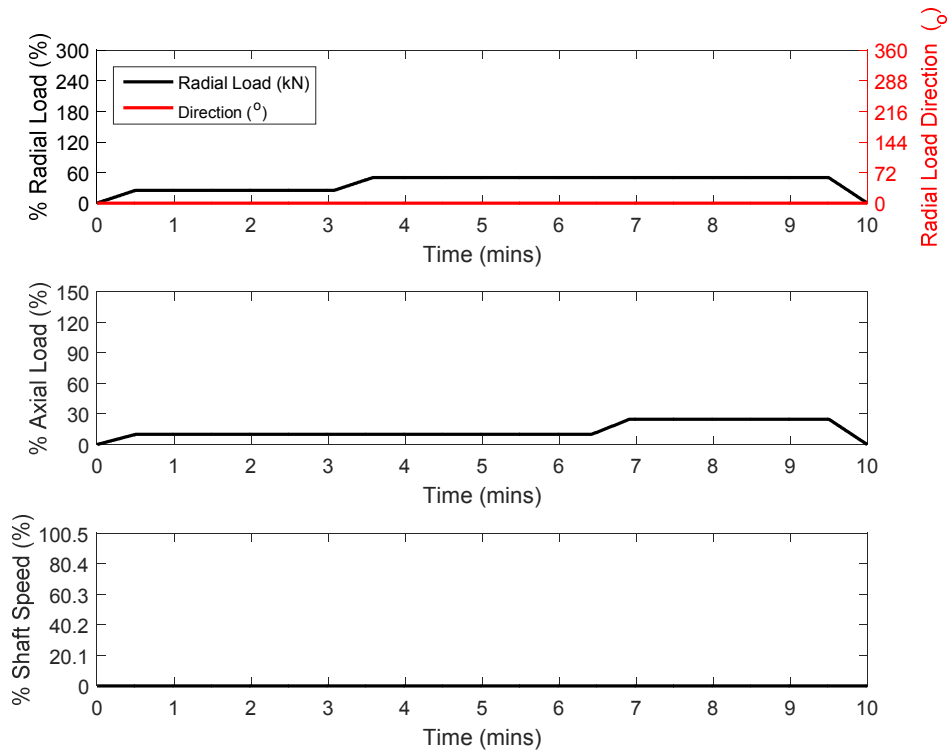


Figure 6.25–Static radial and axial force test profile

6.3.2.4 Thermal and vibration characterisation

Thermal and vibration data are common condition monitoring data that is collected while testing. Thermal and vibration characterisation is a key test which must be conducted to establish the basic performance trends before endurance test. Each of these tests will record the bearing thermal and vibration performance from start till steady state conditions are reached. An estimated 8 hour period is set aside for each testing as steady state conditions may take a long time to achieve.

Due to the long testing time of endurance tests, it is common that tests are broken up into smaller sections. The time to reach steady state thermal conditions after testing starts, can give a good indication of bearing degradation as well as the bearing temperature itself.

Thermal and vibration characterisation will inform the longer fatigue test by establishing baseline performance characteristics which can be tracked to evaluate damage. Through the known thermal and characteristics, potential deterioration can be identified using thermal signal. The same can be achieved using vibration signal. Vibration and temperature data can complement each other because it generally takes longer time for steady state thermal conditions to be reached while vibration levels tend to show little change in short term. Figure 6.26 shows an example of a test profile for performing the baseline temperature and vibration characterisation tests.

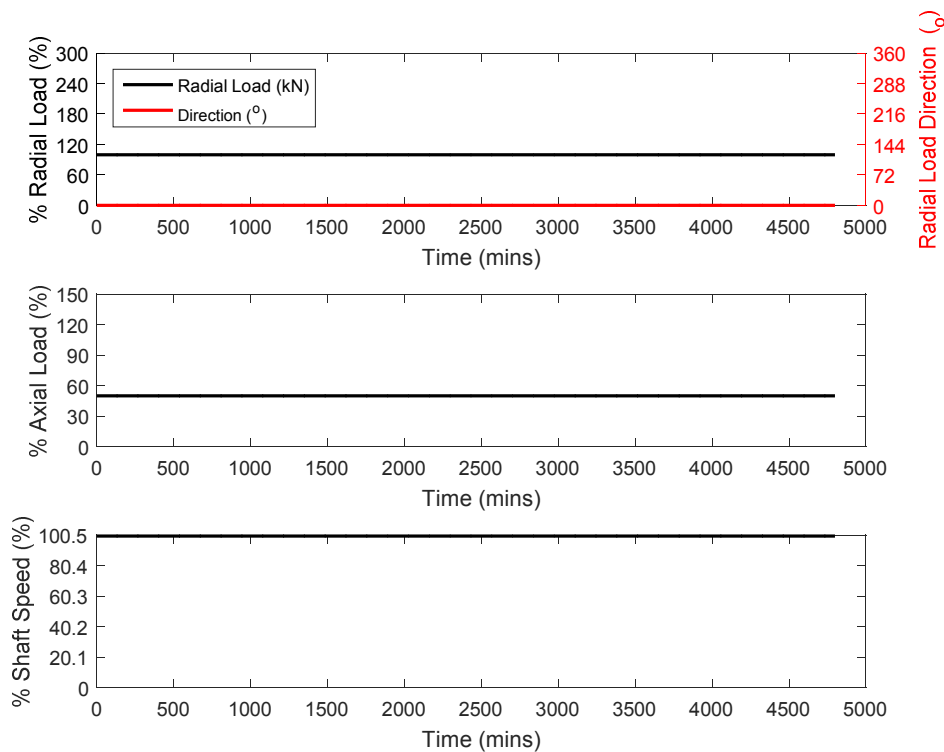


Figure 6.26—Operational (temperature and vibration) characterisation test profile

6.3.2.5 Dynamic test (transient)

This test verifies the dynamic behaviour of the bearing. This is achieved by using service simulated loads to confirm that changes in loading and speed do not lead to unexpected behaviours that lead non-fatigue based failure modes.

The dynamic behaviour of the test piece (main bearings) and the test rig is dependent on the overall system stiffness of the test piece and test rig. The dynamic test will also establish the dynamic range of the test setup before further testing is carried out. This includes the test piece's response to applied load. The test is conducted for a range of loads. The test period must be ample such that the test rig controller can be turned to improve the load applicator performance and endurance. Parameters of interest here include maximum possible load frequencies at different steady state errors, rise time and over shoots.

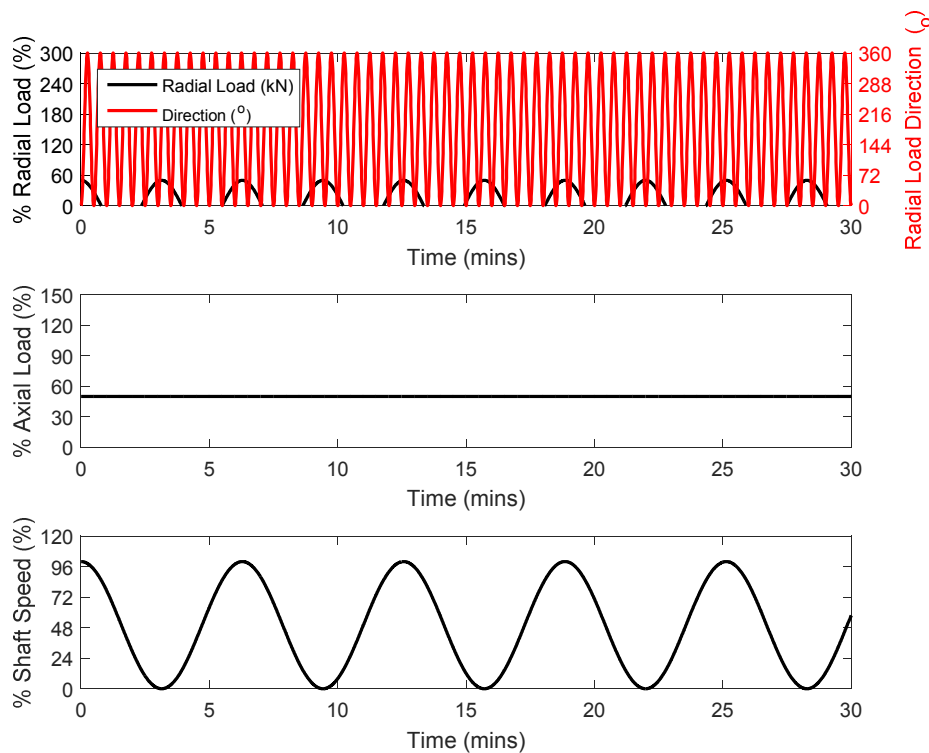


Figure 6.27—Example of a dynamic test profile with varying speed, varying radial force magnitude and direction at a constant axial load

6.3.2.6 Dynamic test (Fatigue)

Fatigue test is aimed at demonstrating the long term performance of the bearing. An accelerated test method is often required here to reduce the testing time to a more suitable period. Due to practical reasons, such large scale bearings tests can be conducted with one or very few samples. This makes it challenging to draw

statistical information from testing. Due to the high scatter of bearing life, applying up to three times the calculated lifetime damage gives more confidence in the fatigue performance of the bearing. The test profile must, therefore, accelerate the degradation process. The AbP method as highlighted above needs to be applied.

Dynamic Fatigue Test Profile development

A range of potential test profiles have been studied to establish the best profile for testing. For all the cases the maximum allowable loads (radial load:1.2MN, axial load: 300kN, speed :11.5rpm) is applied. The potential test profiles include as static radial force which is akin to conventional test methods. Four additional test profiles are designed using the AbP method.

Figure 6.28 compares the evaluated damage using a range of radial loads. The static radial force line (black \pm) represents the conventional approach used for endurance testing of bearings. This is compared to a range of potential test loads developed by the AbP method. In all cases, θ_r is selected to focus the maximum damage in the same location. Where θ_g is not specified θ_g is zero. By increasing θ_g the maximum damage in a unit time is reduced. However, a broader section of the inner race has its damage accelerated.

The time taken to reach the evaluated 20 year lifetime damage is shown in Figure 6.29 for the same range of conditions. As expected, the maximum acceleration is achieved with the AbP method when $\omega_{ir} = \omega_r = \text{inner race rotational speed}$ and θ_g is zero. In this case the twenty year damage can be replicated by a continuous operation in 47 days with an axial load of 300 kN and a radial load of 1.2Mn

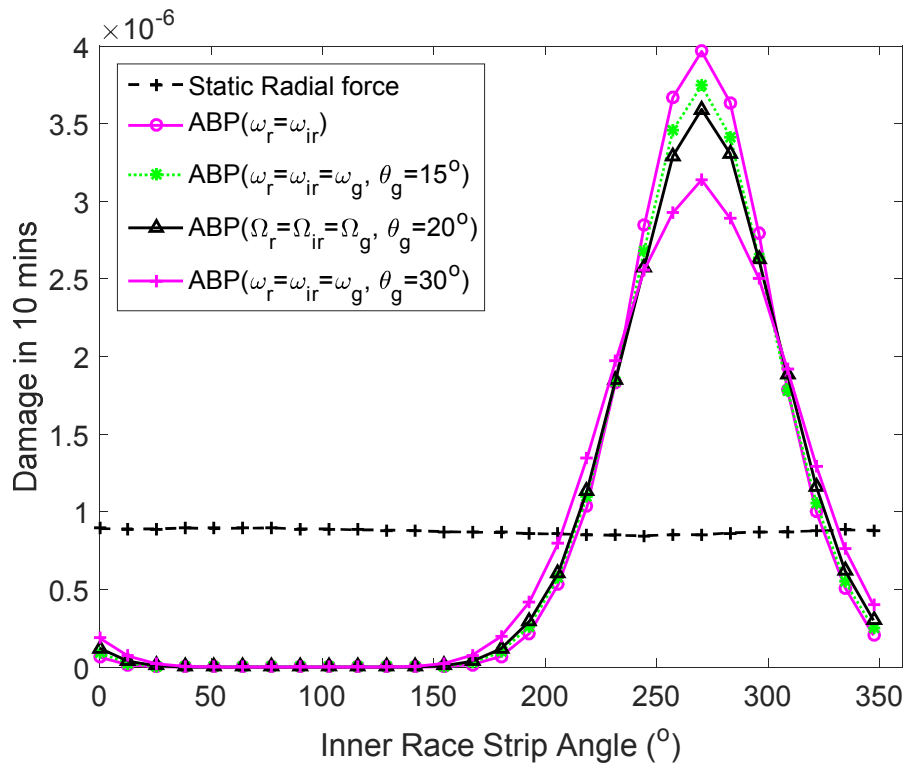


Figure 6.28—Incurred damage for proposed testing loads

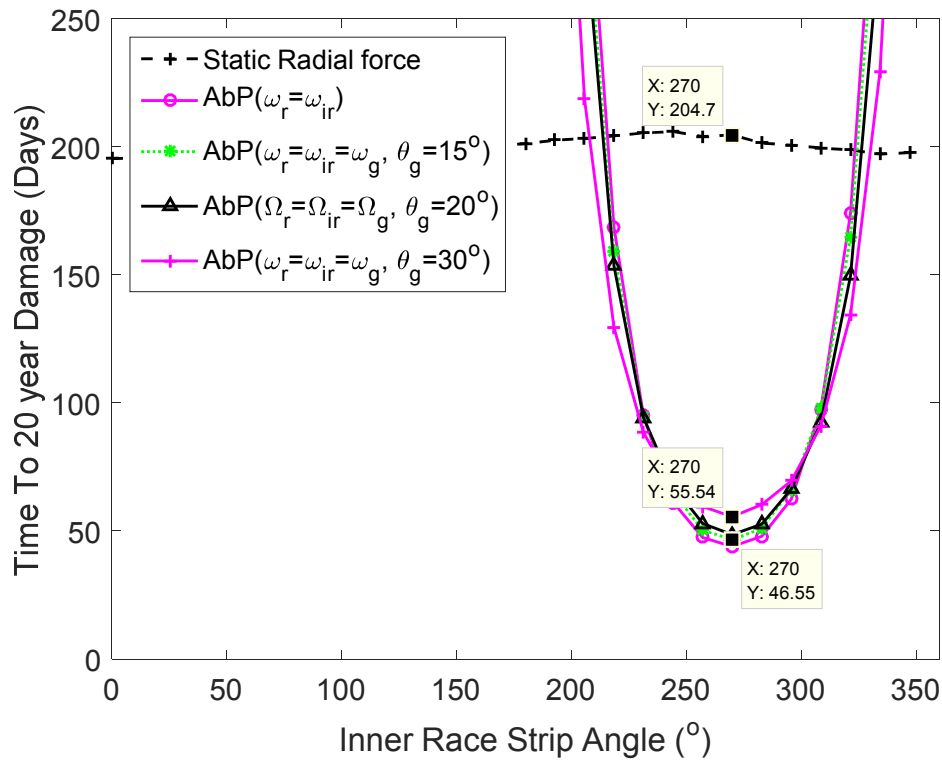


Figure 6.29—Estimated time to reach 20 year damage by using AbP method

Supposing test to failure is the target, it will take considerably longer times to achieve failure. From the basic bearing L_{10} life calculation, the life of a bearing subjected to a static radial load of 1200 kN and an axial load of 300 kN at 11.5 rpm is 6.9863 years. This is in good agreement with the calculated 10.6 years (3873.7 days) from Figure 6.30. Evidently, the time to failure can be reduced by a factor of 4.4 to 2.4 years (860 days) if reducing time to failure is the target for accelerated testing.

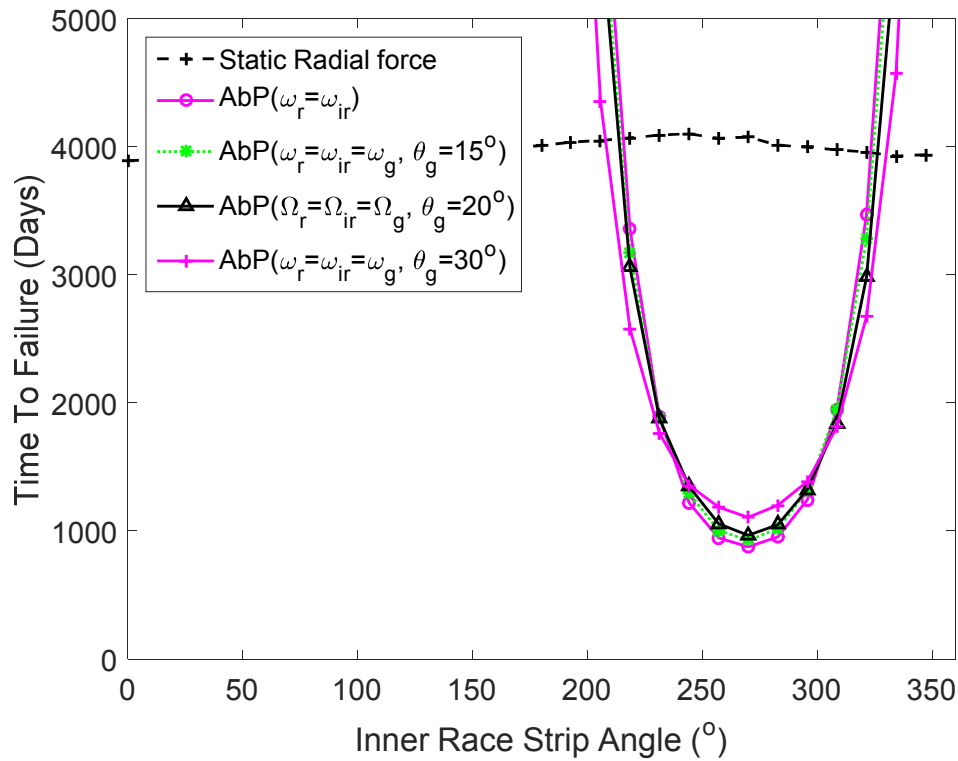


Figure 6.30–Estimated Time to failure in testing under various testing condition

Using the AbP method, the test profile for performing fatigue test will be as shown below in Figure 6.31. The test profile in Figure 6.31 is repeated from 66240 to 198720 times to represent 3 times the calculated damage on the turbine components. Due to the long testing time, testing is often stopped at some point to allow regular inspection. The number of repeated cycles must be recorded and tallied up to ensure representative loading cycles are achieved during the testing.

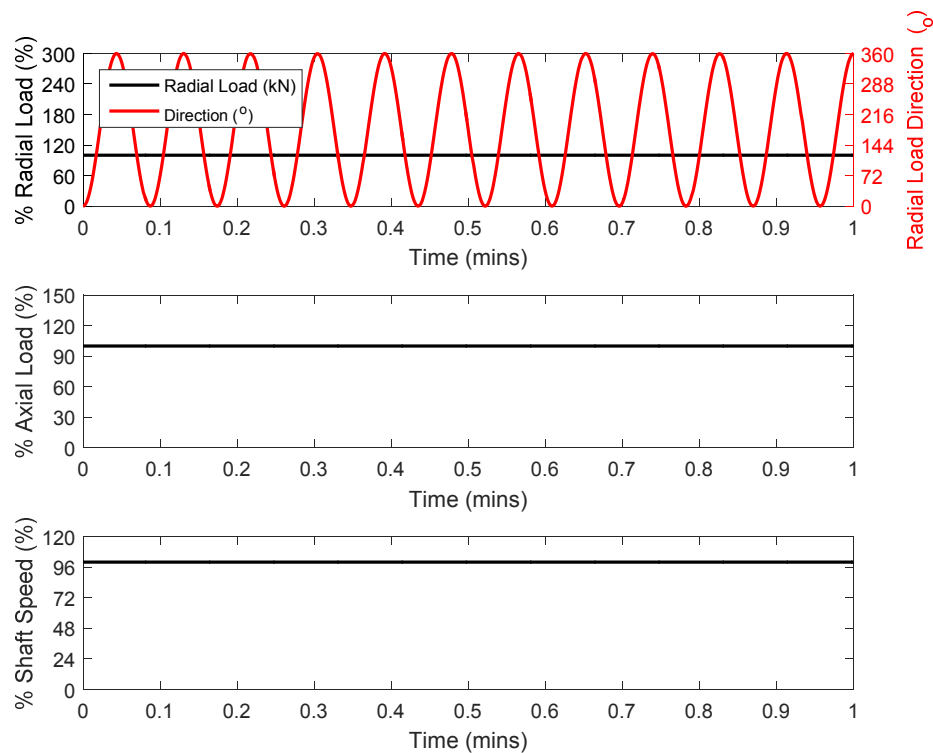


Figure 6.31–Accelerated fatigue test profile

6.3.2.7 Extreme load test

The turbine is expected to encounter some extreme loads during its operational life. These loads rarely happen, but can have a tremendous effect on the bearing life. This work considers fatigue damage which largely occurs at much lower loads. Nonetheless, to gain confidence in the reliability of the turbine over its life time, its propensity to survive extreme loads must be verified. This confirms that after an extreme load event is encountered somewhere in life, the bearing returns to normal operating conditions and accumulates further fatigue damage. These extreme loads although short lived, are likely to lead to over loading which may cause plastic deformation and create stress risers which will also affect the fatigue life of the bearing. A test profile for extreme loads may be generated based on the expected design extreme loads as shown in Figure 6.5.

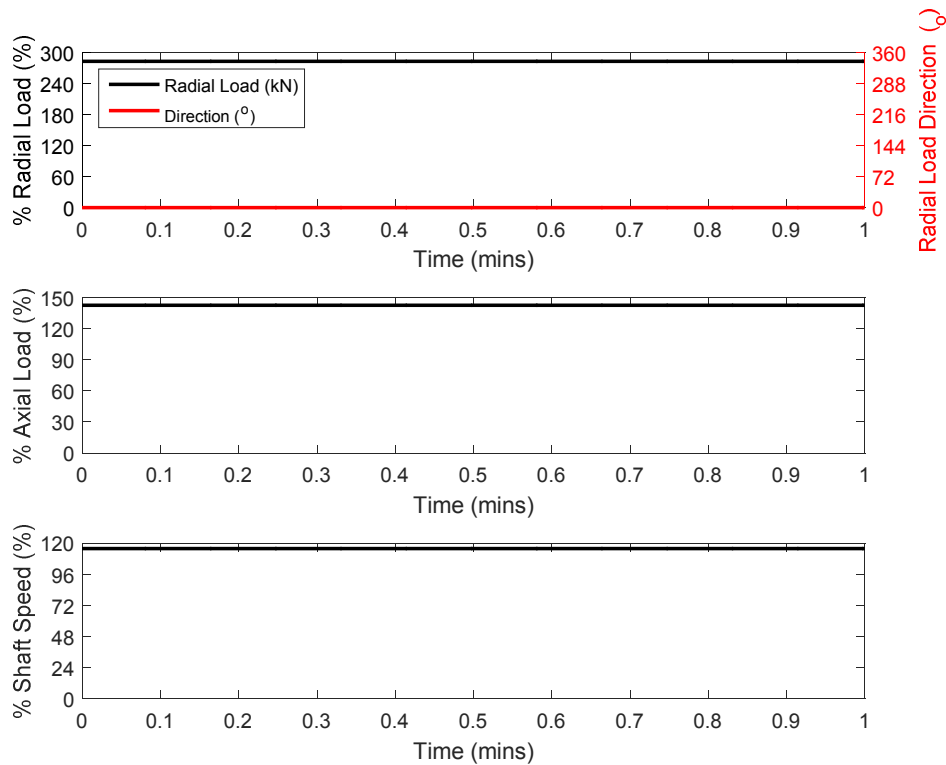


Figure 6.32–Extreme loads test profile

6.3.3 Generalised test plan for main bearings

A large variety of tests can be performed for a range of reasons ranging from design validation, power performance assessment, reliability demonstration and so on. This work is focused on reliability demonstration therefore relevant tests which demonstrate reliability when carried out are discussed.

A test may enquire the reliability and performance at specific operating conditions as well as general operating conditions that are experienced over the lifetime of a turbine. To simplify this range the conditions are categorised under extreme events, transient events and fatigue events. These conditions are defined to be dependent on the time scales at which damage caused by these events occur.

Extreme events tests are those severe events that rarely happen and are often encountered for a short time. They may be introduced as a result of extreme conditions or a synergetic effect between several less extreme conditions coming

together, leading to loads that are much larger than observed in normal operation time. These are likely to cause catastrophic failure when they are encountered. Transient load on the other hand happen more often than extreme loads and can include extreme loads, also often take place over a short time period. These tend to be high loads which are encountered in events such as starts, emergency stops (with brake), and grid failures and so on. These can lead to catastrophic failure but often result in acceleration of the degradation process rather than catastrophic failure. Fatigue loads on the other hand include those moderate loading conditions which tend to cause damage by accumulating high numbers of loading cycles.

For each loading condition, specific bearing performance figures can be chosen as target for testing. For example, film thickness, traction distribution, load distribution, noise, life, wear, damage etc. This work focuses on the fatigue damage of the inner race; as such testing such damage under these loading conditions is of interest. However damage can be swapped with other performance indicators.

Table 6.4 details a range of tests that are performed to demonstrate design lifetime reliability. Each type of test will consist of a test profile which may have constant or varying loads. Duration of tests and number of sub-test profiles that are performed is generally dependent on customer preferences due to changes in design from one manufacturer to the other. As such each test is bespoke however typical values to test specification ranges are provided in Table 6.4.

Table 6.4: summary of test plan for an accelerated testing campaign

Test Type	Duration (days)	Comments	Example of test Profile	% Radial load	% Axial load	% Speed	Extreme	Transient	Fatigue
Functional Test	0.5-1		Figure 6.24	0-5	0	0-100	●	●	●
Static Test (radial load)	0.5		Figure 6.25	0-50	0	0	●	●	●
Static test (axial load)	0.5		Figure 6.26	0-50	0-50	0	●	●	●
Temperature & vibration characterisation	4-5	+	Figure 6.27	0-100	0-100	0-100	○	○	●
Dynamic test	5-6	**	Figure 6.28	0-100	0-100	0-100		●	○
Fatigue Test (dynamic)	55-60	++	Figure 6.32	100	100	100			●
Extreme Test	0.5	--	Figure 6.33	283	140	116-150	●		

Key : ●-Mandatory ○-Recommended

Comments

- + Based on 5 test profiles with 20% load step increments with combined axial, radial and speed increments. Figure 6.27
- ++ This is based on the application of the AbP method to reduce testing time from a possible 200 days (from Figure 6.30) to 55 days. This assumes continuous operation throughout test duration. Typically testing may be extended to gain more confidence in the survivability of the test piece for twice or thrice its lifetime without failure.
- ** Based on 6 dynamic load cases at different speeds and load. Tests are run till steady state conditions are reached at each load level.
- This test uses the maximum design load as given in Table 6.2 and Figure 6.5. Generally 50% over speed condition is also recommended

To demonstrate the reliability of bearings over their lifetime, all the tests identified in Table 6.4 are necessary. Notice that the most time consuming test is the fatigue test. Nevertheless a considerable time saving has been achieved using the AbP method to reduce testing time for the fatigue test to such low levels.

Chapter 7 Conclusions

7.1 Introduction

For remotely located devices such as tidal turbines, operational reliability is of utmost importance. Laboratory testing offers a great way to demonstrate reliability in a safe controlled environment before deployment. However, due to the long operating time of tidal turbines, demonstrating the reliability of their main bearings in real time is impractical due to time constraints. This work has presented a methodology for carrying out testing of main bearings in an accelerated manner to reduce test time while applying representative lifetime damage. The process for testing main bearings has been categorised under design evaluation damage replication.

Conventionally, design load cases are supplied by turbine developers to test centres. This includes many design assumptions, which must be representative of real turbines, if the evaluated bearing damage that is then replicated is to be accurate. The process for evaluating the design loads is treated in Chapter 3, including discussions on how the bearings environment, design and control affects the main bearing load cases. Supposing design loads are readily available, they can be used as input into the methodology as shown in Figure 1.3. The global bearing loads can be transformed into a stress history as outlined in Chapter 4. The chapter also outlines the process of evaluating the damage based on the stress life method. Chapter 5 presented an unconventional method of accelerating the damage of main bearings using a full scale nacelle test facility capable of applying dynamic 6 DOF loads. The influence of the different parameters involved in the test methodology was also discussed. Chapter 6 then combined the methodologies in the previous 3 chapters to illustrate the process of achieving the aims and objectives of this work

by showing how the work in this thesis can be applied in realistic test plans for the main bearings in a tidal turbine. The Overall conclusions of this work are presented below.

Since the conclusions are based on analyses conducted on a hypothetical turbine, the results may be interpreted as qualitative since the results may deviate from reality. For example, micro-geometry modifications are performed on roller-raceway contacts to relief high stresses in the contact zone but these have not been considered here. To add to that, the level of potential test acceleration will not only depend on the loading on the turbine but also depends on factors such as geometry. Consequently, the observations from this work may not be generalised but can be applied to specific applications. Some outputs such as Figure 6.21 and Table 6.4 however, can be used as a starting point for the design of test plans regardless of the design or components.

7.2 Main shaft load case evaluation

The main shaft design load cases are typical inputs provided by device developers to test centres. For the validity of the assessed lifetime damage, realistic environmental conditions, as well as turbine behaviour that affect the main shaft loading, must be well understood. It was found that. It must be stressed that the elastic model used in this work has not been verified by experimentation. On the other hand, device developers that are ready for full-scale nacelle testing often possess validated datasets which allow conclusions such as outlined below to be drawn.

- The most influential environmental condition that affects the main shaft loading is the average tidal velocity. As such, critical evaluation of this for potential tidal sites is necessary. The used of ADCPs and tidal harmonic analysis to predict long term average flow speeds is recommended.
- The controller's performance in response to the environmental conditions has a massive effect on the turbine's loading and eventual life. Accurate modelling of the control system is critical. As a result, the so-called

“Hardware in the loop” system may enable better examination of the control system in nacelle test facilities before they are deployed.

- Increased turbulence can increase non torque loads on the main shaft, therefore, characterising turbulence intensity for tidal sites is important.
- The axial component of turbulence is of paramount importance. It has a much bigger effect on the main shaft loading than the off-axis components of turbulence.
- Wave induced water particle velocities affect the main shaft loading. Mainly at high wave heights and periods.
- The shear profile of a potential turbine deployment site must be carefully studied. Although the effect of the shear profile may be small in terms of torque and axial loads, the effect on the off-axis forces and moments can be staggering. The popular $1/7^{\text{th}}$ power law gives a good range of loading, although there are large increases in some non-torque loading as the power law exponent increases.
- Cavitation can have an influence on shaft loading, but its inception is unlikely for properly designed blades.

7.3 Bearing component load analysis

- Time domain roller loads are effectively calculated using a rigid dynamics package. Dynamic effects and the effect of gravity can be included.
- It has been confirmed that spherical roller bearing may not be an appropriate main bearing of choice for tidal turbines, despite its larger load carrying capacity and tolerance of misalignment. The axial to radial force at operating speeds are such that the downwind bearing remains seated while the upwind bearing is relatively unloaded.
- The presence of roller edge loading was confirmed through FE modelling.
- Edge stresses can far exceed the stress at the middle of the roller. Hence, stress induced by edge loading is likely to cause the initial fatigue spall.
- The depth of the maximum stress caused by edge loading at the edge of a roller is closer to the surface of the contact than maximum stress in the middle of a roller, hence shallower spalls may form.

- The stress induced by edge loading is likely to cause the initial fatigue spall due to its magnitude.
- A Force-Stress look up table was employed to convert roller loads into stresses caused at the roller-raceway contact.
- Stress history of the inner race can be analysed using the stress-life model to predict damage and time to failure.

7.4 Accelerated test methodologies for turbine main bearings

- Conventional methods for testing tidal turbine drivetrain do not necessarily apply representative lifetime damage in test facilities.
- Conventional methods for accelerating endurance testing of isolated bearings can be used in nacelles but not to the full extent as can be achieved for smaller bearings.
- Damage on the inner race of a bearing can be accelerated while maintaining a constant magnitude of radial load and speed. This can be achieved by redefining the radial load to focus the maximum damage of specific sections of the bearing
- Acceleration by Phase-shift (AbP) method has been developed and is recommended for accelerating the damage on the inner raceway of the bearing. This method concentrates the overall damage that can be applied in one cycle to a smaller section of the bearing, therefore reducing time to failure to about a factor of 4.5
- A comprehensive test plan was presented to put the procedure for carrying out accepted tests in context.
- This work is based on a hypothetical turbine and contains many assumptions therefore the results provide qualitative indicators which may be applied to specific devices to achieve quantitative outputs.

7.5 Future work

This work has treated accelerated testing methodology for tidal turbine main bearing considering sub-surface initiated spalling. Spalling is the eventual failure mode for properly lubricated bearings which are used in suitable applications, but in reality bearings may be subjected to imperfect conditions, which enable other failure modes to develop. These failure modes, many of which are lubrication dependent, are competing failure modes, and it may not be known which one may terminate the failure process. The primary failure modes of bearings include pitting (micro and macro), scuffing, abrasive wear, fretting, brinelling (true and false).

The process of assessing wear in surfaces in rolling contact has been studied by many researchers. Most of these have focused on rail wheel contacts. One such model is presented by Totten [190] and follows the schematic as shown in Figure 7.1 below:

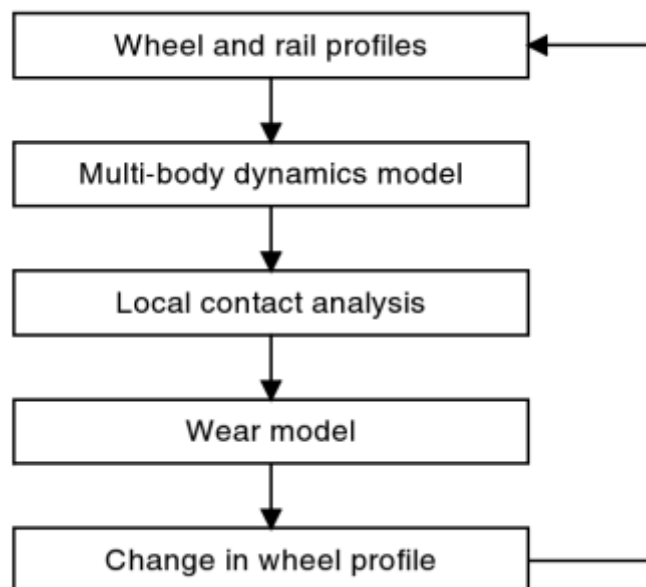


Figure 7.1: Schematic for wear evolution evaluation tool

Pitting is another failure mode that must be studied. Unlike spalling, pitting damage is mainly caused by stress on the surface of a rolling contact. The role of the lubricant is, therefore, critical in avoiding the surface asperities from coming in

contact with each other. The study of potential pitting can be performed in a similar fashion as has been done here for spalling. However, the effect of surface shear stress must be included by studying contact traction, lubrication, and surface roughness and so on.

The study of surface initiated failure modes and wear demands finer modelling of the contacting surface. By modelling the traction in the contacting surface, the surface shear stress and its effect on pitting and abrasive wear can be well understood.

Scuffing is also partly influenced by lubrication conditions. The slippage/skidding of a roller to cause scuffing is dependent on the frictional properties of the lubricant surface conditions and loading. The potential for slippage/skidding has been studied by [191].

All in all, the premises for all the further work will look at the effect of lubrication on the life of a bearing. The same approach used in this work can be applied, but further improvements in the approaches used in this work can be achieved by carrying out the following tasks:

- The turbine model must be improved to add effects such as added mass forces, buoyancy, and the simulation of realistic sea states as opposed to superposing of single waves.
- For the nature of the stress in the contact area and the type of fatigue damage in Rolling Contact Fatigue (RCF), a linear elastic fracture mechanics or continuum damage mechanics approach is likely to yield better damage predictions compared to the stress-life method used in this work.
- The AbP method will benefit from experimental validation, be it at full scale or at a small scale.
- Due to the statistical nature of bearing failures, it is not enough to test a single sample for validation but many samples must be tested in order to gain the statistical confidence needed to confirm the theories proposed in this work.

Chapter 8 References

- [1] R. F. Nicholls-Lee and S. R. Turnock, "Tidal energy extraction: renewable, sustainable and predictable," *Sci. Prog.*, vol. 91, no. Pt 1, pp. 81–111, 2008.
- [2] "Tidal devices : EMEC: European Marine Energy Centre."
- [3] F. O Rourke, F. Boyle, and A. Reynolds, "Tidal energy update 2009," *Appl. Energy*, vol. 87, no. 2, pp. 398–409, Feb. 2010.
- [4] M. S. Güney and K. Kaygusuz, "Hydrokinetic energy conversion systems: A technology status review," *Renew. Sustain. Energy Rev.*, vol. 14, no. 9, pp. 2996–3004, Dec. 2010.
- [5] N. Barltrop, K. S. Varyani, A. Grant, D. Clelland, and X. P. Pham, "Investigation into wave—current interactions in marine current turbines," *Proc. Inst. Mech. Eng. Part J. Power Energy*, vol. 221, no. 2, pp. 233–242, Mar. 2007.
- [6] C. Iliev and D. Val, "Tidal current turbine reliability: power take-off train models and evaluation," in *Proc. 3rd International Conference on Ocean Energy, Bilbao*, 2010.
- [7] T. M. Delorm, D. Zappalà, and P. J. Tavner, "Tidal stream device reliability comparison models," *Proc. Inst. Mech. Eng. Part O J. Risk Reliab.*, vol. 226, no. 1, pp. 6–17, Feb. 2012.
- [8] V. Venugopal *et al.*, "EquiMar. Deliverable D2. 2. Wave and tidal resource characterisation," 2011.
- [9] D. M. Ingram, *Protocols for the equitable assessment of marine energy converters*. Lulu. com, 2011.
- [10] R. Pawlowicz, B. Beardsley, and S. Lentz, "Classical tidal harmonic analysis including error estimates in MATLAB using T_TIDE," *Comput. Geosci.*, vol. 28, no. 8, pp. 929–937, Oct. 2002.
- [11] E. Osalusi, "Analysis of wave and current data in a tidal energy test site," Ph.D., Heriot-Watt University, 2010.
- [12] G. McCann, M. Thomson, and S. Hitchcock, "Implications of site-specific conditions on the prediction of loading and power performance of a tidal stream device," in *2nd International Conference on Ocean Energy, Brest, France*, 2008.
- [13] I. G. Bryden, S. J. Couch, A. Owen, and G. Melville, "Tidal current resource assessment," *Proc. Inst. Mech. Eng. Part J. Power Energy*, vol. 221, no. 2, pp. 125–135, Mar. 2007.

-
- [14] E. Osalusi, "Analysis of wave and current data in a tidal energy test site," Thesis, Heriot-Watt University, 2010.
- [15] P. Mycek, B. Gaurier, G. Germain, G. Pinon, and E. Rivoalen, "Experimental study of the turbulence intensity effects on marine current turbines behaviour. Part I: One single turbine," *Renew. Energy*, vol. 66, pp. 729–746, Jun. 2014.
- [16] I. A. Milne, R. N. Sharma, R. G. J. Flay, and S. Bickerton, "Characteristics of the turbulence in the flow at a tidal stream power site," *Philos. Trans. R. Soc. Lond. Math. Phys. Eng. Sci.*, vol. 371, no. 1985, p. 20120196, Feb. 2013.
- [17] S. Gooch, J. Thomson, B. Polagye, and D. Meggitt, "Site characterization for tidal power," in *OCEANS 2009, MTS/IEEE Biloxi - Marine Technology for Our Future: Global and Local Challenges*, 2009, pp. 1–10.
- [18] J. MacEnri, M. Reed, and T. Thiringer, "Influence of tidal parameters on SeaGen flicker performance," *Philos. Transact. A Math. Phys. Eng. Sci.*, vol. 371, no. 1985, p. 20120247, Feb. 2013.
- [19] Y. Li, J. A. Colby, N. Kelley, R. Thresher, B. Jonkman, and S. Hughes, "Inflow Measurement in a Tidal Strait for Deploying Tidal Current Turbines: Lessons, Opportunities and Challenges," pp. 569–576, Jan. 2010.
- [20] D. V. Val, L. Chernin, and D. V. Yurchenko, "Reliability analysis of rotor blades of tidal stream turbines," *Reliab. Eng. Syst. Saf.*, vol. 121, pp. 26–33, Jan. 2014.
- [21] H. L. Grant, R. W. Stewart, and A. Moilliet, "Turbulence spectra from a tidal channel," *J. Fluid Mech.*, vol. 12, no. 02, pp. 241–268, Feb. 1962.
- [22] A. Kolmogorov, "The Local Structure of Turbulence in Incompressible Viscous Fluid for Very Large Reynolds' Numbers," *Akad. Nauk SSSR Dokl.*, vol. 30, pp. 301–305, 1941.
- [23] R. K. Walter, N. J. Nidzieko, and S. G. Monismith, "Similarity scaling of turbulence spectra and cospectra in a shallow tidal flow," *J. Geophys. Res. Oceans*, vol. 116, no. C10, p. C10019, Oct. 2011.
- [24] J. Kaimal, J. Wyngaard, Y. Izumi, and O. Cote, "Spectral characteristics of surface-layer turbulence," *Q. J. R. Meteorol. Soc.*, vol. 098, no. 417, pp. 563–589, Jul. 1972.
- [25] J. Thomson, B. Polagye, V. Durgesh, and M. C. Richmond, "Measurements of Turbulence at Two Tidal Energy Sites in Puget Sound, WA," *IEEE J. Ocean. Eng.*, vol. 37, no. 3, pp. 363–374, Jul. 2012.
- [26] M. J. Lewis, S. P. Neill, M. R. Hashemi, and M. Reza, "Realistic wave conditions and their influence on quantifying the tidal stream energy resource," *Appl. Energy*, vol. 136, pp. 495–508, 2014.
- [27] P. L. Fraenkel, "Marine current turbines: pioneering the development of marine kinetic energy converters," *Proc. Inst. Mech. Eng. Part J. Power Energy*, vol. 221, no. 2, pp. 159–169, 2007.
- [28] R. F. Nicholls-Lee, S. R. Turnock, and S. W. Boyd, "Simulation based optimisation of marine current turbine blades," 2008.
- [29] W. M. J. Batten, A. S. Bahaj, A. F. Molland, and J. R. Chaplin, "Hydrodynamics of marine current turbines," *Renew. Energy*, vol. 31, no. 2, pp. 249–256, Feb. 2006.

-
- [30] A. F. Molland, A. S. Bahaj, J. R. Chaplin, and W. M. J. Batten, "Measurements and predictions of forces, pressures and cavitation on 2-D sections suitable for marine current turbines," *Proc. Inst. Mech. Eng. Part M J. Eng. Marit. Environ.*, vol. 218, no. 2, pp. 127–138, Jun. 2004.
- [31] A. S. Bahaj, A. F. Molland, J. R. Chaplin, and W. M. J. Batten, "Power and thrust measurements of marine current turbines under various hydrodynamic flow conditions in a cavitation tunnel and a towing tank," *Renew. Energy*, vol. 32, no. 3, pp. 407–426, Mar. 2007.
- [32] C. B. B. Byrne *et al.*, "An investigation into the possible effects of cavitation on a horizontal axis tidal turbine," 2011.
- [33] J. N. Goundar, M. R. Ahmed, and Y.-H. Lee, "Numerical and experimental studies on hydrofoils for marine current turbines," *Renew. Energy*, vol. 42, pp. 173–179, Jun. 2012.
- [34] D. C. Maniaci and Y. Li, *Investigating the influence of the added mass effect to marine hydrokinetic horizontal-axis turbines using a General Dynamic Wake wind turbine code*. IEEE, 2011.
- [35] J. I. Whelan, J. M. R. Graham, and J. Peiro, "Inertia effects on horizontal axis tidal-stream turbines," in *the 8th European Wave and Tidal Energy Conference*, 2009.
- [36] C. Faudot and O. G. Dahlhaug, "Prediction of Wave Loads on Tidal Turbine Blades," *Energy Procedia*, vol. 20, pp. 116–133, 2012.
- [37] W. Shi, H.-C. Park, J.-H. Baek, C.-W. Kim, Y.-C. Kim, and H.-K. Shin, "Study on the marine growth effect on the dynamic response of offshore wind turbines," *Int. J. Precis. Eng. Manuf.*, vol. 13, no. 7, pp. 1167–1176, 2012.
- [38] J. A. C. Orme, I. Masters, and R. T. Griffiths, "Investigation of the effect of biofouling on the efficiency of marine current turbines," in *Proceedings of MAREC2001, International Conference on Marine Renewable Energies. Institute of Marine Engineers, London*, 2001, pp. 91–99.
- [39] B. Polagye and J. Thomson, "Screening for biofouling and corrosion of tidal energy device materials: in-situ results for admiralty inlet, puget sound, Washington," Northwest National Marine Renewable Energy Center, 2010.
- [40] G. N. McCann, R. I. Rawlinson-Smith, and K. Argyriadis, "Load simulation for tidal turbines using wind turbine experience," *ICOE*, vol. 31, no. 3, pp. 31–42, 2006.
- [41] E. A. Bossanyi, "GH Tidal Bladed theory manual," *GH Partn. Ltd*, 2007.
- [42] M. L. S\’a eterstad, "Dimensioning Loads for a Tidal Turbine," 2011.
- [43] S. Faulstich, B. Hahn, and P. J. Tavner, "Wind turbine downtime and its importance for offshore deployment," *Wind Energy*, vol. 14, no. 3, pp. 327–337, Apr. 2011.
- [44] H. Yoshikawa and N. H. Taniguchi, "Fundamentals of mechanical reliability and its application to computer aided machine design," *CIRP Ann.*, vol. 24, p. 297, 1975.
- [45] T. R. Moss and J. D. Andrews, "Reliability Assessment of Mechanical Systems," *Proc. Inst. Mech. Eng. Part E J. Process Mech. Eng.*, vol. 210, no. 3, pp. 205–216, Oct. 1996.

-
- [46] B. Sharma and O.P. Gandhi, "Digraph-based reliability assessment of a tribo-pair," *Ind. Lubr. Tribol.*, vol. 60, no. 3, pp. 153–163, May 2008.
- [47] V. Anes, L. Reis, B. Li, and M. de Freitas, "New cycle counting method for multiaxial fatigue," *Int. J. Fatigue*, vol. 67, pp. 78–94, Oct. 2014.
- [48] "Elements of Metallurgy and Engineering Alloys 001," *Scribd*. [Online]. Available: <https://www.scribd.com/doc/186682152/Elements-of-Metallurgy-and-Engineering-Alloys-001>. [Accessed: 27-May-2015].
- [49] K. Smolders, H. Long, Y. Feng, and P. Tavner, "Reliability analysis and prediction of wind turbine gearboxes," in *European Wind Energy Conference, Warsaw, Poland, 2010*.
- [50] N. S. W. Center, "Handbook of Reliability Prediction Procedures for Mechanical Equipment," 1998.
- [51] H. Zaghar, M. Sallaou, and A. Chaaba, "Preliminary Design Support by Integrating a Reliability Analysis for Wind Turbine," *Energy Power Eng.*, vol. 04, no. 04, pp. 233–240, 2012.
- [52] M. Wilkinson *et al.*, "Measuring wind turbine reliability, results of the reliawind project," in *EWEA Conference, 2011*, pp. 1–8.
- [53] M. Wilkinson *et al.*, "Methodology and results of the ReliaWind reliability field study," in *European Wind Energy Conference and Exhibition 2010, EWEC 2010, 2010*, vol. 3, pp. 1984–2004.
- [54] J. Ribrant and L. M. Bertling, "Survey of Failures in Wind Power Systems With Focus on Swedish Wind Power Plants During 1997 ndash;2005," *IEEE Trans. Energy Convers.*, vol. 22, no. 1, pp. 167–173, Mar. 2007.
- [55] B. H. S. Faulstich, "Appropriate failure statistics and reliability characteristics: Presentation held at DEWEK 2008, 9th German Wind Energy Conference, Bremen, November 27th 2008," *Fraunhofer IWES, 2008*.
- [56] F. Spinato, P. J. Tavner, G. J. W. van Bussel, and E. Koutoulakos, "Reliability of wind turbine subassemblies," *IET Renew. Power Gener.*, vol. 3, no. 4, pp. 387–401, Dec. 2009.
- [57] H. Guo, S. Watson, P. Tavner, and J. Xiang, "Reliability analysis for wind turbines with incomplete failure data collected from after the date of initial installation," *Reliab. Eng. Syst. Saf.*, vol. 94, no. 6, pp. 1057–1063, Jun. 2009.
- [58] P. J. Tavner, G. J. W. van Bussel, and F. Spinato, "Machine and converter reliabilities in wind turbines," 2006, vol. 2006, pp. 127–130.
- [59] W. E. Mason and B. G. Jones, "Reliability and quality assurance on the MOD 2 wind system," 1981.
- [60] L. Rademakers, A. J. Seebregts, B. A. Horn, J. N. T. Jehee, and B. M. Blok, "Methodology for probabilistic safety assessment of wind turbines: demonstrated by a case study of the LAGERWEY LW 15/75 design," 1993.
- [61] S. Faulstich, S. Pfaffel, P. Kühn, and P. Lyding, "Monitoring Offshore Wind Energy Use in Europe–Offshore WMEP," *Energy Procedia*, vol. 24, pp. 322–327, 2012.
- [62] K. Harman, R. Walker, and M. Wilkinson, "Availability trends observed at operational wind farms," in *European Wind Energy Conference, 2008*.

-
- [63] M. Wilkinson, T. van Delft, and K. Harman, "The effect of environmental parameters on wind turbine reliability," *EWEA 2012*, pp. 174–178, 2012.
- [64] G. Lloyd, *Guideline for the certification of offshore wind turbines*. Edition, 2005.
- [65] N. Veritas, *Guidelines for design of wind turbines*. Det Norske Veritas: Wind Energy Department, Ris National Laboratory, 2002.
- [66] I. TC88-MT, "IEC 61400-3: Wind Turbines–Part 1: Design Requirements," *Int. Electrotech. Comm. Geneva*, 2005.
- [67] M. White, "Microelectronics reliability: physics-of-failure based modeling and lifetime evaluation," 2008.
- [68] C. S. Gray and S. J. Watson, "Physics of Failure approach to wind turbine condition based maintenance," *Wind Energy*, vol. 13, no. 5, pp. 395–405, Jul. 2010.
- [69] E. E. Kostandyan and J. D. Sørensen, "Physics of failure as a basis for solder elements reliability assessment in wind turbines," *Reliab. Eng. Syst. Saf.*, vol. 108, pp. 100–107, Dec. 2012.
- [70] H. S. Toft and J. D. Sørensen, "Reliability Analysis of Wind Turbines," in *The International ASRANet Colloquium*.
- [71] E. P. S. M. Association and others, "Guidelines to understanding reliability prediction," *Revis. Oct.*, vol. 13, 2004.
- [72] D. V. Val and L. Chernin, "Reliability-Based Design of Rotor Blades in Tidal Stream Turbines."
- [73] P. R. Thies, J. Flinn, and G. H. Smith, "Reliability assessment and criticality analysis for Wave Energy Converters," *Is it a showstopper? Reliability assessment and criticality analysis for Wave Energy Converters*, Sep. 2009.
- [74] N. S. W. Center, *Handbook of reliability prediction procedures for mechanical equipment*. Carderock Division, Naval Surface Warfare Center, 1998.
- [75] O. Participants, *OREDA Offshore Reliability Data Handbook*. DNV, PO Box, 2002.
- [76] Telcordia Technologies, "Reliability Prediction Procedure for Electronic Equipment," Telcordia Technologies, Piscataway, Issue 1, May 2001.
- [77] P. R. Thies, J. Flinn, and G. H. Smith, "Is it a showstopper? Reliability assessment and criticality analysis for Wave Energy Converters," 2009.
- [78] J. Wolfram, "On Assessing the Reliability and Availability of Marine Energy Converters: The Problems of a New Technology," *Proc. Inst. Mech. Eng. Part O J. Risk Reliab.*, vol. 220, no. 1, pp. 55–68, Jun. 2006.
- [79] W.-S. Lee, D. L. Grosh, F. A. Tillman, and C. H. Lie, "Fault Tree Analysis, Methods, and Applications – A Review," *Reliab. IEEE Trans. On*, vol. 34, no. 3, pp. 194–203, 1985.
- [80] P. R. Thies, L. Johanning, and G. H. Smith, "Towards component reliability testing for marine energy converters," *Ocean Eng.*, vol. 38, no. 2–3, pp. 360–370, Feb. 2011.

-
- [81] S. Barbati, "Common reliability analysis methods and procedures," *Reliawind WP*, vol. 2, 2008.
- [82] P. R. Thies, G. H. Smith, and L. Johanning, "Addressing failure rate uncertainties of marine energy converters," *Renew. Energy*, vol. 44, pp. 359–367, Aug. 2012.
- [83] H. Stiesdal and P. H. Madsen, "Design for reliability," in *Proc. Copenhagen Offshore Wind International Conference, Copenhagen, Denmark*, 2005.
- [84] B. Lanternier, P. Lyonnet, and R. Toscano, "Modèle à hasard proportionnel pour la fiabilité des composants mécaniques," *Mec. Ind.*, vol. 9, no. 5, p. 397, 2009.
- [85] J. Andrawus, J. Watson, and M. Kishk, "Wind turbine maintenance optimisation: principles of quantitative maintenance optimisation," *Wind Eng.*, vol. 31, no. 2, pp. 101–110, 2007.
- [86] G. J. Herbert, S. Iniyar, and R. Goic, "Performance, reliability and failure analysis of wind farm in a developing country," *Renew. Energy*, vol. 35, no. 12, pp. 2739–2751, 2010.
- [87] L. H. Crow, "Evaluating the reliability of repairable systems," in *Reliability and Maintainability Symposium, 1990. Proceedings., Annual, 1990*, pp. 275–279.
- [88] V. M. Catuneanu and A. N. Mihalache, *Reliability fundamentals*, vol. 10. Elsevier, 2012.
- [89] E. Byon, L. Ntaimo, C. Singh, and Y. Ding, "Wind energy facility reliability and maintenance," in *Handbook of Wind Power Systems*, Springer, 2013, pp. 639–672.
- [90] J. G. McLeish, "Enhancing MIL-HDBK-217 reliability predictions with physics of failure methods," in *Reliability and Maintainability Symposium (RAMS), 2010 Proceedings-Annual, 2010*, pp. 1–6.
- [91] U. S. of A. D. of Defense, *Military Handbook: Reliability Prediction of Electronic Equipment: MIL-HDBK-217F: 2 December 1991*. Department of defense, 1991.
- [92] Y. Feng, Y. Qiu, C. J. Crabtree, H. Long, and P. J. Tavner, "Monitoring wind turbine gearboxes," *Wind Energy*, vol. 16, no. 5, pp. 728–740, 2013.
- [93] W. Musial, S. Butterfield, and B. McNiff, "Improving wind turbine gearbox reliability," in *European Wind Energy Conference, Milan, Italy, 2007*, pp. 7–10.
- [94] T. A. Harris and M. N. Kotzalas, *Advanced Concepts of Bearing Technology,: Rolling Bearing Analysis, Fifth Edition*. CRC Press, 2006.
- [95] P. TAVNER and others, "Studies in Electrical Machines & Wind Turbines associated with developing Reliable Power Generation," Durham University, 2012.
- [96] D. ISO, "15243: 2004,," *Roll. Bear. Fail. Charact. Causes*, 2004.
- [97] Y. Ding and J. A. Gear, "Spalling depth prediction model," *Wear*, vol. 267, no. 5–8, pp. 1181–1190, Jun. 2009.

-
- [98] R. D. Evans, "Classic bearing damage modes," in *National renewable energy laboratory wind turbine tribology seminar*, 2011.
- [99] K. Fischer, F. Besnard, and L. Bertling, "Reliability-centered maintenance for wind turbines based on statistical analysis and practical experience," *Energy Convers. IEEE Trans. On*, vol. 27, no. 1, pp. 184–195, 2012.
- [100] J. Keller, Y. Guo, W. LaCava, H. Link, and B. McNiff, "Gearbox Reliability Collaborative Phase 1 and 2: Testing and Modeling Results," 2012.
- [101] M. Malkin, "Supporting wind turbine research and testing-gearbox durability study," Oak Ridge, Tenn., USA: Technical Information Center, 2012.
- [102] R. Dupuis, "Application of oil debris monitoring for wind turbine gearbox prognostics and health management," in *Proceedings of the annual conference of the prognostics and health management society*, 2010.
- [103] D. Astridge and M. Savage, "Rotorcraft Drivetrain Life Safety and Reliability (Cycle de Vie, Securite et Fiabilite des Chaines Dynamiques des Avions a Voilure Tournante)," DTIC Document, 1990.
- [104] A. Milburn, "Wind Turbine Gearbox Wear and Failure Modes and Detection Methods," in *NREL-Wind Turbine Condition Monitoring Workshop-September*, 2011, pp. 19–21.
- [105] K. Mori, N. Kasashima, T. Yoshioka, and Y. Ueno, "Prediction of spalling on a ball bearing by applying the discrete wavelet transform to vibration signals," *Wear*, vol. 195, no. 1, pp. 162–168, 1996.
- [106] M. N. Kotzalas and G. L. Doll, "Main Shaft Bearings: Life-Limiting Wear and Solutions," The Timken Company, Technical Report.
- [107] R. Errichello and J. Muller, "Gearbox reliability collaborative gearbox 1 failure analysis report," *Contract*, vol. 303, pp. 275–3000, 2012.
- [108] F. Chaari, T. Fakhfakh, and M. Haddar, "Dynamic analysis of a planetary gear failure caused by tooth pitting and cracking," *J. Fail. Anal. Prev.*, vol. 6, no. 2, pp. 73–78, 2006.
- [109] Z. Cheng, N. Hu, F. Gu, and G. Qin, "Pitting damage levels estimation for planetary gear sets based on model simulation and grey relational analysis," *Trans. Can. Soc. Mech. Eng.*, vol. 35, no. 3, pp. 403–417, 2011.
- [110] F. Oyague, *Gearbox modeling and load simulation of a baseline 750-kW wind turbine using state-of-the-art simulation codes*. National Renewable Energy Laboratory Golden, CO, 2009.
- [111] K. G. Scott, D. Infield, N. Barltrop, J. Coultate, and A. Shahaj, "Effects of extreme and transient loads on wind turbine drive trains," in *Proc. 30th ASME Wind Energy Symp*, 2012, pp. 9–12.
- [112] Y. Guo, J. Keller, and R. Parker, "Dynamic analysis of wind turbine planetary gears using an extended harmonic balance approach," in *International Conference on Noise and Vibration Engineering, Leuven, Belgium*, 2012.
- [113] Y. Guo, J. Keller, and W. LaCava, "Planetary gear load sharing of wind turbine drivetrains subjected to non-torque loads," *Wind Energy*, vol. 18, no. 4, pp. 757–768, 2015.

-
- [114] Y. Feng, Y. Qiu, C. J. Crabtree, H. Long, and P. J. Tavner, "Use of SCADA and CMS signals for failure detection and diagnosis of a wind turbine gearbox," in *European Wind Energy Conference and Exhibition 2011, EWEC 2011*, 2011, pp. 17–19.
- [115] P. Fraenkel, "Marine Current Turbines: from prototype to product," in *Proceedings of ICE/IAHR Marine Renewable Energy conference, London Stock Exchange*, 2006, vol. 21.
- [116] Y. Guo, J. Keller, and W. LaCava, "Combined effects of gravity, bending moment, bearing clearance, and input torque on wind turbine planetary gear load sharing," in *AGMA fall technical meeting, Dearborn*, 2012.
- [117] Y.-J. Park, G.-H. Lee, J.-S. Song, and Y.-Y. Nam, "Characteristic Analysis of Wind Turbine Gearbox Considering Non-Torque Loading," *J. Mech. Des.*, vol. 135, no. 4, pp. 044501–044501, Mar. 2013.
- [118] T. A. Harris and M. N. Kotzalas, *Rolling bearing analysis*, vol. 3. Wiley New York, 2001.
- [119] H. R. Hertz, "Ueber die Beruehrung elastischer Koerper (On Contact Between Elastic Bodies)," *Gesammelte Werke Collect. Works*, vol. Vol 1, 1882.
- [120] B. V. Derjaguin, V. M. Muller, and Y. P. Toporov, "Effect of contact deformations on the adhesion of particles," *J. Colloid Interface Sci.*, vol. 53, no. 2, pp. 314–326, 1975.
- [121] D. Tabor, "Surface forces and surface interactions," *J. Colloid Interface Sci.*, vol. 58, no. 1, pp. 2–13, 1977.
- [122] D. Maugis and B. Gauthier-Manuel, "JKR-DMT transition in the presence of a liquid meniscus," *J. Adhes. Sci. Technol.*, vol. 8, no. 11, pp. 1311–1322, 1994.
- [123] D. S. Dugdale, "Yielding of steel sheets containing slits," *J. Mech. Phys. Solids*, vol. 8, no. 2, pp. 100–104, 1960.
- [124] R. W. Carpick, D. F. Ogletree, and M. Salmeron, "A general equation for fitting contact area and friction vs load measurements," *J. Colloid Interface Sci.*, vol. 211, no. 2, pp. 395–400, 1999.
- [125] G. G. Adams and M. Nosonovsky, "Contact modeling—forces," *Tribol. Int.*, vol. 33, no. 5, pp. 431–442, 2000.
- [126] J. A. Greenwood and J. B. P. Williamson, "Contact of nominally flat surfaces," in *Proceedings of the Royal Society of London A: Mathematical, Physical and Engineering Sciences*, 1966, vol. 295, pp. 300–319.
- [127] J. Pullen and J. B. P. Williamson, "On the plastic contact of rough surfaces," in *Proceedings of the Royal Society of London A: Mathematical, Physical and Engineering Sciences*, 1972, vol. 327, pp. 159–173.
- [128] E. J. Abbot and F. A. Firestone, "Specifying surface quality," *Mech Eng*, vol. 55, no. 9, pp. 569–572, 1933.
- [129] Y. Zhao, D. M. Maietta, and L. Chang, "An asperity microcontact model incorporating the transition from elastic deformation to fully plastic flow," *J. Tribol.*, vol. 122, no. 1, pp. 86–93, 2000.

-
- [130] A. Othmani and C. Kaminsky, “Three dimensional fractal analysis of sheet metal surfaces,” *Wear*, vol. 214, no. 2, pp. 147–150, 1998.
- [131] J. E. Shigley, R. G. Budynas, and C. R. Mischke, “Mechanical engineering design,” 2004.
- [132] M. N. Kotzalas and G. L. Doll, “Tribological advancements for reliable wind turbine performance,” *Philos. Trans. R. Soc. Lond. Math. Phys. Eng. Sci.*, vol. 368, no. 1929, pp. 4829–4850, Oct. 2010.
- [133] M. N. Webster and C. J. J. Norbart, “An experimental investigation of micropitting using a roller disk machine,” *Tribol. Trans.*, vol. 38, no. 4, pp. 883–893, 1995.
- [134] F. W. Carter, “On the action of a locomotive driving wheel,” in *Proceedings of the Royal Society of London A: Mathematical, Physical and Engineering Sciences*, 1926, vol. 112, pp. 151–157.
- [135] J. J. KALKER, “Survey of Wheel—Rail Rolling Contact Theory,” *Veh. Syst. Dyn.*, vol. 8, no. 4, pp. 317–358, Sep. 1979.
- [136] N. Bosso, M. Spiryagin, A. Gugliotta, and A. Somà, *Mechatronic modeling of real-time wheel-rail contact*. Springer, 2013.
- [137] K. L. Johnson, “The effect of spin upon the rolling motion of an elastic sphere on a plane,” *J. Appl. Mech.*, vol. 25, no. 3, pp. 332–338, 1958.
- [138] P. J. Vermeulen and K. L. Johnson, “Contact of nonspherical elastic bodies transmitting tangential forces,” *J. Appl. Mech.*, vol. 31, no. 2, pp. 338–340, 1964.
- [139] J. J. Kalker, “On the rolling contact of two elastic bodies in the presence of dry friction,” TU Delft, Delft University of Technology, 1967.
- [140] D. J. Haines, E. Ollerton, and others, “Contact stress distributions on elliptical contact surfaces subjected to radial and tangential forces,” *Proc. Inst. Mech. Eng.*, vol. 177, no. 1, pp. 95–114, 1963.
- [141] J. J. Kalker, “Simplified theory of rolling contact,” *Delft Prog. Rep.*, vol. 1, no. 1, pp. 1–10, 1973.
- [142] J. J. Kalker, “A fast algorithm for the simplified theory of rolling contact,” *Veh. Syst. Dyn.*, vol. 11, no. 1, pp. 1–13, 1982.
- [143] O. Polach, “Creep forces in simulations of traction vehicles running on adhesion limit,” *Wear*, vol. 258, no. 7, pp. 992–1000, 2005.
- [144] L. Houpert, E. Ioannides, J. C. Kuypers, and J. Tripp, “The Effect of the EHD Pressure Spike on Rolling Bearing Fatigue,” *J. Tribol.*, vol. 109, no. 3, pp. 444–450, Jul. 1987.
- [145] L. E. Stacke and D. Fritzon, “Dynamic behaviour of rolling bearings: simulations and experiments,” *Proc. Inst. Mech. Eng. Part J J. Eng. Tribol.*, vol. 215, no. 6, pp. 499–508, 2001.
- [146] L. Houpert, “CAGEDYN: a contribution to roller bearing dynamic calculations. Part III: experimental validation,” *Tribol. Trans.*, vol. 53, no. 6, pp. 848–859, 2010.

-
- [147] L. Houpert, “CAGEDYN: a contribution to roller bearing dynamic calculations part I: basic tribology concepts,” *Tribol. Trans.*, vol. 53, no. 1, pp. 1–9, 2009.
- [148] L. Houpert, “CAGEDYN: A Contribution to Roller Bearing Dynamic Calculations Part II: Description of the Numerical Tool and Its Outputs,” *Tribol. Trans.*, vol. 53, no. 1, pp. 10–21, 2009.
- [149] N. Ghaisas, C. R. Wassgren, and F. Sadeghi, “Cage Instabilities in Cylindrical Roller Bearings,” *J. Tribol.*, vol. 126, no. 4, pp. 681–689, Nov. 2004.
- [150] A. Ashtekar and F. Sadeghi, “A New Approach for Including Cage Flexibility in Dynamic Bearing Models by Using Combined Explicit Finite and Discrete Element Methods,” *J. Tribol.*, vol. 134, no. 4, pp. 041502–041502, Sep. 2012.
- [151] Y. Guo and R. G. Parker, “Stiffness matrix calculation of rolling element bearings using a finite element/contact mechanics model,” *Mech. Mach. Theory*, vol. 51, pp. 32–45, 2012.
- [152] T. Sakaguchi and K. Ueno, “Dynamic analysis of cage behavior in a cylindrical roller bearing,” *Spec. Issue Spec. Suppl. Ind. Mach.*, 2004.
- [153] F. Fritz, *Modellierung von Wälzlagern als generische Maschinenelemente einer Mehrkörpersimulation*, vol. 14. KIT Scientific Publishing, 2011.
- [154] R. Teutsch, *Kontaktmodelle und Strategien zur Simulation von Wälzlagern und Wälzführungen*. Lehrstuhl für Maschinenelemente und Getriebetechnik MEGT, Verlag Technische Universität Kaiserslautern, 2005.
- [155] W. Qian and G. Jacobs, “Dynamic simulation of cylindrical roller bearings,” Lehrstuhl und Institut für Maschinenelemente und Maschinengestaltung, 2014.
- [156] F. Sadeghi, B. Jalalahmadi, T. S. Slack, N. Rajee, and N. K. Arakere, “A Review of Rolling Contact Fatigue,” *J. Tribol.*, vol. 131, no. 4, pp. 041403–041403, Sep. 2009.
- [157] J.-H. Kang, B. Hosseinkhani, and P. E. Rivera-Díaz-del-Castillo, “Rolling contact fatigue in bearings: multiscale overview,” *Mater. Sci. Technol.*, vol. 28, no. 1, pp. 44–49, 2012.
- [158] G. Lundberg and A. Palmgren, “Dynamic capacity of roller bearing,” *Acta Polytech Mech. Eng. Ser.*, vol. 2, 1952.
- [159] E. V. Zaretsky, “Rolling bearing life prediction, theory, and application,” 2013.
- [160] I. S. O. Standard and B. ISO, *Rolling Bearing–Dynamic Load Ratings and Rating Life*. ISO, 2007.
- [161] J. Hoo and W. Green, Eds., *Bearing Steels: Into the 21st Century*. 100 Barr Harbor Drive, PO Box C700, West Conshohocken, PA 19428-2959: ASTM International, 1998.
- [162] J. J. Hoo, *Rolling Contact Fatigue Testing of Bearing Steels: A Symposium*. ASTM International, 1982.
- [163] E. V. Zaretsky, “Rolling bearing steels – a technical and historical perspective,” *Mater. Sci. Technol.*, vol. 28, no. 1, pp. 58–69, Jan. 2012.

-
- [164] M.-H. Evans, “White structure flaking (WSF) in wind turbine gearbox bearings: effects of ‘butterflies’ and white etching cracks (WECs),” *Mater. Sci. Technol.*, vol. 28, no. 1, pp. 3–22, Jan. 2012.
- [165] K. Shiozawa, L. L. Tao, and S. Ishihara, “Subsurface fatigue crack initiation behavior and SN curve characteristics in high carbon-chromium bearing steel,” *J. Soc. Mater. Sci. Jpn.*, vol. 48, no. 10, pp. 1095–1100, 1999.
- [166] T. Sakai *et al.*, “Experimental Reconfirmation of Characteristic *S-N* Property for High Carbon Chromium Bearing Steel in Wide Life Region in Rotating Bending,” *J. Soc. Mater. Sci. Jpn.*, vol. 49, no. 7, pp. 779–785, 2000.
- [167] K. Shiozawa, L. Lu, and S. Ishihara, “S–N curve characteristics and subsurface crack initiation behaviour in ultra-long life fatigue of a high carbon-chromium bearing steel,” *Fatigue Fract. Eng. Mater. Struct.*, vol. 24, no. 12, pp. 781–790, Dec. 2001.
- [168] K. Shiozawa and L. Lu, “Very high-cycle fatigue behaviour of shot-peened high-carbon–chromium bearing steel,” *Fatigue Fract. Eng. Mater. Struct.*, vol. 25, no. 8–9, pp. 813–822, Sep. 2002.
- [169] M. Nakajima, T. Sakai, and T. Shimizu, “An Observation of Fish-eye Fracture Process in High Strength Steel SUJ2,” *Trans. Jpn. Soc. Mech. Eng. Ser. A*, vol. 65, no. 640, pp. 2504–2510, 1999.
- [170] K. Shiozawa, L. Lu, and S. Ishihara, “S–N curve characteristics and subsurface crack initiation behaviour in ultra-long life fatigue of a high carbon-chromium bearing steel,” *Fatigue Fract. Eng. Mater. Struct.*, vol. 24, no. 12, pp. 781–790, Dec. 2001.
- [171] Bathias, “There is no infinite fatigue life in metallic materials,” *Fatigue Fract. Eng. Mater. Struct.*, vol. 22, no. 7, pp. 559–565, Jul. 1999.
- [172] C. Bathias, “Gigacycle Fatigue: A New Tool for Exploring Bearing Steel,” in *Bearing Steel Technologies: 9th Volume, Advances in Rolling Contact Fatigue Strength Testing and Related Substitute Technologies*, J. Beswick, Ed. 100 Barr Harbor Drive, PO Box C700, West Conshohocken, PA 19428-2959: ASTM International, 2012, pp. 181–202.
- [173] A. P. Abir Bhattacharyya, “Cyclic Constitutive Response and Effective S-N Diagram of M50 NiL Case-Hardened Bearing Steel Subjected to Rolling Contact Fatigue,” *J. Tribol.*, vol. 137, no. 4, 2015.
- [174] A. Gabelli, J. Lai, T. Lund, K. Rydén, I. Strandell, and G. E. Morales-Espejel, “The fatigue limit of bearing steels – Part II: Characterization for life rating standards,” *Int. J. Fatigue*, vol. 38, pp. 169–180, May 2012.
- [175] M. Nakajima, K. Tokaji, H. Itoga, and T. Shimizu, “Effect of loading condition on very high cycle fatigue behavior in a high strength steel,” *Int. J. Fatigue*, vol. 32, no. 2, pp. 475–480, Feb. 2010.
- [176] H. K. D. H. Bhadeshia, “Steels for bearings,” *Prog. Mater. Sci.*, vol. 57, no. 2, pp. 268–435, Feb. 2012.
- [177] T. Furusawa *et al.*, “Development of multi-type fatigue testing machine in axial loading and verification of its fundamental performance,” *Nihon Kikai Gakkai Ronbunshu Hen Transactions Jpn. Soc. Mech. Eng. Part A*, vol. 72, no. 6, pp. 886–894, 2006.

-
- [178] A. Palmgren, "The service life of ball bearings," *Z. Vereines Dtsch. Ingenieure*, vol. 68, no. 14, pp. 339–341, 1924.
- [179] B. L. Vlcek, *Rolling-Element Fatigue Testing and Data Analysis— A Tutorial*. 2013.
- [180] A.) Symposium on Rolling Contact Fatigue Testing of Bearing Steels: Phoenix, *Rolling contact fatigue testing of bearing steels*. Philadelphia, Pa: American Society for Testing and Materials, 1982.
- [181] R. Bearings, "Dynamic Load Ratings and Rating Life," *Int. Organ. Stand. Int. Stand. ISO*, vol. 281, 2007.
- [182] G. S. Bir, M. J. Lawson, and Y. Li, "Structural design of a horizontal-axis tidal current turbine composite blade," in *ASME 2011 30th International Conference on Ocean, Offshore and Arctic Engineering*, 2011, pp. 797–808.
- [183] K. A. Karikari-Boateng, C. Ng, L. Johannng, M. A. Mueller, and N. Barltrop, "CAUSES OF TIDAL TURBINE MAIN BEARING FAILURE."
- [184] H. R. Olesen, S. E. Larsen, and J. Højstrup, "Modelling velocity spectra in the lower part of the planetary boundary layer," *Bound.-Layer Meteorol.*, vol. 29, no. 3, pp. 285–312, Jul. 1984.
- [185] S. Gant and T. Stallard, "Modelling a tidal turbine in unsteady flow," in *Proceedings of the Eighteenth (2008) International Offshore and Polar Engineering Conference*, 2008, pp. 473–480.
- [186] M. Drela and H. Youngren, *XFOIL User's Manual*. 2000.
- [187] E. Ioannides and T. A. Harris, "A new fatigue life model for rolling bearings," *J. Tribol.*, vol. 107, no. 3, pp. 367–377, 1985.
- [188] S. Ooi and H. Bhadeshia, "Duplex Hardening of Steels for Aeroengine Bearings," *ISIJ Int.*, vol. 52, no. 11, pp. 1927–1934, 2012.
- [189] H. Bhadeshia, "Steels for bearings," *Prog. Mater. Sci.*, vol. 57, no. 2, pp. 268–435, 2012.
- [190] G. E. Totten, *Handbook of Lubrication and Tribology: Volume I Application and Maintenance, Second Edition*. CRC Press, 2006.
- [191] S. Jain and H. Hunt, "A dynamic model to predict the occurrence of skidding in wind-turbine bearings," in *Journal of Physics: Conference Series*, 2011, vol. 305, p. 012027.

Appendix A Publications

The following papers were produced during the EngD programme:

- 2013 **K. A. Karikari-Boateng**, C. Ng, J. Grimwade, L. Johanning, M.A. Mueller, N. Barltrop (2013). Reliability of Tidal Turbines using Wind Turbine Experience. In proceeding of the European Wave and Tidal Energy Conference(EWTEC) 2013, Aalborg, Denmark.
- 2014 **Karikari-Boateng, K. A.**, Ng, C., Johanning, L., Mueller, M. A., & Barltrop, N. CAUSES OF TIDAL TURBINE MAIN BEARING FAILURE.; In proceeding of the 2Nd Asian Wave and Tidal Energy Conference(AWTEC) 2014, Tokyo, Japan.
- 2015 **K.A. Karikari-Boateng**, C. Little, H. Lee, “Life estimation method for a wind turbine main shaft bearing”, special OPTIMUS session at 12th International Conference on Condition Monitoring and Machinery Failure Prevention Technologies, Oxford, UK, June 2015.
- 2015 Thies, P. R., Johanning, L., **Karikari-Boateng, K. A.**, Ng, C., & McKeever, P. (2015). Component reliability test approaches for marine renewable energy. Proceedings of the Institution of Mechanical Engineers, Part O: Journal of Risk and Reliability, 1748006X15580837.

Appendix B Tidal Turbine Modelling

B.1 Turbine Blade properties

```

-----
----- FAST INDIVIDUAL BLADE FILE -----
-----
1. MW tidal blade based on Bir et al 2011..
----- BLADE PARAMETERS -----
-----
  74      NBlInpSt   - Number of blade input stations (-)
False     CalcBMode - Calculate blade mode shapes internally {T:
ignore mode shapes from below, F: use mode shapes from below} [CURRENTLY
IGNORED] (flag)
  3.882   BldFlDmp(1) - Blade flap mode #1 structural damping in
percent of critical (%)
  3.882   BldFlDmp(2) - Blade flap mode #2 structural damping in
percent of critical (%)
  5.900   BldEdDmp(1) - Blade edge mode #1 structural damping in
percent of critical (%)
----- BLADE ADJUSTMENT FACTORS -----
-----
  1.0     FlStTunr(1) - Blade flapwise modal stiffness tuner, 1st mode
(-)
  1.0     FlStTunr(2) - Blade flapwise modal stiffness tuner, 2nd mode
(-)
  1.0     AdjBlMs    - Factor to adjust blade mass density (-)
  1.0     AdjFlSt    - Factor to adjust blade flap stiffness (-)
  1.0     AdjEdSt    - Factor to adjust blade edge stiffness (-)
----- DISTRIBUTED BLADE PROPERTIES -----
-----
BlFract  AeroCent  StrcTwst  BMassDen  FlpStfff      EdgStfff      GJStfff
EASTfff  Alpha      FlpIner   EdgIner   PrecrvRef    PreswpRef    FlpcgOf
EdgcgOf  FlpEAOf   EdgEAOf
(-)      (-)        (deg)     (kg/m)     (Nm^2)       (Nm^2)       (Nm^2)
(N)      (m)        (-) (kg m)   (kg m)     (m)         (m)         (m)
(m)
0  0.25  12.86  204.67  243000000  252000000  70900000
3170000000  0  14.7  12.8  0.0  0.0  0.0  0.000
0.0  0
0.00847457627118644  0.25  12.86  208.4  247000000  269000000
73700000  3210000000  0  15  13.7  0.0  0.0  0.0
0.000  0.0  -0.003
0.0169491525423729  0.25  12.86  211.61  247000000  284000000
76000000  3240000000  0  15.1  14.5  0.0  0.0
0.0  0.000  0.0  -0.007
0.0254237288135593  0.25  12.86  214.67  246000000  300000000
78100000  3270000000  0  15.1  15.4  0.0  0.0
0.0  0.000  0.0  -0.01
0.0338983050847458  0.25  12.86  217.58  244000000  315000000
80000000  3300000000  0  15  16.3  0.0  0.0  0.0
0.000  0.0  -0.014
0.0423728813559322  0.25  12.86  225.16  250000000  359000000
87000000  3400000000  0  15.5  18.7  0.0  0.0
0.0  0.000  0.0  -0.024
0.0508474576271186  0.25  12.86  233.16  249000000  403000000

```

93300000	3480000000	0	15.6	21.2	0.0	0.0	
0.0	0.000	0.0	-0.035				
0.0593220338983051	0.25	12.86	170.33	170000000	112000000		
54200000	2560000000	0	8.13	5	0.0	0.0	0.0
0.000	0.0	0.076					
0.0677966101694915	0.25	12.86	157	148000000	111000000		
51100000	2340000000	0	7.25	4.98	0.0	0.0	
0.0	0.000	0.0	0.069				
0.076271186440678	0.25	12.86	143.82	130000000	110000000		
49200000	2070000000	0	6.64	4.96	0.0	0.0	
0.0	0.000	0.0	0.058				
0.0847457627118644	0.25	12.86	132.24	112000000	107000000		
46800000	1830000000	0	6	4.92	0.0	0.0	0.0
0.000	0.0	0.045					
0.0932203389830508	0.25	12.86	114.73	88200000	95600000		
39500000	1520000000	0	4.97	4.64	0.0	0.0	
0.0	0.000	0.0	0.032				
0.101694915254237	0.25	12.86	100.4	67200000	85500000		
34700000	1250000000	0	4.05	4.28	0.0	0.0	
0.0	0.000	0.0	0.017				
0.110169491525424	0.25	12.86	102.79	64500000	91500000		
36600000	1250000000	0	3.96	4.51	0.0	0.0	
0.0	0.000	0.0	0.003				
0.11864406779661	0.25	12.86	102.57	60000000	95300000		
38200000	1220000000	0	3.8	4.58	0.0	0.0	0.0
0.000	0.0	-0.013					
0.127118644067797	0.25	12.86	103.84	56200000	101000000		
40100000	1220000000	0	3.6	4.65	0.0	0.0	0.0
0.000	0.0	-0.029					
0.135593220338983	0.25	12.86	105.25	51700000	106000000		
42100000	1220000000	0	3.38	4.7	0.0	0.0	0.0
0.000	0.0	-0.047					
0.144067796610169	0.25	12.86	105.32	49400000	108000000		
42800000	1210000000	0	3.24	4.66	0.0	0.0	
0.0	0.000	0.0	-0.054				
0.152542372881356	0.25	12.86	105.35	47000000	110000000		
43600000	1210000000	0	3.1	4.6	0.0	0.0	0.0
0.000	0.0	-0.062					
0.161016949152542	0.25	12.86	106.24	44500000	112000000		
44400000	1210000000	0	2.97	4.58	0.0	0.0	
0.0	0.000	0.0	-0.07				
0.169491525423729	0.25	12.86	108.87	43000000	116000000		
45600000	1240000000	0	2.86	4.61	0.0	0.0	
0.0	0.000	0.0	-0.077				
0.177966101694915	0.25	12.53	107.1	40900000	113000000		
44400000	1230000000	0	2.72	4.48	0.0	0.0	
0.0	0.000	0.0	-0.076				
0.186440677966102	0.25	12.2	105.97	38900000	110000000		
43200000	1210000000	0	2.59	4.35	0.0	0.0	
0.0	0.000	0.0	-0.075				
0.194915254237288	0.25	11.87	108.92	38400000	115000000		
47500000	1260000000	0	2.54	4.05	0.0	0.0	
0.0	0.000	0.0	-0.077				
0.203389830508475	0.25	11.54	107.65	36200000	112000000		
46200000	1240000000	0	2.4	3.91	0.0	0.0	0.0
0.000	0.0	-0.076					
0.211864406779661	0.25	11.265	108.63	35700000	111000000		
45400000	1260000000	0	2.34	3.93	0.0	0.0	
0.0	0.000	0.0	-0.075				
0.220338983050847	0.25	10.99	107.57	34100000	109000000		
44200000	1250000000	0	2.24	3.81	0.0	0.0	
0.0	0.000	0.0	-0.074				
0.228813559322034	0.25	10.715	106.51	32600000	106000000		
43100000	1240000000	0	2.14	3.7	0.0	0.0	0.0
0.000	0.0	-0.074					
0.23728813559322	0.25	10.44	105.46	31100000	103000000		
42000000	1220000000	0	2.05	3.59	0.0	0.0	
0.0	0.000	0.0	-0.073				
0.254237288135593	0.25	9.97	103.75	29100000	98400000		
40200000	1200000000	0	1.92	3.42	0.0	0.0	
0.0	0.000	0.0	-0.072				

0.271186440677966	0.25	9.5	102.8	27200000	95400000		
38500000	1210000000	0	1.77	3.28	0.0	0.0	
0.0	0.000	0.0	-0.07				
0.288135593220339	0.25	9.105	98.97	25400000	89600000		
36700000	1160000000	0	1.66	3.05	0.0	0.0	
0.0	0.000	0.0	-0.07				
0.305084745762712	0.25	8.71	97.6	24300000	85900000		
35200000	1140000000	0	1.59	2.93	0.0	0.0	
0.0	0.000	0.0	-0.069				
0.322033898305085	0.25	8.365	94.46	22600000	80600000		
33500000	1090000000	0	1.49	2.71	0.0	0.0	
0.0	0.000	0.0	-0.068				
0.338983050847458	0.25	8.02	90.61	21500000	73400000		
28600000	1060000000	0	1.4	2.78	0.0	0.0	0.0
0.000	0.0	-0.064					
0.355932203389831	0.25	7.725	86.87	20000000	68700000		
27200000	1010000000	0	1.3	2.54	0.0	0.0	0.0
0.000	0.0	-0.064					
0.372881355932203	0.25	7.43	83.9	18500000	64200000		
25800000	967000000	0	1.22	2.35	0.0	0.0	0.0
0.000	0.0	-0.064					
0.389830508474576	0.25	7.17	82.66	17700000	61400000		
24600000	953000000	0	1.17	2.24	0.0	0.0	0.0
0.000	0.0	-0.063					
0.406779661016949	0.25	6.91	79.74	16300000	57200000		
23300000	908000000	0	1.09	2.07	0.0	0.0	0.0
0.000	0.0	-0.063					
0.423728813559322	0.25	6.68	75.71	15000000	53300000		
22100000	863000000	0	1	1.88	0.0	0.0	0.0
0.000	0.0	-0.062					
0.440677966101695	0.25	6.45	74.56	14300000	50900000		
21100000	850000000	0	0.958	1.79	0.0	0.0	
0.0	0.000	0.0	-0.062				
0.457627118644068	0.25	6.245	71.78	13200000	47300000		
19900000	807000000	0	0.89	1.64	0.0	0.0	0.0
0.000	0.0	-0.061					
0.474576271186441	0.25	6.04	66.81	11900000	41200000		
16400000	750000000	0	0.807	1.62	0.0	0.0	
0.0	0.000	0.0	-0.058				
0.491525423728814	0.25	5.86	64.17	10900000	38100000		
15400000	709000000	0	0.748	1.48	0.0	0.0	
0.0	0.000	0.0	-0.058				
0.508474576271186	0.25	5.68	62.49	10400000	36200000		
14700000	697000000	0	0.703	1.39	0.0	0.0	
0.0	0.000	0.0	-0.057				
0.525423728813559	0.25	5.515	59.92	9420000	33300000		
13800000	657000000	0	0.648	1.26	0.0	0.0	
0.0	0.000	0.0	-0.057				
0.542372881355932	0.25	5.35	56.94	8540000	30600000		
12900000	618000000	0	0.597	1.15	0.0	0.0	
0.0	0.000	0.0	-0.056				
0.559322033898305	0.25	5.2	53.91	7730000	28100000		
12100000	581000000	0	0.542	1.02	0.0	0.0	
0.0	0.000	0.0	-0.056				
0.576271186440678	0.25	5.05	51.54	6970000	25800000		
11300000	544000000	0	0.498	0.914	0.0	0.0	
0.0	0.000	0.0	-0.056				
0.593220338983051	0.25	4.91	47.2	6170000	21700000		
8900000	495000000	0	0.442	0.909	0.0	0.0	
0.0	0.000	0.0	-0.052				
0.610169491525424	0.25	4.77	44.95	5510000	19700000		
8280000	460000000	0	0.403	0.816	0.0	0.0	
0.0	0.000	0.0	-0.052				
0.627118644067797	0.25	4.64	44.07	5190000	18500000		
7800000	451000000	0	0.38	0.769	0.0	0.0	0.0
0.000	0.0	-0.051					
0.64406779661017	0.25	4.51	41.33	4610000	16800000		
7240000	417000000	0	0.34	0.669	0.0	0.0	0.0
0.000	0.0	-0.051					
0.661016949152542	0.25	4.385	39.2	4070000	15100000		
6700000	385000000	0	0.307	0.592	0.0	0.0	

0.0	0.000	0.0	-0.051					
0.677966101694915		0.25	4.26	36.22	3570000	13600000		
6190000	353000000	0	0.273	0.51	0.0	0.0	0.0	
0.000	0.0	-0.052						
0.694915254237288		0.25	4.145	34.2	3110000	12100000		
5710000	323000000	0	0.245	0.444	0.0	0.0		
0.0	0.000	0.0	-0.052					
0.711864406779661		0.25	4.03	32.23	2690000	10800000		
5250000	293000000	0	0.219	0.384	0.0	0.0		
0.0	0.000	0.0	-0.052					
0.728813559322034		0.25	3.915	29.84	2310000	9550000		
4820000	265000000	0	0.192	0.317	0.0	0.0		
0.0	0.000	0.0	-0.053					
0.745762711864407		0.25	3.8	27.99	1960000	8420000		
4410000	237000000	0	0.17	0.267	0.0	0.0	0.0	
0.000	0.0	-0.054						
0.76271186440678		0.25	3.685	25.75	1650000	7390000		
4030000	211000000	0	0.147	0.211	0.0	0.0		
0.0	0.000	0.0	-0.055					
0.779661016949153		0.25	3.57	23.68	1370000	6450000		
3670000	185000000	0	0.129	0.173	0.0	0.0		
0.0	0.000	0.0	-0.056					
0.796610169491525		0.25	3.46	21.99	1120000	5570000		
3320000	160000000	0	0.113	0.136	0.0	0.0		
0.0	0.000	0.0	-0.058					
0.813559322033898		0.25	3.35	19.94	891000	4770000		
2990000	137000000	0	0.095	0.0929	0.0	0.0		
0.0	0.000	0.0	-0.061					
0.830508474576271		0.25	3.24	18.38	693000	4050000		
2690000	114000000	0	0.0817	0.0634	0.0	0.0		
0.0	0.000	0.0	-0.065					
0.847457627118644		0.25	3.13	17.86	636000	3720000		
2460000	111000000	0	0.0749	0.0581	0.0	0.0		
0.0	0.000	0.0	-0.063					
0.864406779661017		0.25	3.015	16	476000	3110000	2190000	
8990000	0	0.0618	0.0258	0.0	0.0	0.0		
0.000	0.0	-0.068						
0.88135593220339		0.25	2.9	14.31	338000	2560000	1920000	
7000000	0	0.0521	0.00761	0.0	0.0	0.0		
0.000	0.0	-0.077						
0.898305084745763		0.25	2.785	12.59	219000	2040000		
1640000	51100000	0	0.0417	-0.0186	0.0	0.0		
0.0	0.000	0.0	-0.091					
0.915254237288136		0.25	2.67	12.17	198000	1840000		
1480000	49400000	0	0.0376	-0.0168	0.0	0.0		
0.0	0.000	0.0	-0.088					
0.932203389830509		0.25	2.55	11.75	178000	1660000		
1330000	47700000	0	0.0338	-0.0151	0.0	0.0		
0.0	0.000	0.0	-0.085					
0.949152542372881		0.25	2.43	11.33	159000	1490000		
1190000	46000000	0	0.0303	-0.0136	0.0	0.0		
0.0	0.000	0.0	-0.082					
0.966101694915254		0.25	2.305	11.69	198000	1510000		
1130000	58700000	0	0.0296	-0.000149	0.0	0.0		
0.0	0.000	0.0	-0.065					
0.983050847457627		0.25	2.18	11.01	176000	1340000		
1010000	56500000	0	0.0263	0.00149	0.0	0.0		
0.0	0.000	0.0	-0.062					
1	0.25	2.06	10.57	156000	1190000	892000	5420000	
0	0.0232	0.00132	0.0	0.0	0.0	0.0	0.000	0.0
-0.06								
----- BLADE MODE SHAPES -----								

0.0838	BldF11Sh(2)	-	Flap mode 1,	coeff of x^2				
1.6525	BldF11Sh(3)	-		, coeff of x^3				
-1.5682	BldF11Sh(4)	-		, coeff of x^4				
1.6947	BldF11Sh(5)	-		, coeff of x^5				
-0.8628	BldF11Sh(6)	-		, coeff of x^6				
-0.3008	BldF12Sh(2)	-	Flap mode 2,	coeff of x^2				
-1.9968	BldF12Sh(3)	-		, coeff of x^3				
-4.6564	BldF12Sh(4)	-		, coeff of x^4				

16.9661	BldFl2Sh(5)	-	, coeff of x^5
-9.0121	BldFl2Sh(6)	-	, coeff of x^6
0.3165	BldEdgSh(2)	- Edge mode 1,	coeff of x^2
3.2618	BldEdgSh(3)	-	, coeff of x^3
-6.4005	BldEdgSh(4)	-	, coeff of x^4
6.0367	BldEdgSh(5)	-	, coeff of x^5
-2.2146	BldEdgSh(6)	-	, coeff of x^6

B.2 Sample Aerodyne input file

Tidal					
SI	SysUnits	- System of units for used for input and output [must be SI for FAST] (unquoted string)			
BEDDOES	StallMod	- Dynamic stall included [BEDDOES or STEADY] (unquoted string)			
No_CM	UseCm	- Use aerodynamic pitching moment model? [USE_CM or NO_CM] (unquoted string)			
EQUIL	InfModel	- Inflow model [DYNIN or EQUIL] (unquoted string)			
SWIRL	IndModel	- Induction-factor model [NONE or WAKE or SWIRL] (unquoted string)			
0.001	AToler	- Induction-factor tolerance (convergence criteria) (-)			
PRANDTL	TLModel	- Tip-loss model (EQUIL only) [PRANDTL, GTECH, or NONE] (unquoted string)			
NONE	HLModel	- Hub-loss model (EQUIL only) [PRANDTL, or NONE] (unquoted string)			
"newfield.wnd"		Name of file containing wind data (quoted string)	"test.WND"		
20.0	HH	- Wind reference (hub) height [TowerHt+Twr2Shft+OverHang*SIN(NacTilt)] (m)			
0.0	TwrShad	- Tower-shadow velocity deficit (-)			
9999.9	ShadHWid	- Tower-shadow half width (m)			
9999.9	T_Shad_Refpt	- Tower-shadow reference point (m)			
1030	Rho	- Air density (kg/m^3)			
1.83e-6	KinVisc	- Kinematic air viscosity [CURRENTLY IGNORED] (m^2/sec)			
0.005	DTAero	- Time interval for aerodynamic calculations (sec)			
2	NumFoil	- Number of airfoil files (-)			
"cylinder.dat"	FoilNm	- Names of the airfoil files [NumFoil lines] (quoted strings)			
"Naca63_424.dat"					
75	BldNodes	- Number of blade nodes used for analysis (-)			
RNodes	AeroTwst	DRNodes	Chord	NFoil	PrnElm
1.0375	12.86	0.075	0.8	1	NOPRINT
1.1125	12.86	0.075	0.823	1	NOPRINT
1.1875	12.86	0.075	0.823	1	NOPRINT
1.2625	12.86	0.075	0.847	2	NOPRINT
1.3375	12.86	0.075	0.871	2	NOPRINT
1.4125	12.86	0.075	0.894	2	NOPRINT
1.4875	12.86	0.075	0.95	2	NOPRINT
1.5625	12.86	0.075	1.006	2	NOPRINT
1.6375	12.86	0.075	1.062	2	NOPRINT
1.7125	12.86	0.075	1.118	2	NOPRINT
1.7875	12.86	0.075	1.185	2	NOPRINT
1.8625	12.86	0.075	1.252	2	NOPRINT
1.9375	12.86	0.075	1.319	2	NOPRINT
2.0125	12.86	0.075	1.386	2	NOPRINT
2.0875	12.86	0.075	1.442	2	NOPRINT

2.1625	12.86	0.075	1.498	2	NOPRINT
2.2375	12.86	0.075	1.554	2	NOPRINT
2.3125	12.86	0.075	1.61	2	NOPRINT
2.3875	12.86	0.075	1.633	2	NOPRINT
2.4625	12.86	0.075	1.657	2	NOPRINT
2.5375	12.86	0.075	1.681	2	NOPRINT
2.6125	12.86	0.075	1.704	2	NOPRINT
2.6875	12.53	0.075	1.694	2	NOPRINT
2.7625	12.2	0.075	1.683	2	NOPRINT
2.8375	11.87	0.075	1.673	2	NOPRINT
2.9125	11.54	0.075	1.662	2	NOPRINT
2.9875	11.265	0.075	1.651	2	NOPRINT
3.0625	10.99	0.075	1.64	2	NOPRINT
3.1375	10.715	0.075	1.63	2	NOPRINT
3.2125	10.44	0.075	1.619	2	NOPRINT
3.325	9.97	0.15	1.598	2	NOPRINT
3.475	9.5	0.15	1.577	2	NOPRINT
3.625	9.105	0.15	1.556	2	NOPRINT
3.775	8.71	0.15	1.534	2	NOPRINT
3.925	8.365	0.15	1.513	2	NOPRINT
4.075	8.02	0.15	1.492	2	NOPRINT
4.225	7.725	0.15	1.471	2	NOPRINT
4.375	7.43	0.15	1.45	2	NOPRINT
4.525	7.17	0.15	1.429	2	NOPRINT
4.675	6.91	0.15	1.407	2	NOPRINT
4.825	6.68	0.15	1.386	2	NOPRINT
4.975	6.45	0.15	1.365	2	NOPRINT
5.125	6.245	0.15	1.344	2	NOPRINT
5.275	6.04	0.15	1.322	2	NOPRINT
5.425	5.86	0.15	1.301	2	NOPRINT
5.575	5.68	0.15	1.279	2	NOPRINT
5.725	5.515	0.15	1.257	2	NOPRINT
5.875	5.35	0.15	1.235	2	NOPRINT
6.025	5.2	0.15	1.214	2	NOPRINT
6.175	5.05	0.15	1.192	2	NOPRINT
6.325	4.91	0.15	1.17	2	NOPRINT
6.475	4.77	0.15	1.148	2	NOPRINT
6.625	4.64	0.15	1.125	2	NOPRINT
6.775	4.51	0.15	1.103	2	NOPRINT
6.925	4.385	0.15	1.081	2	NOPRINT
7.075	4.26	0.15	1.058	2	NOPRINT
7.225	4.145	0.15	1.035	2	NOPRINT
7.375	4.03	0.15	1.012	2	NOPRINT
7.525	3.915	0.15	0.989	2	NOPRINT
7.675	3.8	0.15	0.966	2	NOPRINT
7.825	3.685	0.15	0.943	2	NOPRINT
7.975	3.57	0.15	0.92	2	NOPRINT
8.125	3.46	0.15	0.896	2	NOPRINT
8.275	3.35	0.15	0.872	2	NOPRINT
8.425	3.24	0.15	0.848	2	NOPRINT
8.575	3.13	0.15	0.824	2	NOPRINT
8.725	3.015	0.15	0.8	2	NOPRINT
8.875	2.9	0.15	0.776	2	NOPRINT
9.025	2.785	0.15	0.751	2	NOPRINT
9.175	2.67	0.15	0.726	2	NOPRINT
9.325	2.55	0.15	0.701	2	NOPRINT
9.475	2.43	0.15	0.676	2	NOPRINT
9.625	2.305	0.15	0.651	2	NOPRINT
9.775	2.18	0.15	0.626	2	NOPRINT
9.925	2.06	0.15	0.601	2	NOPRINT

B.3 Sample FAST input file

--	--

```

----- FAST INPUT FILE -----
1 MW Tidal Turbine based on FAST certification Test #13: WindPACT 1.5 MW Baselin
Compatible with FAST v7.02.00.
----- SIMULATION CONTROL -----
False Echo - Echo input data to "echo.out" (flag)
  1 ADAMSPrep - ADAMS preprocessor mode {1: Run FAST, 2: use FAST as a
preprocessor to create an ADAMS model, 3: do both} (switch)
  1 AnalMode - Analysis mode {1: Run a time-marching simulation, 2: create a periodic
linearized model} (switch)
  3 NumBl - Number of blades (-)
  700 TMax - Total run time (s)
  0.05 DT - Integration time step (s)
----- TURBINE CONTROL -----
  0 YCMode - Yaw control mode {0: none, 1: user-defined from routine UserYawCont, 2:
user-defined from Simulink/Labview} (switch)
9999.9 TYCon - Time to enable active yaw control (s) [unused when YCMode=0]
  1 PCMode - Pitch control mode {0: none, 1: user-defined from routine PitchCntrl, 2: user-
defined from Simulink/Labview} (switch)
  0 TPCOn - Time to enable active pitch control (s) [unused when PCMode=0]
  1 VSContrl - Variable-speed control mode {0: none, 1: simple VS, 2: user-defined from
routine UserVSCont, 3: user-defined from Simulink/Labview} (switch)
1000 VS_RtGnSp - Rated generator speed for simple variable-speed generator control (HSS
side) (rpm) [used only when VSContrl=1]
10000 VS_RtTq - Rated generator torque/constant generator torque in Region 3 for simple
variable-speed generator control (HSS side) (N-m) [used only when VSContrl=1]
0.01 0.91 VS_Rgn2K - Generator torque constant in Region 2 for simple variable-speed
generator control (HSS side) (N-m/rpm^2) [used only when VSContrl=1]
9999.9 VS_SIPc - Rated generator slip percentage in Region 2 1/2 for simple variable-speed
generator control (%) [used only when VSContrl=1]
  1 GenModel - Generator model {1: simple, 2: Thevenin, 3: user-defined from routine
UserGen} (switch) [used only when VSContrl=0]
True GenTiStr - Method to start the generator {T: timed using TimGenOn, F: generator
speed using SpdGenOn} (flag)
True GenTiStp - Method to stop the generator {T: timed using TimGenOf, F: when generator
power = 0} (flag)
9999.9 SpdGenOn - Generator speed to turn on the generator for a startup (HSS speed)
(rpm) [used only when GenTiStr=False]
  0.0 TimGenOn - Time to turn on the generator for a startup (s) [used only when
GenTiStr=True]
9999.9 TimGenOf - Time to turn off the generator (s) [used only when GenTiStp=True]
  1 HSSBrMode - HSS brake model {1: simple, 2: user-defined from routine UserHSSBr, 3:
user-defined from Labview} (switch)
9999.9 THSSBrDp - Time to initiate deployment of the HSS brake (s)
9999.9 TiDynBrk - Time to initiate deployment of the dynamic generator brake [CURRENTLY
IGNORED] (s)
9999.9 TTpBrDp(1) - Time to initiate deployment of tip brake 1 (s)
9999.9 TTpBrDp(2) - Time to initiate deployment of tip brake 2 (s)
9999.9 TTpBrDp(3) - Time to initiate deployment of tip brake 3 (s) [unused for 2 blades]
9999.9 TBDeplSp(1) - Deployment-initiation speed for the tip brake on blade 1 (rpm)
9999.9 TBDeplSp(2) - Deployment-initiation speed for the tip brake on blade 2 (rpm)
9999.9 TBDeplSp(3) - Deployment-initiation speed for the tip brake on blade 3 (rpm) [unused
for 2 blades]
9999.9 TYawManS - Time to start override yaw maneuver and end standard yaw control (s)
9999.9 TYawManE - Time at which override yaw maneuver reaches final yaw angle (s)
  0.0 NacYawF - Final yaw angle for yaw maneuvers (degrees)
9999.9 TPitManS(1) - Time to start override pitch maneuver for blade 1 and end standard pitch
control (s)
9999.9 TPitManS(2) - Time to start override pitch maneuver for blade 2 and end standard pitch
control (s)
9999.9 TPitManS(3) - Time to start override pitch maneuver for blade 3 and end standard pitch
control (s) [unused for 2 blades]
9999.9 TPitManE(1) - Time at which override pitch maneuver for blade 1 reaches final pitch (s)
9999.9 TPitManE(2) - Time at which override pitch maneuver for blade 2 reaches final pitch (s)
9999.9 TPitManE(3) - Time at which override pitch maneuver for blade 3 reaches final pitch (s)
[unused for 2 blades]
  -1 BIPitch(1) - Blade 1 initial pitch (degrees)
  -1 BIPitch(2) - Blade 2 initial pitch (degrees)
  -1 BIPitch(3) - Blade 3 initial pitch (degrees) [unused for 2 blades]
  -4 BIPitchF(1) - Blade 1 final pitch for pitch maneuvers (degrees)
  -4 BIPitchF(2) - Blade 2 final pitch for pitch maneuvers (degrees)

```

-4	BIPitchF(3)	- Blade 3 final pitch for pitch maneuvers (degrees) [unused for 2 blades]
----- ENVIRONMENTAL CONDITIONS -----		
9.80665	Gravity	- Gravitational acceleration (m/s^2)
----- FEATURE FLAGS -----		
false	FlapDOF1	- First flapwise blade mode DOF (flag)
false	FlapDOF2	- Second flapwise blade mode DOF (flag)
false	EdgeDOF	- First edgewise blade mode DOF (flag)
False	TeetDOF	- Rotor-teeter DOF (flag) [unused for 3 blades]
false	DrTrDOF	- Drivetrain rotational-flexibility DOF (flag)
True	GenDOF	- Generator DOF (flag)
False	YawDOF	- Yaw DOF (flag)
false	TwFADOF1	- First fore-aft tower bending-mode DOF (flag)
false	TwFADOF2	- Second fore-aft tower bending-mode DOF (flag)
false	TwSSDOF1	- First side-to-side tower bending-mode DOF (flag)
false	TwSSDOF2	- Second side-to-side tower bending-mode DOF (flag)
True	CompAero	- Compute aerodynamic forces (flag)
False	CompNoise	- Compute aerodynamic noise (flag)
----- INITIAL CONDITIONS -----		
0.0	OoPDefl	- Initial out-of-plane blade-tip displacement (meters)
0.0	IPDefl	- Initial in-plane blade-tip deflection (meters)
0.0	TeetDefl	- Initial or fixed teeter angle (degrees) [unused for 3 blades]
0.0	Azimuth	- Initial azimuth angle for blade 1 (degrees)
11.5	RotSpeed	- Initial or fixed rotor speed (rpm)
0.0	NacYaw	- Initial or fixed nacelle-yaw angle (degrees)
0.0	TTDspFA	- Initial fore-aft tower-top displacement (meters)
0.0	TTDspSS	- Initial side-to-side tower-top displacement (meters)
----- TURBINE CONFIGURATION -----		
10	TipRad	- The distance from the rotor apex to the blade tip (meters)
1.	HubRad	- The distance from the rotor apex to the blade root (meters)
1	PSPnEIN	- Number of the innermost blade element which is still part of the pitchable portion of the blade for partial-span pitch control [1 to BldNodes] [CURRENTLY IGNORED] (-)
0.0	UndSling	- Undersling length [distance from teeter pin to the rotor apex] (meters) [unused for 3 blades]
0.0	HubCM	- Distance from rotor apex to hub mass [positive downwind] (meters)
-2	OverHang	- Distance from yaw axis to rotor apex [3 blades] or teeter pin [2 blades] (meters)
-0.1449	NacCMxn	- Downwind distance from the tower-top to the nacelle CM (meters)
0.0	NacCMyn	- Lateral distance from the tower-top to the nacelle CM (meters)
1.3890	NacCMzn	- Vertical distance from the tower-top to the nacelle CM (meters)
19.25	TowerHt	- Height of tower above ground level [onshore] or MSL [offshore] (meters)
0.75	Twr2Shft	- Vertical distance from the tower-top to the rotor shaft (meters)
0.0	TwrRBHt	- Tower rigid base height (meters)
0	ShftTilt	- Rotor shaft tilt angle (degrees)
0.0	Delta3	- Delta-3 angle for teetering rotors (degrees) [unused for 3 blades]
0.0	PreCone(1)	- Blade 1 cone angle (degrees)
0.0	PreCone(2)	- Blade 2 cone angle (degrees)
0.0	PreCone(3)	- Blade 3 cone angle (degrees) [unused for 2 blades]
0.0	AzimBlUp	- Azimuth value to use for I/O when blade 1 points up (degrees)
----- MASS AND INERTIA -----		
0.0	YawBrMass	- Yaw bearing mass (kg)
60.0E3	NacMass	- Nacelle mass (kg)%%%
15.148E3	HubMass	- Hub mass (kg)
0.0	TipMass(1)	- Tip-brake mass, blade 1 (kg)
0.0	TipMass(2)	- Tip-brake mass, blade 2 (kg)
0.0	TipMass(3)	- Tip-brake mass, blade 3 (kg) [unused for 2 blades]
49.130E3	NacYIner	- Nacelle inertia about yaw axis (kg m^2)
250	GenIner	-53.36 Generator inertia about HSS (kg m^2) % 250
34.600E3	HubIner	- Hub inertia about rotor axis [3 blades] or teeter axis [2 blades] (kg m^2)
----- DRIVETRAIN -----		
100.0	GBoxEff	- Gearbox efficiency (%)
95.0	GenEff	- Generator efficiency [ignored by the Thevenin and user-defined generator models] (%)
87.27	GBRatio	- Gearbox ratio (-)87.965
False	GBRevers	- Gearbox reversal {T: if rotor and generator

rotate in opposite directions) (flag)		
9999.9	HSSBrTqF	- Fully deployed HSS-brake torque (N-m)
9999.9	HSSBrDT	- Time for HSS-brake to reach full deployment once initiated (sec) [used only when HSSBrMode=1]
"unused"	DynBrkFi	- File containing a mech-gen-torque vs HSS-speed curve for a dynamic brake [CURRENTLY IGNORED] (quoted string)
1.566E6	DTTorSpr	- 5.6E9 Drivetrain torsional spring (N-m/rad)
3046	DTTorDmp	- 1.0E Drivetrain torsional damper (N-m/(rad/s))
----- SIMPLE INDUCTION GENERATOR -----		

9999.9	SIG_SlPc	- Rated generator slip percentage (%) [used only when VSContrl=0 and GenModel=1]
9999.9	SIG_SySp	- Synchronous (zero-torque) generator speed (rpm) [used only when VSContrl=0 and GenModel=1]
9999.9	SIG_RtTq	- Rated torque (N-m) [used only when VSContrl=0 and GenModel=1]
9999.9	SIG_PORT	- Pull-out ratio (Tpullout/Trated) (-) [used only when VSContrl=0 and GenModel=1]
----- THEVENIN-EQUIVALENT INDUCTION GENERATOR -----		

9999.9	TEC_Freq	- Line frequency [50 or 60] (Hz) [used only when VSContrl=0 and GenModel=2]
9998	TEC_NPol	- Number of poles [even integer > 0] (-) [used only when VSContrl=0 and GenModel=2]
9999.9	TEC_SRes	- Stator resistance (ohms) [used only when VSContrl=0 and GenModel=2]
9999.9	TEC_RRes	- Rotor resistance (ohms) [used only when VSContrl=0 and GenModel=2]
9999.9	TEC_VLL	- Line-to-line RMS voltage (volts) [used only when VSContrl=0 and GenModel=2]
9999.9	TEC_SLR	- Stator leakage reactance (ohms) [used only when VSContrl=0 and GenModel=2]
9999.9	TEC_RLR	- Rotor leakage reactance (ohms) [used only when VSContrl=0 and GenModel=2]
9999.9	TEC_MR	- Magnetizing reactance (ohms) [used only when VSContrl=0 and GenModel=2]
----- PLATFORM -----		

0	PtfmModel	- Platform model {0: none, 1: onshore, 2: fixed bottom offshore, 3: floating offshore} (switch)
"unused"	PtfmFile	- Name of file containing platform properties (quoted string) [unused when PtfmModel=0]
----- TOWER -----		

10	TwrNodes	- Number of tower nodes used for analysis (-)
"Baseline_Tower.dat"	TwrFile	- Name of file containing tower properties (quoted string)
----- NACELLE-YAW -----		

0.0	YawSpr	- Nacelle-yaw spring constant (N-m/rad)
0.0	YawDamp	- Nacelle-yaw damping constant (N-m/(rad/s))
0.0	YawNeut	- Neutral yaw position--yaw spring force is zero at this yaw (degrees)
----- FURLING -----		

False	Furling	- Read in additional model properties for furling turbine (flag)
"unused"	FurlFile	- Name of file containing furling properties (quoted string) [unused when Furling=False]
----- ROTOR-TEETER -----		

0	TeetMod	- Rotor-teeter spring/damper model {0: none, 1: standard, 2: user-defined from routine UserTeet} (switch) [unused for 3 blades]
0.0	TeetDmpP	- Rotor-teeter damper position (degrees) [used only for 2 blades and when TeetMod=1]
0.0	TeetDmp	- Rotor-teeter damping constant (N-m/(rad/s)) [used only for 2 blades and when TeetMod=1]
0.0	TeetCDmp	- Rotor-teeter rate-independent Coulomb-damping moment (N-m) [used only for 2 blades and when TeetMod=1]
0.0	TeetSStP	- Rotor-teeter soft-stop position (degrees)

[used only for 2 blades and when TeetMod=1]	0.0	TeetHStP	- Rotor-teeter hard-stop position (degrees)
[used only for 2 blades and when TeetMod=1]	0.0	TeetSSSp	- Rotor-teeter soft-stop linear-spring constant (N-m/rad) [used only for 2 blades and when TeetMod=1]
[used only for 2 blades and when TeetMod=1]	0.0	TeetHSSp	- Rotor-teeter hard-stop linear-spring constant (N-m/rad) [used only for 2 blades and when TeetMod=1]
----- TIP-BRAKE -----			
0.0	TBDrConN	- Tip-brake drag constant during normal operation, Cd*Area (m^2)	
0.0	TBDrConD	- Tip-brake drag constant during fully-deployed operation, Cd*Area (m^2)	
0.0	TpBrDT	- Time for tip-brake to reach full deployment once released (sec)	
----- BLADE -----			
"Baseline_Blade.dat"	BldFile(1)	- Name of file containing properties for blade 1 (quoted string)	
"Baseline_Blade.dat"	BldFile(2)	- Name of file containing properties for blade 2 (quoted string)	
"Baseline_Blade.dat"	BldFile(3)	- Name of file containing properties for blade 3 (quoted string) [unused for 2 blades]	
----- AERODYN -----			
"ADfile.ipt"	ADFile	- Name of file containing AeroDyn input parameters (quoted string)	
----- NOISE -----			
"unused"	NoiseFile	- Name of file containing aerodynamic noise input parameters (quoted string) [used only when CompNoise=True]	
----- ADAMS -----			
"Baseline_ADAMS.dat"	ADAMSFile	- Name of file containing ADAMS-specific input parameters (quoted string) [unused when ADAMSPrep=1]	
----- LINEARIZATION CONTROL -----			
"Baseline_Linear.dat"	LinFile	- Name of file containing FAST linearization parameters (quoted string) [unused when AnalMode=1]	
----- OUTPUT -----			
True	SumPrint	- Print summary data to "<RootName>.fsm" (flag)	
1	OutFileFmt	- Format for tabular (time-marching) output file(s) (1: text file [<RootName>.out], 2: binary file [<RootName>.outb], 3: both) (switch)	
True	TabDelim	- Use tab delimiters in text tabular output file? (flag)	
"E510.3E2"	OutFmt	- Format used for text tabular output (except time). Resulting field should be 10 characters. (quoted string) [not checked for validity!]	
100.0	TStart	- Time to begin tabular output (s)	
1	DecFact	- Decimation factor for tabular output {1: output every time step} (-)	
1.0	SttsTime	- Amount of time between screen status messages (sec)	
0.0	NcIMUxn	- Downwind distance from the tower-top to the nacelle IMU (meters)	
0.0	NcIMUyn	- Lateral distance from the tower-top to the nacelle IMU (meters)	
0.0	NcIMUzn	- Vertical distance from the tower-top to the nacelle IMU (meters)	
0.99	ShftGagL	- Distance from rotor apex [3 blades] or teeter pin [2 blades] to shaft strain gages [positive for upwind rotors] (meters)	
2	NTwGages	- Number of tower nodes that have strain gages for output [0 to 9] (-)	
4,7	TwrGagNd	- List of tower nodes that have strain gages [1 to TwrNodes] (-) [unused if NTwGages=0]	
0	NBlGages	- Number of blade nodes that have strain gages for output [0 to 9] (-)	
0	BldGagNd	- List of blade nodes that have strain gages [1	

```

to BldNodes] (-) [unused if NBlGages=0]
      OutList      - The next line(s) contains a list of output
parameters.  See OutList.xlsx for a listing of available output
channels, (-)
"WindVxi, WindVyi, WindVzi"          - Wind-speed components
"HorWndDir, VerWndDir"                - Wind directions
"BldPitch2, RootFxc1"                 - Blade 2 pitch angle
"LSShftFxa"                           - IP blade 1,2 tip deflections
"TwstDefl1, TwstDefl2, TwstDefl3"     - Blade torsional tip twist
deflections
"RootMxb2, RootMyb2, RootMzb2"       - Blade 2 root moments
"LSShftFys, LSShftFzs, LSShftFxs"    - Non-rotating LSS shear forces
"LSSTipMzs, LSSTipMys, LSShftMxs, LSShftPwr, RotSpeed, GenTq, RotCp"
END of FAST input file (the word "END" must appear in the first 3
columns of this last line).
-----
-----

```

Appendix C Rigid Dynamics Input Files

C.1 Python Code Input File

General code
<pre> import math # imports module for matemactical operations Env=CS_Environment.FindFirstNonNull()# finds the environment(rigid dynamics) optional CS_Environment.GetDefault() Sys=Env.System # gets the system from the environment , system is the model #print dir(CS_Body) Damping=System.Array[float] ([1500]) RYDamping=System.Array[float] ([900]) RZDamping=System.Array[float] ([900]) RXDamping=System.Array[float] ([900]) M_RY_stiffness=System.Array[float] ([1]) M_RZ=stiffness=System.Array[float] ([1]) Cage_stiffness=System.Array[float] ([1000]) pi=22.0/7 Rad2Deg=180/pi# is 1 radian import cmath import math RY_stiff=System.Array.CreateInstance(float,3,2) RY_stiff[0,0]=-1 RY_stiff[0,1]=1000 RY_stiff[1,0]=0.0 RY_stiff[1,1]=0.0 RY_stiff[2,0]=1 RY_stiff[2,1]=1000 def GetStiffness(file): fich=open(file,'r') data=[] data2=[] n=0# for ignoring the first line of CSV file for line in fich: if n>0:# number of text rows data.append(line.strip().split('/n')) n=n+1# n can be modifioed to romove text from csv file data_len=data.Count for i in range(0,data_len): datastr=data[i] data2.append(datastr[0].split(',')) col_len=data2[i].Count #print col_len #print data_len </pre>

```

array =System.Array.CreateInstance(float,data_len,col_len )
for k in range (0,data_len):
    DT=data2[k]

    for l in range (0,col_len):
        array[k,l]=float(DT[l])
return array
def GetBasis(angle,Joint_Name):
print angle[0]*180/pi
if angle[0]>0 and angle[0]<pi/2:
    anglex=angle[2]
elif angle[0]>pi/2:
    anglex=angle[2]
elif angle[0]<0 and angle[0]>-pi/2:
    anglex=angle[2]
elif angle[0]<-pi/2:
    anglex=angle[2]
else:
    raise Exception("wrong angle")
anglez=pi-(angle[0])
angley=angle[1]
#anglez=0
#anglex=0
angley=0#-0.8/(180/pi)
#print anglex*180/pi
#print angley*180/pi
#print anglez*180/pi
Basis_matrix=System.Array.CreateInstance(float,3,3)#
Basis_matrix[0,0]=(math.cos(angley)*math.cos(anglez))
Basis_matrix[0,1]=-
((math.cos(anglez)*math.sin(anglex)*math.sin(angley))-
(math.cos(anglex)*math.sin(anglez)))

Basis_matrix[0,2]=(math.cos(anglez)*math.cos(anglex)*math.sin(angley)
)+(math.sin(anglex)*math.sin(anglez))
    Basis_matrix[1,0]=-(math.cos(angley)*math.sin(anglez))

Basis_matrix[1,1]=(math.cos(anglex)*math.cos(anglez))+(math.sin(angl
ex)*math.sin(angley)*math.sin(anglez))
    Basis_matrix[1,2]=-((-
math.cos(anglez)*math.sin(anglex))+(math.cos(anglex)*math.sin(angley)
)*math.sin(anglez))
    Basis_matrix[2,0]=-(math.sin(angley))
    Basis_matrix[2,1]=-(math.cos(angley)*math.sin(anglex))
    Basis_matrix[2,2]=math.cos(anglex)*math.cos(angley)
    for q in range(0,3):
        for qq in range (0,3):
            #print Basis_matrix[q,qq]
            qp=1
    return Basis_matrix

def Getangles (Body_id_CS,Bodyname):
    IRC=CS_PositionMeasure (Body_id_CS)
    Pos_measure=Bodyname.Name+' _Pos=CS_PositionMeasure (Body_id_CS) '
    exec(Pos_measure)

Fillvals=Bodyname.Name+' _Pos_data='+Bodyname.Name+' _Pos.FillDataThro
ughTime'
    #print (Fillvals)
    exec(Fillvals)

g2="globals().Add('"+Bodyname.Name+"_Pos_data','"+Bodyname.Name+"_Pos
_data)"
    exec(g2)
    addmeasure='Sys.AddMeasure ('+Bodyname.Name+' _Pos) '
    exec(addmeasure)
    print addmeasure

```

```

Arr=IRC.Values
#print dir(IRC)
#xcalc=((Arr[2])/((Arr[1])))
Anglesx=(cmath.phase((Arr[1])+((Arr[2])*1j)))-((cmath.pi)/4)
#Anglesx=math.atan(xcalc)
ycalc=((Arr[2])/(0.612+(Arr[0])))
Anglesy=math.atan(ycalc)
Anglesy=0
zcalc=(0.612+(Arr[0]))/(Arr[1])
#Anglesz=math.atan(zcalc)
Anglesz=(cmath.phase((Arr[1])+((0.612+ Arr[0])*1j)))
#print Anglesx*Rad2Deg
#print (Arr[0])
#print (Arr[1])
#print (Arr[2])
#Anglesx=0
Anglesy=0
if Pos_measure[0]=='M':
    if Pos_measure[3]=='1':
        Anglesz=-0.139622177964977-(pi/2)#
        Anglesx=Anglesx+(pi/2)
    elif Pos_measure[3]=='2':
        Anglesz=-0.139622177964977#
elif Pos_measure[0]=='S':
    if Pos_measure[3]=='1':
        Anglesz=0.139622177964977# must be chnaged
    elif Pos_measure[3]=='2':
        Anglesz=-0.139622177964977# must be chnaged
return Anglesx,Anglesy,Anglesz

def
Set_Parameters(Bearing_Name,Row_Number,Component_Type,Joint_Type,sti
ffness,Joint_Angle):# definition of a function to set joint
parameters
    Base_Name=Bearing_Name+'_Row'+Row_Number+'_'+Component_Type#
    identiofies which bearing in the entire system
    Joint_Name=Base_Name+Joint_Type# joint type identifies which
    joint in a specific bearing
    Find_Joint=Joint_Name+'=CS_Joint.Find(_jid)'# synthesize command
    for getting the joint ID;
    exec(Find_Joint)#executes command

Jiont_Stiffness_Variable=Joint_Name+'_Stiffness_Variable'+'=CS_Varia
ble()'# synthesize the definition a variable to hold the stiffness
values of the selected joint
    exec(Jiont_Stiffness_Variable)#execute
    Jiont_Stiffness_Array=Joint_Name+'_Stiffness_Array'+
    '=GetStiffness("radial_stiffness.csv")'
    exec(Jiont_Stiffness_Array)
    Jiont_Stiffness_Table=Joint_Name+'_Stiffness_Table'+
    '=CS_PointsTable('+Joint_Name+'_Stiffness_Array+')'
    exec(Jiont_Stiffness_Table)

Variable_Table=Joint_Name+'_Stiffness_Variable'+'.SetTable('+Joint_N
ame+'_Stiffness_Table'+ ') '
    exec(Variable_Table)

Apply_Stiffness=Joint_Name+'.SetStiffnessTerm(1,1,'+Joint_Name+'_Sti
ffness_Variable'+') '
    #print type(Main_Row1_Ball4_IR_to_Ball)
    exec(Apply_Stiffness)
    ##### axial stiffness
    Jiont_axStiffness_Array=Joint_Name+'_AXStiffness_Array'+
    '=GetStiffness("rad.csv") '
    exec(Jiont_axStiffness_Array)
    Jiont_Stiffness_Table=Joint_Name+'_Stiffness_Table'+
    '=CS_PointsTable('+Joint Name+'_ AXStiffness Array'+') '

```

```

exec(Joint_Stiffness_Table)
Joint_axStiffness_Table=Joint_Name+'_AXStiffness_Table'+
'=CS_PointsTable('+Joint_Name+'_AXStiffness_Array'+')'
exec(Joint_axStiffness_Table)

Joint_axStiffness_Variable=Joint_Name+'_AXStiffness_Variable'+'=CS_V
ariable()'# synthesize the definition a variable to hold the
stiffness values of the selected joint
exec(Joint_axStiffness_Variable)#execute

Variable_axTable=Joint_Name+'_AXStiffness_Variable'+'.SetTable('+Joi
nt_Name+'_AXStiffness_Table'+')'
exec(Variable_axTable)

Apply_axStiffness=Joint_Name+'.SetStiffnessTerm(0,0,'+Joint_Name+'_A
XStiffness_Variable'+')'
#exec(Apply_axStiffness)

#                               Basis
#####
#####
#####

Joint_Basis_Matrix=Joint_Name+'_Basis_Matrix'+'=GetBasis(Joint_Angle
,Joint_Name)'
exec(Joint_Basis_Matrix)

Apply_Basis_Matrix=Joint_Name+'.ReferenceCoordinateSystem.Basis.Matr
ix='+Joint_Name+'_Basis_Matrix'
exec(Apply_Basis_Matrix)

#exec('basprin('+Joint_Name+'.ReferenceCoordinateSystem.Basis.Matrix
)')
##### damping

Joint_Damping_Variable=Joint_Name+'_Damping_Variable'+'=CS_Variable(
)'
exec(Joint_Damping_Variable)
#print 'variable made'

Damping_Variable=Joint_Name+'_Damping_Variable'+'.SetConstantValues(
Damping)'
exec(Damping_Variable)

Apply_Damping=Joint_Name+'.SetDampingTerm(1,1,'+Joint_Name+'_Damping
_Variable'+')'
exec(Apply_Damping)

#####
#####
#####
#                               Measue
#####
#####
#####
Bushmeasure=Joint_Name+'_Forces'+ Joint_Name+'.GetForce()'
exec(Bushmeasure)
glob='global '+Joint_Name+'_Forces_Vals'
exec(glob)

Bushmeasurevals=Joint_Name+'_Forces_Vals'+Joint_Name+'_Forces.FillD
ataThroughTime'
exec(Bushmeasurevals)
addmeasure='Sys.AddMeasure('+Joint_Name+'_Forces)'
print addmeasure

```

```

exec(addmeasure)

g2="globals().Add('" + Joint_Name + "_Forces_Vals', '" + Joint_Name + "_Forces
_Vals)"
exec(g2)

#####
#####
#                               Damping correction
#####
#####
Load_Name=Joint_Name+'_Damp_Load'
Define_Load=Load_Name+'=CS_JointDOFLoad('" + Joint_Name + ',1)'
exec(Define_Load)

(ret,found,time)=Sys.FindOrCreateInternalMeasure(CS_Measure.E_Measure
eType.E_Time)
Set_Time_Input= Load_Name+'.SetInputMeasure(time)'
exec(Set_Time_Input)
Velocities_Name=Joint_Name+'_Velocities'
Get_Velocity=Velocities_Name+'=' + Joint_Name+'.GetVelocity()'
exec(Get_Velocity)
Y_Velocity_Name=Joint_Name+'_Y_Velocity'

Get_Component_velocity=Y_Velocity_Name+'=CS_ComponentMeasure('" + Veloc
ities_Name + ',1)'
exec(Get_Component_velocity)
Addmeasure='Sys.AddMeasure('" + Velocities_Name + ') '
exec(Addmeasure)
Addmeasure='Sys.AddMeasure('" + Y_Velocity_Name + ') '
exec(Addmeasure)
setloadmeasure=
Load_Name+'.SetInputMeasure('" + Y_Velocity_Name + ') '
exec (setloadmeasure)
SetLoadFunc=Load_Name+'.SetFunc('" + Y_Velocity_Name + '*-1500",0)'
exec(SetLoadFunc)

#####
#####
#                               Load condition
#####
#####
Translation_Name=Joint_Name+'_Translations'
Y_Translation_Name=Joint_Name+'_Y_Translation'

Get_Translation=Translation_Name+'=' + Joint_Name+'.GetTranslation()'
exec(Get_Translation)

Get_Y_Component_Translation=Y_Translation_Name+'=CS_ComponentMeasure
('" + Translation_Name + ',1)'
exec(Get_Y_Component_Translation)
Addmeasure='Sys.AddMeasure('" + Translation_Name + ') '
#exec(Addmeasure)
Addmeasure='Sys.AddMeasure('" + Y_Translation_Name + ') '
exec(Addmeasure)
Condition_Name=Joint_Name+'_Damping_condition'

Condition=Condition_Name+'=CS_Condition('" + Y_Translation_Name + ',0.000
1,0.5)'
exec(Condition)
print Condition
Apply_conddition=Load_Name+'.Condition=' + Condition_Name
exec(Apply_conddition)
AddLoads='Env.Loads.Add('" + Load_Name + ') '
exec(AddLoads)

```

```

def Cage_code(Bearing_Name,Row_Number,Component_Type,Joint_Type):#
definition of a function to set joint parameters
    Base_Name=Bearing_Name+'_Row'+Row_Number+'_'+Component_Type#
identiofies which bearing in the entire system
    Joint_Name=Base_Name+Joint_Type# joint type identifies which
joint in a specific bearing
    Find_Joint=Joint_Name+'=CS_Joint.Find(_jid) '# synthesize command
for getting the joint ID;
    exec(Find_Joint)#executes command

Jiont_Stiffness_Variable=Joint_Name+'_XX_Stiffness_Variable'+'=CS_Va
riable() '# synthesize the definition a variable to hold the
stiffness values of the selected joint
    exec(Jiont_Stiffness_Variable)#execute

Variable_Table=Joint_Name+'_XX_Stiffness_Variable'+'.SetConstantValu
es(Cage_stiffness)'
    exec(Variable_Table)

Apply_Stiffness=Joint_Name+'.SetStiffnessTerm(1,1, '+Joint_Name+'_XX_
Stiffness_Variable'+')'
    #exec(Apply_Stiffness)

def GetCageIR(file):
    fich=open(file,'r')
    dataIR=[]
    dataIR2=[]
    n=0# for ignoring the first line of CSV file
    for line in fich:
        if n>0:# number of text rows
            dataIR.append(line.strip().split('/n'))
            n=n+1# n can be modified to romove text from csv file
    dataIR_len=dataIR.Count
    for i in range(0,dataIR_len):
        dataIRstr=dataIR[i]
        dataIR2.append(dataIRstr[0].split(','))
    col_len=dataIR2[i].Count
    #print col_len
    #print dataIR_len
    array =System.Array.CreateInstance(float,dataIR_len,col_len )
    for k in range (0,dataIR_len):
        DT=dataIR2[k]
        #print DT
        for l in range (0,col_len):
            if l==1:
                pp=(float(DT[l])*-
1)+(0.45251645592106043*float(DT[l]))
            else:
                pp=DT[l]
            array[k,l]=float(pp)
    return array

def GetCageOR(file):
    fich=open(file,'r')
    dataOR=[]
    dataOR2=[]
    n=0# for ignoring the first line of CSV file
    for line in fich:
        if n>0:# number of text rows
            dataOR.append(line.strip().split('/n'))
            n=n+1# n can be modified to romove text from csv file
    dataOR_len=dataOR.Count

```

<pre> for i in range(0,dataOR_len): dataORstr=dataOR[i] dataOR2.append(dataORstr[0].split(',')) col_len=dataOR2[i].Count array =System.Array.CreateInstance(float,dataOR_len,col_len) for k in range (0,dataOR_len): DT=dataOR2[k] #print DT for l in range (0,col_len): if l==1: pp2=float(DT[l])*0.45251645592106043 else: pp2=DT[l] array[k,l]=float(pp2) return array def noth(): IR=CS_Body.Find(_bid) IRC=IR.InertiaBodyCoordinateSystem ddt=CS_PositionMeasure(IRC) glob='ddtx=ddt.FillDataThroughTime' exec(glob,locals()) g2="globals().Add('ddtx',ddtx)" exec(g2) #exec(glob)# in globals() Sys.AddMeasure(ddt) return ddtx def bodycode(Bodyname): bodyid=Bodyname+'_CS_Body.Find(_bid)' exec(bodyid) bodyCS=Bodyname+'_CS'+Bodyname+'.InertiaBodyCoordinateSystem' exec(bodyCS) angles=Bodyname+'_Joint_Angle=Getangles('+ Bodyname+'_CS,'+Bodyname+')' exec(angles) #retn='return '+Bodyname+'_Joint_Angle' #exec(retn) rtv=Bodyname+'_Joint_Angle' return eval(rtv) </pre>	
<pre> Set_Parameters('M','R1','Ball1','_OR_to_Ball','stiffness.csv',M_R1_B 1_ANG) </pre>	
<pre> Environment Code </pre>	<pre> d_m=((2*0.36416)+(2*0.4325))/2# pitch diameter D=0.0764#rolling element diameter alpha=8/(180/pi)# contact angle gamma=(D*math.cos(alpha))/d_m rat=rpm*(0.5*gamma) driver=CS_Driver(shaft,System.Array[int]([0]),CS_Driver.E_MotionType .E_Velocity) (ret,found,time) = Sys.FindOrCreateInternalMeasure(CS_Measure.E_MeasureType.E_Time) driver_Array=GetStiffness('RPM.csv')# Get stiffness converts CSV file to array of floats driver_Table=CS_PointsTable(driver_Array)# table has to be a CS_points table </pre>

```

driver.SetInputMeasure(time)
#ww=CS_Variable()
driver.SetTable(driver_Table)
Env.Drivers.Add(driver)

M_R2_IC_driver=CS_Driver(M_R2_IC,System.Array[int]([0]),CS_Driver.E_MotionType.E_Velocity) #### minus
(ret,found,time) =
Sys.FindOrCreateInternalMeasure(CS_Measure.E_MeasureType.E_Time)
M_R2_IC_Array=GetCageOR('RPM.csv')#
M_R2_IC_Table=CS_PointsTable(M_R2_IC_Array)# table has to be a
CS_points table
M_R2_IC_driver.SetInputMeasure(time)
M_R2_IC_driver.SetTable(M_R2_IC_Table)
Env.Drivers.Add(M_R2_IC_driver)

M_R2_OC_driver=CS_Driver(M_R2_OC,System.Array[int]([0]),CS_Driver.E_MotionType.E_Velocity) #### plus
(ret,found,time) =
Sys.FindOrCreateInternalMeasure(CS_Measure.E_MeasureType.E_Time)
M_R2_OC_Array=GetCageOR('RPM.csv')#
M_R2_OC_Table=CS_PointsTable(M_R2_OC_Array)# table has to be a
CS_points table
M_R2_OC_driver.SetInputMeasure(time)
M_R2_OC_driver.SetTable(M_R2_OC_Table)
Env.Drivers.Add(M_R2_OC_driver)

(ret,found,time) =
Sys.FindOrCreateInternalMeasure(CS_Measure.E_MeasureType.E_Time)

speedfile='RPM.csv'

M_R1_IC_driver=CS_Driver(M_R1_IC,System.Array[int]([0]),CS_Driver.E_MotionType.E_Velocity) #### minus
(ret,found,time) =
Sys.FindOrCreateInternalMeasure(CS_Measure.E_MeasureType.E_Time)
M_R1_IC_Array=GetCageOR(speedfile)#
M_R1_IC_Table=CS_PointsTable(M_R1_IC_Array)# table has to be a
CS_points table
M_R1_IC_driver.SetInputMeasure(time)
M_R1_IC_driver.SetTable(M_R1_IC_Table)
Env.Drivers.Add(M_R1_IC_driver)

M_R1_OC_driver=CS_Driver(M_R1_OC,System.Array[int]([0]),CS_Driver.E_MotionType.E_Velocity) #### plus
(ret,found,time) =
Sys.FindOrCreateInternalMeasure(CS_Measure.E_MeasureType.E_Time)
M_R1_OC_Array=GetCageOR(speedfile)#
M_R1_OC_Table=CS_PointsTable(M_R1_OC_Array)# table has to be a
CS_points table
M_R1_OC_driver.SetInputMeasure(time)
M_R1_OC_driver.SetTable(M_R1_OC_Table)
Env.Drivers.Add(M_R1_OC_driver)

Sys.SetBuildAllJointsKinematic(0)

##### FX
Hub_Joint_FX_Load=CS_JointDOFLoad(M_R1_IR,0)# inner must be changed
to reflect hub joint
Hub_Joint_FX_Array=GetStiffness('BAF.csv')# Get stiffness converts
CSV file to array of floats
Hub_Joint_FX_Load.SetInputMeasure(time)# Must set input measure time
so that load will be applied at each time step. other input measure
can be added
Hub Joint FX Table=CS_PointsTable(Hub Joint FX Array)# table has to

```

<pre> be a CS_points table Hub_Joint_FX_Load.SetTable(Hub_Joint_FX_Table)# Assign table #Env.Loads.Add(Hub_Joint_FX_Load)# Add load to the solution(environment) ##### FY Hub_Joint_FY_Load=CS_JointDOFLoad(M_R1_IR,1)# inner must be changed to reflect hub joint Hub_Joint_FY_Array=GetStiffness('BFY.csv')# Get stiffness converts CSV file to array of floats Hub_Joint_FY_Load.SetInputMeasure(time)# Must set input measure time so that load will be applied at each time step. other input measure can be added Hub_Joint_FY_Table=CS_PointsTable(Hub_Joint_FY_Array)# table has to be a CS_points table Hub_Joint_FY_Load.SetTable(Hub_Joint_FY_Table)# Assign table #Env.Loads.Add(Hub_Joint_FY_Load)# Add load to the solution(environment) ##### FZ Hub_Joint_FZ_Load=CS_JointDOFLoad(M_R1_IR,2)# inner must be changed to reflect hub joint Hub_Joint_FZ_Array=GetStiffness('BFZ.csv')# Get stiffness converts CSV file to array of floats Hub_Joint_FZ_Load.SetInputMeasure(time)# Must set input measure time so that load will be applied at each time step. other input measure can be added Hub_Joint_FZ_Table=CS_PointsTable(Hub_Joint_FZ_Array)# table has to be a CS_points table Hub_Joint_FZ_Load.SetTable(Hub_Joint_FZ_Table)# Assign table #Env.Loads.Add(Hub_Joint_FZ_Load)# Add load to the solution(environment) </pre>	
<pre> Results Code bs=(1, 2,3,4,5,6,7,8,9,10,11,12,13,14,15,16,17,18,19,20,21,22,23,24,25,26,2 7,28) for b in bs: ballname='M_R1_B'+ str(b) Jointname='M_RowR1_Ball'+str(b)+'_OR_to_Ball' force_values='Force_values='+Jointname+'_Forces_Vals()' exec(force_values) Position_values='Position_values='+ballname+'_Pos_data()' exec(Position_values) fname='filename="'+ballname+'.csv"' exec(fname) fich=open(filename,'w') fich.write('Time,X_Pos,Y_Pos,Z_Pos,FX,FY,FZ,MX,MY,MZ\n') nbValues=Force_values.GetLength(0) for i in range(0,nbValues): fich.write('{0:11.5f},{1:11.4e},{2:11.4e},{3:11.4e},{4:11.4e},{5:11. 4e},{6:11.4e},{7:11.4e},{8:11.4e},{9:11.4e}\n'.format(Position_value s[i,0],Position_values[i,1],Position_values[i,2],Position_values[i,3],Force_values[i,1],Force_values[i,2],Force_values[i,3],Force_values [i,4],Force_values[i,5],Force_values[i,6])) fich.close() #Force_values=M_RowR1_Ball1_IR_to_Ball_Forces() #Position_values=M_R1_B1_Pos_data() bs=(1, 2,3,4,5,6,7,8,9,10,11,12,13,14,15,16,17,18,19,20,21,22,23,24,25,26,2 7,28) </pre>	

```

for b in bs:
    ballname='M_R2_B'+ str(b)
    Jointname='M_RowR2_Ball'+str(b)+'_OR_to_Ball'
    force_values='Force_values='+Jointname+'_Forces_Vals()'
    exec(force_values)
    Position_values='Position_values='+ballname+'_Pos_data()'
    exec(Position_values)
    fname='filename="'+ballname+'.csv"'
    exec(fname)
    fich=open(filename, 'w')
    fich.write('Time,X_Pos,Y_Pos,Z_Pos,FX,FY,FZ,MX,MY,MZ\n')
    nbValues=Force_values.GetLength(0)
    for i in range(0,nbValues):

fich.write('{0:11.5f},{1:11.4e},{2:11.4e},{3:11.4e},{4:11.4e},{5:11.
4e},{6:11.4e},{7:11.4e},{8:11.4e},{9:11.4e}\n'.format(Position_value
s[i,0],Position_values[i,1],Position_values[i,2],Position_values[i,3
],Force_values[i,1],Force_values[i,2],Force_values[i,3],Force_values
[i,4],Force_values[i,5],Force_values[i,6]))
    fich.close()

IRF=velvals()
len=IRF.GetLength(0)
fich=open('IRFs.csv', 'w')
fich.write('Time,MX\n')
for i in range(0,len):
    fich.write('{0:11.5f},{1:11.4e}\n'.format(IRF[i,0],IRF[i,1]))
fich.close()

IRF=None

IRF=Row2_H_force_vals()
len=IRF.GetLength(0)
fich=open('Row2_H.csv', 'w')
fich.write('Time,FX,FY,FZ,MX,MY,MZ\n')
for i in range(0,len):

print([IRF[i,0],IRF[i,1],IRF[i,2],IRF[i,3],IRF[i,4],IRF[i,5],IRF[i,6
]])

fich.write('{0:11.5f},{1:11.4e},{2:11.4e},{3:11.4e},{4:11.4e},{5:11.
4e},{6:11.4e}\n'.format(IRF[i,0],IRF[i,1],IRF[i,2],IRF[i,3],IRF[i,4]
,IRF[i,5],IRF[i,6]))
fich.close()

IRF=None

IRF=Row1_H_force_vals()
len=IRF.GetLength(0)
fich=open('Row1_H.csv', 'w')
fich.write('Time,FX,FY,FZ,MX,MY,MZ\n')
for i in range(0,len):

fich.write('{0:11.5f},{1:11.4e},{2:11.4e},{3:11.4e},{4:11.4e},{5:11.
4e},{6:11.4e}\n'.format(IRF[i,0],IRF[i,1],IRF[i,2],IRF[i,3],IRF[i,4]
,IRF[i,5],IRF[i,6]))
fich.close()

IRF=None

IRF=Row12_H_force_vals()
len=IRF.GetLength(0)

```

```
fich=open('Row12_H.csv','w')
fich.write('Time,FX,FY,FZ,MX,MY,MZ\n')
for i in range(0,len):

fich.write('{0:11.5f},{1:11.4e},{2:11.4e},{3:11.4e},{4:11.4e},{5:11.4e},
{6:11.4e}\n'.format(IRF[i,0],IRF[i,1],IRF[i,2],IRF[i,3],IRF[i,4],
,IRF[i,5],IRF[i,6]))
fich.close()
```